THE APPLICATION OF PASSIVE FLOW CONTROL TO BILEAFLET MECHANICAL HEART VALVE LEAKAGE JETS

A Thesis
Presented To
The Academic Faculty

By

David W. Murphy

In Partial Fulfillment
Of the Requirements for the Degree
Master of Science in Mechanical Engineering

Georgia Institute of Technology

December, 2009

THE APPLICATION OF PASSIVE FLOW CONTROL TO BILEAFLET MECHANICAL HEART VALVE LEAKAGE JETS

Approved By:

Dr. Ajit Yoganathan, Advisor
Wallace H. Coulter Department
of Biomedical Engineering
Georgia Institute of Technology

Dr. Ari Glezer, Co-Advisor
George W. Woodruff School of
Mechanical Engineering
Georgia Institute of Technology

Dr. Rudy Gleason
George W. Woodruff School of
Mechanical Engineering
Georgia Institute of Technology

Date Approved: Oct. 10, 2009

ACKNOWLEDGEMENTS

It's done! Many thanks to all who have helped out along the way. In no particular order:

- Thanks to Jelena Vukasinovic for helping make the valve mounting system.
- Thanks to Jack and Erica and the rest of the nurses in the Georgia Tech Health Clinic phlebotomy lab for drawing blood.
- Thanks to my many blood donors, without whom this work would really not have been possible (and to whom I am now known as Dracula!)
- I am thankful for the financial support provided by a National Science Foundation Graduate Research Fellowship
- I would like to thank my advisors, Dr. Ajit Yoganathan and Dr. Ari Glezer, for helping me to develop professionally as a researcher and engineer.
- Thanks to the whole CFM Lab for their friendship, advice, and good humor. Thanks especially to Prasad for being a never-ending supply of good advice, to Helene for actually reading every word of this thesis (you and I may be the only ones!), to Yap for his friendship and keen interest and good advice. Thanks to the rest of Wing 2A, too, especially Dave Bark, William, and Julia.
- Thanks to the guys at the A1 House, past and present, especially Josh, Marc, Manny, Tim, Dan, Bing, and Masa for their friendship, fellowship, and encouragement.
- Also thanks to the Communist Dinner Club, especially Valli, Elisha, and Hiroko for many fun evenings, good community, and delicious food.

- Thanks to the “OM Girls” (Heidi, Anna, Jill M., Ashley, and Jill L.) for their friendship and encouragement
- Thanks to my new advisors, Dr. Jeannette Yen and Dr. Don Webster, for their understanding and support when this thesis dragged out further than anyone thought humanly possible.
- Everlasting thanks to my family: Mom, Dad, Michael, and Katie (plus one in the oven!)
- I am nothing if not grateful to my Creator and God, Jesus Christ, for sustaining me through the often difficult, sometimes exhilarating, life that is grad school.

TABLE OF CONTENTS

LIST OF TABLES

LIST OF FIGURES

NOMENCLATURE

α	Fin angle
D	Distance between two sets of fins
d_1	Distance between two adjacent fins
h	Fin height
l	Fin length
u	Streamwise velocity component
u_{rms}	Streamwise velocity root-mean-square
v	Cross-stream velocity component
v_{rms}	Cross-stream velocity root-mean-square
ω	Vorticity
τ_{xy}	Reynolds shear stress
σ_m	Standard error
PE	Percent error
$\bar{x}$	Population mean
St	Strouhal number
f_f	Frequency of jet flapping
Re	Reynolds Number
ρ	Fluid density
V	Bulk mean velocity
μ	Dynamic viscosity
$Y_{0.5}$	Jet half-width

W	B-datum gap width
η_k	Kolmogorov length scale
CFD	Computational Fluid Dynamics
FFT	Fast Fourier Transform
LDV	Laser Doppler Velocimetry
DPIV	Digital Particle Image Velocimetry
RBC	Red Blood Cell
SJM	Saint Jude Medical
TAT	Thrombin-Antithrombin III
VG	Vortex Generators

SUMMARY

Bileaflet mechanical heart valves (BMHVs), though a life-saving tool in treating heart valve disease, are often associated with serious complications, including a high risk of hemolysis, platelet activation, and thromboembolism. One likely cause of this hyper-coagulative state is the nonphysiologic levels of stress experienced by the erythrocytes and platelets flowing through the BMHVs. Research has shown that the combination of shear stress magnitude and exposure time found in the highly transient leakage jet emanating from the b-datum gap during valve closure is sufficient to cause hemolysis and platelet activation. Regions of flow stasis in the valve vicinity may also allow activated platelets to aggregate and form thrombus.

This thesis addresses the hypothesis that passive flow control may have the potential to reduce flow-induced thrombogenicity by altering the fluid mechanics of bileaflet mechanical heart valves. To test this hypothesis, a steady model of the regurgitant b-datum line jet was developed and studied. This model served as a test bed for various vortex generator array designs. The fluid mechanics of the b-datum line jet model was investigated with flow visualization and particle image velocimetry. *In vitro* tests with whole human blood were performed with and without the vortex generators in order to determine how the presence of the passive flow control affected the propensity of the blood to form thrombus. An effort was then made to correlate the fluid mechanics of the jet model with the procoagulant potential results from the blood experiments. The effect of the vortex generators on the fluid mechanics of the valve under physiologic pulsatile

conditions was also investigated via flow visualization in the Georgia Tech Left Heart Simulator.

By studying a steady model of the regurgitant b-datum line jet, it was found, using an *in vitro* system with whole human blood, that the presence of vortex generators significantly decreased the blood's propensity for thrombus formation. The potential of applying passive flow control to cardiovascular hardware in order to mitigate the injurious effects of shear-induced platelet activation is thus demonstrated.

The investigation into the effect of vortex generators on the fluid mechanics of the b-datum line jet showed that the jet oscillated aperiodically and that the effect of the applied flow control was played out at both the scale of the chamber (large-scale) and on the scale of the vortex generator fins (small-scale). On the large scale, the presence of vortex generators appeared to decrease the magnitude or frequency of jet oscillation, thereby stabilizing the jet. After removing the effect of the large-scale oscillations via phase averaging, the effect of the vortex generators on the small scale was examined. On the small scale, the jet without flow control was found to have higher levels of velocity RMS, particularly on the jet periphery, and higher levels of Reynolds shear stress. It is proposed that the vortex generators effect this change by generating vorticity in the plane of the jet. This vorticity is theorized to stabilize the jet, delaying roll-up of the jet shear layer which occurs via the Kelvin-Helmholtz instability.

The method by which the vortex generators acted on the fluid mechanics of the steady jet system to decrease the blood's procoagulant potential was investigated via flow visualization and DPIV. The results from these studies implicate two possible mechanisms by which the vortex generators may act. First, the peak turbulent shear stresses in the jet were reduced by 10-20% with the application of vortex generators. Even if only a few platelets were activated in each passage through the valve, the cumulative effect of this difference in peak stresses after many passes would be greatly magnified. Thus, this reduction in turbulent shear stresses may be sufficient to explain the change seen in the blood's procoagulant potential with the application of passive flow control. It is suspected, though, that the second mechanism is dominant. The flow fields revealed that the presence of the vortex generators delayed or prevented the roll-up of the Kelvin-Helmholtz instability in the b-datum jet's shear layers into discrete vortices. By doing so, it is thought that opportunities for the interaction of activated and unactivated platelets entrained in these vortices were prevented, thereby inhibiting further propagation of the coagulation cascade. Even if the rate at which platelets were activated was similar for cases with and without flow control, it seems that the flow fields experienced by the platelets subsequent to activation can determine the level of procoagulant potential. Under the steady conditions observed in this experiment, the jet influenced by vortex generators was thus shown to induce significantly lower levels of procoagulant potential.

CHAPTER 1

INTRODUCTION

Heart valve disease is a serious medical condition often caused by congenital malformations, rheumatic scarring of valve tissue, or age-related calcification. Such diseases cause valve regurgitation or stenosis and, if left untreated, can eventually lead to death. In fact, these diseased valves annually account for 20,000 deaths in the US alone (Thom, 2006). Malfunctioning valves are commonly replaced with prosthetic heart valves. Over 180,000 valves are replaced annually worldwide, and about 55% of these are replaced with mechanical prosthetic heart valves (Thai and Gore, 2000; Yoganathan, 1995). The bileaflet mechanical heart valve (BMHV) is currently the mechanical prosthesis of choice for valve replacement. However, despite their widespread use, mechanical prosthetic valves are likely to damage the blood elements due to the non-physiologic nature of blood flow through them, therefore putting the patient at an elevated risk of thromboembolism. In fact, thromboembolism is the most common complication associated with mechanical prosthetic heart valves, with incidence ranging from 0.1% to 5.7% per patient-year (Thai and Gore, 1995). To avoid this complication, all mechanical heart valve recipients must be treated preventatively with anticoagulants, a therapy that increases the risk of hemorrhage. Major improvements in mechanical heart valve designs are thus needed to address the high frequency of thromboembolism caused by their implantation.

Recent studies suggest that a potential contributor to valve-induced thromboembolism is the non-physiologic levels of shear stress in the near vicinity of the valve (Fallon, 2006a). *In vitro* blood studies have found that the shear stress magnitude, the exposure time, and the past shear stress history are major factors in determining the level of red blood cell hemolysis and platelet activation, both of which contribute to thromboembolism (Jesty *et al*, 2003; Fallon, 2006a).

Shear stresses above the threshold for blood damage have, in fact, been measured in the vicinity of BMHVs and are believed to be responsible for the increased incidence of thromboembolism seen in BMHV recipients. Of particular concern is the flow through the b-datum line during valve closure. During this phase, a transient, regurgitant jet emanates from the b-datum line gap into the region upstream of the valve as the valve leaflets close. Previous research has shown that this flow phenomenon exposes blood elements to high levels of shear stress, thus indicating an elevated risk for blood damage. To date, all studies have focused on characterizing the flow field and quantifying the shear stress in the vicinity of the valve. However, no studies to this point have attempted to diminish these shear stresses through valve design modification with the goal of reducing overall shear stress-related complications.

The goal of this study is thus to explore the effectiveness of passive flow control to reduce the shear stress levels experienced by blood elements flowing through the b-datum region of a BMHV at valve closure. Passive flow control, in particular vortex generators, has been shown in the field of aerodynamics to be a simple, effective method for

manipulating flow fields (Gad-el-Hak, 2000). The current study therefore proposes to manipulate the valvular flow field using various vortex generator designs mounted on BMHV leaflets and investigate the effect of such flow control on the shear stress field and on the blood damage potential. This aim was accomplished through two sets of experiments. In the first set of experiments, an "almost-closed' BMHV with the peripheral gaps blocked was placed in a steady flow. The leakage flow field through the b-datum line was visualized and quantified using flow visualization and digital particle image velocimetry (DPIV), respectively. In addition, *in vitro* experiments with human blood were conducted to determine the thromboembolic potential of the leakage flow field. In the second set of experiments, a BMHV valve was mounted in the aortic position of a pulsatile left heart simulator. Flow visualization and DPIV were used to examine the flow upstream of a BMHV. Both sets of experiments were conducted with a control valve (with no vortex generators) and with an altered valve (with vortex generators) in order to characterize and quantify the effect of this passive flow control technique.

The results of this study provide new insight into the relationship between valve-related thrombogenicity and valvular flow fields. The results characterize the effect of vortex generators on the blood damage potential and thus impart a new understanding of how the thrombogenicity of BMHVs can be reduced via the implementation of passive flow control. This research therefore opens up new avenues of investigation for mechanical heart valve design optimization.

This thesis is organized as follows: Background information concerning valvular heart disease, prosthetic heart valves, blood properties, the effect of shear stress on blood elements, and passive flow control will be presented in Chapter 2. Chapter 3 will then present the hypothesis and specific aims of this research. The experimental methods by which these specific aims are achieved are described in Chapter 4. Chapter 5 will then present the relevant results. Chapter 6 will discuss these results and draw out the clinical implications. Chapter 7 will draw out some of the limitations of the current study while Chapter 8 will draw conclusions from what has been learned. Chapter 9 will present opportunities and directions for future work. Appendices will then present additional results and details.

CHAPTER 2

BACKGROUND

Organization of Background

This chapter will first examine the function of the heart and the origins and consequences of heart valve disease. Prosthetic heart valves, both mechanical and bioprosthetic, will then be described and compared in terms of complications resulting from their implantation. In order to better understand the complications arising from mechanical heart valve implantation, the physiology of blood, the coagulation cascade, and the effect of shear stress on blood elements will then be described. The flow fields associated with bileaflet mechanical heart valves (BMHVs) and the blood damage induced by these flow fields will be detailed. Finally, the technique of passive flow control will be described, and several examples of its application will be presented.

2.1. Cardiac Physiology

The heart, seen in Figure 2.1, is a four-chambered, muscular pump that drives blood throughout the body's circulatory system. The right side of the heart pumps blood to the lungs to release carbon dioxide and to become oxygenated. The left side of the heart pumps the oxygenated blood through the body to deliver nutrients to and remove wastes from each cell in the body.

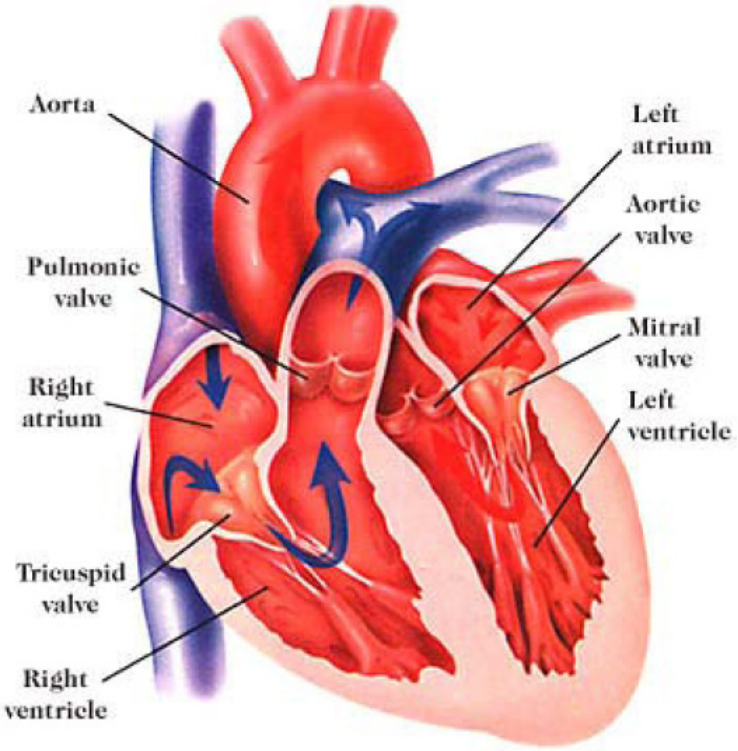

Figure 2.1: Diagram of the heart

Each side of the heart is divided into two chambers. On each side, the atrium receives blood and primes the subsequent chamber, the ventricle, to provide the major driving force to pump the blood throughout the body. One set of one-way valves, the atrioventricular valves, separates these chambers from one another. On the left side of the heart this purpose is served by the mitral valve. The mitral valve is composed of two leaflets and of chordae tendinae which connect the leaflets to the papillary muscles on the heart wall. On the heart's right side, the tricuspid valve, composed of three leaflets, separates the atrium and ventricle. A second set of valves separates the ventricular chambers from the blood vessels that carry the blood away from the heart. The pulmonary valve, with three leaflets or cusps, separates the right ventricle from the

pulmonary artery, which leads to the lungs. The aortic valve, also composed of three leaflets, prevents backflow from the ascending aorta to the left ventricle.

In a healthy, normal, adult human under resting conditions, the heart pumps blood at a flow rate of about 5 L/min. This pumping is accomplished by alternating periods of muscular contraction and relaxation which constitute a cardiac cycle. This cardiac cycle, which lasts approximately 860 ms in a resting human, is composed of systole (contraction) and diastole (relaxation). Figure 2.2 shows idealized pressure waveforms for the left side of the heart and will be referred to throughout the following description. In the left heart during early diastole, blood from the vena cavae enters the left atrium and, since pressure in the atrium exceeds that in the ventricle, the mitral valve opens, allowing filling of the left ventricle up to 75%. Late in ventricular diastole, the left atrium contracts, squeezing the last 25% of the blood into the ventricle (Point a in Figure 2). The volume of blood in the ventricle at the end of diastole, which averages 135 mL, is known as the end-diastolic volume. Ventricular systole then begins at the point of ventricular contraction (Point b). As ventricular contraction begins, the pressure in the ventricle immediately exceeds that in the atrium, resulting in the closure of the mitral valve. Before the aortic valve opens, the left ventricle continues to contract, thus increasing its pressure in a 0.02 to 0.03 second period known as isovolumic ventricular contraction. When the ventricular pressure exceeds the aortic pressure (at about 80 mmHg), the aortic valve is forced open and approximately 70 mL of blood, the stroke volume, is ejected into the aorta (Point c). About 70% of the stroke volume is ejected during the first third of the ejection period, and the pressure in the ventricle and aorta reaches approximately 120

mmHg (Point d). As the ventricles relax, the ventricular pressure decreases suddenly, resulting in a rush of blood back towards the ventricle and closure of the aortic valve. Valve closure occurs when the pressure drops to about 100 mmHg (Point d). Both the aortic valve and the mitral valve are then closed for another 0.03 to 0.06 seconds, a time known as the isovolumic relaxation period. As the ventricle relaxes further, the mitral valve re-opens to allow filling to begin again (Point f). The cardiac cycle on the right heart is similar, except that the pressures are much lower. For instance, the pressure in the right ventricle must only exceed 8 mmHg in order for the pulmonary valve to open (Sherwood, 2003; Guyton and Hall, 2006).

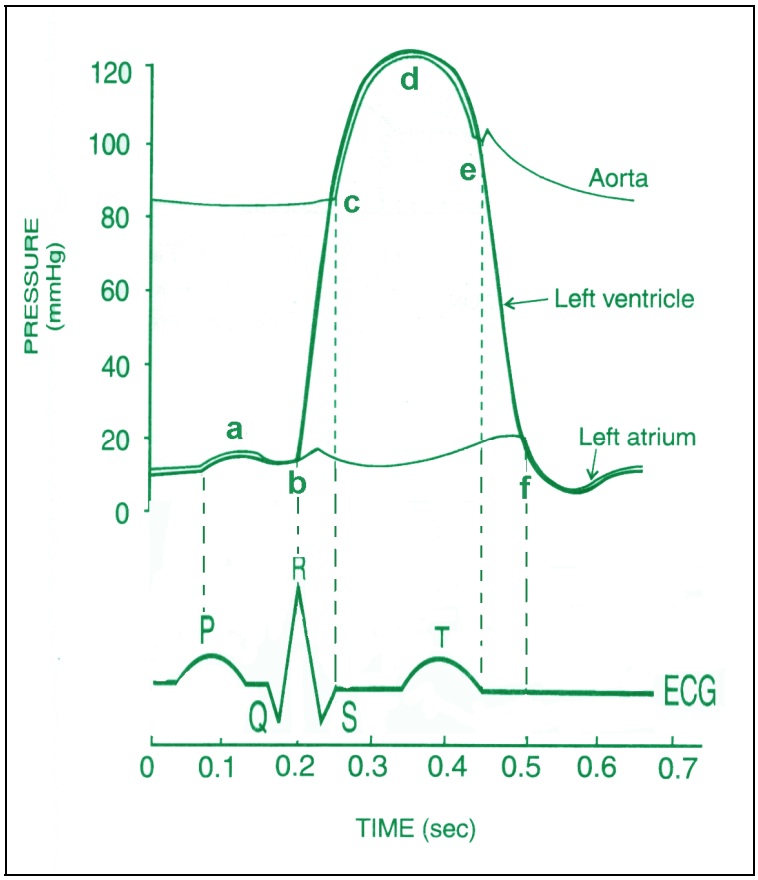

Figure 2.2: The Wiggers Diagram showing idealized pressure waveforms in the left heart and aorta throughout the cardiac cycle and their correspondence to the heart's electrical events as recorded by ECG. (www.technion.ac.il)

2.2. Heart Valve Disease

Valvular heart disease can be defined as any dysfunction or defect of one or more of the heart valves. In the United States, valvular heart disease is responsible for almost 20,000 deaths each year and is a contributing cause in about 43,000 deaths. Aortic valve disorders were responsible for about 12,000 of these deaths while mitral valve disorders were responsible for another 3,000. In order to treat this disease, an estimated 95,000 inpatient valve procedures were performed in the US in 2003 (AHA, 2006).

Disorders of the heart valves usually arise from several major sources. First, the defect may be congenital. For instance, aortic valves with two cusps instead of three occur in 1 to 2% of the general population (Farb *et al*, 2000). This congenital defect is the most frequent cause of aortic stenosis in the 50- to 70-year-old age group and puts patients at an increased risk of infective endocarditis (Farb *et al*, 2000). Other examples of congenital valve defects include mitral valve prolapse, cleft mitral valve, Ebstein's anomaly, and unicuspid aortic valve (Farb *et al*, 2000). A second cause of valvular heart disease is rheumatic fever which is usually associated with scar formation on the leaflets. In Western countries, rheumatic heart disease was a major source of valvular heart disease until the 1960s. The sudden decrease in this disease's incidence was attributed to a combination of improved socioeconomic conditions, a lower incidence of streptococcal infections, and the introduction of antibiotics (Farb *et al*, 2000). In the developing world, however, rheumatic heart disease remains one of the most common causes of cardiovascular mortality and morbidity. Due to valvular damage, rheumatic heart disease in developing countries accounts for up to 40% of cardiovascular admissions to hospitals, the majority of which must undergo cardiac surgery (Vijaykumar *et al*, 1994). Age-related calcification around the leaflets is a third major cause of valvular heart disease across the globe. For instance, calcification around the annulus of the mitral valve is found in 10% of patients dying after the age of fifty (Farb *et al*, 2000). Other sources of damage to the valve include bacterial endocarditis, a microbial infection of the valve endocardial surface, and mitral valve malfunction due to papillary muscle ischemia and infarction.

Regardless of the source of valvular heart disease, the result is usually valve stenosis or valve insufficiency. A stenotic valve is often characterized by thickened cusps, calcium deposits around the annulus, and fusion of the valve commissures. These features prevent the valve from opening fully, resulting in an increased resistance to the flow. As a result of the backed-up flow, the patient may experience pulmonary hypertension. Valve insufficiency describes a valve that does not close properly, resulting in regurgitation of blood through the valve. As a result, the blood flow to the body decreases, leaving the patient lethargic and short of breath. With time, the left ventricle may become unhealthily enlarged so that it can exert more force with each beat. The valves on the left side of the heart are particularly prone to insufficiency because of the higher pressures that they must withstand. Stenosis and insufficiency often occur together. For instance, about two thirds of patients with calcific aortic stenosis also have some degree of aortic regurgitation (Paraskos, 2000).

2.3. Prosthetic Heart Valves

In many cases of stenosis or insufficiency, a malfunctioning heart valve can be surgically repaired. For instance, balloon valvuloplasty may be used to open up a stenotic pulmonary valve while a patch of synthetic material may be used to repair a damaged leaflet (Enriquez-Sarano, 2000). In more severe cases, the natural heart valve must be replaced by a prosthetic heart valve. The first prosthetic heart valves, consisting of a ball-and-cage design, were implanted in 1960 both in the aortic and mitral positions (Harken *et al*, 1960; Starr and Edward, 1961). Prosthetic heart valve designs have changed dramatically since then, with more than fifty designs developed and with hundreds of

thousands actually implanted (Thai and Gore, 2000; Yoganathan, 1995). Today, more than 60,000 prosthetic heart valves are implanted yearly in the US alone, and over 180,000 are implanted worldwide each year (Thai and Gore, 2000; Yoganathan, 1995). Valve replacement is thus the most common operation for adults with symptomatic valvular heart disease (Thai and Gore, 2000).

The design of new and better prosthetic heart valves has been ongoing for almost fifty years. As far back as 1962, Harken elucidated criteria that would define the ideal valve substitute. According to Harken *et al*, the optimal prosthetic valve should have "lasting physical geometric features and be capable of permanent fixation in the normal anatomic site. It should be chemically inert, nonthrombogenic, harmless to blood elements and must not annoy the patient. It must open and close promptly during the appropriate phase of the cardiac cycle and should offer no resistance to physiological blood flow." Additional criterion elucidated by Yoganathan (1995) include full sterility at implantation, conformability to the heart structure, convenient surgical insertion, minimal reverse flow, long-lasting performance, radiographic visibility, and acceptable cost. Currently implanted prosthetic heart valves that meet most of these criteria generally fall into one of following two categories: mechanical or bioprosthetic. More than 60% of valve replacements are made with mechanical prostheses (Garver et al, 1998). An effort is currently underway to develop a third type, a polymeric valve that mimics the native valve function. Examples of these valves are shown in Figure 2.3.

Carpentier-Edwards S.A.V.
Aortic Bioprosthesis

Aortech trileaflet
Aortic polymeric Valve

Starr-Edwards Silastic Ball
Valve Prosthesis

Medtronic Hall Valve

St Jude Medical
Regent Valve

CarboMedics Standard
Aortic Valve

Figure 2.3: Examples of mechanical, bioprosthetic, and polymeric valves (Courtesy of Simon, 2004)

2.3.1. Mechanical Prosthetic Heart Valves

Mechanical valves are made of metal and synthetic materials such as Teflon, Dacron, pyrolytic carbon, silicone rubber, and graphite. A sewing ring, comprised of cloth, is used to sew the mechanical valve to the valve annulus after the native valve has been excised. The original prosthetic heart valve design, the ball-and-cage, featured a central ball occluder and a cage made of several struts projecting from the outflow surface of the valve ring. This valve design was found to have suboptimal flow properties, however, due to the fact that the ball obstructs the forward flow, creating resistance and unnatural, turbulent flow (Thai and Gore, 2000; Yoganathan, 1995). In the late 1960s, the tilting-disc valve was introduced. This prosthetic valve features an eccentric, free-floating occluder that pivots open and closed, thereby allowing laminar flow through the two orifices of the valve (Thai and Gore, 2000). In 1978, the bileaflet valve was introduced by St. Jude Medical, Inc. (SJM) and today remains the most widely implanted mechanical valve prosthesis. The SJM design features two semicircular, hinged leaflets that pivot open to provide minimal flow disturbance and pivot closed to prevent backflow. The leaflets pivot within butterfly-shaped grooves in the valve orifice housing. When fully open, the leaflets are at an angle of only 5° relative to the flow, providing very little flow obstruction (Yoganathan, 1995). Other bileaflet mechanical heart valve (BMHV) designs, including the Carbomedics valve, Sorin Bicarbon valve, and the On-X valve, have also been successfully developed (Yoganathan). Approximately 75% of the mechanical heart valves implanted today are of the bileaflet design (Yoganathan, 1995). Because BMHVs are the most commonly implanted design, this thesis will focus solely on this design.

2.3.2. Bioprosthetic Heart Valves

Bioprosthetic valves, which consist of valve tissue derived from human homografts or porcine or bovine tissue, were invented in an attempt to create a prosthetic heart valve that provided hemodynamics that were more natural than those produced by BMHVs. These valves have been widely used since the mid-1970s. The first of these valves used antibiotic tissue derived from human cadavers (homografts) that had been cryo-treated. Porcine bio-prostheses soon became available with the Hancock Porcine Xenograft in 1970. In this design, three chemically treated porcine leaflets are attached to a rigid ring with three flexible stent posts. Another popular design, the Carpentier-Edwards Bioprosthesis, uses a completely flexible support frame (Yoganathan, 1995). A major advantage of bioprosthetic valves, seen in Figure 2.3, is that they provide excellent hemodynamics with unobstructed bulk forward flow. Another advantage is their ability to deform with the surrounding cardiac muscle.

2.3.2.1. Valve Complications

Although the replacement of a diseased native valve is highly likely to prolong a patient's life, it is by no means considered a cure. For instance, a study of operative survivors who received Starr-Edwards ball-in-cage valves in both the mitral and aortic positions showed a 10 year survival of only 60% (Selzer, 1983). Complications resulting from prosthetic valve implantation include thromboembolism, an increased propensity for infective endocarditis, hemolysis and resulting anemia, and structural valve deterioration (Thai and Gore, 2000).

2.3.2.1.1. Mechanical Valve Complications

Patients who receive mechanical heart valves are at an increased risk of thrombogenesis and thromboembolism, which can result in stroke or other ischemic events. Thromboembolism is the most common complication associated with mechanical prosthetic heart valves, with incidence ranging from 0.1% to 5.7% per patient-year (Thai and Gore, 2000). One extreme example of device failure due to blood damage is the Medtronic Parallel bileaflet valve, which was found to have unacceptably high rates of valvular thrombosis during clinical trials and was subsequently removed from the market (Yoganathan, 2000). Even the St. Jude Medical and Carbomedics bileaflet valves, which are known for their superior hemodynamic performance and low thrombogenicity, still cause patient mortality due to valvular thrombosis (Baudet *et al*, 1985; Masters *et al*, 1995; Chang *et al*, 2001; Ibrahim *et al* 2001).

Because of the risk of thromboembolism associated with the use of cardiovascular devices, patients are often treated preventatively with anticoagulants. Prophylactic antithrombotic therapy, however, puts patients at an increased risk of hemorrhage. The International Normalized Ratio (INR), which is a measure of the clotting tendency of blood, is used to help determine the appropriate dosage for anticoagulant drugs such as warfarin. A healthy person's INR is generally in the range of 0.87 – 1.26, and increasing values indicate an increasing propensity for bleeding (Whyte *et al*, 2000). In the case of implanted mechanical heart valves, the recommended INR level at which physicians should aim to keep their patients in order to counteract the procoagulant effect of the implant is in the range of 2.0 to 3.5, depending on the type of valve implanted and the

health of the patient (Stein *et al*, 2001). Several studies have documented the increased risk of hemorrhage due to an increased INR (van der Meer *et al* 1993; Cannegieter *et al*, 1995; Stein *et al*, 2001). A study by van der Meer (1993) found that each one point increase in the INR from three to six resulted in a 42% increase in major bleeding events in patients with mechanical heart valves. Another investigation studied the incidence of adverse events across a range of INR values in patients with mechanical hearts valves and found a small increase in hemorrhagic strokes once the INR became larger than four and a steep increase once the INR rose above five (Cannegieter *et al*, 1995). The optimal INR level is thus the one at which the lowest incidence of both thromboembolic and bleeding complications is achieved (Cannegieter *et al*, 1995). Achieving this delicate balance between coagulation and hemorrhage while maximizing patient time in the target INR range through oral anticoagulation is no small feat, though. Complicating factors include changes in the pharmacokinetics and pharmacodynamics of the anticoagulant due to interacting drugs or illnesses, dietary and gastrointestinal factors affecting the availability of certain vitamins, patient-specific factors such as adherence to the therapeutic regimen, and the physician's ability to make correct dosing decisions (Ansell *et al*, 2001).

2.3.2.1.2. Bioprosthetic Valve Complications

The most common complication associated with bioprosthetic heart valves is structural valve deterioration. Structural valve deterioration includes wear on the valve, tears in the leaflets, stent creep, and valve calcification. For instance, a recent 10-year study of the St. Jude Toronto Stentless Porcine Valve showed actuarial freedom from structural valve deterioration of 79.9% (Desai, 1994). Common causes of structural valve deterioration in

this study included leaflet tears, calcific stenosis, and aortic root dilatation with poor leaflet coaptation (Desai, 1994). Other studies have shown a 10-30% failure rate of bioprosthetic valves after 10 years (O'Brien *et al*, 1995) This lack of durability limits the usage of bioprosthetic valves among children and young people.

2.3.2.1.3. Comparison of Bioprosthetic and Mechanical Heart Valve Complications

In comparing the suitability of mechanical and bioprosthetic heart valves for various patients, both have advantages and disadvantages. In general, mechanical heart valves are known for their durability but are also thrombogenic, resulting in the need for patient anticoagulation. Bioprosthetic valves, on the other hand, are nonthrombogenic (and thus do not usually require lifelong anticoagulation) but are much less durable (Hammermeister, 1993). This situation was well illustrated by an eleven-year study which compared the outcomes of 575 men who received either a mechanical valve or a bioprosthetic valve. Although there was no significant difference in the probability of death between the two groups, a statistically significant difference was found when comparing the probability of structural valve failure and bleeding complications. The probability of bioprosthetic valve failure in the aortic position was .15 (and .36 for the mitral position) while no valve failures were recorded for the mechanical valves. However, a higher rate of bleeding complications was found for those with mechanical valves versus those with bioprosthetic valves (respective probabilities of 0.42 vs 0.26) (Hammermeister *et al*, 1993).

2.4. Blood and the Coagulation Cascade

In order to understand the connection between mechanical heart valves and thromboembolism, it is first necessary to examine the composition and mechanical properties of blood, the function of the coagulation cascade, and the effect of shear stress on blood elements.

2.4.1. Blood Composition

Blood is a tissue composed of the liquid plasma containing the following three types of specialized cellular elements: erythrocytes, leukocytes, and platelets. The plasma itself is 90% water, with a number of substances, both inorganic and organic, dissolved and suspended in the liquid. Plasma proteins, which comprise 6-8% of plasma's total weight, are the most plentiful organic constituents and exist in a colloidal suspension in the blood. The three types of plasma proteins are albumins, globulins, and fibrinogen. Erythrocytes, or red blood cells, make up 45% of the whole blood volume and are shaped like biconcave discs about 8 μm in diameter and 2 μm thick. The major purpose of erythrocytes is to transport oxygen and carbon dioxide, a task made possible by the presence of hemoglobin molecules. Leukocytes, or white blood cells, occupy less than 1% of the volume of whole blood and function in the body's immune system. Platelets are cell fragments about 1-2μm in diameter that shed off of extremely large cells known as megakaryocytes in the bone marrow. Platelets function in hemostasis, the arrest of bleeding from a broken blood vessel. In a cubic millimeter of blood, the counts of red blood cells, white blood cells, and platelets would be about five million, seven thousand, and two hundred and fifty thousand, respectively (Sherwood, 2003).

2.4.2. Blood Properties

Plasma is a Newtonian fluid with a viscosity between 1.16 and 1.35 cP at 37°C. About 98% of the increase in viscosity above that of water (.69 cP at 37°C) is due to the presence of the plasma proteins in colloidal suspension. Blood, on the other hand, exhibits significant non-Newtonian behavior in that the apparent fluid viscosity depends on the rate of shear. Blood viscosity is thus a function of hematocrit, plasma viscosity, red blood cell aggregation, and the mechanical properties of the red blood cells (Baskurt and Meiselman, 2003). Above the yield stress but below a shear rate of 100 s^{-1}, the apparent blood viscosity depends on the shear rate raised to a power (a power law fluid). At the larger shear rates experienced in the major arteries and veins, blood is often assumed to behave as a Newtonian fluid. Nevertheless, the shear-thinning behavior has been found to have a quantifiable effect on both the wall shear stress and the velocity profile (Truskey *et al*, 2004).

2.4.3. Hemolysis

Red blood cells, which carry oxygen throughout the body, have a typical lifespan of about 120 days and must be replaced at the average rate of 2 to 3 million cells per second. This short lifespan is due to the absence of the normal intracellular organelles such as the nucleus and mitochondria. As the cell ages, the nonreparable lipid bilayer membrane becomes fragile as a result of cumulative or instantaneous damage. The cell then tends to rupture when the membrane is stretched. This often occurs naturally when the cell is squeezing through tight passages in the microcirculation, especially those in the spleen.

These passages are often as small as 3 μm in diameter. The rupturing process, known as hemolysis, results in the release of hemoglobin into the blood stream. Anemia, a lack of oxygen-carrying capacity in the blood, will result if too many red blood cells are destroyed.

2.4.4. Platelet Function and the Coagulation Cascade

Platelets function as part of the coagulation cascade to effect hemostasis and form blood clots. Damage to the vessel endothelium exposes collagen to the blood. Circulating platelets bind to the exposed collagen with the collagen-specific glycoprotein Ia/IIa receptor and become activated, forming a hemostatic platelet plug. The von Willebrand Factor (vWF) protein then strengthens this adhesion by bonding between the platelet and the collagen fibrils. The platelets release adenosine diphosphate (ADP) from their granules into the blood, thus activating more platelets and initiating platelet-to-platelet aggregation. The resulting platelet plug is often sufficient to seal minute tears in capillaries. Larger tears to the vessel require the clotting action of the coagulation cascade.

Blood coagulation is the transformation of blood from a flowing liquid to a solid clot. The resulting clot, formed of cross-linked strands of fibrin, stabilizes the underlying platelet plug and helps to seal the wound. Coagulation may occur via two pathways, which eventually converge into several final steps. Both pathways consist of a series of reactions in which a precursor is activated and subsequently catalyzes another reaction. The Contact Activation Pathway, also known as the Intrinsic Pathway, results from blood

contact with exposed collagen or a foreign object such as a test tube. The Tissue Factor Pathway, also known as the Extrinsic Pathway, is initiated when traumatized tissue, such as the endothelium or even a damaged red blood cell, releases a protein complex called Tissue Factor. As shown in Figure 2.4, the pathways converge when factor X (FX) is activated. FXa (Activated factor X) and its co-factor FVa then form the prothrombinase complex. Prothrombinase then activates prothrombin to form thrombin. Thrombin then initiates the key event of coagulation, the conversion of soluble fibrinogen into fibrin. Other roles of thrombin include activating FXIII to stabilize the fibrin mesh by forming crosslinks, acting in a positive-feedback manner to facilitate its own formation, and boosting platelet aggregation (Sherwood, 2003).

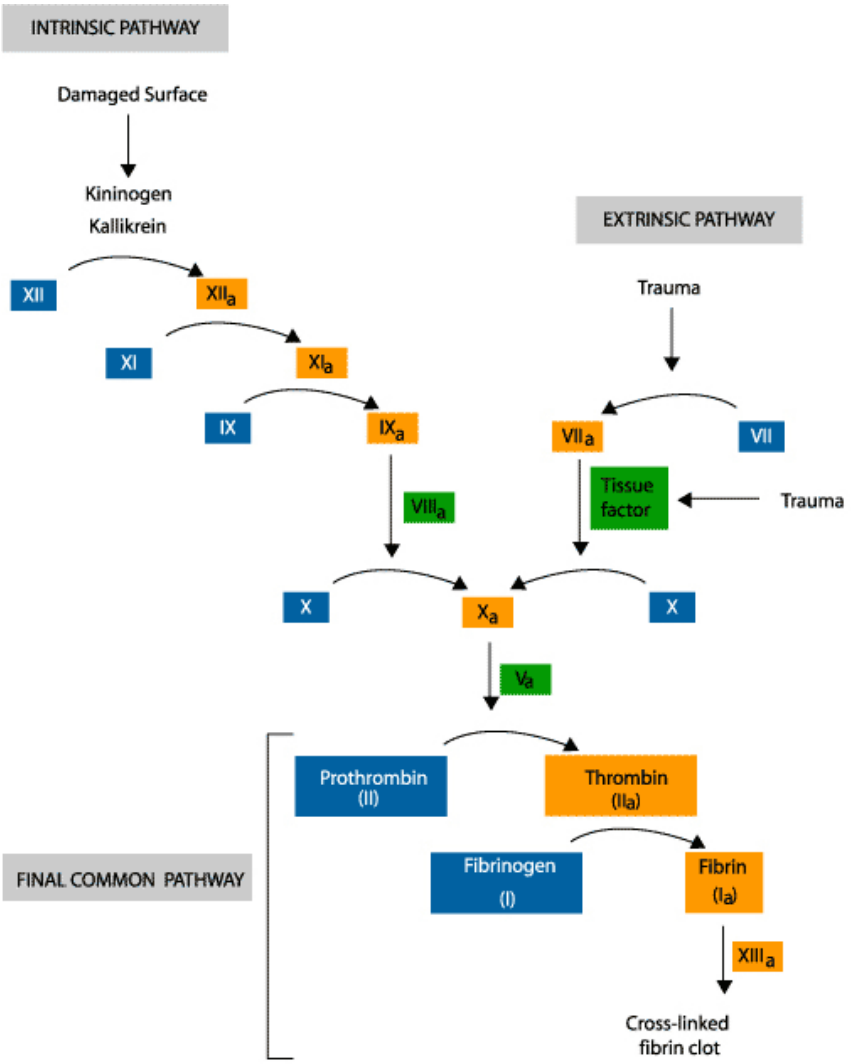

Figure 2.4: Diagram of the blood coagulation cascade (www.anaesthesiauk.com)

Abnormalities in the coagulation cascade can lead to a propensity for thrombus formation. The clotting process is usually retarded by three mechanisms. The first, protein C, degrades the factors FVa and FVIIIa. Secondly, thrombin is inhibited by antithrombin III, a serpin (serine protease inhibitor) to form thrombin-antithrombin III (TAT III). Finally, Tissue Factor Pathway Inhibitor (TFPI) inhibits FVIIa-related activation of FIX and FX after its original initiation (Shewood, 2003).

2.4.5. Shear Stress and Blood Elements

Just as a fluid element entrained in a jet will experience shear, so will a cellular blood element in a shear layer experience a distributed shear stress over its membrane. In response to this shear stress exerted by the fluid, the cell's viscoelastic membrane will deform. The effect of this deformation will depend on the cell's position and orientation with respect to the shear field, as well as on the proximity of other cells or of a wall. The end result of the deformation may well be cell lysing or irreversible damage to the cell membrane (Sutera, 1977). Blood elements may experience the following two types of shear stresses: viscous and Reynolds (turbulent). Viscous shear stresses arise from the interaction of the fluid viscosity and applied shear rate while Reynolds stresses correspond to the average momentum flux due to the fluctuating component of the velocity (Truskey *et al*, 2004). Finally, viscous shear stresses and Reynolds (turbulent) shear stresses are thought to affect different types of cellular elements in different manners and at different thresholds and exposure times.

2.4.5.1. Shear Stress and Red Blood Cells

The effect of shear stress on red blood cells has been investigated using a number of devices, including concentric-cylinder viscometers, capillary tubes, cone-and-plate viscometers, Couette cells, liquid jets, ultrasonically pulsating gas bubbles, and oscillating wires (Bacher and Williams, 1970; Leverett *et al*, 1972; Rooney, 1970; Williams *et al*, 1970). Those flow systems with simple, well-defined flow fields such as concentric-cylinder viscometers are advantageous because of the practically uniform

shear stress generated (Sutera, 1977). Using a concentric-cylinder viscometer that produced laminar flow, Leverett *et al* (1972) clarified much of the controversy concerning previous seemingly contrary investigations into the threshold at which shear stress caused hemolysis. Leverett's investigation showed that a threshold existed at about 1500 dynes/cm^2. Above this shear stress, hemolysis increased monotonically with time and cell damage could be attributed directly to shear stress and not to secondary effects such as solid surface interaction, centrifugal force, air interface interaction, mixing of sheared and unsheared layers, cell-cell interaction, and viscous heating. In addition, Leverett *et al* (1972) made sense of prior investigations by showing that both exposure time and shear stress are primary factors affecting hemolysis levels.

Other researchers have found similar thresholds in turbulent flow and have shown the detrimental effect of shear stress at subhemolytic levels. For instance, Sutera and Mehrjardi (1975) used glutaraldehyde to "fix" human red blood cells that were suspended in a turbulent flow with shear levels ranging from 100 to 4500 dyn/cm^2. The level of hemolysis was determined by means of microphotography and by assaying for free hemoglobin. After four minutes at a shear stress of 500 dyn/cm^2, the scanning electron microscope images showed that cells began to lose their concavity. Erythrocyte shape was drastically altered to a prolate ellipsoidal shape after four minutes at 1500 dyn/cm^2. Fragmentation, indicating hemolysis, became apparent at about 2500 dyn/cm^2. It was also at this level that the concentration of free hemoglobin began to rise. At 4500 dyn/cm^2, many and more erythrocyte fragments were seen. Ninety percent hemolysis was seen at this shear stress level (Sutera and Mehrjardi, 1975).

More recently, Sallam and Hwang (1984) investigated the effect of turbulent shear stress on red blood cell hemolysis by a submerged axisymmetric jet. A one-component laser Doppler anemometer system was used to produce a detailed map of the flow field, including mean velocity, turbulent intensities, and Reynolds shear stress. After detailing the flow field, a unique sampling collection system was devised in order to allow sampling of blood elements from specific points. Thus a relationship between the local shear stress and blood damage was developed. Sallam and Hwang established a threshold of 400 Pa, below which no hemolysis is seen, regardless of exposure time. However, this value was not calculated using the major principal Reynolds shear stress and was thus an underestimation of the true threshold. Lu *et al* later recreated the experimental system, re-measured the flow field with a two-component laser Doppler anemometer system, and revised the threshold up to 800 Pa (Lu *et al*, 2001).

2.4.5.2. Shear Stress and Platelets

The effect of shear stress on platelets was first elucidated in a Couette viscometer in the early 1970s. Brown *et al* showed that at an exposure time of several minutes, a platelet destruction threshold of 150 dyn/cm^2, as indicated by the release of acid phosphatase, existed (Brown *et al*, 1975a). In addition, changes in the platelet activity, as indicated by the level of serotonin, were seen at shear levels as low as 50 dyn/cm^2. Brown *et al* (1975b) also showed the morphological, biochemical, and functional changes in platelets when exposed to shear stress. Electron microscopy revealed that platelets appeared swollen at 50 dyn/cm^2, began to aggregate at 100 dyn/cm^2, and lysed or fragmented at

250 dyn/cm^2 at exposure times as low as 15 seconds. Particle size distribution studies were also used to show platelet aggregation at 100 dyn/cm2 and platelet fragmentation at higher shear stresses (Brown *et al*. 1975b). Similar results were independently obtained by Hung *et al* (1976), who found platelet lysis to occur at 165 dyn/cm^2 after several minutes' exposure. In addition, a recent study by Miyazaki *et al* showed that a shear stress of 108 dyn/cm^2 applied for five minutes led to platelet aggregation and the shedding of procoagulant microparticles from platelets while a shear stress of only 12 dyne/cm^2 applied for the same length of time showed no such effect (Miyazaki *et al*, 1996). Thus, when exposure to shear stress is on the timescale of minutes, human platelets exhibit a much lower threshold to lysis than do erythrocytes (Sutera, 1977). This fact was then supported by a recent study by Bakir *et al* in which sheep blood was sheared in a hemoresistometer and tested for platelet count and free hemoglobin (Bakir *et al*, 2007).

Although the previously discussed studies were helpful in determining the shear stress levels at which platelets were found to lyse, the timescales at which the cellular elements experience these stresses (on the order of minutes) were most likely not physiologic (Sutera, 1975). Ramstack *et al* investigated changes in platelet physiology caused by short-term exposure (25 – 1650 ms) to relatively high shear stress (300 – 1000 dyn/cm^2) and found no significant lysis at these levels but found sublethal trauma (1979). Ramstack *et al* also showed that platelet stimulation was nonlinear, with platelet trauma increasing exponentially with shear rate and time (1979). Hellums subsequently proposed a shear stress-exposure time plane that organized much of the previously gathered data

(1994). The plane, shown in Figure 2.5, is now commonly used as a standard for a platelet activation threshold. In order to account for varying exposure times and the effect of surface reaction versus that of direct stress, Hellums divided the shear stress/exposure time plane into two regimes. Below the curve, the interaction of platelets with solid surfaces is thought to play a dominant role. Above the curve (at higher shear stress levels and exposure time), direct shear stress effects are thought to be observed (Hellums, 1994).

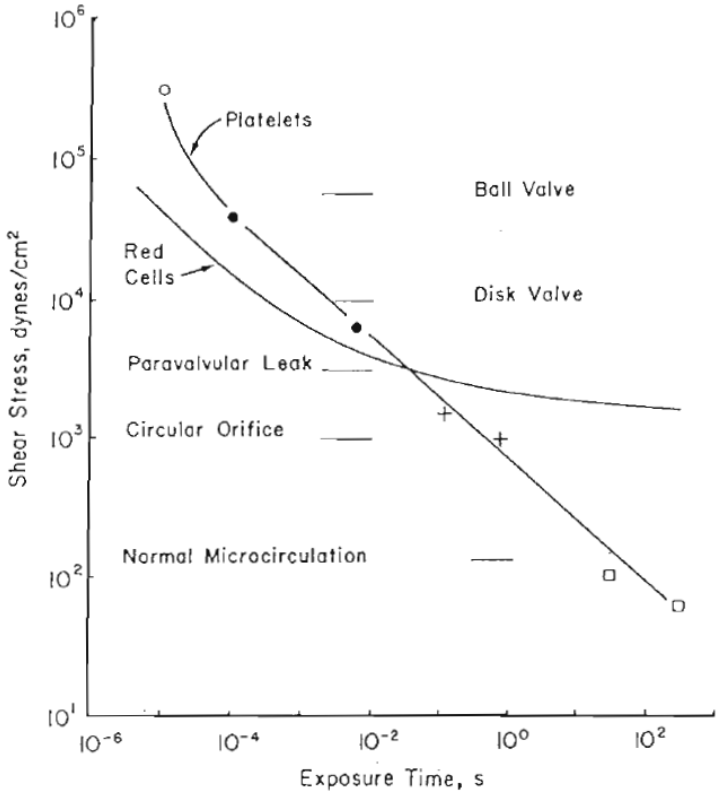

Figure 2.5: The shear stress-exposure time plane developed by Hellums (1994)

Although the shear stress-exposure time plane concept put forward by Hellums was helpful, it represented a constant shear stress experienced by a platelet for a set amount of

time. However, as platelets flow through vessels in the body, they experience varying levels and durations of shear stress, especially as they flow through arterial stenoses or prosthetic cardiovascular devices (Einav and Bluestein, 2004). In an effort to correct this oversimplified view, various researchers have attempted to examine the shear stress history leading to platelet activation under more physiologic flow conditions. For instance, Sutera *et al* showed that pulsed exposure to shear stress resulted in more platelet aggregation than continuous exposure to the same shear stress (Sutera, 1988). Boreda *et al* later derived a platelet stimulation function such that the activation state was linearly dependent on the magnitude of the shear stress and slightly less dependent on the duration (Boreda *et al*, 1995). Jesty *et al* definitively linked shear-mediated platelet responses to coagulation reactions and showed that they depend on the shear stress history of the platelet (Jesty *et al*, 2003).

Several more recent studies have attempted to examine the cumulative effect of shear stress on platelets over time. Einav and Bluestein examined pulsatile flow through stenoses both experimentally and computationally by applying their "Platelet Activation State" assay to a recirculating blood loop, performing digital particle image velocimetry (DPIV) experiments on a stenosis, and by solving the Unsteady Reynolds Averaged Navier Stokes (URANS) equations using the Wilcox k-ω turbulence model. These results were then used to perform particle tracking and to determine the activation level by summing the local shear stresses multiplied by a local residence time (Einav and Bluestein, 2004). Particle trajectories were then validated using 2D PIV. Activation level determined by summing the local shear with the local residence time led to "maps"

detailing the regions where the activation level reached high levels during specific portions of the cardiac cycle (Raz *et al*, 2007).

Shear stress may also interact with other agonists that initiate or modify platelet activation. For example, *ex vivo* blood experiments examining thrombus formation in a stenosis indicated that, at a wall shear stress of 315 dyn/cm2, much more platelet activation occurred when a collagen surface was present than when it was absent (Holme *et al*, 1997). Erythrocytes can also play a complementary role in platelet activation since, under high shear stress conditions, red blood cells may release the platelet agonist ADP (Hathcock, 2006; Alkhamis, 1990). Platelets themselves also contain ADP, and a positive feedback loop resulting in more platelet activation may be initiated upon an initial release of ADP (Hathcock, 2006).

2.4.5.3. Length and Time Scales

A final consideration when examining the effect of turbulent shear stresses on cellular elements is the issue of the length scales of the turbulent eddies relative to the cellular elements. If a rather large eddy forms in the proximity of a red blood cell or platelet, then the cellular element would likely be entrained and be rotated and translated in a way that reduces the net forces on its surface. If, however, a small eddy forms next to a cellular element, then the motion of the cell is more limited and it is thus forced to experience more of the full force of the eddy. If the Reynolds number of the bulk flow is sufficiently high, then the smallest eddies in a turbulent flow field can be considered statistically independent of the larger eddies and of the mean flow. The scale of these smallest eddies

should then depend only on the rate at which energy is supplied from the large eddies and on the kinematic viscosity of the fluid. These smallest scales can then be estimated by the Kolmogorov scales (Croughan *et al*, 1987). The Kolmogorov length scale η_k is given by $\eta_k = (\nu / \varepsilon)^{1/4}$, where ν is the fluid kinematic viscosity and ε is the average rate of energy dissipation per unit mass.

2.5. BMHV Flow and Blood Damage

The non-physiologic flow fields and associated shear stresses caused by bileaflet mechanical heart valves are thought to produce blood damage and consequently lead to increased likelihood of thromboembolism. For instance, clinical studies have shown that patients with mechanical heart valve implants have shortened platelet and red blood cell half lives, and the severity of hemolysis has been related to the type, position, and size of the prosthetic heart valve (Black and Drury, 1994). The propensity for platelet activation leading to thrombus formation is also increased by the presence of low shear recirculation regions created during the cardiac cycle. A low shear stress stagnation or recirculation region provides an opportunity for platelet-platelet binding that may lead to free-floating emboli formation (Hathcock, 2006). The presence of foreign surfaces such as the valve sewing cuff also provides ample opportunity for the deposition and growth of thrombus (Yoganathan, 2006).

2.5.1. BMHV Flow Fields

The flow fields produced by bileaflet mechanical heart valves in the aortic position are generally grouped into three phases within the cardiac cycle (Travis, 2001; Simon, 2004).

In the forward flow phase, the contraction of the heart drives blood through the three orifices created by the open leaflets. In the subsequent closing phase, the pressure gradient reverses and the blood flow reverses. As the leaflets begin to close, blood is forced through the decreasing gap between the two leaflets (b-datum line) and through the peripheral gaps formed between the leaflets and the valve housing. Once the leaflets completely occlude the flow, the leakage phase begins. In this phase, the negative pressure gradient across the valve keeps the leaflets fully closed while a small amount of flow is driven through the hinge regions, the b-datum line, and the peripheral gaps. All three phases create high shear flow conditions that may lead to platelet activation, and each will be examined separately.

2.5.1.1. Forward Flow Phase

Yoganathan *et al* used 2D laser Doppler Velocimetry (LDV) to conduct the first detailed investigations of the forward flow field of an SJM bileaflet valve (Yoganathan *et al*, 1986). During peak systole, a maximum velocity of about 220 cm/s was found, as was a peak turbulent shear stress of 1700 dyn/cm^2 (Yoganathan, 2000). Fontaine *et al* later studied SJM BMHV flow fields using a 3D LDV system and found little difference between Reynolds stresses calculated by three-component vs. two-component LDV (Fontaine *et al*, 1996). Ellis *et al* later investigated the near-field forward flow of a 23mm SJM Regent BMHV in the mitral position and found values of turbulent stresses that were similar, though slightly smaller, to those found previously by Barbaro *et al* (1997) and Yoganathan *et al* (1986). Barbaro *et al* also examined the smallest available aortic BMHVs (19mm) under exercise conditions, thus providing an estimate of the highest

Reynolds shear stresses expected during forward flow. Reynolds shear stresses of approximately 10,000 dyn/cm^2 were found in that study (Barbaro *et al*, 1997).

Other studies have cast doubt on the high magnitudes of the Reynolds stresses found in the previously listed studies. One issue that was not taken into account in theses studies was cycle-to-cycle variation in velocity. This cyclic variation can occur due to slight variations in the direction of a jet which are themselves due to small changes in the opening and closing of the valve. The result is an unrealistically large velocity variance that then elevates the values of the Reynolds stresses and the Kolmogorov length scales (Travis *et al*, 2002). For instance, Tiederman *et al* (1988) examined this matter in the downstream flow field of a tilting disk heart valve. He showed that, at the locations of peak turbulence, the removal of cyclic effects resulted in a 12% decrease in the turbulent shear stresses. Closer to the valve, where the cycle-to-cycle variations were the greatest, removal of cyclic effects resulted in estimates of turbulent shear stresses that were ten times lower than the estimates resulting from a simple ensemble average. In a more recent study of turbulence characteristics downstream of BMHVs, Liu *et al* showed that removal of cyclic effects reduced the magnitudes of the Reynolds shear and normal stresses by 10-40% and 20-30%, respectively (Liu *et al*, 2000).

Two final considerations when examining the effect of the forward flow phase on the blood elements are the length scales and the exposure times. Though early researchers produced complete studies of flow field structures, many lacked extensive research on turbulent scales (Liu *et al*, 2000). Using the Reynolds shear stresses of Barbaro *et al*

(1997) and the correlation coefficient method of Nygaard *et al* (1990), Travis estimated the smallest eddy length scale to be about 16 μm for bileaflet valves (2001). Lamson *et al* (1993) and Baldwin *et al* (1994) made estimates of 49.5 μm and 52 μm, respectively, for tilting disk valves. More recently, Liu *et al* estimated the forward flow Kolmogorov length scale to be about 30 μm for a SJM BMHV and about 20 μm for a Carbomedics BMHV (2000). In addition, the integral time scale of 1-10 s was used as an estimate of the exposure time. Liu *et al* concluded that these shear values, exposure times, and length scales were clearly sufficient to cause direct damage to blood cells (2000).

2.5.1.2. Leakage Phase

Although blood flows through the hinges, b-datum line, and peripheral gaps during the leakage phase in BMHVs, the flow through the hinges has received the most attention and was first seriously studied in bileaflet mechanical heart valves after the Medtronic Parallel bileaflet prosthesis was suspended from clinical trials in February, 1995. Unacceptable rates of thrombus formation were seen with this valve, and many of the thrombi from explanted valves were localized in the hinge inflow regions. A thorough analysis comprising two component LDV measurements (Ellis, 1996), dye visualization within a 5X scale valve model (Healy, 1998), and computational fluid dynamics (CFD) simulations (Gross, 1996) within the hinge region of the valve was thus conducted. Reynolds stresses exceeding 8000 dyn/cm^2 were found, as were regions of stagnation throughout the hinge and a region of recirculation within the hinge inflow region. Further experimental studies of the hinge flows were conducted in other BMHVS. For instance, Ellis *et al* (2000) studied leakage through a SJM Regent BMHV in the mitral position and

found leakage jets with velocities up to 0.72 m/s and Reynolds shear stresses up to 2600 dyn/cm^2 but did not take cyclic variation into account. Leo *et al* (2002) examined leakage flow through a 23 mm Carbomedics BMHV in the mitral position and reported maximum velocities of about 3 m/s and turbulent shear stresses of about 5500 dyn/cm^2. Travis *et al* (2002) studied leakage jets through in a SJM 17 Regent valve in the aortic position, which has a lower transvalvular pressure. He did account for cyclic variation and found maximum turbulent shear stresses of 289 dyn/cm^2 with a range of Kolmogorov scales between 21.2 to 72.5 μm. Finally, Simon *et al* (2004) examined forward flow and leakage flow throughout the hinge regions of a SJM Regent BMHV and a Carbomedics BMHV in both the mitral and aortic positions and found highly complex and unsteady flow patterns. The SJM valve, however, generally exhibited lower velocities and Reynolds shear stresses.

2.5.1.3. Closure Phase

The closure flow phase was first investigated in the late 1980s, initiated by the clinical failure of two bileaflet Edwards-Duromedics Valves. Pitting and erosion, which are markers of cavitation, were seen on the valve surfaces by scanning electron microscopy. It was speculated but never proven that the pitting may have contributed to the fatigue fracture (Klepetko, 1989). Suspicion of cavitation induced in the blood during valve closure thus initiated research into the closing dynamics of bileaflet mechanical heart valves.

Cavitation is characterized by the formation of a gas-filled bubble or field of bubbles in a fluid. It involves the local vaporization of the fluid, which is associated with a local pressure drop below vapor pressure. The bubbles will usually then collapse in a region of higher pressure. As they implode, they generate pressure waves and fluid jets that, if directed toward adjacent surfaces, may cause pitting or erosion. Graf *et al* (1991), who conducted the first extensive investigation into the possibility of cavitation in tilting disk and bileaflet mechanical heart valves, proposed three possible mechanisms of cavitation in mechanical heart prostheses. First, the fluid column downstream of the valve could separate from the closing leaflet due to the sudden deceleration at valve closure, thus leaving a negative pressure proportional to the deceleration. This is also known as the "water hammer" effect (Bluestein *et al*, 1994). Second, a low pressure could be generated in accelerated flow regions such as where an occluder approaches the valve housing. More specifically, this "squeeze flow" results from the rapidly approaching rigid boundaries of the leaflet and valve housing. Third, natural frequency oscillations could generate alternating fields of positive and negative pressures at valve closure (Graf *et al*, 1991). The microbubble formation occurring during cavitation has been shown to induce serious clinical consequences. For instance, these microbubbles, on the order of 200 – 300 μm, can act as gaseous emboli traveling into the cranial circulation, perhaps causing strokes. Several reports have indicated a correlation between brain emboli (likely gaseous emboli formed during cavitation) found by transcranial Doppler and a decline in the neuropsychological function in patients with mechanical heart valves in the mitral position (Markus, 1993).

The flow at valve closure has been studied both experimentally and computationally. On the experimental side, Graf *et al* also showed that cavitation could be induced at valve closure in eight of the ten valves tested in a pulsatile left heart simulator in the mitral position in a pressure variation range up to 5500 mmHg/s. Furthermore, a pressure impulse on the same order of magnitude as the yield point of pyrolytic carbon was found, showing that, even though the damping properties of the native valve surroundings were not accounted for, erosion was definitely possible (Graf *et al*, 1991). Experiments by Lee *et al* (1994) gave support to the theory that squeeze flow was responsible for cavitation. Later experiments by Chandran and Aluri (1997) measured leaflet tip velocities of 2-3.3 m/s and showed that cavitation was not a function of the flexibility of the valve mounting. A later experimental study by Rambod *et al* (1999) of microbubble formation associated with BMHVs in the mitral position revealed that bubbles form for 8-10 μs at the peak of closure backflow and developed a physical model describing their formation and growth at valve closure. Further studies of microbubble formation due to the squeeze flow phenomenon were conducted in tilting disk valves by Lim *et al* (2002). Lim *et al* also simulated valve closure by the rapid impingement of two rods, thereby studying the role of squeeze flow velocity and contact area on the initiation of cavitation (2003). In 2006, Zhang *et al* conducted micro-DPIV on the squeeze flow developed in a model BMHV with transparent leaflets when the gap between the leaflet and valve housing ranged from 1.4 mm down to 0.1 mm. At the smallest gap, maximum velocities of 2 m/s were recorded. Although this work experimentally verified the squeeze flow phenomenon in a BMHV for the first time, it was limited in that the closing dynamics are likely unique to that BMHV model and thus differ from those of commercial valves (Zhang *et al*,

2006). In recent work, Rambod *et al* (2007) sought to clarify the role that regurgitant tip vortices might play in the onset of cavitation at the b-datum line of BMHVs in the mitral position. Using a device that simulated regurgitant flow, they found that a regurgitant vortex drastically increased the size of "seed" hydrogen bubbles injected into the flow.

Much of the research into the valve closure phase has focused on how cavitation occurs and how it could induce blood damage or damage the valve. However, more recent research has begun to examine how other aspects of valve closure, such as the shear stress, could play a role in initiating blood damage. A recent experimental study of particular interest examined the regurgitant flow field of a SJM BMHV in the mitral position using DPIV (Manning *et al*, 2003). The experiments were conducted in a "single shot" experimental *in vitro* test chamber and not in a flow loop under truly physiologic pulsatile conditions. Although there was minimal forward flow through the valve, the conditions were probably sufficient to investigate the valve's closure and leakage phases. PIV vector maps taken 5 ms before valve impact perpendicular to the b-datum line showed a regurgitant jet of almost 1 m/s with two small tip vortices forming along the sides. At 5 ms after the impact the jet velocity had weakened to about 0.55 m/s, and the planar jet emanating from the b-datum line practically ceased soon after. Viscous shear stresses no higher than about 20 dyn/cm^2 were reported around the regurgitant jets, and turbulent stresses were not measured (Manning *et al*, 2003).

More thorough investigations of the closure and leakage flow jets through BMHVs in both the aortic and mitral positions were carried out by Ellis (1999) and Simon (2004)

using Laser Doppler Velocimetry (LDV). Ellis examined a 27 mm SJM Standard valve and a 27 mm Medtronic Parallel (MP) valve. During late systole (just before valve closure), Ellis observed a long, thin jet emanating upstream from the centerline of the SJM valve in the aortic position. The velocity of the jet was about 0.5 m/s while the turbulent shear stresses ranged from 50-200 dyn/cm2. The jet lasted for approximately 60 ms. For the MP valve in the aortic position, higher values of velocity (0.72 m/s) and turbulent shear stress (1200-1800 dyn/cm^2) were recorded in the centerline jet, and the jet lasted for slightly longer (80 ms).

Simon (2004) investigated the closure and leakage flow fields caused by a 23 mm SJM Regent valve and a 23 mm Carbomedics valve during valve closure. In the approximately 80 ms encompassing valve closure, a jet emanating from the Carbomedic valve's centerline was found. The jet velocities ranged from 0.10 m/s to 0.37 m/s while turbulent shear stresses were on the order of 350 dyn/cm^2, with a peak value of 576 dyn/cm^2. A similar jet was found in the SJM Regent valve. The velocity magnitude was on the order of 0.5 m/s, but a peak velocity of 2.34 m/s was found in early diastole. Similarly, turbulent shear stresses were on the order of 400 dyn/cm^2, with a peak value of 1687 dyn/cm^2. These peak velocities and turbulent shear stresses found during valve closure were higher than any of those found during the remainder of diastole.

On the computational side, Bluestein *et al* (1994) first applied CFD and lubrication theory to the squeeze flow generated by the closure of a leaflet on an Edwards Duromedics BMHV. This research found velocities of almost 30 m/s and pressures that

would induce cavitation. In addition, the authors established a threshold velocity of 15 m/s for cavitation to occur (Bluestein *et al*, 1994). Lai *et al* (2002) later simulated the 2D flow dynamics within a mechanical heart valve during valve closure, with the leaflet motion fully specified. The results indicated that negative pressures sufficient to induce cavitation occurred and that leaflet tip geometry and gap width had little effect. Interestingly, they found that the leaflet speed had a large impact on the closure flow dynamics and that slower closure led to reductions in the magnitude of the negative pressures. In more recent work, Cheng *et al* (2004) allowed fluid-structure interaction in their 3D simulation of BMHV closure under mitral conditions. Extremely high velocities, with wall shear stresses sufficient to damage blood, were found in the clearance region in both the initial closing phase and in the rebound phase. The maximum velocity (27.7 m/s) and wall shear stress (17488 Pa) were found in the rebound phase.

Of particular interest is the study performed by Krishnan *et al* (2006). In this study, the investigators developed a 2D model, with fluid-structure interaction, of the fluid dynamics involved in the closure and rebound of one leaflet in a BMHV in the mitral position. Closure of the valve was reported to occur in about 30.6 ms, which matched fairly well with earlier experimental observations indicating a valve closure time of 32 ms. In the b-datum line region, a jet developed while periodic shedding of vortices was observed throughout leaflet closure. Just before closure, velocities of about 8 m/s and low viscous shear stresses (10^{-4} Pa) were reported. At rebound, velocities on the order of 50 m/s and viscous shear stresses on the order of 10-100 Pa were reported. In the peripheral gap region, a jet directed somewhat toward the b-datum line developed as the leaflet

closed. Jet velocities (of about 2m/s) were lower than those seen in the b-datum line jet just before valve closure. At closure, velocities of about 20 m/s were seen, and during leaflet rebound, velocities as high as 120 m/s were recorded. Correspondingly high viscous shear stresses of about 10^2 Pa and 10^3 Pa were seen just before valve closure and during leaflet rebound, respectively. The researchers also noted a recirculation region that formed at the peripheral gap after valve closure, a potential site for thrombus deposition.

2.5.2. BMHV-Induced Blood Damage

Investigators have either used computational models or *in vitro* experimental systems with human or porcine blood to probe the nature of blood damage and platelet activation induced by the nonphysiologic, high shear flow conditions inherent to mechanical heart valves. These researchers have built upon earlier work that determined the shear stress-exposure time threshold levels of blood elements and the shear stresses produced by prosthetic valves in order to directly correlate the two.

2.5.2.1. Computational Models

2.5.2.1.1. Relative Blood Damage Index Model

Giersiepen *et al* (1990) built on the blood damage data of Wurzinger *et al* (1985, 1986) and the valve turbulent shear stress findings of Giersiepen *et al* (1989) to construct a mathematical, power-law model for their Relative Blood Damage Index (RBDI). Exposure times were estimated, and levels of platelet and erythrocyte lysis were estimated by fitting curves to the shear stress-exposure time plane of Wurzinger *et al* (1985, 1986). These data were used to produce the RBDI for 25 prosthesis, both

mechanical and bioprosthetic. The mechanical valves, both tilting disk and bileaflet, showed higher RBDI levels at 13.5 mm downstream of the valve while the bioprosthetic valves showed higher RBDI levels at 40.5 mm downstream. The authors attributed this to the central jet which "frays out further downstream," resulting in the main shear field being generated further downstream (Giersiepen *et al*, 1990). Unfortunately, the authors did not study the closure or leakage phases and did not account for the path-dependent nature of blood damage. Nevertheless, comparison of the RBDI with clinical hemolysis data for five of the original 25 valves resulted in good correlations for four of these five valves. Incidentally, the SJM valve had the lowest RBDI value of all of the mechanical valves tested (Horstkotte *et al*, 1987).

The RBDI has subsequently been used in several investigations. Lim *et al* (2001) utilized the index and DPIV to find blood damage "hotspots" in the downstream flow field produced by a porcine bioprosthetic aortic valve in systole. However, these researchers improved upon Giersiepen's time estimate by following trajectories of fluid particles, thus providing a Lagrangian description of the stresses experienced by the blood cells. Morsi *et al* also used the RBDI in comparing laser Doppler anemometry (LDA) Reynolds shear stress measurements of their "jellyfish" valve and a Bjork-Shiley tilting-disk valve (Morsi *et al*, 1999).

The RBDI model has also come under recent criticism. Grigioni *et al* (2004) drew attention to the limitations inherent to the power-law representation of the RBDI. They

showed how the model fails to incorporate the past history of the platelet and investigated how time-varying loads are not accounted for (Grigioni *et al*, 2004).

2.5.2.1.2. Platelet Level of Activation Model

The platelet level of activation parameter was developed by Bluestein *et al* (1997) in an attempt to quantify the shear stress history of an individual platelet along its trajectory and has been used in numerous studies since that time, mostly to examine blood damage resulting for systolic forward flow. For instance, Bluestein *et al* (2000) examined vortex shedding from leaflets in BMHVs as a possible mechanism for free emboli formation. The authors hypothesized that shed vortices provided relatively long-lasting, semi-closed "flow reactors" where activated platelets could more easily aggregate. Using 2D CFD, the authors computed a much lower level of activation of those platelets that traced a path through the bulk flow than for those that passed near the leaflet shear layer and subsequently became entrained in shed vortices. In a similar study, Bluestein *et al* (2002) investigated the effect of BMHV implantation technique (implant angle and the use of subannular suturing) on the subsequent aortic flow field. The researchers found that a tilted valve produced unfavorable flow fields that tended to produce more platelet-entraining vortices and thus higher levels of activation. In more recent work, Alemu and Bluestein (2007) extended their numerical simulations to calculate 3D flow fields around a BMHV implanted in the aortic position during the forward flow phase of the cardiac cycle. The platelet level of activation model was extended to include total shear (viscous, turbulent, and deformation), and a damage accumulation model was created to

incorporate the effect of past damage and repeated passages through a cardiovascular device.

The platelet level of activation parameter developed by Bluestein *et al* (1997) was also used recently as a first approximation of the platelet activation occurring during the BMHV closure phase (Krishnan *et al* 2006). "Hotspots" of platelet activation occurred in the peripheral gap region just after valve closure and leaflet rebound. This region was characterized by high shear stresses and subsequent recirculation lasting 5 – 10 ms after valve closure. These results indicate that this region may have potential for thrombus deposition.

2.5.2.1.3. Other Models

Other models for blood damage and platelet activation have been developed. For instance, Boreda *et al* (1995) developed a platelet stimulation function (PSF). The distinguishing feature of the PSF is the prediction that platelet activation should vary linearly with shear stress but nonlinearly with time of exposure. This theory was supported by the experimental work of Jesty *et al* (2003). Arora *et al* (2004) developed a tensor-based measure for estimating blood damage in a ventricular assist device that was based on instantaneous deformation of red blood cells and accounted for the "tank-treading" behavior seen in red blood cells in shear flow.

2.5.2.2. In Vitro Blood Experiments

2.5.2.2.1. Platelet Activation State (PAS) Assay

As discussed previously, thrombin is an essential part of the coagulation cascade that enables the conversion of fibrinogen to fibrin and also acts in a positive-feedback loop to activate more platelets. Because of this feedback loop, it is very difficult to directly correlate thrombin production with shear-induced platelet activation. Jesty and Bluestein (1999) therefore developed a procedure that eliminated the feedback loop by adding acetylated prothrombin to the platelets. The resulting Platelet Activation State (PAS) assay has been used extensively to examine the effects of shear stress-initiated platelet activation.

Jesty *et al* (2003) used the PAS assay to investigate the combined effects of shear stress and exposure time on modified human platelets circulating in a flow loop with a shear stress-inducing stenosis and proved the feasibility of such an approach. Bluestein *et al* later investigated the procoagulant potential of Bjork-Shiley tilting disk valves with and without restricted leaflet motion in a pulsatile flow chamber (2004). The results showed that blood flow through compromised mechanical heart valves activated platelets up to eight times more than in normally functioning valves. Using the same PAS assay, Yin *et al* compared platelet activation in bileaflet and tilting disk mechanical heart valves and found that BMHVs activated platelets at twice the rate of tilting disk valves (2004). Yin *et al* also used the PAS method to compare the procoagulant potential of polymeric, tissue, and bileafet mechanical valves and found no significant differences among them

(2005). Yin *et al* also used the PAS assay to investigate the thrombogenic performance of an SJM BMHV in a sheep model (2006). After one and a half years, the sheep with prosthetic valves exhibited significantly higher platelet activation than the control sheep.

Although the PAS assay has been extremely useful, Yin *et al* (2004) pointed out several factors that could negatively affect the results and conclusions. For instance, only specially filtered platelets may be used in the recirculating flow loop. Since the assay is optically based, neither whole blood nor platelet-rich plasma may be used. In addition, freshly drawn platelets cannot be used because of the large volumes required. Instead, outdated pheresis platelets, which are often already partially activated, must be used. These factors could introduce artifacts that negatively affect the way that shear stress affects blood damage levels.

2.5.2.2.2. Whole Blood Assays

Researchers have developed *in vitro* blood systems that allow the use of fresh, whole blood. Thus they are able to focus on specific aspects of BMHV design and specific phases of the cardiac cycle that might be most detrimental to the blood. Travis *et al* (2001a), for example, developed an *in vitro* flow system that uses small volumes of anticoagulated human blood. The sensitivity of certain markers for hemolysis (free hemoglobin) and platelet activation (Platelet Factor 4 (PF4) and annexin V expression) were then investigated by propelling the blood in a recirculating flow loop with a Medtronic Parallel valve in either the forward flow phase position or the leakage position. Results indicated that leakage flow caused significant platelet disruption and that annexin

V binding to platelets and plasma PF4 activity are more sensitive markers of leakage-induced blood damage than plasma hemoglobin concentration. Travis *et al* (2001b) also investigated the effect of bileaflet valve pivot geometry on platelet damage by using a recirculating, steady flow loop with the valve in the leakage position. The researchers investigated the effects of pivot geometry and pivot gap dimensions. Platelet Factor 4 (PF4) and anionic phospholipid (annexin V) expression were used as markers of platelet activation. A significant difference was seen between a clinical quality SJM valve and an SJM valve with a larger than normal pivot gap width.

Fallon *et al* went on to design a similar system capable of exploring shear-induced platelet activation (2006a). In this system, whole human blood was anti-coagulated with sodium citrate. A recirculating blood loop could then driven by a centrifugal pediatric bypass pump. The thrombus-forming potential of the blood was simultaneously enhanced by the continuous recalcification of the blood. The concentration of thrombin could then be measured indirectly by performing an assay for thrombin-antithrombin III. Continuing the work of Travis *et al*, this system was then used to investigate the thrombus-forming potential of leakage flow through various regions of bileaflet mechanical heart valves (2006a, 2006b). The design parameters of the pivot region were also investigated by conducting experiments with simulated hinge regions consisting of circular orifices with various diameters and internal geometries. Flow through the b-datum line was also simulated by slits of various dimensions. Significant TAT III formation was seen for circular orifices of diameters 200 μm and 400μm but not for any large orifices. In addition, no significant TAT III was produced by the slits. This was unexpected since

Travis (2001) found higher Reynolds shear stresses in jets through the b-datum line than in circular jets emanating from the hinge regions. Finally, in another study Fallon *et al* (2007) re-examined the thrombogenic potential of the valves earlier examined by Travis *et al* (2001b). In this study the SJM Standard valve produced a negligible amount of TAT III. The other valves (Medtronic Parallel, High Leaker SJM Standard, Low Leaker SJM Standard) produced significantly more TAT III at various time points throughout the experiment. The sensitivity of the system is thus seen, especially considering that Travis *et al* (2001a) could not detect a significant difference in platelet activation between most of these valves. The system developed by Fallon (2006) is thus advantageous over others systems that are limited to the assessment of platelet activation but cannot assess actual thrombus formation (Fallon *et al*, 2007).

2.6. Passive Flow Control

Flow control is generally an attempt to manipulate a fluid in order to restrict detrimental effects (such as stall) while promoting favorable aspects (such as increased airfoil lift or decreased drag). Attempts to control flow can usually be divided into the following three categories: passive, active, or reactive. In general, an active method adds energy to the flow while a passive approach extracts energy from the flow for control purposes. A reactive method extracts information from the flow with sensors and, based on this information, operates actuators to manipulate the flow (Gad-el-Hak, 2000). The current discussion will focus solely on passive flow control and will examine three relevant examples of this technique. The following three examples will be drawn from both the

biological world and from man-made technologies: leading edge tubercles, jet nozzle modifications, and vortex generators.

2.6.1. Leading Edge Tubercles

Passive flow control is present throughout nature. For instance, "riblets" in shark skin and scallop shells reduce wall shear stress and thus reduce drag (Bechert *et al*, 2000; Anderson *et al*, 1997). In addition, certain porous feathers on bird wings passively function as movable flaps to increase lift during a landing approach (Bechert *et al*, 2000). An example to be examined in more detail is that of large, rounded tubercles (or protuberances) seen on the leading edges of humpback whale pectoral flippers, as seen in Figure 2.6 (Fish and Battle, 1995). These flippers have a wing-like, high aspect ratio planform and are reportedly used in highly acrobatic swimming maneuvers (Fish and Lauder, 2006).

Figure 2.6: A humpback whale (*Megaptera novaeangliae*) flipper, showing tubercles on the leading edge (Fish and Lauder, 2006)

Wind tunnel testing of humpback whale flipper models showed evidence that the leading edge tubercles served to delay the angle at which stall occurred (from 12° to 16.3°) and increased the total lift without increasing drag (Fish and Lauder, 2006). An unsteady Reynolds-averaged Navier-Stokes simulation (RANS) on a NACA 63-021 baseline airfoil with and without equally spaced protuberances showed significantly different flow separation patterns and surface pressures. Separation was delayed almost to the trailing edge for regions downstream of the tubercle crest, and the tubercles generated streamwise vorticity in the troughs as the flow was convected along the leading edge. These effects helped to push the stall line further to the posterior of the flipper, thus giving the whale greater control (Fish and Lauder, 2006).

2.6.2. Jet Nozzle Modification

One typical goal of jet nozzle modification is the elimination of screech noise from supersonic jets by the addition of tabs. A second major goal is that of increased mixing (Zaman *et al*, 1994). Passive flow control via the modification of jet nozzle geometry can generally be categorized as one of two methods. First, flow control can be achieved by the addition of elements (such as tabs, vortex generators, or deflector plates) that protrude into the nozzle opening or sit within the nozzle itself. Alternatively, the projected shape of the nozzle itself (rectangular, elliptical, or more complex shapes) can be modified (with or without the addition of three-dimensional amendments like notches or lobes) to accomplish desired flow control goals.

Bradbury and Khadem (1975) provided evidence of the effect of tabs in a low-speed jet as early as 1975. These researchers placed square tabs and ramps normal to the exit flow at the nozzle of an axisymmetric jet. They found that just two tabs caused accelerated centerline velocity decay and an acute distortion of the velocity field in the cross-stream plane. Zaman *et al* (1994) later investigated tabs of various geometries projecting normally and at an angle into the flow and found that the tabs produced a pair of counter-rotating streamwise vortices. The authors hypothesized that the vortex formation could be due to 1) an upstream pressure gradient generated by the tab and 2) vortex filaments shed from the tab sides and reoriented downstream by the mean shear of the mixing layer. Zaman *et al* showed that, when a triangular tab was tilted downstream by 135°, vortices with the same sense of rotation would be produced, thus strengthening the mixing effect.

Hui *et al* (1999) showed that the streamwise vortices caused an "inward indentation of ambient flow into the core jet flow and an outward ejection of core jet flow into the ambient flow," thus enhancing mixing.

In one study, Yu *et al* (1998) investigated the effect of primary and secondary mixing tabs, both square and triangular, on the flow and mixing characteristics of a confined square jet. A much faster decay of the center-line mean velocity was found with all tab designs tested than for the control case, and, with a tab on each side, the jet was effectively bifurcated into four lobes. The spread of the tabbed jets was about 30% greater than the control cases. Integration of velocity contours over different streamwise stations yielded the mass flux, and the tabbed jets showed much greater entrainment and spreading. Normalized Reynolds shear stress and turbulent kinetic energy were calculated for the tabbed case for several streamwise locations but were not compared with the control case (Yu *et al*, 1998). Various other researchers have investigated optimal tab placement and shape. Reeder and Zaman (1996) found that the trailing edge was the best location for tab placement since upstream or detached settings interfere with the pressure gradient source of vorticity. Tabs that did not exceed the boundary layer were also found to produce noticeable effects (Island *et al*, 1998).

Attempts to passively control flow from jets has also been done by modifying the projected shape of the orifice. Ho and Gutmark (1987), for instance, investigated elliptic jets with small aspect ratios and found that these jets could entrain several times more fluid than a circular or plane jet. The mechanism by which this occurred, they found, was

the self-induction of vorticity distributed around an asymmetric contour, which resulted in azimuthal distortion of the elliptic vortex ring. The part of the vortex near the ellipse's minor axis then moves outward, thus allowing a large amount of the surrounding fluid to move towards the axis and become entrained in the jet (Gutmark and Grinstein, 1999). Zaman (1999, 2001) extensively studied the spreading, mixing, and acoustic properties of jet from nozzles of various geometries, both with and without tabs. Further modifications to jet nozzles with the aim of increasing mixing have included eliminating parts of the nozzle sidewall for a scalloped appearance (Yu *et al*, 1997; Kim and Samimy, 1999).

2.6.3. Vortex Generators

Flow separation occurs when the streamlines of fluid particles nearest to the wall, slowed down by wall friction and perhaps an adverse pressure gradient, break away from the boundary surface. Large energy losses are associated with boundary layer separation, and thus the point of separation plays an important role in the utility of many practical devices. As mentioned previously, the lift of an airfoil will be maintained at a higher angle of attack if flow separation is delayed. In addition, the pressure recovery of a diffuse is improved with delayed separation (Gad-el-Hak and Bushnell, 1991).

Vortex generators are designed to address the issue of flow separation and function by adding momentum to the region near the wall; that is, they supply additional energy to the fluid particles near the wall that are being retarded in the boundary layer. The additional energy comes simply from local redirection of high-momentum fluid, a process also known as re-energizing the boundary layer. Vortex generators function

passively by generating streamwise vortices near the wall, thus overturning the near-wall flow by large-scale motions.

Vortex generators generally consist of vanes with small aspect ratios mounted normal to the surface at an angle to the oncoming flow. Important characteristics of vortex generators include the planform shape, section profile and camber, yaw angle, aspect ratio, and height with respect to the boundary layer thickness. Another important aspect in vortex generator design is the spatial relationship between the devices. When identical vortex generators are mounted in rows, the effect produces co-rotating vortices. When they are mounted in opposing pairs, the devices produce counter-rotating vortices. Interaction between vortex generators can be constructive or destructive. Figure 2.7 shows important design parameters for counter-rotating vortex generators, including the vane length l, the vane height h, the distance between two adjacent vanes d_1, the distance between two sets of vanes D, and the vane angle α.

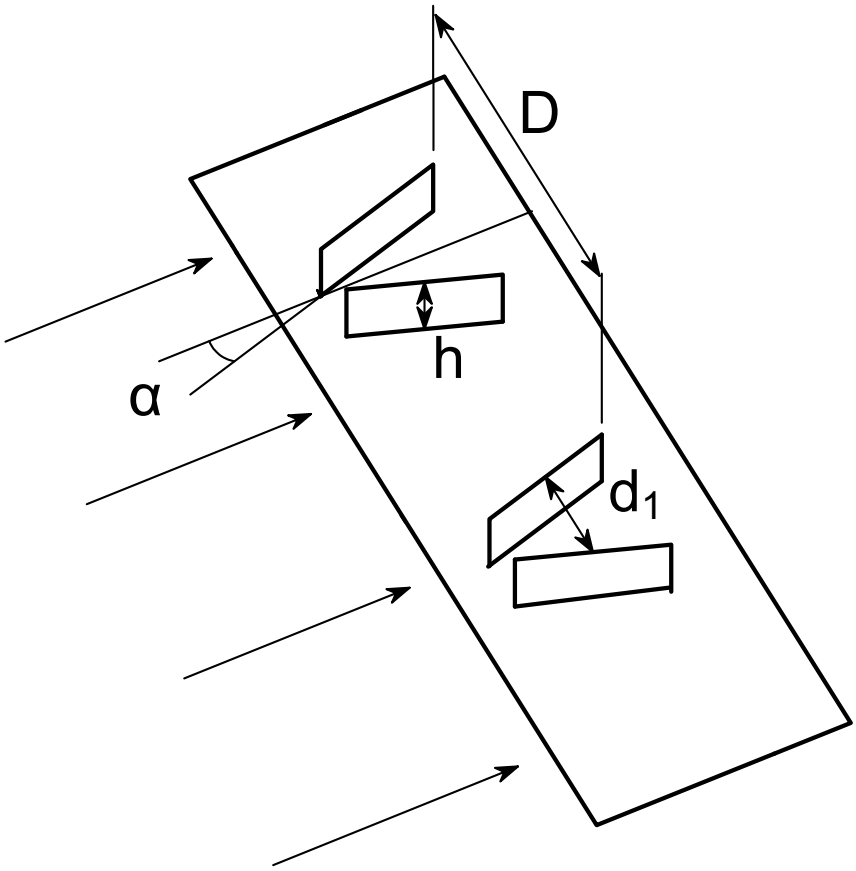

Figure 2.7: A diagram of a typical vortex generator of the counter-rotating design.

Vortex generators were first devised by H. D. Taylor in the 1940s. A thorough study of different vortex generator designs was conducted by Schubauer and Spangenberg (1960). Using a specially designed wind tunnel wherein a selection of adverse pressure gradients could be obtained, they studied the effects of forced mixing in a two-dimensional turbulent boundary layer. Pearcey (1960) published a book with general guidelines for vortex generator design. For the counter-rotating vortex generator design, he found that the parameter values displayed in Table 2.1 worked well.

Table 2.1: Optimum design ratios for vortex generator designs, as found by Pearcey (1960).

Design Ratio	D/h	D/d_1	l/h	α
Optimum Range	5 – 11.25	4 - 4.5	1.6 – 2.5	15° - 20°

Finally, since passive vortex generators do induce drag, it is helpful to construct them to be as small as effectively possible. Several studies have shown that even micro-vortex generators that are "submerged" beneath the boundary layer are still effective in re-energizing the boundary layer (Lin *et al*, 1994; Rao and Kariya, 1988).

2.7. Motivation

Bileaflet mechanical heart valves are used to replace native heart valves failing due to stenosis or insufficiency. However, these devices often initiate thromboembolism, thus necessitating lifelong, prophylactic anticoagulation therapy in the patient. One likely cause of this hyper-coagulative state is the non-physiologic levels of stress, both laminar and turbulent, experienced by the erythrocytes and platelets. These stress levels vary with the complex fluid dynamics experienced throughout the cardiac cycle and in the different regions of the BMHV. The highly transient jet emanating upstream from the b-datum line gap during valve closure is of particular concern. Laser Doppler velocimetry studies have shown that this jet can subject the blood elements to mean and peak levels of turbulent shear stress of 400 dyn/cm^2 and 1687 dyn/cm^2, respectively (Simon, 2004). An upper limit of 30 ms for the exposure time of these blood elements to this elevated shear stress is estimated by measuring the time of valve closure (Krishnan *et al*, 2006). The actual

exposure time is likely an order of magnitude lower. For instance, simulations of a squeeze flow in a BMHV periphal gap showed laminar stresses up to 5000 dyn/cm^2 for the last 2 ms of valve closure and up to 10000 dyn/cm^2 during leaflet rebound (Krishnan *et al*, 2006).

Various studies have also detailed the shear stress and exposure time ranges necessary to lyse a red blood cell or activate a platelet. For instance, Lu *et al* showed hemolysis occurring at turbulent shear stresses of 8000 dyn/cm^2 at an exposure time of 1 ms (2001) and Heuser and Opitz (1980) showed detectable hemolysis in porcine blood after a laminar shear stress of 1000 dyn/cm^2 was applied for 3 ms. Platelet activation has been found to occur in response to short-term exposure (25-1650 ms) to relatively high laminar shear stress levels (300-1000 dyn/cm^2) (Ramstack, 1979). In addition, Colantuoni *et al* found that platelet activation occurred in less than 5 ms at a laminar shear stress level of 6500 dyn/cm^2 (1977). Research has thus indicated that the shear stress magnitudes and exposure times found in the highly transient jet emanating from the b-datum line gap during valve closure are sufficient to cause hemolysis and platelet activation.

CHAPTER 3

HYPOTHESIS AND SPECIFIC AIMS

Bileaflet mechanical heart valves (BMHVs), though a life-saving tool in treating heart valve disease, are often associated with several complications including a high risk of hemolysis, platelet activation, and thromboembolism. To address this risk, patients must undergo prophylactic anticoagulation therapy. One likely cause of this hyper-coagulative state is the nonphysiologic levels of stress experienced by the erythrocytes and platelets flowing through the BMHVs. Research has shown that the combination of shear stress magnitude and exposure time found in the highly transient leakage jet emanating from the b-datum gap during valve closure is sufficient to cause hemolysis and platelet activation (Simon, 2004; Lu et al, 2001; Ramstack et al, 1979). Reducing the shear stresses experienced by the blood flowing through the b-datum gap during valve closure may therefore reduce the prevalence of valve-related blood damage. Such shear stress reduction could be achieved by passive flow control, in particular vortex generators, incorporated onto the BMHV leaflet surface. Vortex generators have been used to control shear flows in various aerodynamic applications, and it is thus thought that their application to BMHV leaflet surfaces may reduce shear stresses by creating streamwise vortices that will serve to dissipate the regurgitant jet originating from the b-datum gap at valve closure.

Hypothesis: Passive flow control may have the potential to reduce flow-induced thrombogenicity by altering the fluid mechanics of bileaflet mechanical heart valves.

This hypothesis was addressed by the three following specific aims:

Specific Aim 1: Determine the effect of various leaflet vortex generator designs on the fluid mechanics of the b-datum leakage jet.

Under physiologic conditions, the b-datum closure jet is transient, a feature that makes the jet difficult to study. Removing this transience is desirable because it creates a simplified proxy of the jet. A steady jet system modeling the physiological, transient jet emanating from the b-datum line during valve closure was therefore developed in order to better understand the effect of vortex generators on the fluid mechanics of the jet. A St. Jude Medical BMHV, with its leaflets fixed in an 'almost-closed' position and its peripheral gaps sealed, was placed in a steady flow loop and subjected to reverse flow. The fluid mechanics of the leakage jet was characterized and quantified for the case of the valve with and without vortex generators affixed to the leaflets so as to assess their effect on the b-datum leakage jets. For all experiments, a flow visualization technique was used to characterize the general jet structure. Digital Particle Image Velocimetry (DPIV) was subsequently used to quantify the velocity, vorticity, viscous stress, and Reynolds shear stress in the jet wake, and the results with and without vortex generators were compared. This study presents both a qualitative and quantitative assessment of the effect of vortex generators on the fluid mechanics of the steady b-datum leakage jet.

***Specific Aim 2*: Determine the effect of leaflet vortex generators on the procoagulant potential of the b-datum leakage jet and correlate that effect with the vortex generator-induced changes to the jet flow structure.**

The steady jet model developed in Specific Aim 1 for the purpose of simplifying the physiologic closure jet was employed to perform *in vitro* experiments with human blood. The valves, with and without one vortex generator design mounted on the valve leaflet surfaces, were tested in the steady flow loop developed in Specific Aim 1. The level of coagulation induced by the flow through the b-datum gap was quantitatively measured over the course of each experiment by assaying for thrombin-antithrombin III (TAT III), a marker in the coagulation cascade indicating thrombus formation. The TAT III results were then compared with the flow field data obtained in Specific Aim 1 so as to link fluid mechanical properties with procoagulant potential and to establish the effect of vortex generators on both mechanical and biological parameters.

Specific Aim 3: Explore the effect of vortex generators under pulsatile conditions on the valvular fluid mechanics throughout the cardiac cycle and in particular during the closure phase.

While the steady flow system considered in Specific Aims 1 and 2 provides valuable insight into the effect of leaflet vortex generators on the fluid mechanics and thromboembolism potential of BMHVs, it cannot truly represent the physiologic b-datum closure jet because it does not incorporate the transient nature of that jet. It is thus

necessary to examine the effect that leaflet vortex generators have on the b-datum closure flow under physiologic, pulsatile conditions. It is also important to consider what consequences the presence of vortex generators might have on BMHV flow fields throughout the entire cardiac cycle. In order to achieve these objectives, valves with and without vortex generators were mounted in the aortic position of the Georgia Tech Left Heart Simulator. A flow visualization technique was employed to examine the flow fields both upstream and downstream of the valve. DPIV was used to quantify the flow field upstream of the valve throughout the cardiac cycle, and highly resolved measurements were made in order to closely examine the valve's closure jet. This study presents qualitative and quantitative evidence of the effect of leaflet vortex generators on BMHV flow fields under physiologic conditions throughout the cardiac cycle.

CHAPTER 4

EXPERIMENTAL METHODS AND PROTOCOLS

Organization of Experimental Methods and Protocols

4.1. Overview

In order to test the hypothesis that vortex generators applied to bileaflet mechanical heart valve leaflets can diminish blood damage caused by the leakage flow during valve closure, two sets of experiments were conducted to characterize the flow through the b-datum line: 1) a set of steady flow experiments and 2) a set of pulsatile physiologic experiments. Both steady and pulsatile experiments were run with and without vortex generators so as to determine the effect of these devices on the overall valve function. The steady flow experiments encompassed flow visualization to obtain an overall picture of the fluid mechanics, particle image velocimetry data acquisition to quantify the flow fields in detail, and *in vitro* experiments with human blood to study thrombus formation. Since the steady experiments focused solely on modeling the leakage during valve closure, pulsatile experiments were also performed to investigate the effect of vortex generators in a realistic, physiologic setting and to understand their effect over the entire cardiac cycle. In this set of pulsatile experiments, the valve was mounted in the aortic position of the Georgia Tech Left Heart Simulator, and flow visualization was performed.

The following methods section will first discuss the vortex generator design and describe the steady and pulsatile flow loops used in these experiments. The techniques of flow visualization and DPIV will then be discussed. A description of the experimental

conditions specific to each type of experiment will then be presented. Finally, the method by which the level of blood coagulation was determined in the steady flow loop will be presented.

4.2. Vortex Generators

4.2.1. Vortex Generator Design

The counter-rotating vortex generators (VGs) designed for these experiments are similar to those used on aircraft wings to re-energize the boundary layer and increase airflow over the wing's control surfaces (Gad el Hak, 2000). The schematic of a vortex generator array in Figure 4.1 shows the important design parameters for counter-rotating vortex generators, including the vane length l, the fin height h, the distance between two adjacent fins d_1, the distance between two sets of fins D, and the fin angle α. In Tables 4.1 and 4.2, the relevant vortex generator dimensions and parameters discussed in Chapter 2 are tabulated for the six vortex generator designs considered in this study. The design codes in these tables designate the fin angle and the fin height. For instance, the code "R05T" indicates a fin angle α of 5° and a "Tall" fin height h of 1 mm while the code "R35S" represents a fin angle α of 35° and a "Short" fin height h of 0.5 mm.

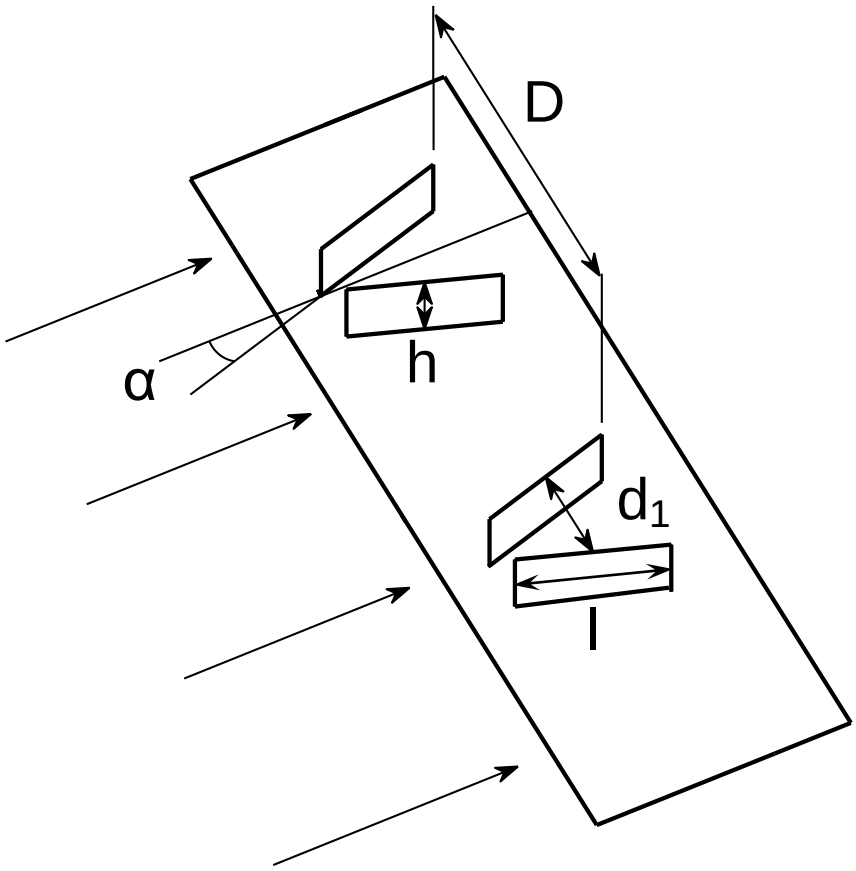

Figure 4.1: A diagram of a typical vortex generator array of the counter-rotating design.

Table 4.1: Dimensions of the six vortex generator designs. All dimensions are in millimeters.

	l (mm)	h (mm)	d_1 (mm)	D (mm)
R05S	4.3	0.5	1.5	3.7
R05T	4.3	1.0	1.5	3.7
R20S	4.5	0.5	2.7	5.6
R20T	4.5	1.0	2.7	5.6
R35S	5.2	0.5	4.7	8.6
R35T	5.2	1.0	4.7	8.6

Table 4.2: Dimensionless parameters describing vortex generator designs used in this study

	l/h	D/d	D/h
R05S	8.6	2.5	7.4
R05T	4.3	2.5	3.7
R20S	9.0	2.1	11.2
R20T	4.5	2.1	5.6
R35S	10.4	1.8	17.2
R35T	5.2	1.8	8.6

The devices, shown in Figure 4.2, are composed of opposing pairs of vertical fins set on a base plate that is 0.5 mm thick. The short edges of the base plate are curved to conform to the leaflet edges of a 23mm SJM Standard bileaflet mechanical heart valve. The fins are swept diagonally across the base plate at one of three fin angles (5°, 20° or 35°). This fin

angle α is the acute angle formed by the intersection of the fin and a line perpendicular to the long edge of the VG base. Due to the rotation of the leaflets during the cardiac cycle, the angle of the fin is not necessarily the angle of attack as it would be in a conventional vortex generator application. Finally, in order to separately investigate the effect of the plate versus that of the plate plus the fins, a plate with no fins was also designed and designated as "No Fins on VG."

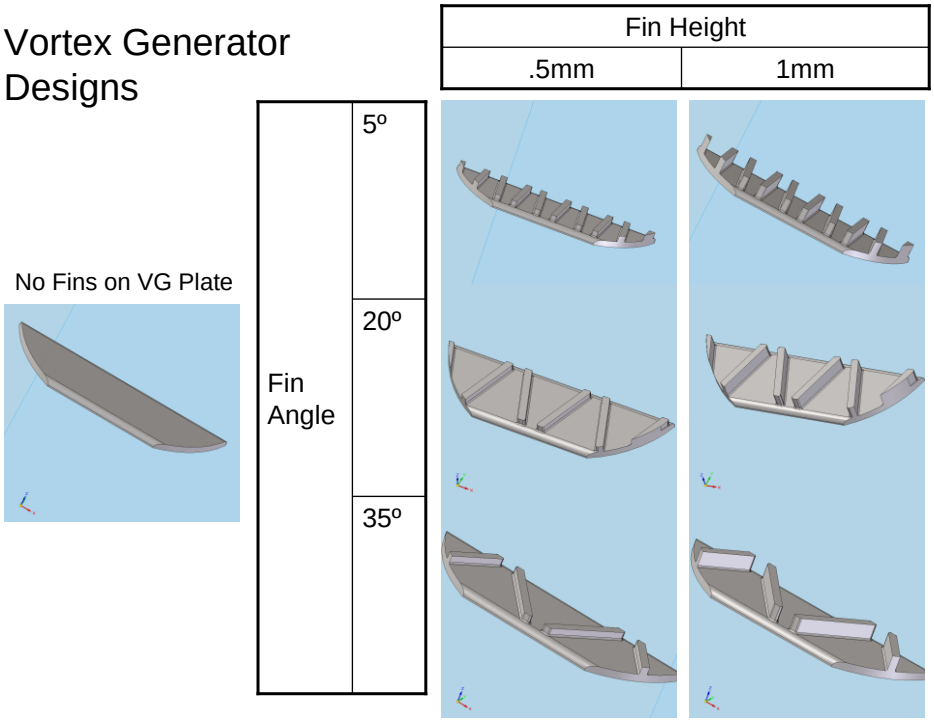

Figure 4.2: Vortex Generator Designs

4.2.2. Vortex Generator Construction and Mounting

The vortex generator designs were drawn in CAD and manufactured via high-resolution stereolithography, with the smallest resolvable feature being approximately 3/1000th of

an inch. See Appendix A for CAD-generated drawings of the vortex generators. A Viper Si2 stereolithography machine (3D Systems; Rock Hill, SC) with Waterclear resin (DSM Somos, Elgin, IL) was used to build the devices. The vortex generators were affixed to the downstream surfaces of the BMHV leaflets using a thin film of silicone. The location of the vortex generator with respect to the leaflet edge was kept constant at 2.16 mm by using a guide tool. This "L"-shaped tool fit along the leaflet edge and protruded onto the leaflet surface 2.16 mm. By pressing the vortex generator plate against the tool edge, the VG plate could be reproducibly positioned with respect to the leaflet edge. The plate was then visually centered on the leaflet. Figure 4.2 shows the vortex generator placement with respect to the leaflet edges.

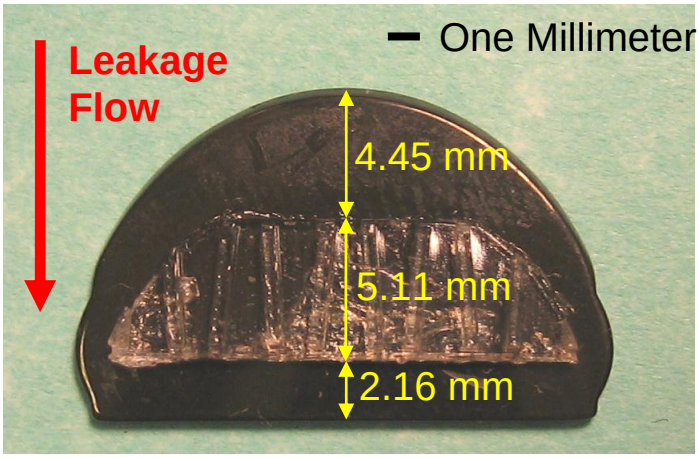

Figure 4.3: Leaflet from a 23mm Saint Jude Medical Standard BMHV, showing vortex generator placement and direction of leakage flow.

4.3. Fluid Mechanical Assessment

4.3.1. Steady Flow Experiments

4.3.1.1. Valve Mounting System and Valve Chamber

A 23mm Saint Jude Medical Standard BMHV with the sewing cuff removed was used for all steady flow experiments. The valve was set in a mold, seen in Figure 4.3, that surrounded it and held its leaflets in a predetermined position.

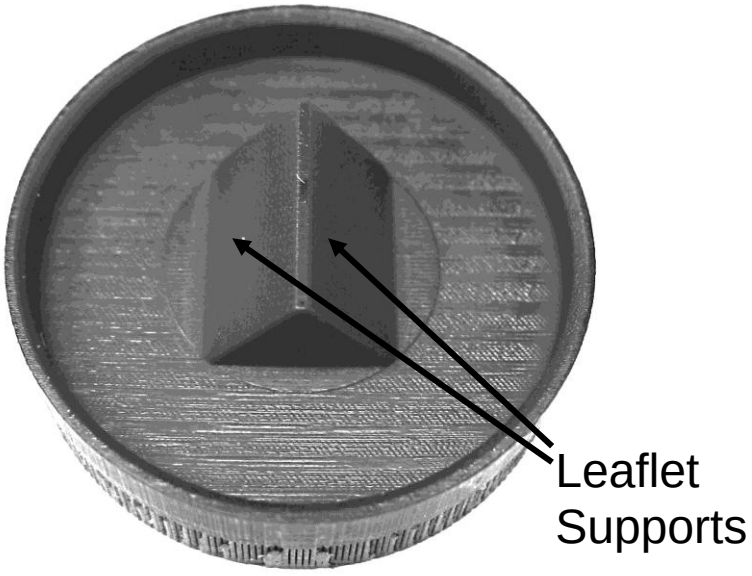

Figure 4.4: Mold used to manufacture PDMS mounting system.

Liquid polydimethylsiloxane (PDMS) was then mixed from a Sylgard 184 Silicone Elastomer Kit (Dow Corning) and was poured into the mold and allowed to cure. The PDMS around the valve thus formed a pliant mounting ring, as shown in Figure 4.4. The PDMS system blocked both the hinge and peripheral gaps while maintaining the b-datum gap open at a known width of 0.86 mm. This width corresponds to the width at the

instance of valve closure when the strongest closure jet is seen to emanate from the b-datum gap (Chandran and Aluri, 1997). The flow system used in this study thus provides a steady leakage jet that serves as a model of the transient jet found in an implanted heart valve subjected to pulsatile flow conditions.

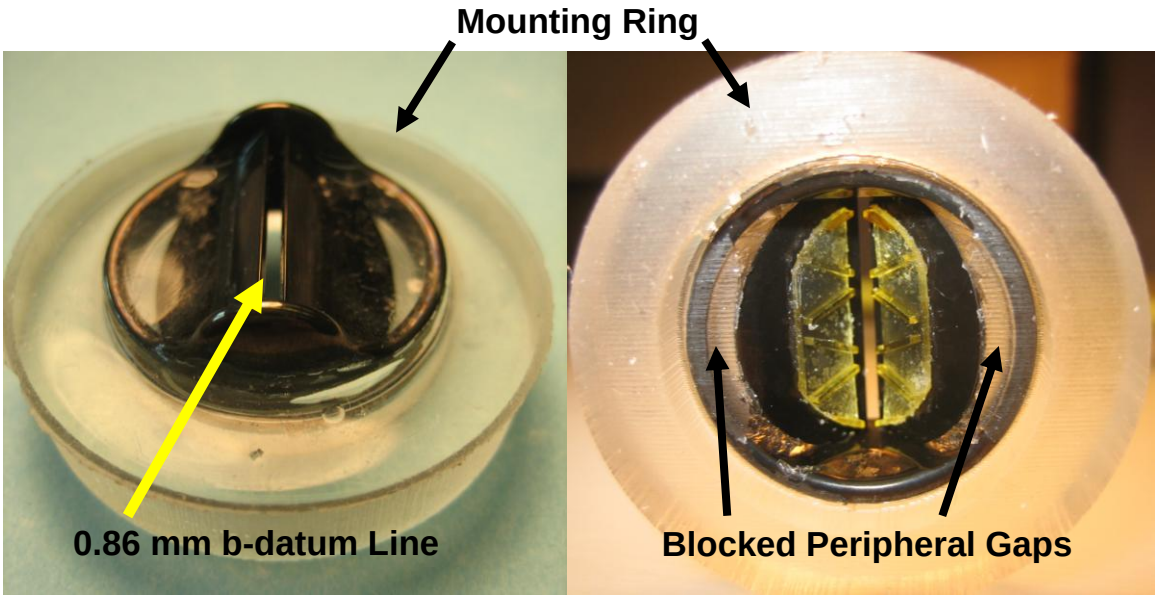

Figure 4.5: The valve in its PDMS mounting system, with the vortex generators

The design of the chamber in which the valve was mounted is shown in Figure 4.5. This chamber, designed by Fallon (2006), was made in two pieces that could be clamped together with two end plates and four threaded rods in order to secure the valve. This design was used to machine a polycarbonate chamber for the blood experiments. However, because of the high opacity of the polycarbonate material, a second chamber of highly translucent cast acrylic was machined for the PIV and flow visualization experiments. Figure 4.6 shows the valve mounted in the acrylic chamber.

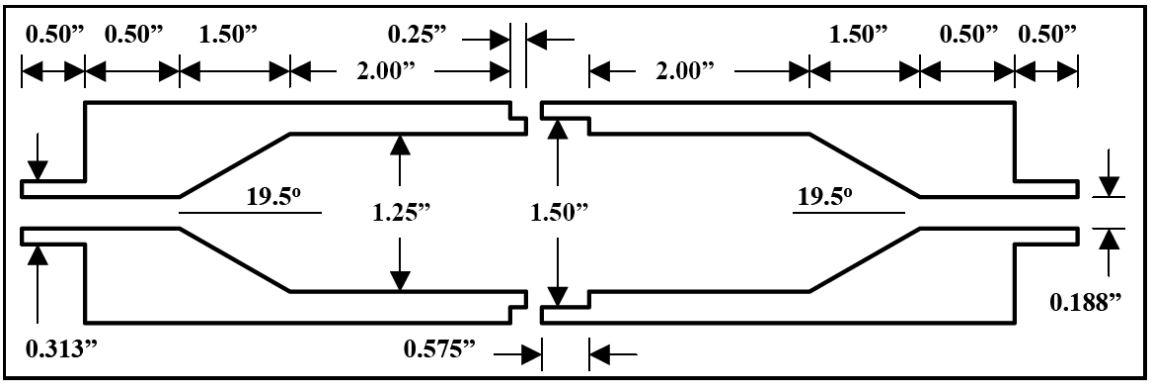

Figure 4.6: Diagram showing the dimensions of the valve mounting chamber

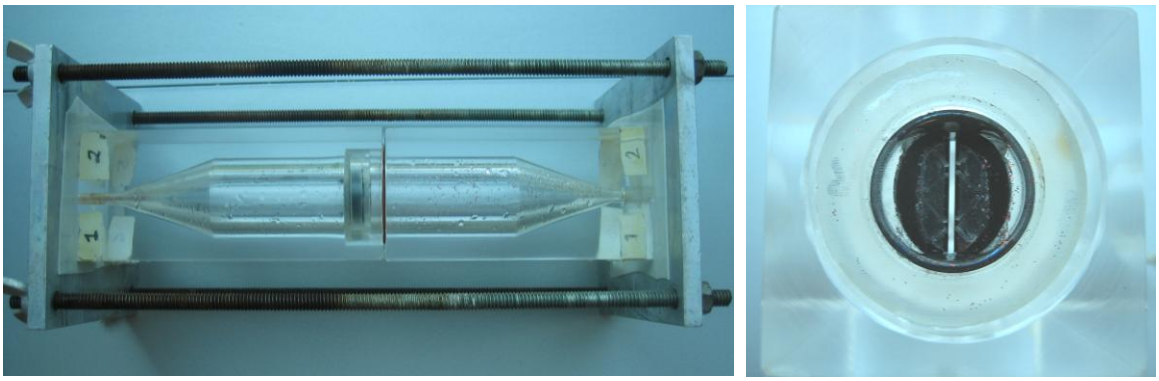

Figure 4.7: View of the transparent, cast acrylic chamber with the mounted valve (left) and close-up view of the mounted valve (right).

4.3.1.2. Steady Flow Loop

In all steady flow experiments, a flow loop was constructed by connecting the valve mounting chamber to a centrifugal bypass pump (Medtronic Biomedicus 540; Minneapolis, MN) using 6.35 mm ID silicone tubing (VWR Scientific). The following two types of pump heads were used: 1) a pediatric pump head (Model BP-50, Medtronic) with a 48 mL priming volume for the blood experiments and 2) an adult-sized pump head with a slightly larger priming volume (Model BP-80, Medtronic) for the PIV and flow visualization experiments. An inline, Bio-Probe flow transducer (TX50, Medtronic) was

used to measure the flow rate. In addition, a 150 mL bubble trap created from two large, end-to-end syringes was inserted into the flow loop to ease the removal of microbubbles. A schematic of the flow loop is shown in Figure 4.7.

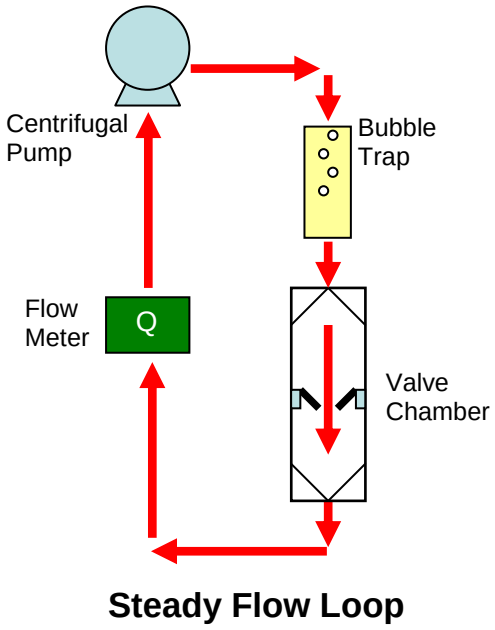

Figure 4.8: Schematic of the steady flow loops used for DPIV and flow visualization experiments.

4.3.2. Pulsatile Flow Experiments

4.3.2.1. Valve and Mounting Chamber

The valve mounting system for the pulsatile experiments was the same as that for the steady flow experiments except that the PDMS blocking the peripheral gaps was removed, thus allowing free movement of the valve leaflets. The chamber employed for the pulsatile experiments was machined out of highly transparent cast acrylic and featured an axisymmetric expansion just downstream of the valve mounting position in order to mimic the presence of the human aortic sinuses. The two parts of the chamber

were clamped together by two end plates and four threaded rods. A schematic of this chamber is seen in Figure 4.8.

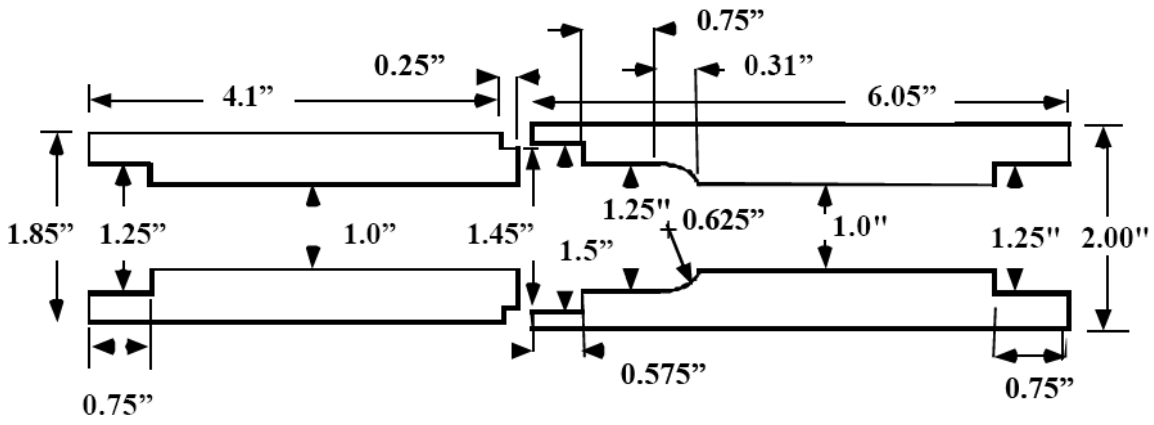

Figure 4.9: A diagram of the chamber used in the pulsatile experiments (courtesy of Travis, 2001)

4.3.2.2. <u>Flow Loop</u>

The Georgia Tech Left Heart Simulator, shown in Figure 4.9, was used for all pulsatile experiments. This system has been extensively used in the past (Simon, 2004; Leo, 2005; Travis, 2001) to model the left ventricle and aorta of the human heart by recreating physiologic flow and pressure waveforms. The essential components of this pulsatile loop included a reservoir, two valve chambers, a pneumatically driven bulb pump, and compliance and resistance sections.

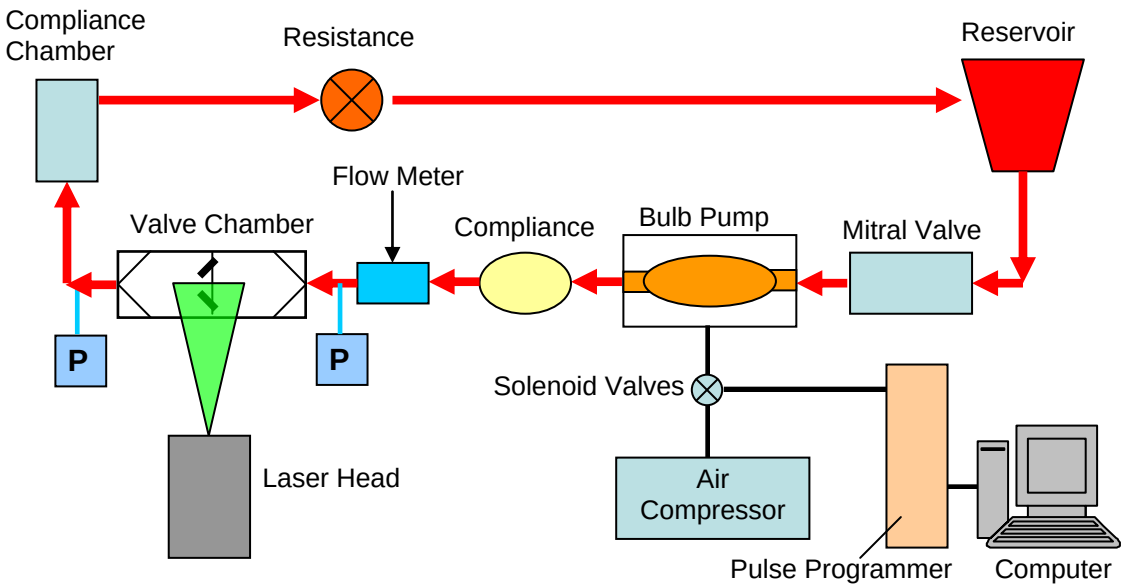

Figure 4.10: A diagram of the Georgia Tech Left Heart Simulator

The pneumatically driven bulb pump was used to drive the flow through the loop. The pulsatile system consisted of a bulb pump, an air compressor (Ultra AirPac, T2820P, Rietschle Thomas, Sheboygan, WI), a throttle valve (R1804-GOGO, Wilkerson Corporation, Englewood, CO), three solenoid valves (130B-111CAAA, Mac Valves Inc, Wixon, MI), and a computer interfaced with a pulse programmer. The bulb pump consisted of a flexible bladder in line with the flow loop; the bladder itself was sealed inside an acrylic chamber. The pressure between the bladder and the chamber wall could be regulated in order to periodically compress the bladder, thus forcing flow out of the bladder. The intensity of the bladder compression was controlled by the throttle valve on the air compressor while the timing of the compression was controlled by the computer via the pulse programmer and solenoid valves. During systole, one solenoid valve between the air compressor and the bulb pump would open, providing forward flow through the aortic valve. During diastole, the first solenoid valve would close while the

other two solenoid valves would open to the atmosphere. The bulb pump bladder would then relax to its normal position, allowing fluid to fill it again.

As seen in Figure 4.9, fluid flowed from an elevated reservoir through a tilting disc valve and into the bulb pump. The tilting disk valve served as a mitral valve by preventing backward flow when the bulb pump was compressed. After the bulb pump, the fluid flowed first through a flexible bladder which served as a compliance section. The next component was a long, straight ¾ inch PVC pipe with flow straighteners, which forced the flow to become well developed. An inline flow meter (T108, Transonic; Ithaca, NY), was placed next in order to measure the volume flow rate. The fluid then flowed through the aortic valve chamber and was then ejected into another compliance section, consisting of a vertical, acrylic chamber partially filled with air. The effect of this compliance chamber could be adjusted by raising or lowering the level of the fluid. Further downstream, a clamp on a flexible rubber tubing section served as resistance. The fluid was then returned to the reservoir via ¾ inch PVC pipe. Rubber tubing and hose clamps served to secure pieces together and to prevent leaks. Pressure measurements were made immediately upstream (ventricular pressure) and downstream (aortic pressure) of the valve chamber using a Cardiomed 4008 pressure measurement system (Medistim; Oslo, Norway) with disposable pressure transducers (Uniflow, Baxter; Deerfield, IL).

4.3.3. Flow Visualization

In order to gain insight into the global nature of the flow inside the chamber during both pulsatile and steady flow experiments, flow visualization was conducted. A blood analog

solution consisting of 60% water and 40% glycerin by volume was manufactured. The kinematic viscosity of this fluid was measured with a viscometer (Size 75, N663, Cannon Instrument Company, State College, PA), and adjusted to match that of blood (3.5 cSt). Several types of seeding were used, depending on the application: 1) air bubbles, 2) irregularly shaped polyvinyl chloride (PVC) particles, 3) glitter, or 4) a mixture of bubbles and PVC particles. A high-speed monochromatic camera with a 1280 x 1084 pixel CMOS sensor (Model A504K, Basler Vision Technologies; Exton, PA) was used with a Nikkor zoom lens (Nikon; Melville, NY) to image the flow. For the steady experiments, a frame capture rate of 167 frames per second was generally used, and footage of the flow was captured downstream of the valve.

For the pulsatile experiments, data was collected for the control case and for the R35T vortex generator design using the Georgia Tech Left Heart Simulator. The cardiac cycle duration was set to 860 ms, with a systolic period of 250 ms. A heart rate of 70 beats per minute was thus maintained, with a cardiac output of 5 L/min, a peak systolic flow rate of approximately 25 L/min, and a mean aortic pressure of about 100 mmHg. Flow and pressure waveforms averaged over 10 cycles are shown in Figure 4.13. The flow field upstream and downstream of the valve in the aortic position with and without vortex generators was captured at a frame capture rate of 500 frames per second.

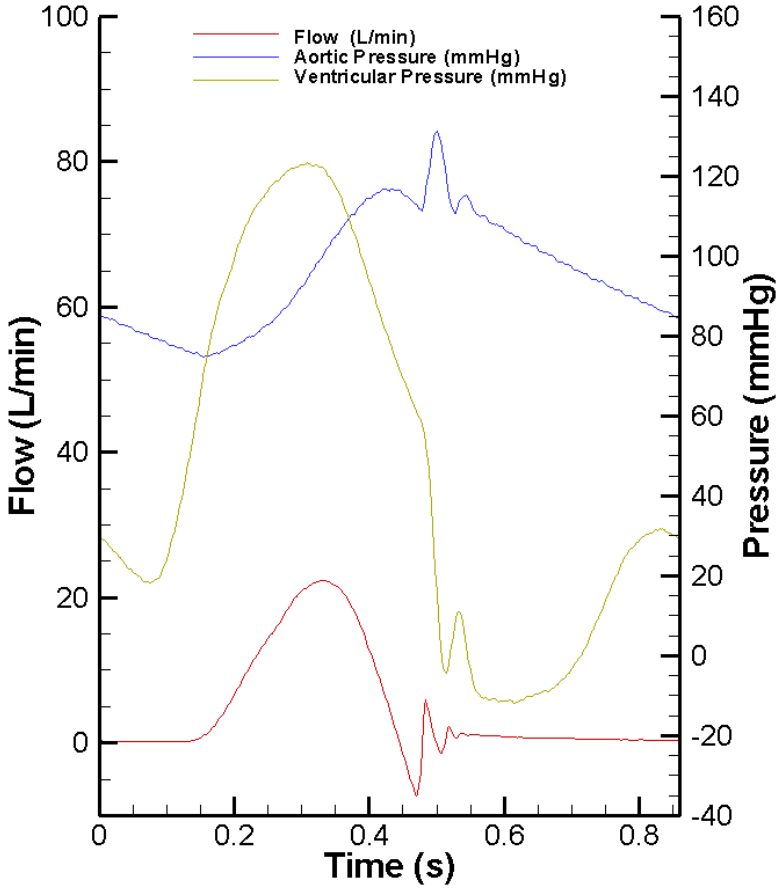

Figure 4.11: Typical flow and pressure waveforms for the pulsatile flow loop

Table 4.3: A summary of the pulsatile flow loop experiments

Flow conditions	**Experiments**	**Vortex Generator Configuration**								
		Control (No VG)	Valve with VG							
			Plate with No Fins	Short Fins			Tall fins			
				5	20	35	5	20	35	
Pulsatile	Flow vis.	X							X	

4.3.4. Digital Partical Image Velocimetry

4.3.4.1. Theory of PIV

Digital PIV is a widely used, non-intrusive technique that enables the measurement of an instantaneous velocity vector field in a plane of fluid flow. The flow is seeded with neutrally buoyant tracer particles, and the plane of interest is illuminated by a high energy laser light sheet. In quick succession, two images of the plane of interest are then captured by a charge-coupled device (CCD) camera, using two separate laser flashes as illumination. In order to prevent blurring of the particle motion in the acquired images, very short exposure times are used. These extremely short exposure times are not provided in the usual way by the rapid opening and closing of the camera aperture because of the physical limitations associated with that mechanical system. Instead, the duration of the laser pulse itself (~5ns) defines the exposure time, thus allowing one to "freeze" particles in images of even supersonic flows. A Q-switched Nd:Yag laser typically provides these short pulses of high energy light.

Once a pair of images is obtained, each image is divided into a number of zones known as interrogation regions. A statistical approach known as cross correlation is used to calculate average displacements between the two images' corresponding interrogation regions. Since the time between the camera exposures is known, average velocity can be calculated. The result is a two-dimensional velocity vector field describing the plane of interest in the fluid flow.

4.3.4.2. Experimental Setup

4.3.4.2.1. Working Fluid

A blood analog solution, consisting of a solution of deionized water, glycerin, and saturated sodium iodide (NaI) solution in a volumetric ratio of 1:20:79, was employed. The kinematic viscosity of the solution was adjusted to match that of blood at a high shear rate (3.5 cSt) and at the working temperature of the fluid, thus providing dynamic similarity between the cardiovascular system and these *in vitro* experiments. Additionally, the solution was mixed so that the refractive index of the fluid matched that of the acrylic chamber (n=1.49) in order to reduce optical distortion. The refractive index of the solution at the fluid's working temperature was measured with a refractometer (Model 2192, Extech; Waltham, MA). It should be noted that the temperature of the solution in the large volume pulsatile flow loop remained close to room temperature throughout the experiments, while in the small-volume steady flow loop, the action of the centrifugal pump quickly raised the temperature of the fluid to approximately 35° C. Therefore, the composition of the fluid was adjusted to ensure that, at the working temperature (room temperature for the pulsatile experiments and 35° C for the steady experiments), the blood analog solution had the correct optical and blood analog properties. Two batches of solution were thus mixed, one at room temperature and another one at 35° C using a heated water bath.

In order to perform DPIV, the fluid was seeded with fluorescent polymer particles (FPP-RgB-10, Dantec Dynamics; Skovlunde, Denmark). These particles are based on a

melamine resin polymer and are homogeneously coated with the fluorescent dye Rhodamine B. This dye absorbs maximum laser light at a wavelength of 532 nm (the same as that emitted by the laser used in these experiments) and subsequently emits maximum fluorescence at a wavelength of 590 nm. When coupled with a camera-mounted orange filter (Quantaray (Sigma); Ronkonkoma, NY), which allows the passage of light only in the same range at which the particles emit light, it was ensured that only the fluorescent particles would be detected by the camera. By thus eliminating the detection of dust particles, bubbles, or other debris that may happen to be in the fluid, the signal-to-noise ratio is improved. The particle diameter ranged from 1 to 20 μm, with a mean diameter of 10μm. The density of the particles was 1.5 g/cm^3, which closely matches the density of the sodium iodide solution (1.64 g/cm^3).

4.3.4.2.2. Laser and Optics

The laser pulses were produced by two 50 mJ Nd:YAG lasers (Model: SoloPIV III, New Wave Research, Fremont, CA) with a combined controller and power supply. These lasers have a maximum repetition rate of 15 Hz. The lasers and optics necessary to create a laser sheet were mounted on a Science Desk breadboard (07OSP002, Melles Griot; Rochester, NY). The laser was emitted from the laser head as a 4 mm diameter beam and was directed via a high energy mirror (16MFB153) to a 25 mm diameter plano-convex lens with a 500 mm focal length (01LPX319/066, Melles Griot). The converging laser was then directed vertically by another high energy mirror (16MFB415, Melles Griot) along an optical rail (07ORN001, Melles Griot), along which lenses and mirrors could be mounted. The laser next traveled through a cylindrical concave lens (01LCN001/066,

Melles Griot) with focal length of -12.7 mm. This lens transformed the cylindrical beam into a diverging sheet of light. The sheet, approximately 1 mm thick, was then directed horizontally into the test chamber by another high energy mirror. The region of interest was located approximately at the laser waist, 500 mm from the plano-convex lens, measured along the laser line. This laser setup remained the same for all DPIV experiments.

4.3.4.2.3. Cameras

In the steady flow loop, two 12-bit 1600x 1200 gray scale CCD Imager Pro cameras (MegaPlus II, ES2001; LaVision; Goettingen, Germany) were used to image the region of interest. One camera, placed orthogonal to the light sheet, was used with a 1-5 X fixed focal length zoom lens (Edmund Optics) to image an 8 mm x 6 mm small-scale field of view in the immediate proximity of the jet nozzle (the b-datum gap). The second camera was used with a 60 mm f/2.8D AF Micro-Nikkor zoom lens (Nikon) and an orange filter (Quantaray) to image a large-scale field of view that encompassed the chamber walls (approximately 45mm x 34mm). Because it was impossible for both cameras to be placed exactly orthogonal to the laser sheet and image the same area, the large-scale view camera was angled slightly and thus was mounted with a Scheimpflug camera lens adapter (1108196, LaVision) to reduce image distortion. Figure 4.10 shows the camera positions in relation to the valve and valve chamber.

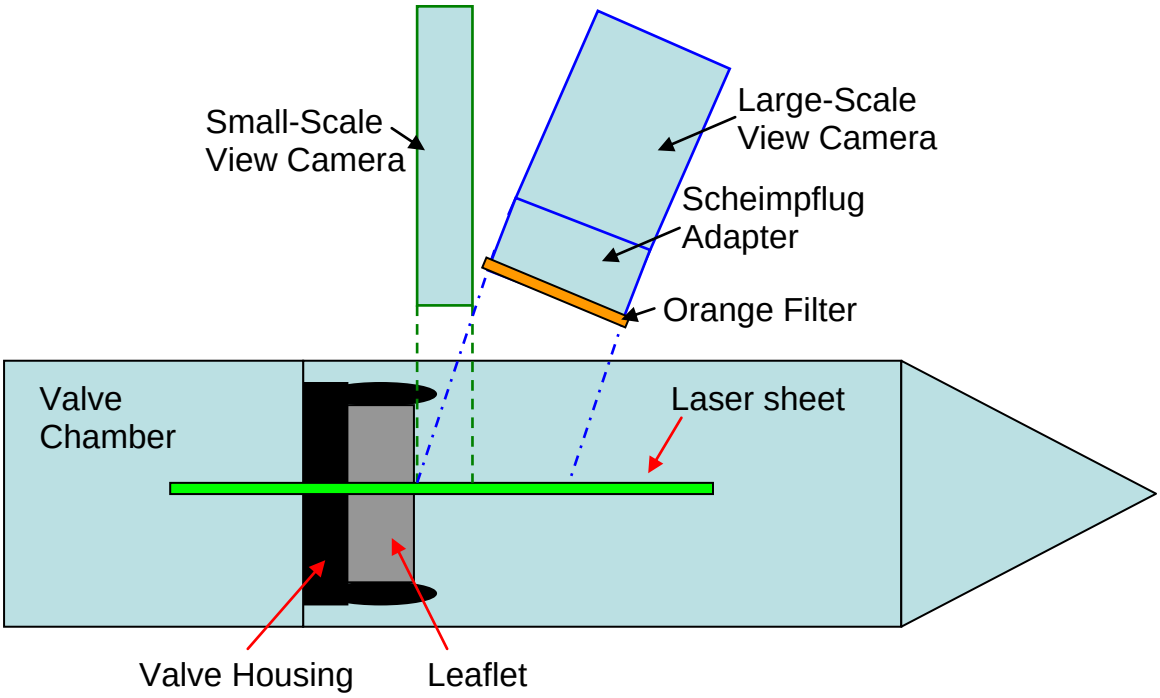

Figure 4.12: Schematic of the laser sheet relative to the camera, valve, and valve chamber (not to scale) for the steady flow experiments.

4.3.4.2.4. System Control

A programmable timing unit (Model # 1108013; LaVision) was used to synchronize the image capture with the laser pulse, and an A/D converter was used to integrate sampling control and data logging of the images. The software DaVis (version 7.0.11, LaVision GmBH, Germany) was used to integrate and control the lasers, cameras, programmable timing unit (PTU), and A/D converter with the host computer and to acquire all data to the same computer. The optimal separation time between the two laser pulses, which depends on the particle velocity, flow seeding, and interrogation window size, was found by trial and error for each experimental variation and for each camera.

4.3.4.2.5. Data Processing and Analysis

The cross-correlation of the image pairs collected during all PIV experiments was performed using the software DaVis 7.1.1.90 (LaVision, Germany), resulting in maps of instantaneous velocity vectors. Erroneous vectors inevitably arise during the cross-correlation because the Fast Fourier Transform (FFT) processing used to speed the cross-correlation always provides an outcome, regardless of whether the input is meaningful. These outlying vectors may be identified and removed by validation algorithms in the software. For instance, a median filter was generally used to remove outlying vectors which were then replaced by the average of the neighboring vectors. A smoothing function was also generally applied. Specific data processing and analysis steps will be described in subsequent sections.

4.3.5. PIV Experiments

4.3.5.1. Calibration

Calibration of the cameras is required before data acquisition and was thus performed independently for each camera because of the differing fields of view. Calibration was performed for the camera with the large-scale view by imaging a calibration grid consisting of a transparency sheet with a rectangular grid of points printed 1 mm apart. Ideally, this grid could be placed in the fluid-filled valve chamber in the same plane as the laser in order to account for the effects of refraction. However, this was not physically possible with the current chamber. Instead, the calibration grid was imaged while submerged in the sodium iodide solution. The depth from the fluid free surface to the calibration grid was the same distance as that from the top of the valve chamber to the

laser sheet plane during the experiments. Since the acrylic chamber and the sodium iodide solution have the same refractive index, the sodium iodide solution substituted for the presence of the actual chamber. Calibration for the small-scale view was carried out in a similar manner with a glass calibration plate with points spaced 0.5 mm apart.

4.3.5.2. Experimental Conditions

Two sets of experiments were carried out.

1) In one set of experiments, 6000 image pairs were acquired from the small-scale view camera for the R20T vortex generator design and for the Control case with no flow modification. These image pairs were taken in the plane bisecting the b-datum line, as seen in Figure 4.12.

2) In a second set of experiments, 350 image pairs were acquired from the large-scale view camera for all eight experimental cases. This data set was also taken in the plane bisecting the b-datum line.

For all of the experimental cases described above, the pump was operated at approximately 2500 RPM in order to achieve a volume flow rate of 3 L/minute. These setting resulted in a bulk velocity of about 2.3 m/s with maximum jet velocities up to 4 m/s. These velocities are on the same order of magnitude as the peak velocities found experimentally in BMHV closure flow (Simon, 2004). These setting resulted in a bulk Reynolds number of approximately 570. For the steady flow experiments with the large-scale view camera, a pulse separation of 50 ms was used while a pulse separation of 20

ms was used for the small-scale view camera. Table 4.4 shows a summary of the experimental conditions.

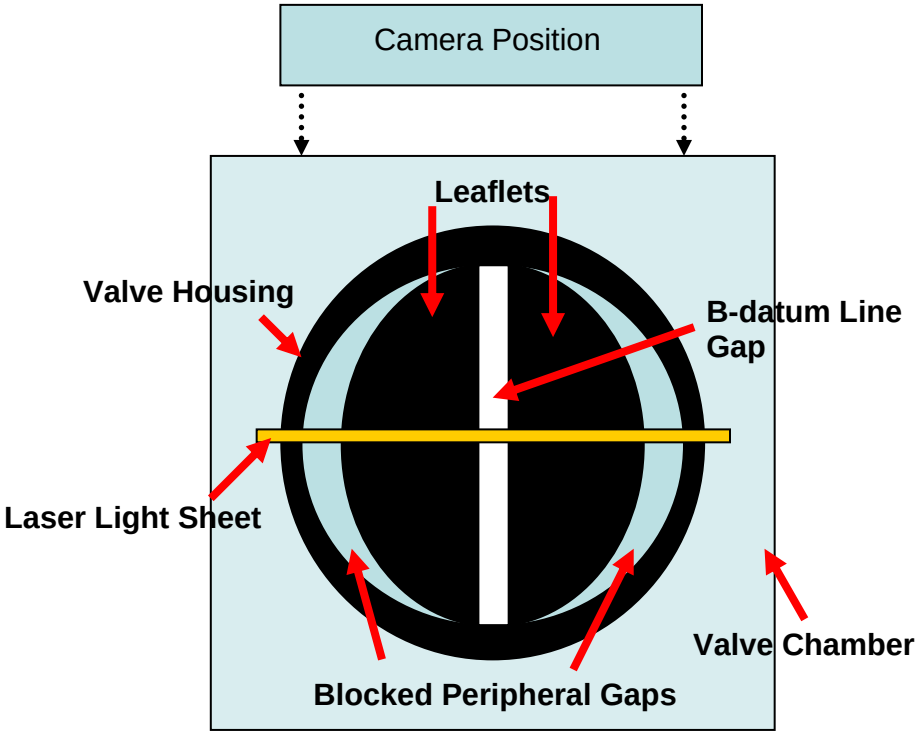

Figure 4.13: Laser sheet relative to the valve

Table 4.4: A summary of all the steady flow experiments

Flow conditions	**Experiments**	**Vortex Generator Configuration**							
		Control (No VG)	Valve with VG						
			Plate with No Fins	Short Fins			Tall fins		
				5	20	35	5	20	35
Steady	Flow vis.	X							X
	PIV	X	X	X	X	X	X	X	X

4.3.5.3. Data Processing

The processing was performed using DaVis software (LaVision Inc.) A mask outlining the area in which particles were present was created for the image pairs in each experimental condition. The area outside the mask (i.e. outside the chamber) was discarded so as to optimize the processing time by computing vectors only in the region of interest. A multi-pass cross-correlation algorithm was used to calculate vectors, beginning with a 64x64 pixel interrogation region and moving down to an 8x8 pixel interrogation region. An overlap of 50% between the interrogation regions was used in order to increase vector resolution. This multi-pass processing algorithm automatically activates a post-processing step that occurs between cross-correlations with different window sizes. In this step, a median filter and smoothing function are used. The final vector fields of the small-scale view steady experiments were filtered and smoothed. However, in the large scale view steady experiments, where large velocity regions are adjacent to low velocity areas, a median filter was not used for the final vector fields. Indeed, it was found that many of the high velocity vectors were removed because of the neighboring low velocity vectors. Instead, these vector fields were simply smoothed. The filtered vectors were then used to calculate the ensemble-averaged velocity fields with streamwise and cross-stream components of u and v, the root-mean-square velocity fields u_{rms} and v_{rms}, mean vorticity ω, and the Reynolds shear stress τ_{xy} by the following equations:

$$u_{rms} = \sqrt{\frac{\sum_{i=1}^{n} (u - \bar{u})^2}{n}}$$ Equation 4.1

$$v_{rms} = \sqrt{\frac{\sum_{i=1}^{n} (v - \bar{v})^2}{n}}$$ Equation 4.2

$$\omega = \frac{d\bar{v}}{dx} - \frac{d\bar{u}}{dy}$$ Equation 4.3

$$\tau_{xy} = \overline{\rho u' v'}$$ Equation 4.4

4.3.5.4. Vector Resolution

The quality of the vector fields resulting from cross-correlation depends on many factors. In the steady experiments, the vector spacing of the large-scale view was 28.4 μm per pixel. Using a 50% overlap between interrogation regions in the cross-correlation resulted in a resolution of 151 μm per vector. For the small-scale view, the vector spacing was 5.0 μm per pixel, resulting in a resolution of 26.4 μm per vector.

4.3.5.5. Phase Averaging Analysis

Because the jet was found to aperiodically oscillate about the b-datum line, a binning analysis was completed to remove the effect of that oscillation. For instance, jet oscillation artificially inflates the magnitude of the Reynolds shear stress and could obscure the effect of the vortex generators on the jet fluid mechanics. In order to account for this possibly confounding factor, the factor of jet oscillation was itself quantified and subsequently removed. This analysis was carried out on both the large-scale and small-scale data with one difference. For the small-scale data, the data were divided into nine

bins. In the large-scale data, the data were divided into only 5 bins because of the smaller number of samples.

In order to accomplish this analysis, the instantaneous jet position was identified at a point 12 gap widths (12W) downstream of the jet nozzle in all vector field realizations. As seen in Figure 4.14, the edges of the jet were arbitrarily defined as the points along the profile where the streamwise velocity exceeded 0.5 m/s. This jet width was then bisected to obtain an estimation of the instantaneous jet position. Histograms and standard deviations of the instantaneous jet position distributions for the Control and R20T VG cases are shown in Figure 4.15. The x axis shows the position within the chamber with x = 0mm corresponding to the jet nozzle. The y axis shows the number of occurrences where the instantaneous jet position falls into the bin represented on the x axis. The histograms thus qualitatively show that the Control case jet oscillates more and with a larger magnitude than the R20T case. This is seen because the bins extend to x = ±3mm for the Control case while they only extend to x = ±2.5mm for the R20T VG case. The slope on the sides of the distribution in the R20T VG case is also steeper than that in the Control case. In addition, the histograms in both cases are slightly skewed with respect to the zero position towards the right side , indicating that the jet is more often pointed in one direction (towards the bottom wall) than in the other (upper wall). The standard deviation (and thus the level of jet oscillation) for the Control case is higher than that for the R20T VG case.

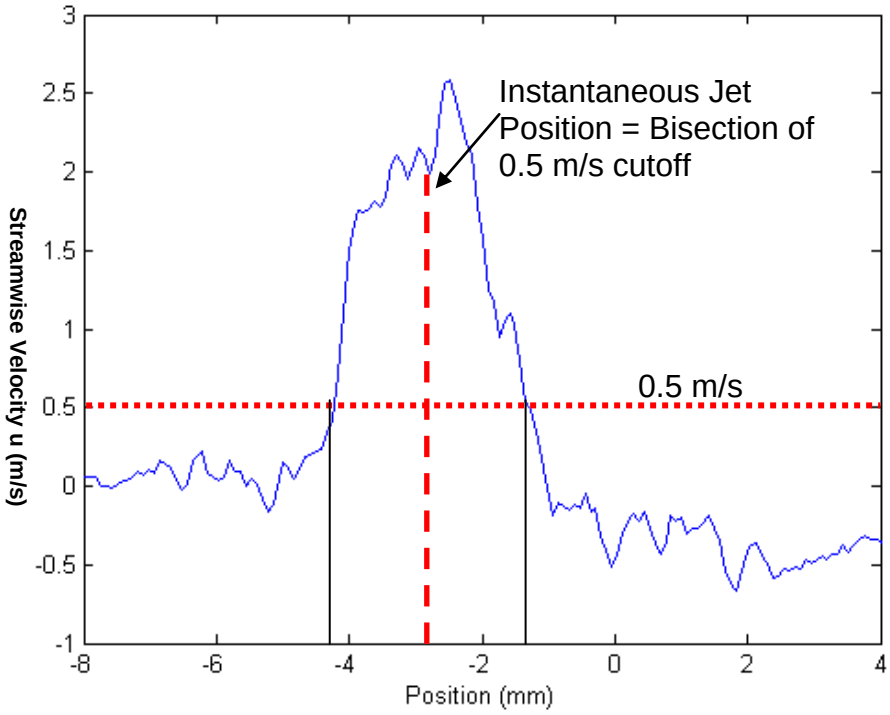

Figure 4.14: An example jet profile showing the method by which the instantaneous jet location was determined, where x = 0mm is the jet nozzle.

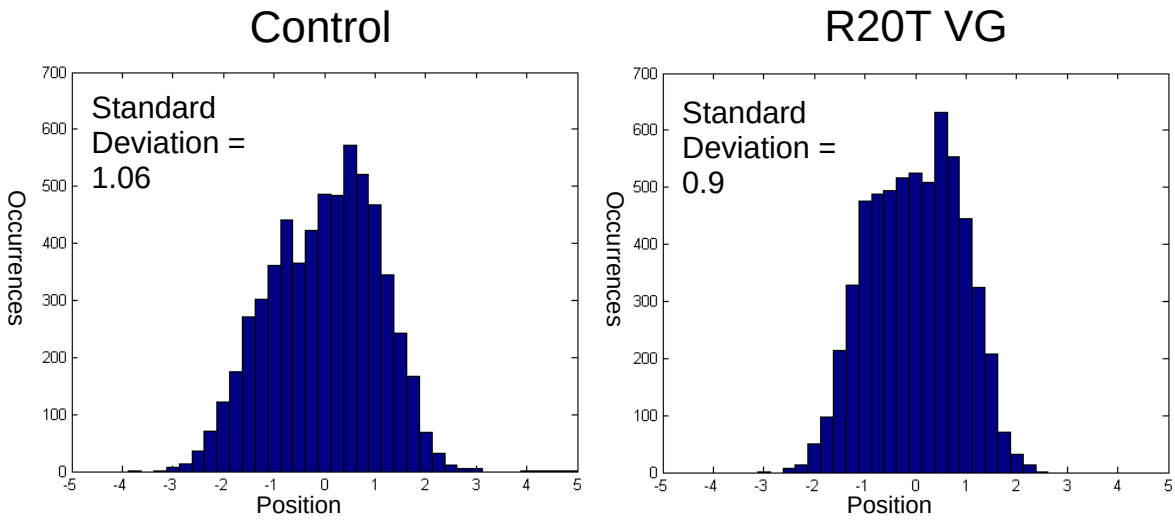

Figure 4.15: Histograms of 6000 instantaneous velocity field realizations for both Control and R20T cases where x =0 mm on the x axis corresponds to the jet nozzle.

In order to analyze and remove the effect of the jet oscillation, the velocity field realizations were first divided into bins based on instantaneous jet position. Bins 2 through 7 were equally spaced at 0.5mm while the extreme bins (1 and 9) were extended to encompass outlying data points. As shown in Figure 4.16, most bins contained at least 400 instantaneous velocity field realizations, with the exception of the most extreme bins (1 and 9) which contained fewer. The instantaneous images corresponding to each bin were identified and then averaged so as to calculate for each bin the ensemble-averaged velocity field. Further filtering of the instantaneous velocity field realizations in each bin was performed by cross-correlating the velocity components of each instantaneous velocity field realization with the corresponding component of the mean velocity field of that particular bin. (See Matlab code in Appendix A.) As shown in the scatter plot of Figure 5.12, the cross-correlation coefficients computed for each velocity component were used to select the instantaneous velocity field realizations that most closely correlated with the mean velocity field. Specifically, the instantaneous velocity field realizations for which both the u and v correlation coefficients were above the corresponding mean correlation coefficients were selected (gray quadrant in Figure 4.17). Ensemble-averaged velocity magnitude, the root-mean-square velocity fields, the mean vorticity, and the Reynolds shear stress were then calculated for the instantaneous velocity field realizations remaining in each of the nine bins.

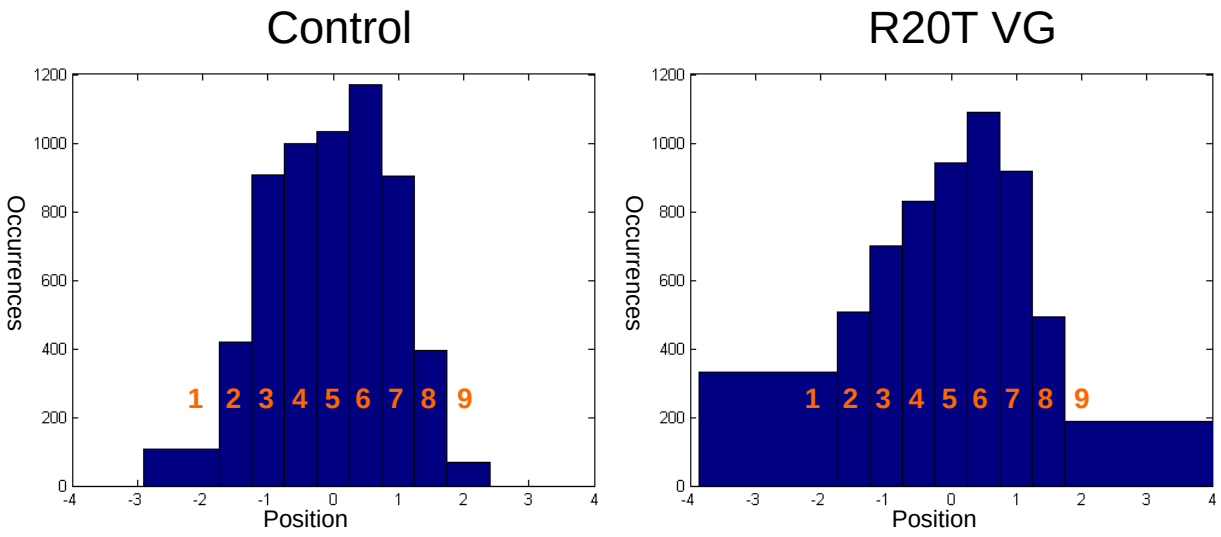

Figure 4.16.: Histograms showing the division of the 6000 instantaneous velocity field realizations into 9 bins for both the Control and R20T VG cases.

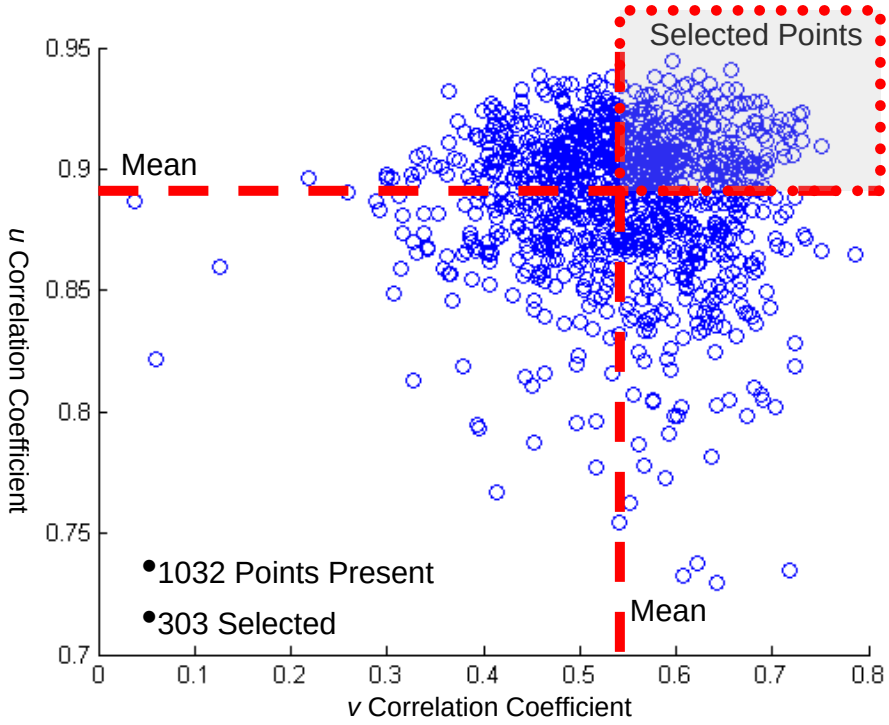

Figure 4.17: Example scatter plot of correlation coefficients showing the selected quadrant of instantaneous velocity field realizations which most closely correlate with the mean velocity field.

4.4. Blood Coagulation Assessment

4.4.1. IRB Approval Specifics

These *in vitro* experiments utilizing human blood were approved by the Institutional Review Board (IRB) at the Georgia Institute of Technology under the Protocol Number H02152 and the project title "Characterization of Clot Disposition on Mechanical Heart Valves." The protocol, including an example of a stamped consent form, is included as Appendix A.

4.4.2. Experiment Overview

In vitro experiments using human blood were performed using a system designed to assess the thrombogenic potential of various devices in the steady flow loop. This system was developed by Fallon *et al* (2006) in order to study the procoagulant potential of BMHV hinge geometries. The system is unique in that it provides for the recalcification of the recirculating citrated blood. This addition dramatically increases the magnitude of the reactions that lead to thrombus formation and also increases the sensitivity for their detection. The levels of the marker used to determine coagulation in this study, TAT III, could then be quantitatively ascertained via an ELISA assay.

4.4.3. Protocol

4.4.3.1. Blood Experiment

Blood was drawn from the donor by venipuncture using a 21 gauge needle from a vein collection set. Blood was drawn by a certified phlebotomist at the Georgia Tech Health Center. Volunteers were randomly selected from a population of healthy individuals, both

male and female, who had not taken aspirin for the previous two weeks. Donor age ranged from approximately 21 to 35, with an average of about 26. Blood was used within 1.5 hours of the time when it was drawn.

The blood was drawn into 60 ml syringes which contained 5.4 ml of anticoagulant (3.2% sodium citrate solution), resulting in a blood to sodium citrate solution ratio of approximately 10:1. The anticoagulated blood was then used to fill a steady blood flow loop with a total volume of 180 ml. All air bubbles were removed from the loop. Because the volume of the blood drawn by the phlebotomist varied somewhat, it was usually necessary to add a small volume of saline to the 180 ml loop in order to completely fill it. The mean (± standard deviation) of this volume across all the blood experiments was 10.4 ml (± 5.1 ml). This dilution was accounted for in the final calculation of TAT. In addition, a temperature gauge was affixed to the tubing in order to estimate the blood temperature throughout the experiment. A detailed schematic of the blood loop is given in Figure 4.18.

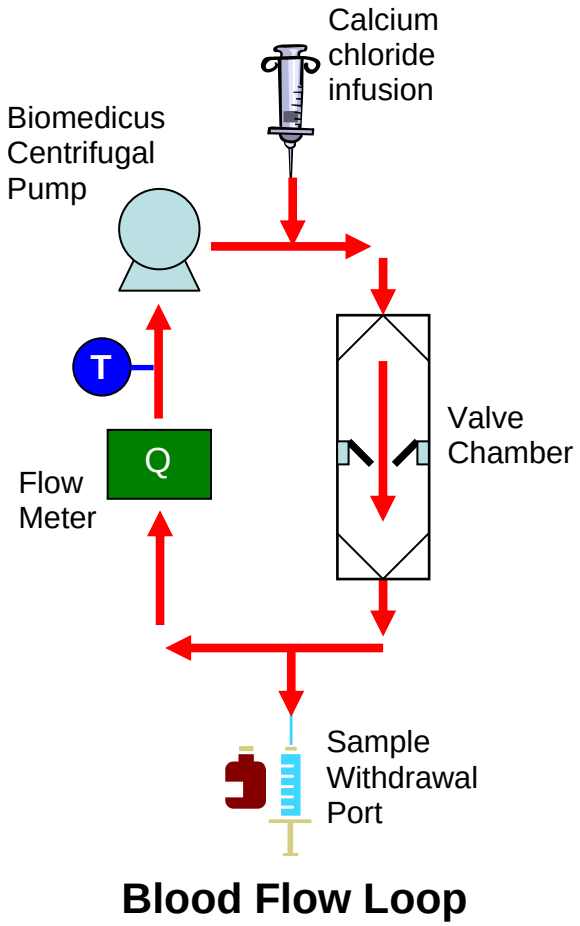

Figure 4.18: A schematic of the steady flow loop used in the blood experiments

The pump flow rate was set to 2.7 L/min. A 100 mM calcium chloride solution was continuously infused into the loop at a rate of 38.6 μL/min using a syringe pump (Harvard Apparatus; Holliston, MA). This solution, used to partially reverse the anticoagulant effect of the sodium citrate, was injected just before entry into the valve chamber. The flow visualization experiments show complete mixing of substances injected at this point. Experiments were run for 60 minutes, resulting in an end calcium chloride volume of 2.3 mL. The sodium citrate:calcium chloride (Ca^{2+}) ratio for the experiment was thus fixed at an end ratio of 8.3:1 after 60 minutes.

During the experiments, blood samples were withdrawn from the loop at 0, 15, 30, 45, and 60 minutes and equal volumes of saline were added each time. First, 0.3 mL was withdrawn to clear the sample port of stagnant blood. This sample was discarded. Next, another syringe was used to draw a 0.5 mL sample. This sample was immediately placed in a 3 mL EDTA Vacutainer tube to prevent further coagulation from occurring. The volume of blood that was withdrawn from the flow loop (0.8mL) was then replaced with an equal volume of saline. The final TAT levels were adjusted to account for this dilution. The temperature of the blood and the RPM of the pump were recorded at all five sample time points. After the experiment was over, the five blood samples were centrifuged at 14,000 RPM for 15 minutes. The supernatant, platelet-poor plasma, was then removed and frozen at -20°C until the assay for TAT III could be performed. In addition, the chamber and valve were inspected for clots as a qualitative indication of procoagulant potential.

As seen in Table 4.5, blood experiments were performed only with the control condition (no vortex generators on the leaflets) and with the vortex generator with the 1 mm tall fins set at a 20° fin angle (R20T).

Table 4.5: Summary of the blood experiments

Flow conditions	**Experiments**	**Vortex Generator Configuration**							
		Control (No VG)	Valve with VG						
			Plate with No Fins	Short Fins			Tall fins		
				5	20	35	5	20	35
Steady	Blood loop	X						X	

4.4.3.2. TAT III Assay

One of the key events in the process of blood coagulation is the conversion of prothrombin to thrombin. Once it is generated, thrombin (a serine protease) can convert fibrinogen to fibrin with the release of fibrinopeptides A and B or it can act on clotting factors V, VIII, XIII, protein C, or blood factors. Alternatively, thrombin may be inhibited by antithrombin III (AT III) to form thrombin/antithrombin III (TAT III), an inactive protease-inhibitor complex (Pelzer *et al*, 1988). TAT III concentration is therefore a positive indication of cumulative thrombin generation. Ideally, thrombin itself could be specifically detected as a measure of blood damage. However, since thrombin is very rapidly bound and inactivated by antithrombin III, this is not possible Therefore, either a byproduct of thrombin function or the end product, TAT III, must be measured (Hoek *et al*, 1988).

The Enzygnost TAT micro assay (Dade Behring, Germany) was used to quantitatively determine the level of thrombin/antithrombin III complex in the plasma samples resulting from the human blood experiments. This enzyme-linked immunosorbent assay (ELISA),

developed by Pelzer *et al* (1988), is used clinically in the diagnosis of thrombotic events. The basic principle of the test is illustrated in Figure 4.19. The wells of the microtitration plate are coated with antibodies which bind to thrombin. When the thawed plasma sample is placed in the well and incubated at 37° C (body temperature), the thrombin end of the TAT III complex binds to this antibody. The wells are then washed with a mild detergent solution to remove unbound constituents. Another solution, which contains the enzyme peroxidase conjugated with AT III antibodies, is then added to the wells. During a second incubation period, these antibodies bind to the AT III end of the TAT complex. The excess enzyme-conjugated antibodies are removed by again washing the wells. A chromogen solution is then added to the wells and allowed to incubate. The peroxidase (POD) reacts with the chromogen to produce a change in the color intensity of the solution. The reaction is stopped after a certain amount of time by the addition of a dilute sulfuric acid solution. The color intensity of each well then corresponds to the concentration of TAT III present. The absorbance of each well can then be read by a photospectrometer.

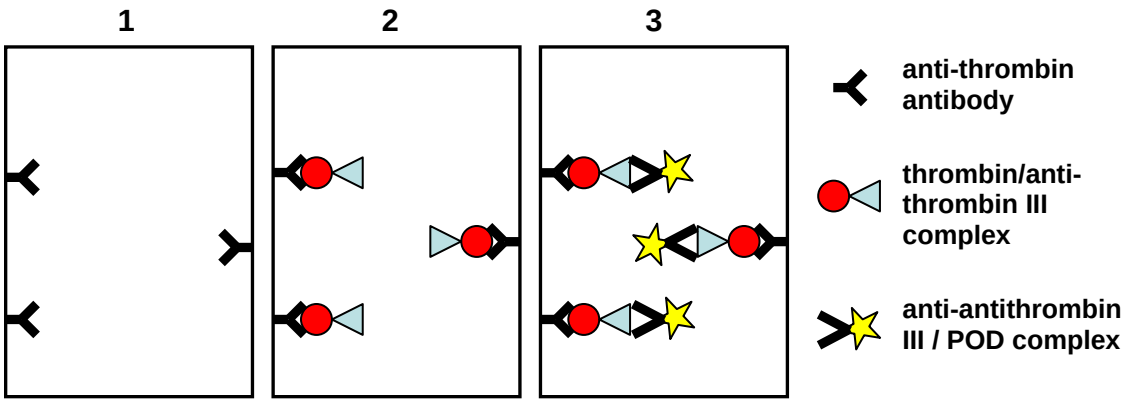

Figure 4.19: An illustration of the principle behind a sandwich ELISA

All samples were assayed in duplicate, and the absorbance values were averaged. A microtiter absorbance plate reader (SpectraMax Plus 384, Molecular Devices, Sunnyvale, California) was used to read the samples at a wavelength of 492 nm. Standard samples provided with the assay allowed the construction of a reference curve in the range of 2 µg/L to 60 µg/L in order to convert absorbance values into TAT concentrations. The standard samples were plotted on a log-log plot, and a power law function was used to interpolate between each of the four standards.

4.4.3.3. Statistical Analysis

Various statistical analyses were performed on the resulting TAT levels. One of the requirements for a two-sample t-test is that the data be normally distributed. An Anderson-Darling test was thus performed on the data from each time point for each experimental condition to determine if they were normally distributed. For those data sets that fit the criterion of normality, a two-sample t-test was performed to determine if the mean TAT levels were significantly different. For those data sets that were not normally distributed, a non-parametric statistical test, the Mann-Whitney test, was performed to determine if the mean TAT levels were significantly different. Linear regressions were performed for both the control and vortex generator cases, and an analysis of covariance (ANCOVA) was performed to determine if the slopes, representing the TAT growth rate, were significantly different.

4.5. Error Analysis

4.5.1. PIV

Error may be introduced into PIV measurements in a number of ways. For instance, particles may lag behind the actual fluid velocity, a concern that was minimized by matching the particle density with that of the fluid (less than 10% difference). Distortion and diffraction in the imaging system may also introduce error. Utilizing a Scheimpflug camera mounting system and matching the refractive index of the sodium iodide solution with that of the acrylic chamber served to address this issue.

The number of images can also affect the accuracy of calculated quantities such as the mean velocity and Reynolds shear stress fields. An increased number of image pairs will invariably lead to a better signal-to-noise ratio and lower percentage errors in the calculated values. However, accuracy must be balanced by the increased time necessary to acquire and process more image pairs and by the high cost of data storage space.

Standard error σ_m can be calculated by the formula

$$\sigma_m = \frac{\sigma_x}{\sqrt{n}}$$

where σ_x is the standard deviation of the population and n is the number of samples. The estimated percent error PE can then be found by the formula

$$PE = \frac{\sigma_m}{\bar{x}} \times 100$$

where $\bar{x}$ is the mean of the population. Standard error and percent error were calculated for the mean velocity components and the Reynolds shear stress at three locations within the flow field for the small-scale PIV data. One point was located in the jet core (Point 1).

The second was located along the edge of the jet (Point 2), and the third point was located in a recirculation region outside of the jet (Point 3). Calculations were performed for sample sizes of both 350 and 6000 instantaneous vector field realizations and are shown in Table 4.6.

Table 4.6: Percent Error in PIV data for mean velocity components and Reynolds shear stress.

		Percent Error		
		v	u	u'v'
3000 Samples	Point 1	9.4	0.6	0.9
	Point 2	51.4	1.3	1.1
	Point 3	0.8	2.7	0.4
350 Samples	Point 1	31.3	2.4	4.0
	Point 2	311.4	5.6	4.9
	Point 3	3.1	14.8	1.1

For 3000 samples, the percent error for the streamwise mean velocity component u is less than one percent inside the jet core and increases with distance from the jet (at Point 2 and Point 3). For 350 samples, the percent errors increase only slightly. The calculated percent error in the cross-stream velocity component v is large because the velocity at these points fluctuates around zero. This situation leads to a small mean cross-stream velocity in the denominator of the percent error formula, thus inflating the percent error. The error in the Reynolds shear stress was consistently less than five percent.

4.5.2. Blood Studies

One known source of error in the blood studies is the TAT III assay kit. A plasma sample with a specified concentration of TAT III is included in each assay kit as a control to ensure that the assay results are trustworthy. The manufacturer claims the intra-assay coefficient of variation (within the series) to be 4-6% and the inter-assay coefficient of variation (between kits) to be 6-9% (Dade Behring, 2003). Since only one kit was used in the analysis of the blood samples, the likely error in the TAT levels due to the assay kit is about ±0.3 ug/L.

4.6. Experimental Summary

In summary, steady and pulsatile flow loops have been used with a variety of fluid mechanics and biological experimental techniques to investigate the effect of various vortex generator designs. Table 4.7 summarizes the experimental variations performed for each vortex generator configuration in both the steady and pulsatile loops.

Table 4.7: Summary of all experiments conducted in both steady and pulsatile loops

Flow conditions	**Experiments**	**Vortex Generator Configuration**							
		Control (No VG)	Valve with VG						
			Plate with No Fins	Short Fins			Tall fins		
				5	20	35	5	20	35
Steady	Blood loop	X						X	
	Flow vis.	X							X
	PIV	X	X	X	X	X	X	X	X
Pulsatile	Flow vis.	X							X

CHAPTER 5

RESULTS

Organization of Results

The results are presented in three sections based on the different experiments performed:

- 1) *In vitro* blood experiments: The results of the blood experiments corresponding to Specific Aim 2 will first be presented. This section will focus on the TAT level progression as a function of time over the duration of the experiment.
- 2) Steady flow PIV experiments: Results of the flow experiments corresponding to Specific Aim 1, with the steady jet issuing from the B-datum line with and without vortex generators, will be shown. This section will contain a qualitative description of the steady jet fluid mechanics as drawn from flow visualization, followed by a quantitative presentation of the vortex generator-induced changes to the jet structure as drawn from particle image velocimetry.
- 3) Pulsatile flow experiments: Finally, the data gathered from the pulsatile system studied under Specific Aim 3 will be presented. Focus will be placed on flow visualization of the valve closure.

5.1. *In Vitro* Blood Experiments

5.1.1. Temporal changes in mean TAT levels

Temporal changes of the TAT levels obtained during the *in vitro* blood experiments and analyzed with the ELISA assay are shown in Figure 5.1. Also shown is the percentile range of TAT levels for healthy adults (1 to 4 μg/L) (Pelzer et al, 1988). The 'Control'

case corresponds to the valve with no vortex generator on the leaflets, while the 'VG' case corresponds to the valve with the tall rectangular fins mounted at a 20° angle on the leaflets (R20T vortex generator design). Spreadsheets of the raw blood data for both cases are presented in Appendix B.1.

Control case: At the first time point (0 min), the mean TAT level for the pooled data of the Control and VG cases was 4.0 ± 1.82 μg/L, a level within the normal range for healthy adults. For the Control case, the mean TAT levels increased from 4.0 μg/L at the zero minute time point to a maximum of 6.0 μg/L at the 30 minute time point. The mean TAT levels for the Control subsequently maintained a TAT concentration of about 6.0 μg/L for the 45 minute time point and slightly decreased for the 60 minute time points. The apparent decrease at the next-to-last time point (5.93 μg/L at 45 min.) is within the assay resolution, though this is not the case for the last time point (5.58 μg/L at 60 min.). As previously mentioned in the methods section, the resolution of the ELISA assay is 0.3 μg/L at the TAT levels being tested. The increase in TAT levels seen from the zero minute time point to any of the subsequent time points did not reach significance as measured by a student's t-test.

VG case: For the case with the vortex generators (VG), the mean TAT levels did not increase over the first three time points, but remained constant at 3.94 ± 0.18 μg/L. The apparent decrease in the TAT level at the 15 minute time point was within the assay resolution. At 45 minutes, the TAT level increased to 4.37 μg/L; at the 60 minute time point, the TAT level increased to reach 4.43 μg/L. This slight increase from the 45

minute to the 60 minute time point was within the resolution of the assay. As noted for the Control case, the increase in TAT levels from the zero minute time point to the subsequent time points did not reach significance as measured by a student's t-test.

Comparison of Control and VG cases: The mean TAT levels of the Control case and the case with vortex generators were also compared at each of the five time points. The TAT levels in the VG case were lower than in the control case at all time points, but this difference was not significant for all of the time points. A significant difference in the mean TAT levels was noted only at the 30 minute time point ($p \leq 0.05$).

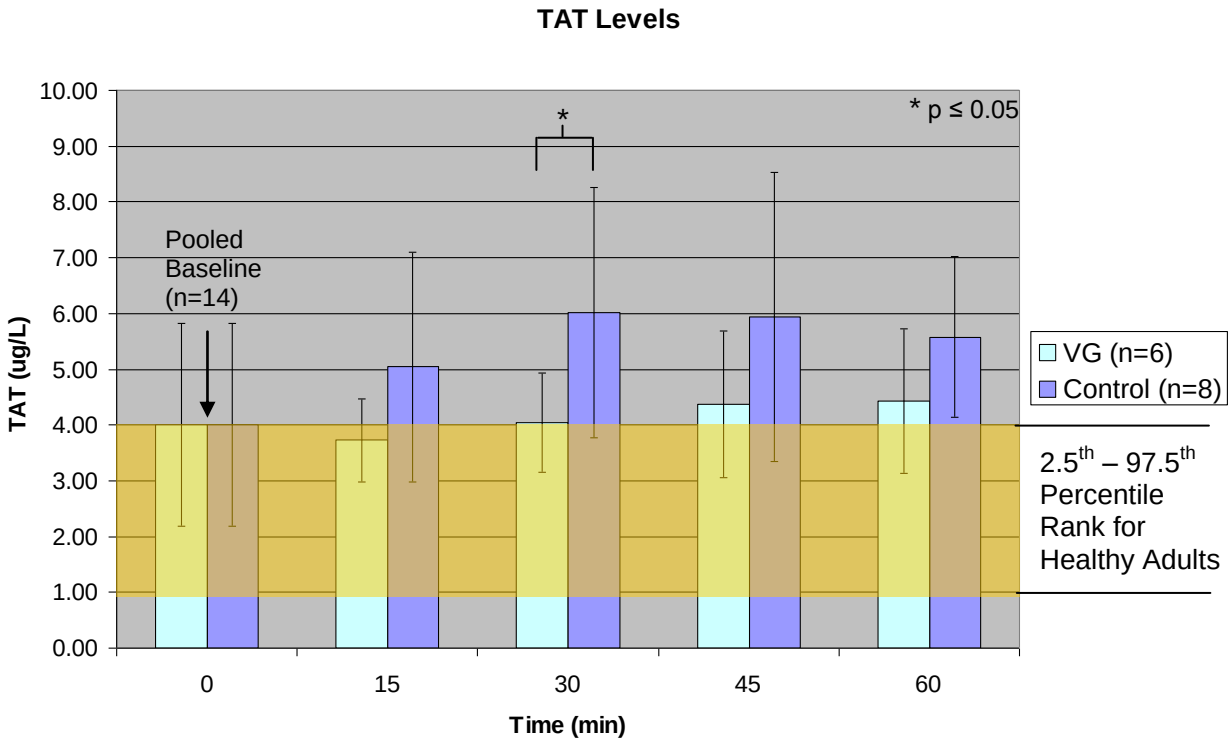

Figure 5.1: Variation of the mean TAT levels over 5 experimental time points for the Control and VG cases.

5.1.2: TAT Temporal Growth Rate

Figure 5.2 shows a scatter plot of all measured TAT points and the mean TAT levels for both Control (blue) and VG (yellow) cases. Linear regression lines and their respective equations are also shown. The slopes of these linear regression lines represent the rate of production of the TAT III complex. The slope for the Control case (0.03 mg/L/min) was nearly four times larger than that of the VG case (0.0082 mg/L/min). In order to determine if the rate of TAT III growth for the Control case was statistically significantly different from that of the VG case, an analysis of covariance (ANCOVA) was performed. This ANCOVA analysis revealed that the slopes were not significantly different, with a p-value of 0.216.

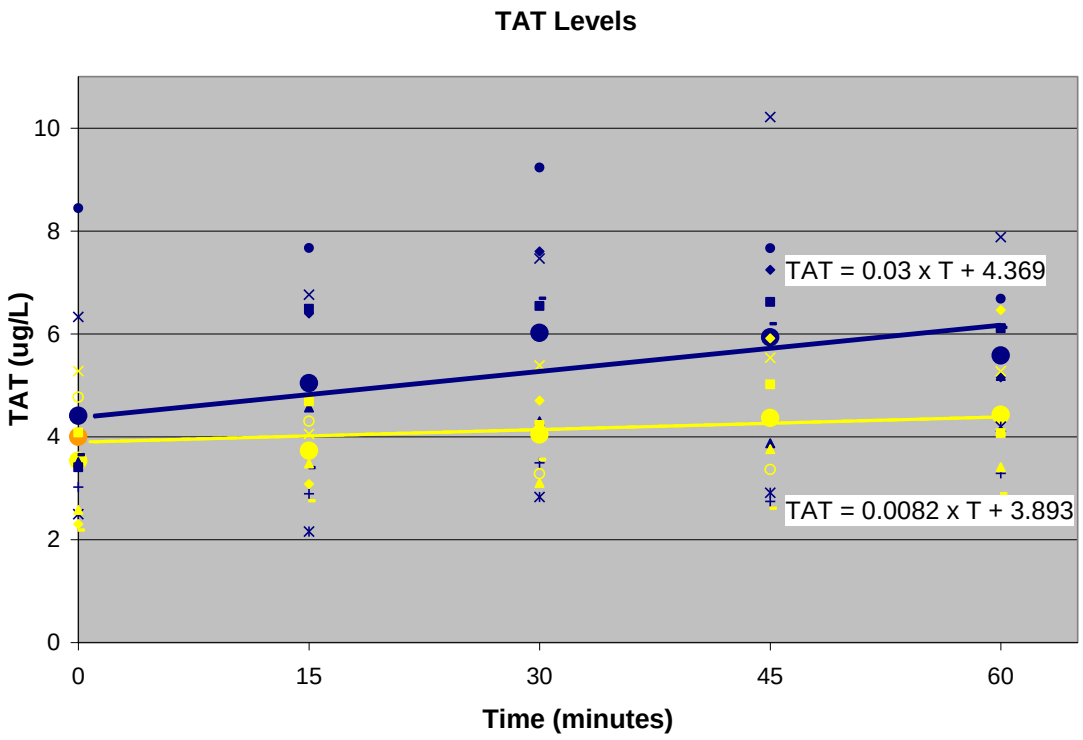

Figure 5.2: Variation of the TAT levels over 5 experimental time points for the Control (blue) and VG (yellow) cases. Individual data points as well as mean levels (filled circles) are shown. Also included are the linear regression lines and their equations.

Because of the apparent leveling off of the mean TAT level for the Control case after 30 minutes (Figure 5.1), the first three time points (0,15, and 30 minutes) were alone considered. The TAT growth rate was then computed by performing a linear regression of these three time points. Results are shown in Figure 5.3. The growth rate was found to be 0.067 mg/L/min for the Control case and -0.0006 mg/L/min for the VG case. An ANCOVA analysis suggested that, with a p-value of .081 ($p < 0.1$), the difference between these slopes was significant.

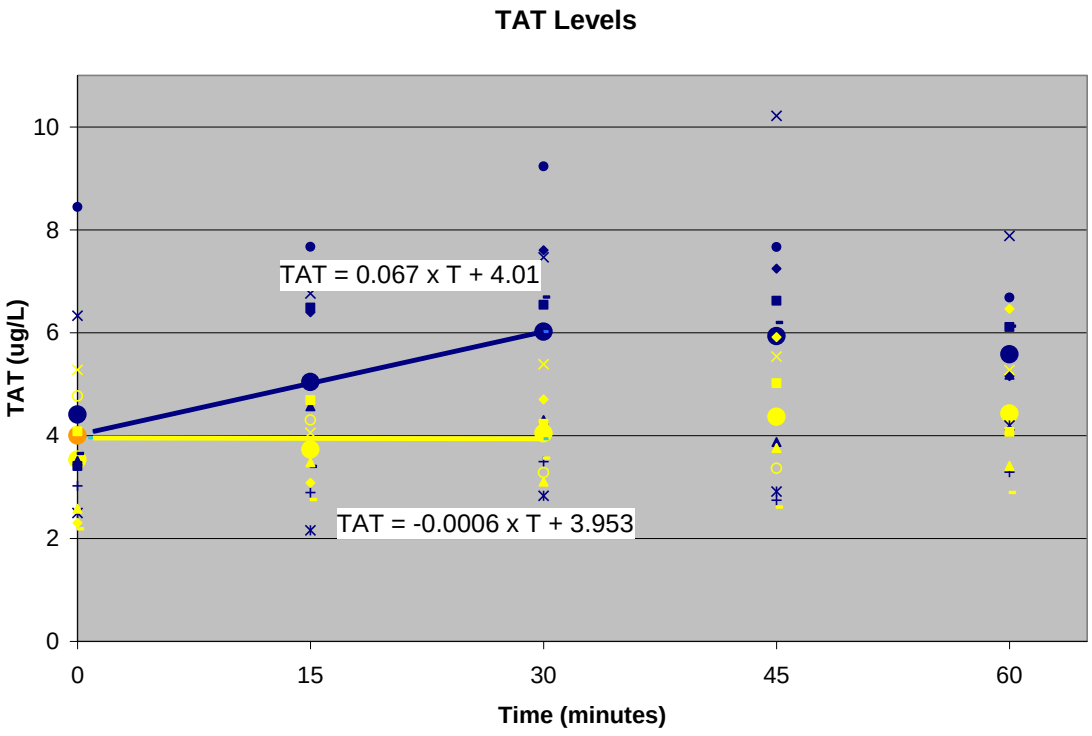

Figure 5.3: Variation of the TAT levels over the first three experimental time points for the Control (blue) and VG (yellow) cases. Individual data points as well as mean levels (filled circles) are shown. Also included are the linear regression lines and their equations.

5.2. Steady Flow Results

5.2.1. Flow Visualization

Figure 5.4 shows a typical image of the steady leakage flow emanating from the 'almost-closed' BMHV. For ease of understanding, a schematic of the valve setup is also included. Note that, because of the presence of the opaque thumbnail region characteristic of the SJM valve design, a portion of the flow domain at the opening formed by the converging leaflets could not be imaged. The jet was thus captured starting at about 1 mm downstream of the opening. The image in Figure 5.4 shows the jet emanating from left to right out of the opening. The jet is surrounded by large recirculation regions seen on either side of the jet in these images. The recirculation regions are non-symmetric and dependent on the orientation of the instantaneous jet. In Figure 5.4, the upper recirculation region is slightly larger than that on the bottom of the chamber.

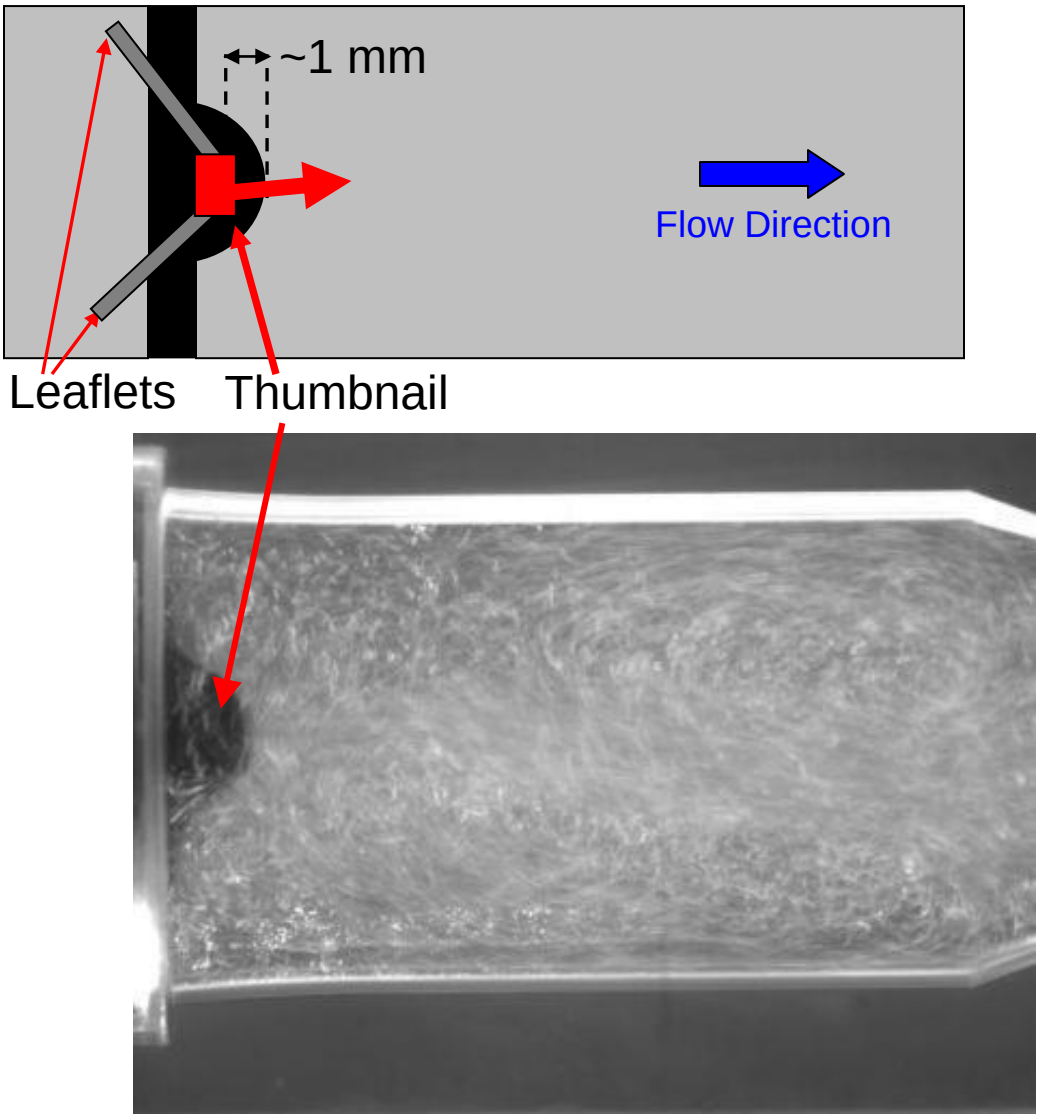

Figure 5.4: Example image of flow visualization of the steady jet emanating from the b-datum line of the "almost-closed" BMHV (bottom). A schematic of the valve and valve chamber used to perform flow visualization is shown in the top panel. Note that the jet nozzle formed by the valve leaflets could not be viewed due to the presence of the opaque thumbnail region.

The fluid mechanics of the confined jet emanating into the chamber is found to be highly unsteady and complex and is best seen in the high-speed flow visualization movies.

Control case: In footage of the Control case slowed 17 times in Figure 5.5, the flow is visualized by microbubbles.

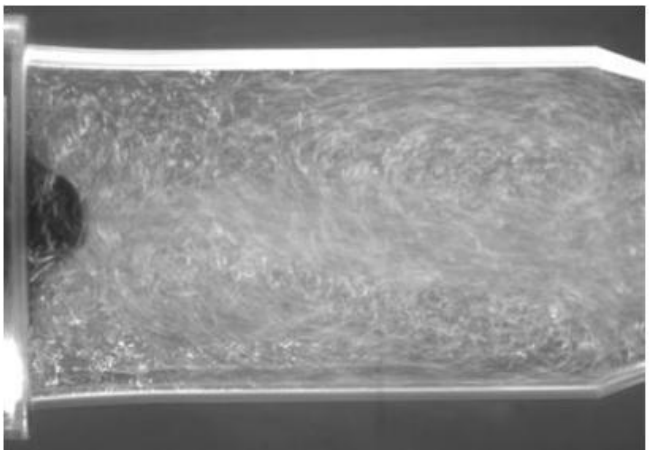

Figure 5.5: Flow visualization of the Control case
(murphy_david_w_200912_mast_Fig5-5_ControlFlowVis.avi, 23,371 K)

It can be seen that the jet rapidly oscillates in the direction normal to the B-datum line as it aperiodically cycles between two extreme positions. This variation can be visualized in the series of consecutive snapshots shown in Figure 5.8. Arrows depicting the main flow direction have been inserted in order to assist in visualizing the flow features. Solid arrows represent the main flow while dashed arrows represent secondary or weakening flow. As shown in Figure 5.8a, the jet first impinges on the far upper wall of the valve chamber. This asymmetric impingement and the converging chamber geometry cause a large clockwise rotating recirculation cell to develop on the lower side of the jet, as seen in Figure 5.8b. This recirculation cell develops an upward, azimuthal crossflow at the jet base that then directs the jet further towards the lower wall, as seen in Figure 5.8c. As time passes, this recirculation region grows progressively smaller and moves upstream, allowing the jet to return to its central position. The jet, which no longer feeds the

disintegrating recirculation cell, begins to form a secondary recirculation region further downstream in the converging chamber, as shown in Figure 5.8d. This secondary, counterclockwise rotating recirculation cell grows stronger and forms a downward azimuthal crossflow around the valve thumbnail, as shown in Figure 5.8e. As seen in Figure 5.8f, the secondary recirculation cell eventually weakens and the large primary clockwise rotating recirculation cells begins to form again. This aperiodic cycle, with the successive formation of two counter-rotating cells, is repeated indefinitely.

It is important to note that the aperiodic nature of the jet direction is uneven. That is, the clockwise recirculation region (Figure 5.8a and b) is consistently maintained for a longer period of time than the counterclockwise recirculation cell (Figure 5.8e). Since these recirculation cells initiate cross flow at the jet base, the direction of the jet is therefore consistently skewed towards the lower chamber wall for longer than it is directed towards the upper chamber wall.

VG case: Figure 5.6 and Figure 5.7 show the flow visualization with the R35T vortex generator design. Both use irregularly shaped PVC particles for flow visualization. Figure 5.6 shows footage slowed 17 times and essentially shows the same behavior as that seen for the Control case jet. The flow alternately forms clockwise and counterclockwise recirculation regions as the jet oscillates back and forth across the chamber. As seen in the Control case, the aperiodic nature of the jet is again uneven. The clockwise recirculation region is again maintained for a longer period of time than the counterclockwise recirculation cell.

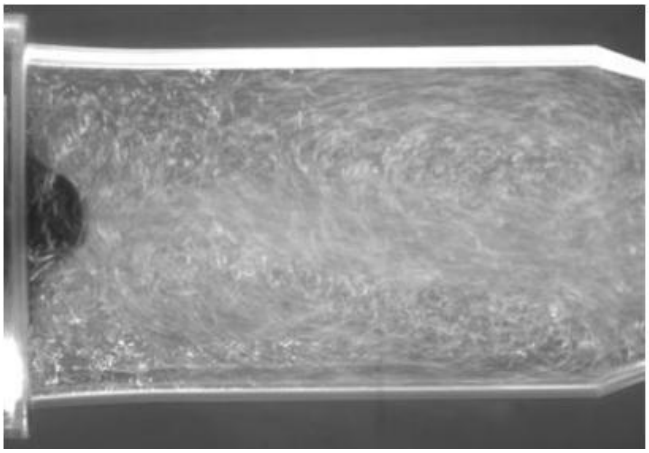

Figure 5.6: Flow visualization of the VG case (murphy_david_w_200912_mast_Fig5-6_VGFlowVis.avi, 72,266 K)

Figure 5.7 consists of footage slowed 10 times and is helpful in realizing the dynamic, intense nature of the mixing in the flow chamber. The flow again forms recirculation regions that alternate in their direction as the jet oscillates back and forth. This movie covers approximately one cycle of jet oscillation and clearly shows the azimuthal crossflow that occurs at the base of the jet around the valve thumbnail.

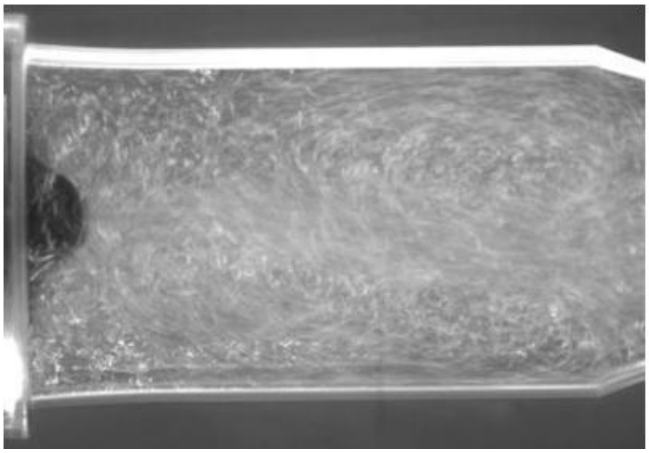

Figure 5.7: Flow visualization of the Control case (murphy_david_w_200912_mast_Fig5-7_VGFlowVis2.avi, 7,287 K)

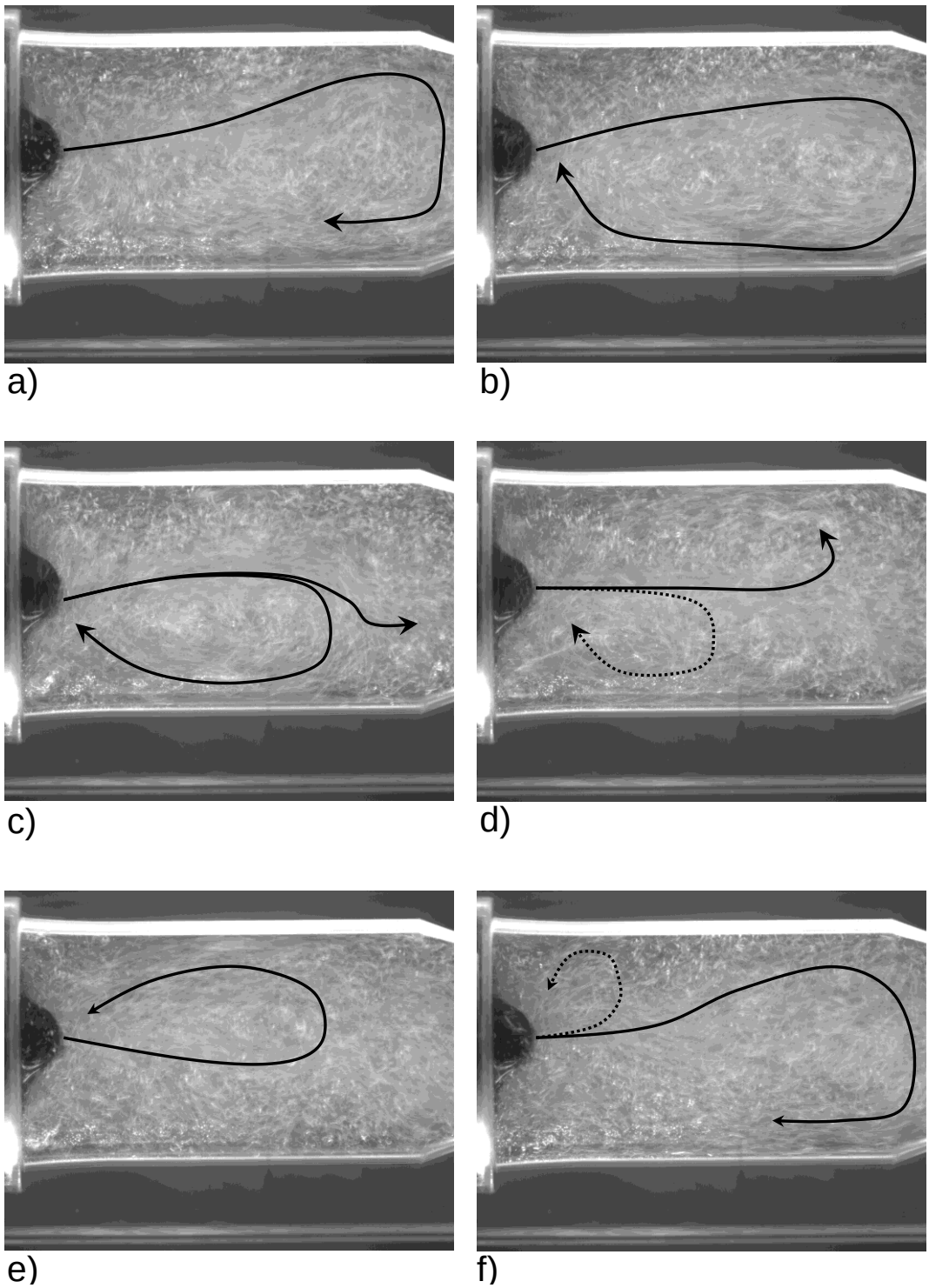

Figure 5.8: Series of consecutive high speed flow visualization images showing the dynamic behavior of the steady jet emanating from the "almost closed" BMHV. The images shown correspond to the Control case.

5.2.2. Digital Particle Image Velocimetry

The DPIV results are organized in two sections. In the first section, the high resolution, small-scale data for the Control and R20T vortex generator cases are presented. In the second section, the large-scale data for all eight test configurations (Control case, six different VG designs, and one design with the base plate but no fins) are presented.

5.2.2.1. Small Scale Results: Comparison of Control and R20T Cases

In order to characterize the B-datum jet with and without vortex generators, the ensemble-averaged velocity fields with streamwise (u velocity) and cross-stream (v velocity) velocity components, the root-mean-square (RMS) velocity fields u_{rms} and v_{rms}, the mean vorticity ω, and the Reynolds shear stress (RSS) τ_{xy} were calculated. The results are presented in Figures 5.9 through 5.11. Note that the streamwise velocity RMS and vorticity fields are available in Appendix C.1.

Figure 5.9 shows the velocity magnitude contours downstream of the jet nozzle for both Control and VG cases. It is seen that, although the peak velocities are the same (3.2 m/s), the high velocity jet core in the R20T case extends slightly further (up to 3.07 mm for a velocity of 3 m/s) than that in the Control case (up to 2.72 mm for a velocity of 3 m/s). In addition, the spreading of the Control case jet in the y-direction is greater than that for the R20T case. For instance, the mean jet width at x = 10 mm is 5.25 mm for the Control case while only 4.56 mm for the R20T VG case.

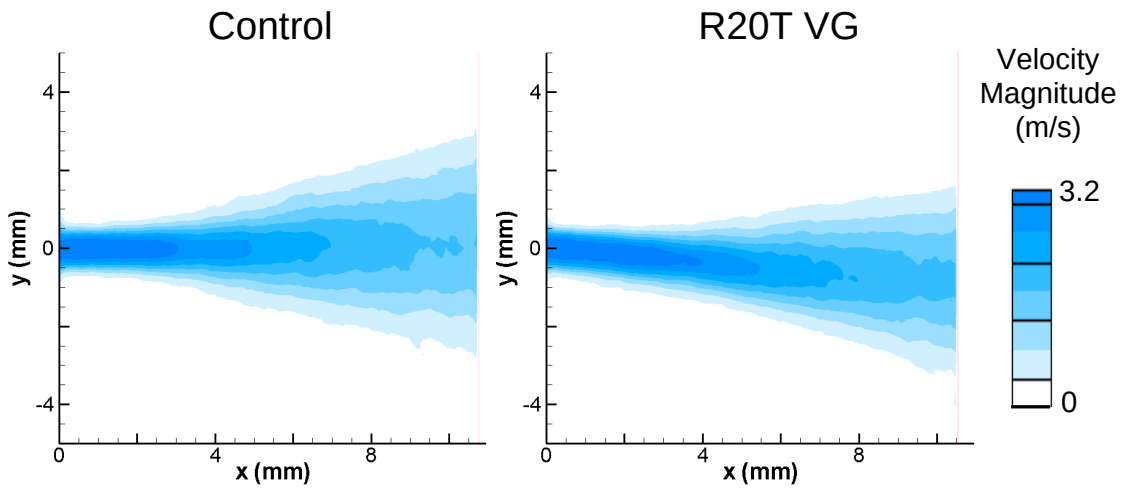

Figure 5.9: Velocity magnitude contours for the Control and R20T cases.

Figure 5.10 shows the cross-stream velocity RMS contours for the Control and R20T VG cases. The Control case exhibits higher values (0.7 m/s) of the cross-stream velocity RMS than the R20T case (0.6 m/s). These higher values are concentrated in the core of the jet (from x = 6 mm to x = 9 mm). In addition, higher values of cross-stream velocity RMS are seen along the edges of the jet. For instance, along a line formed at x = 10 mm, elevated RMS values are seen at y = ±0.4 mm in the Control case while only background levels are seen in the R20T VG case. These dissimilarities are likely due to the differences in jet spreading characteristics seen in Figure 5.9.

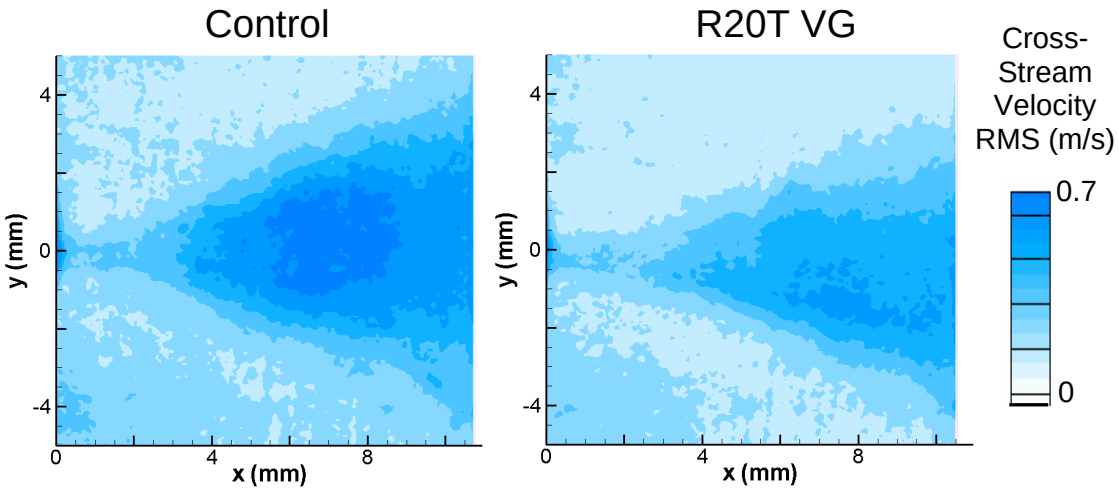

Figure 5.10: Cross-stream velocity RMS contours for Control and VG (R20T) cases

Figure 5.11 shows the RSS contours for the Control and R20T VG cases. As seen for the cross-stream velocity RMS contours, the Control case exhibits higher levels of RSS than the R20T case. The peak RSS for the Control case is approximately 570 Pa while that for the R20T VG case is approximately 490 Pa. Not only is the peak greater for the Control case, the extent of the higher RSS values is also greater for the Control case than for the R20T VG case.

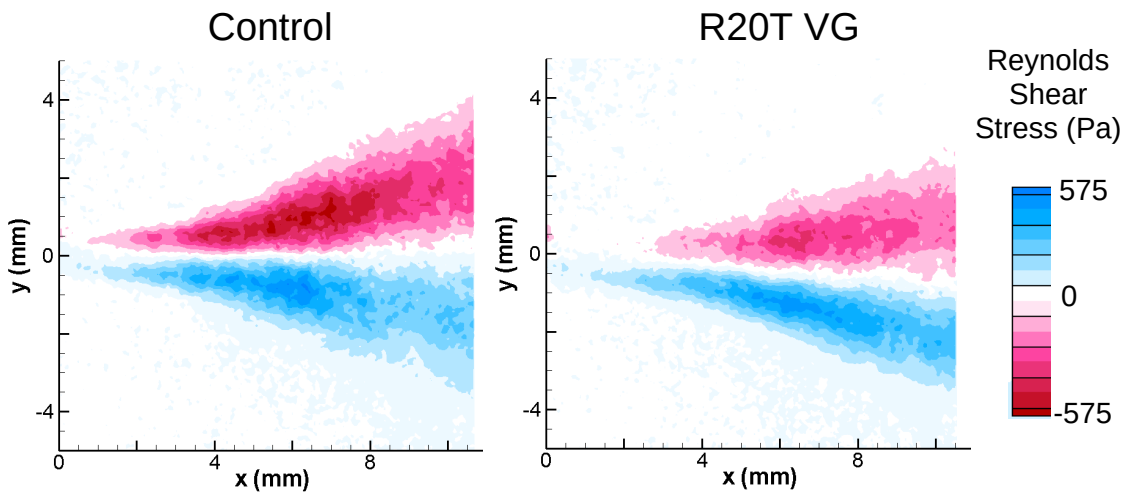

Figure 5.11: Reynolds shear stress (RSS) contours for Control and R20T cases.

The results based on the binning analysis and subsequent conditional statistics for the RSS will now be presented. This analysis procedure was described in the methods chapter. The results obtained for the conditional statistics of the velocity magnitude, the root-mean-square velocity fields, and the mean vorticity fields are shown in Appendix C.2. Figure 5.12 shows the RSS conditional statistics for each bin for both the Control and R20T cases. With the effect of the jet oscillation on the statistics removed, Figure 5.12 shows that the magnitude and extent of the RSS is still consistently greater for the Control case than for the R20T case. It is interesting to note that, in the central bins (bins 4-6), the extent of the RSS values between the Control and R20T cases seems to be about equal. However, in the extreme bins (bins 1 to 3 and 7 to 9) the extent of the high RSS values is much greater for the Control case than for the R20T case. It is also interesting to note that, in the extreme bins, the concave side of the jet experiences more intense RSS values than the opposite side.

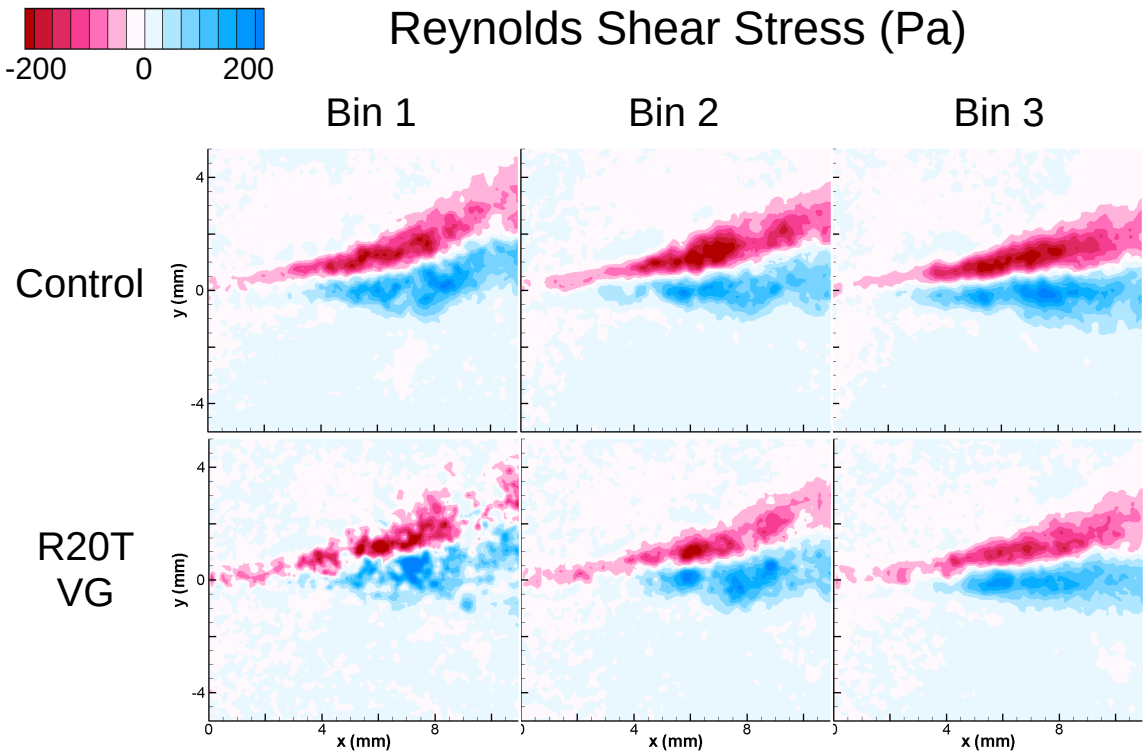

Figure 5.12a: Reynolds Shear Stress plots of Bins 1 to 3 for Control and R20T VG cases.

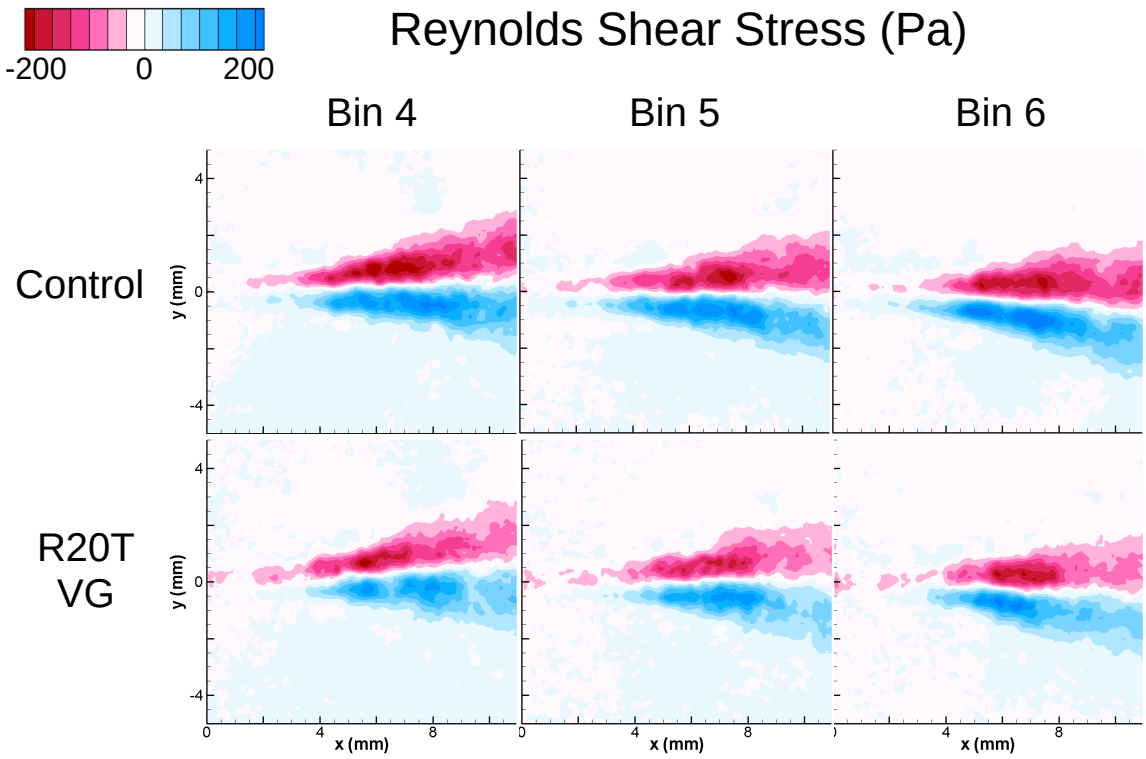

Figure 5.12b: Reynolds Shear Stress plots of Bins 4 to 6 for Control and R20T VG cases.

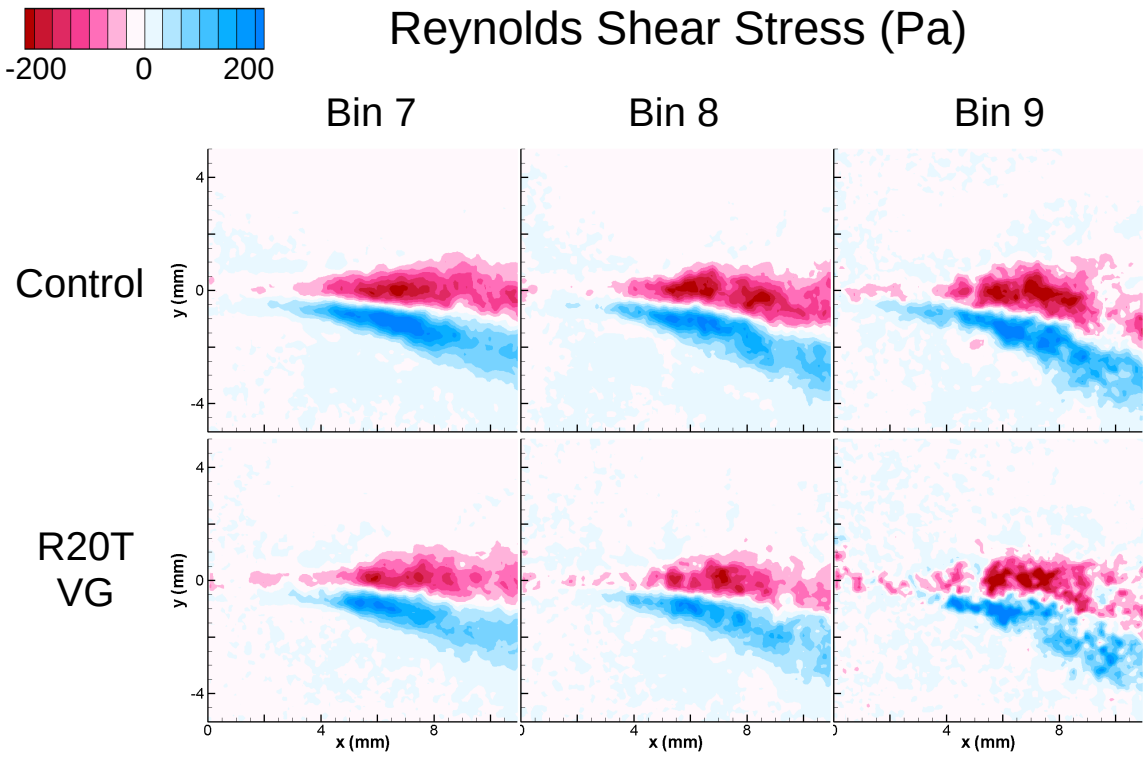

Figure 5.12c: Reynolds Shear Stress plots of Bins 7 to 9 for Control and R20T VG cases.

Figure 5.13 shows the difference between the absolute value of the RSS for the Control case and that of the R20T VG case for each bin. Blue contours indicate areas in which the Control case RSS levels are greater while red contours indicate areas where the R20T VG case RSS levels are greater. As also seen in Figure 5.12, the Control case jet consistently exhibits higher levels of RSS. In the central bins (Bins 4-6), this difference is about 100 Pa, and very few areas are seen in which the R20T VG RSS levels are greater than those of the Control case. In the peripheral bins (Bins 1-3 and 7-9), however, the red contours increase, indicating areas in which the RSS levels for the Control case are less than those of the R20T VG case.

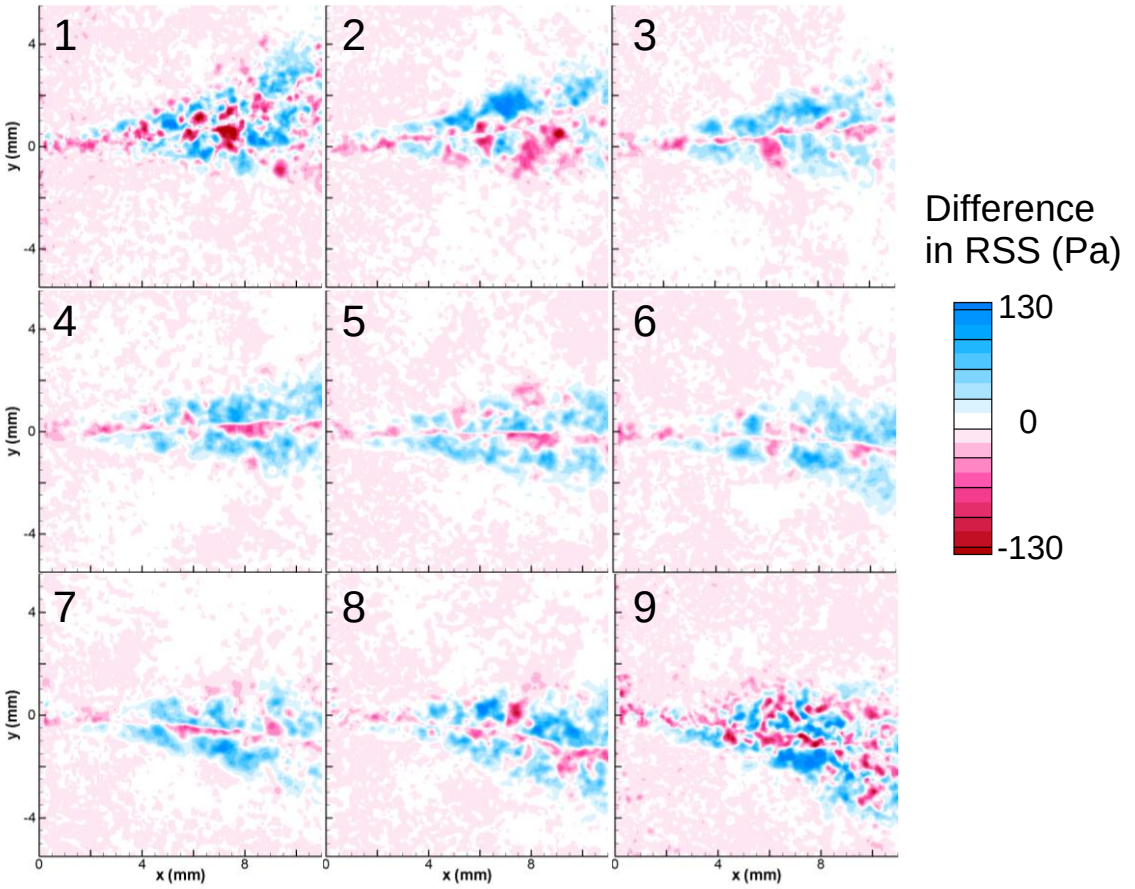

Figure 5.13: Contour plots showing the absolute value of the RSS magnitude of the Control case minus the absolute values of the RSS magnitude for the R20T VG case. The Bin number is shown in the upper left hand corner of each contour plot.

The peak RSS value in each bin is plotted for both cases in Figure 5.14, which shows that, except for Bins 1 and 9, the peak RSS is lower for the case with the vortex generators. To better visualize the difference between these peak RSS levels, the differences (expressed in percentage) between the 2 cases are shown in Figure 5.15. Bins 2 to 8 are associated with a peak RSS that is consistently 10-20% greater in the Control case than in the R20T case. Bins 1 and 9, on the other hand, show higher peak RSS values for the R20T case than for the Control case. This trend is likely reflective of the

smaller number of samples in those two bins, which could lead to higher error values in the calculations.

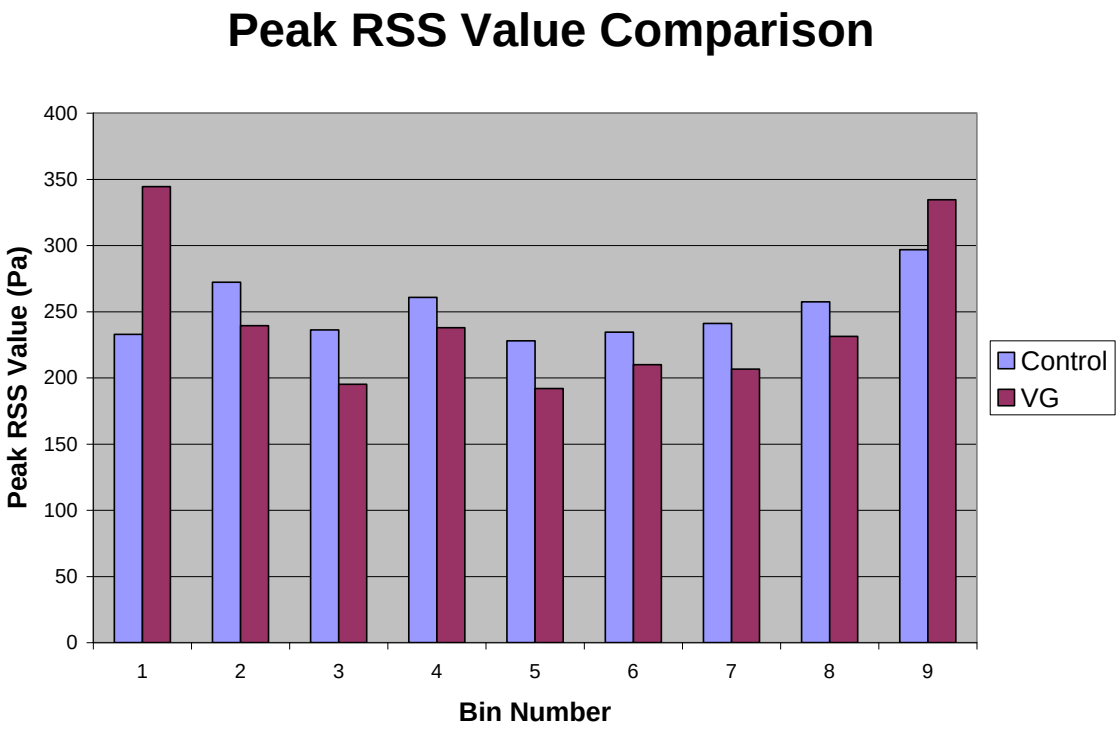

Figure 5.14: A comparison of the peak RSS values for each bin for both the Control and R20T VG cases

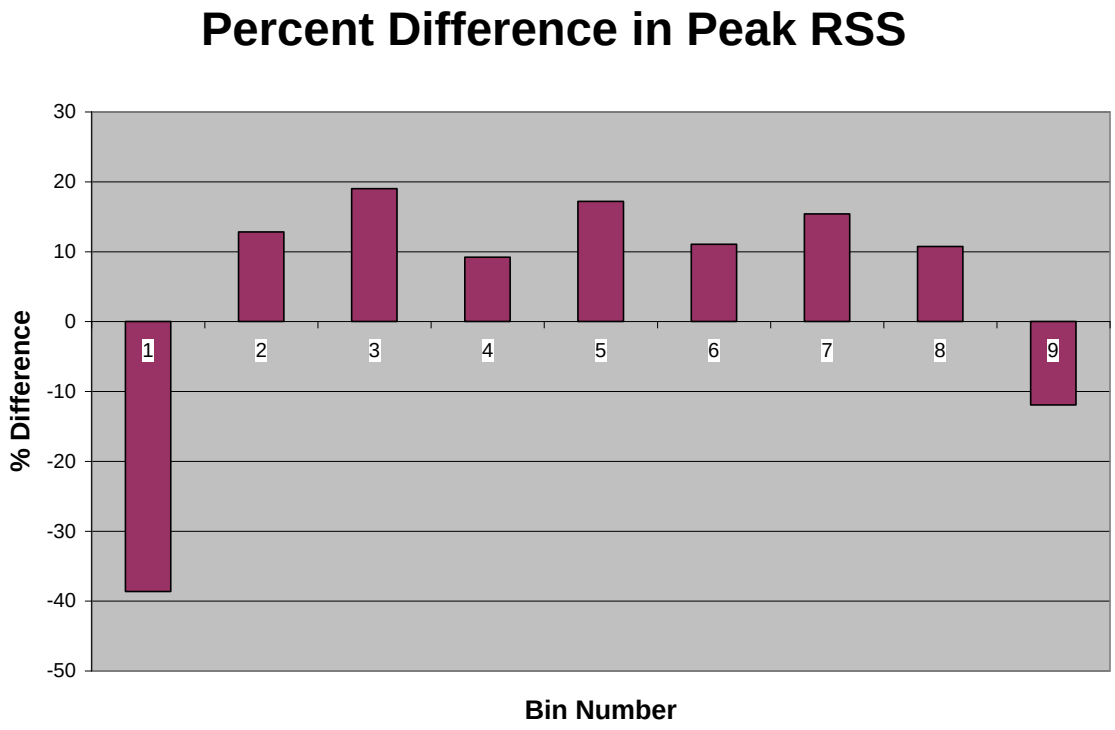

Figure 5.15: A comparison of the peak RSS values for each bin for both the Control and R20T VG cases

5.2.2.2. Large Scale Results: Comparison of All Eight Cases

In order to characterize the b-datum jet under the influence of various vortex generator designs, the ensemble-averaged velocity magnitude, the RMS fields u_{rms} and v_{rms}, the mean vorticity ω, and the RSS fields were calculated for the large-scale data. The ensemble-averaged velocity magnitude and RSS fields are shown in Figures 5.16 and 5.17, respectively, while all other parameters are shown in Appendix C.3. In the data shown below, the jet field of view was captured beginning 1 mm beyond the nozzle due to the camera angle and the presence of the valve thumbnail.

Figure 5.16 shows that all of the test cases exhibit similar features, with a peak velocity magnitude of approximately 3 m/s. However, the mean jet direction appears to be a variable flow characteristic of the jet throughout the various test cases. While several of the cases (i.e. Control, R20S) exhibit jet flow that remains parallel to the bulk flow, others (i.e. R05T, R05S) exhibit considerable jet skewing.

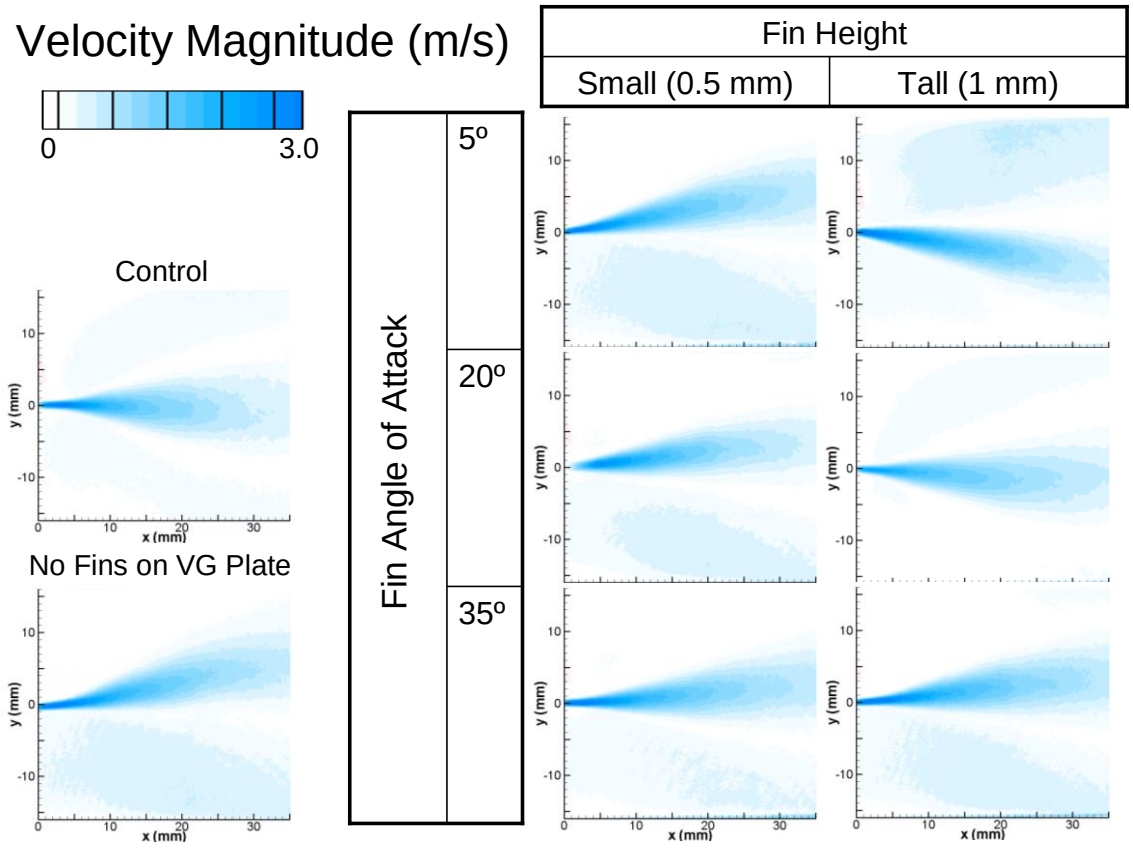

Figure 5.16: Velocity magnitude fields of the b-datum jet for all eight test cases.

Figure 5.17 shows that the Control case generates peak levels of RSS of about 550 Pa while the VG case with the highest RSS levels, R35T, generates peak RSS levels of approximately 380 Pa. When comparing among the different test cases with vortex

generators, the R05S, R05T, and 'No Fins on VG Plate' cases appear to exhibit the lowest levels of peak RSS (approximately 300 Pa). Regardless of the test case, the elevated RSS levels appear to originate at approximately 5 mm downstream of the orifice (x = 4 mm).

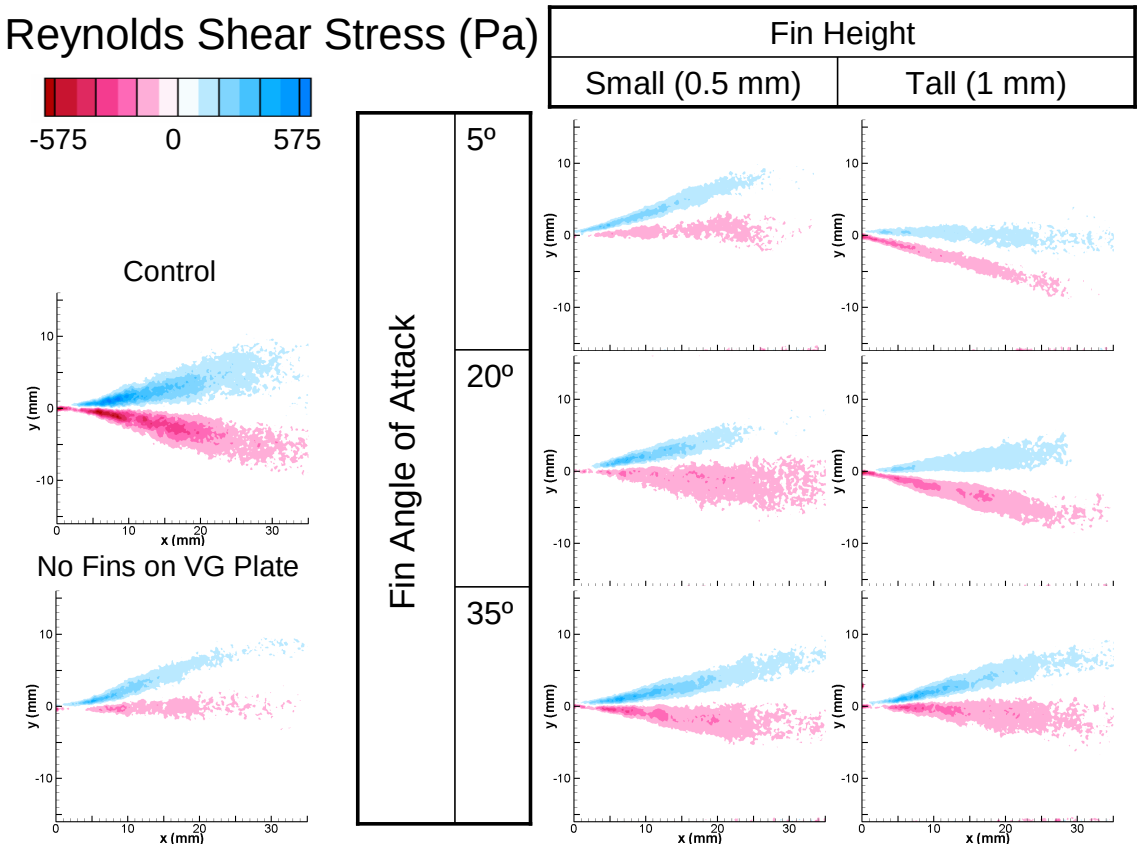

Figure 5.17: Reynolds Shear Stress fields for all eight test cases

The results based on the binning analysis and subsequent conditional statistics for the RSS of the large-scale data, described in the methods chapter, will now be presented. Figure 5.18 shows histograms of the distribution of the 350 instantaneous jet position values at 12 gap widths downstream of the beginning of the field of view. Histograms are

shown for each of the vortex generator design configurations. The standard deviation of the instantaneous jet position for each vortex generator configuration was calculated and is shown in Figure 5.19. Figure 5.18 and 5.19 show that the Control case jet exhibits the greatest variation in instantaneous position and thus has the highest standard deviation. The cases with fin angles of 5° show the least variability in jet position and thus the smallest standard deviations in instantaneous jet position. A degree of skew is also evident in many of the histograms shown in Figure 5.18.

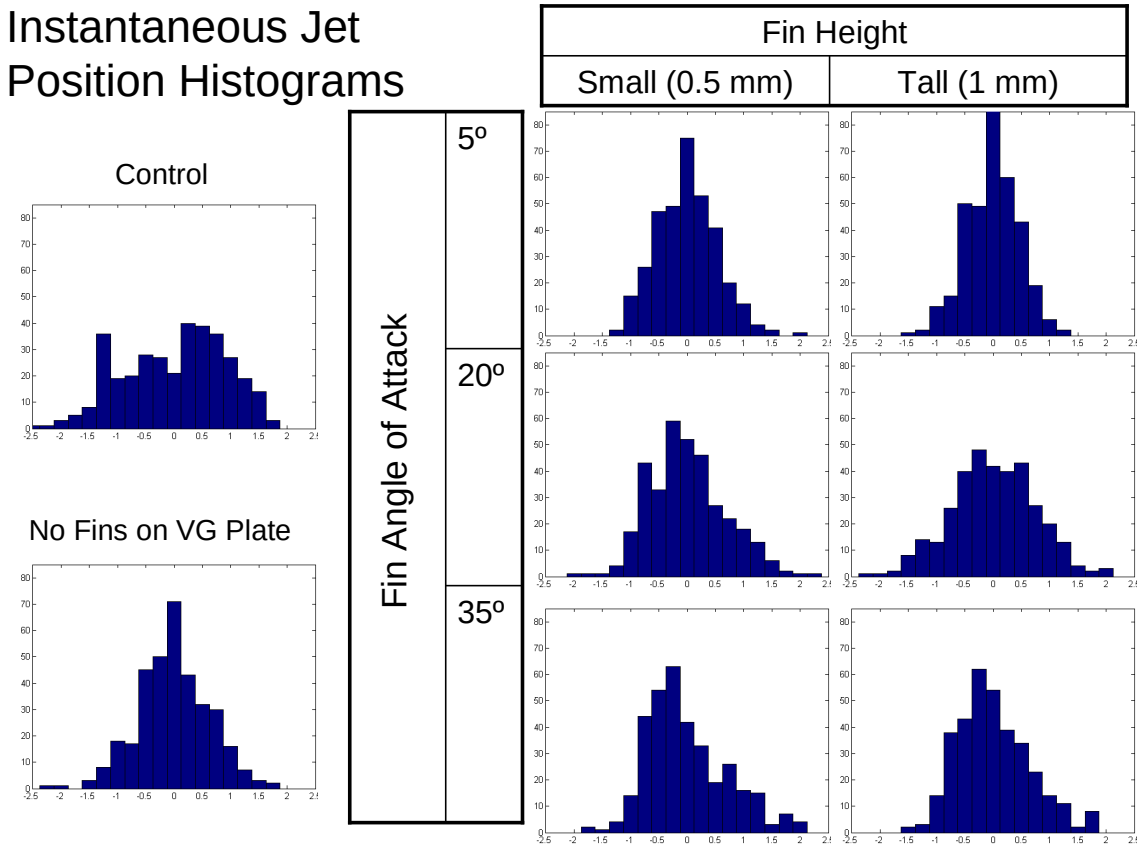

Figure 5.18: Histograms showing the distribution of the 350 instantaneous jet position values at 12 gap widths downstream of the beginning of the field of view. Histograms are shown for each of the vortex generator design configurations.

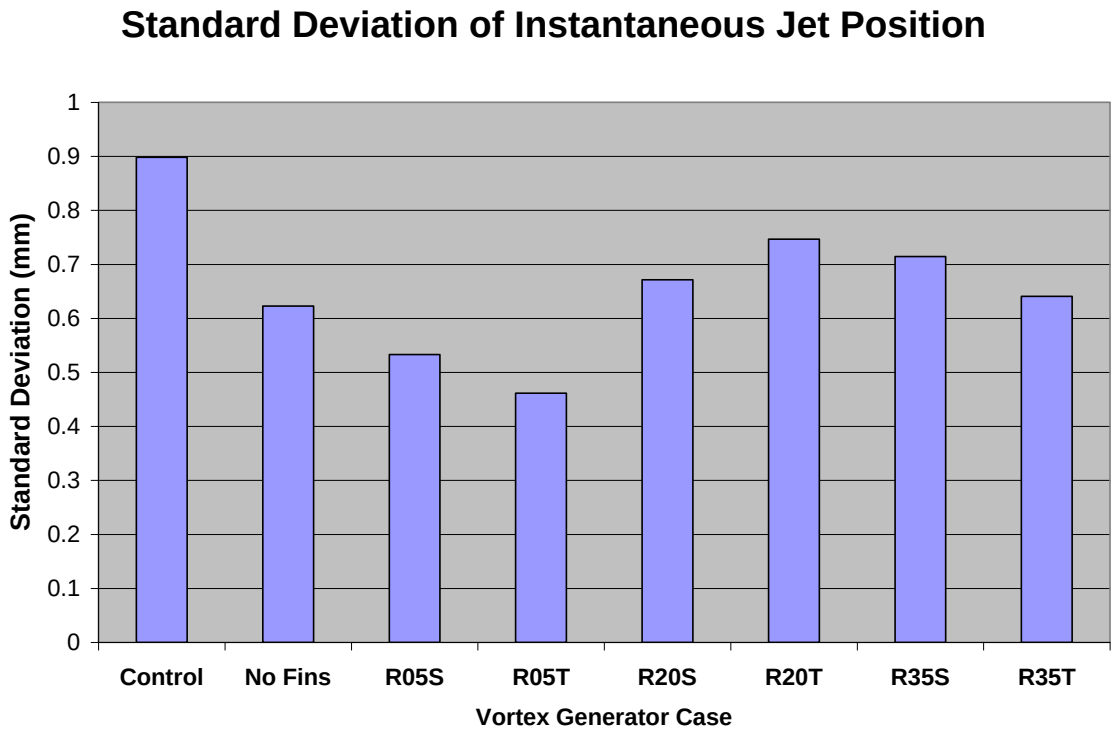

Figure 5.19: A comparison of the standard deviations of instantaneous jet position at 12 gap widths downstream 12 gap widths downstream of the beginning of the field of view, showing that the Control case jet exhibited the most variation in position.

Figure 5.20 shows a comparison of the RSS among the various test cases for Bin 3. Bin 3 is shown because it is the central bin (since the large-scale data was divided into only 5 bins, based on a smaller sample size). Figures showing the RSS data for the remaining bins for each of the test cases are presented in Appendix C.3 along with velocity magnitude and velocity RMS contour plots for all of the bins. Figure 5.20 shows that the RSS magnitude and extent is less for the cases with vortex generators than for the control case. Peak values of RSS for the Control case are about 540 Pa while those for the other cases are about 220 Pa. Levels of peak RSS for the Control case and the cases with vortex generators remain about the same as before the binning (as seen in Figure 5.17), but the

extent of the high magnitude RSS levels decreases. No major differences in RSS levels are seen among the various vortex generator cases.

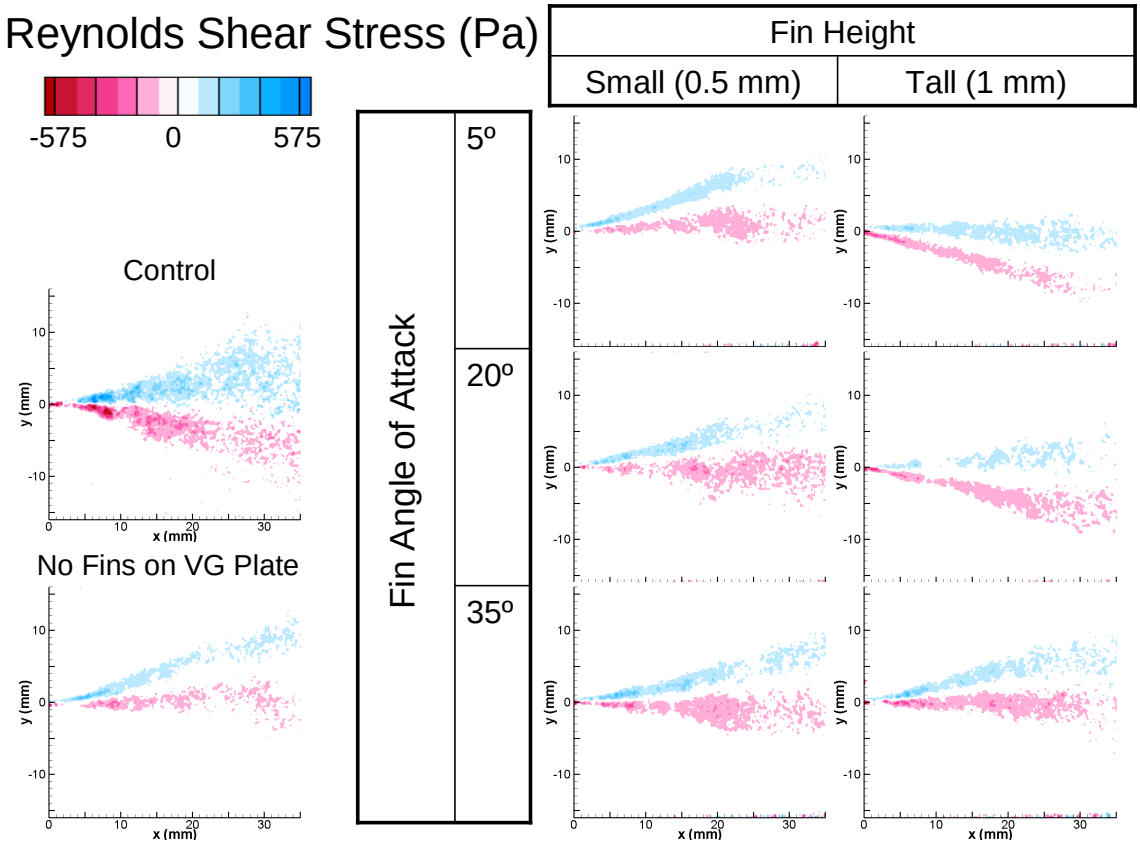

Figure 5.20: Conditional statistics showing the Reynolds Shear Stress in Bin 3 for each of the eight test cases.

5.3. Pulsatile Flow Results

Flow visualization of the pulsatile flow setup will be presented here while the DPIV results of the pulsatile flow setup are shown in Appendix D. Flow visualization of the valve operating in a pulsatile flow loop that replicates physiologic pressure and flow conditions provides an opportunity to examine the effect of the vortex generators on the flow throughout the cardiac cycle, not just during the closing period. A schematic of the

pulsatile flow setup is shown in Figure 5.21 in order to orient the viewer. In this setup, the forward flow that occurs during systole goes from left to right. The transient closing jet through the b-datum line (the subject of the previously described steady flow experiments) flows from right to left. Figure 5.22 is a sample image of the flow visualization and highlights regions of interest for particular phases of the cardiac cycle. These outlined areas correspond to the flow snapshots shown in the following figures.

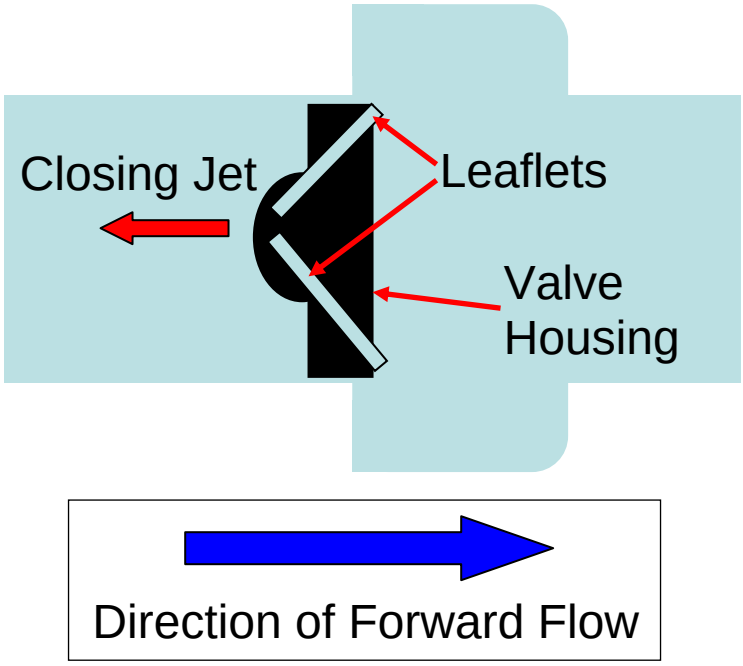

Figure 5.21: Schematic of the pulsatile flow setup used in flow visualization experiments.

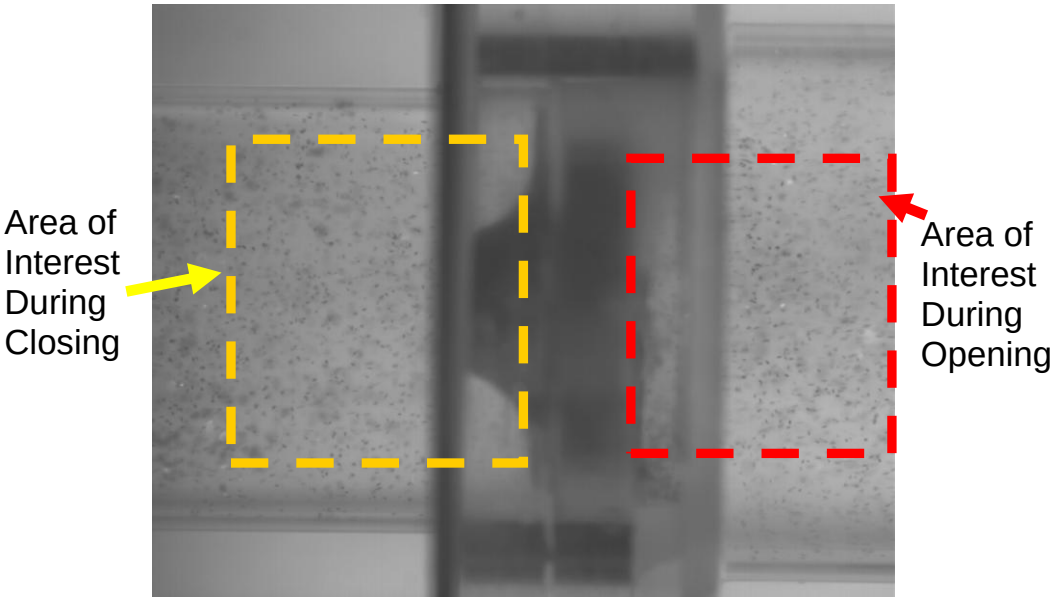

Figure 5.22: Sample Image of the flow visualization. The area outlined in yellow is of interest during the valve closure while that outlined in red is of interest during valve opening.

5.3.1. Flow Visualization of Valve Closure

Control case: Flow visualization of the closing of a BMHV operating under physiologic conditions with no vortex generators (Control case) is shown in Figure 5.23, recorded at 500 frames per second and slowed 17 times.

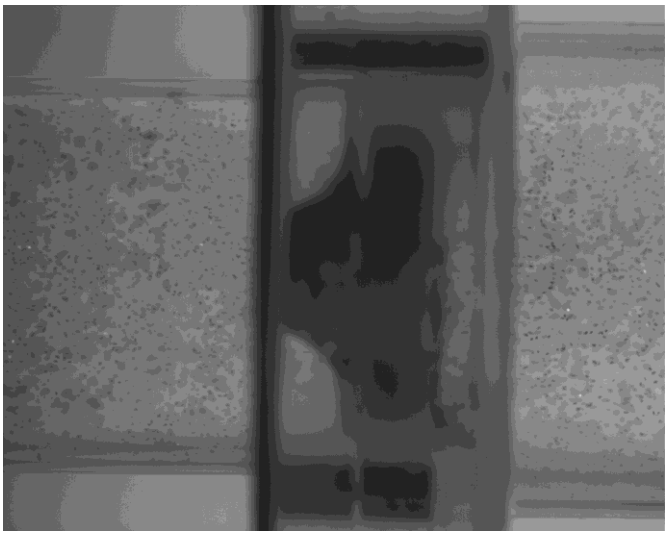

Figure 5.23: Flow visualization of BMHV under pulsatile conditions with no VG (murphy_david_w_200912_mast_Fig5-23_Puls-closure-Control.avi, 28,940 K)

Figure 5.23 begins near the end of systole when the forward flow is weakening. At this point in time, the tips of the open leaflets can be seen on the right side of the valve housing. As the flow slows further, the fluid along the walls is seen to reverse direction and begins to flow upstream. The core flow soon follows, initiating valve closure. The leaflet tips disappear into the valve housing as the leaflets rotate toward their closed position. As the leaflets close, a high velocity closing jet, seen in Figure 5.24, emerges from the right. This momentary planar jet, directed left and slightly upward, initiates counter-rotating vortices above and below it. In this valve closure, the counterclockwise vortex above the jet is much stronger than the one below it. In other cases, however, the jet direction and relative vortex strength may differ.

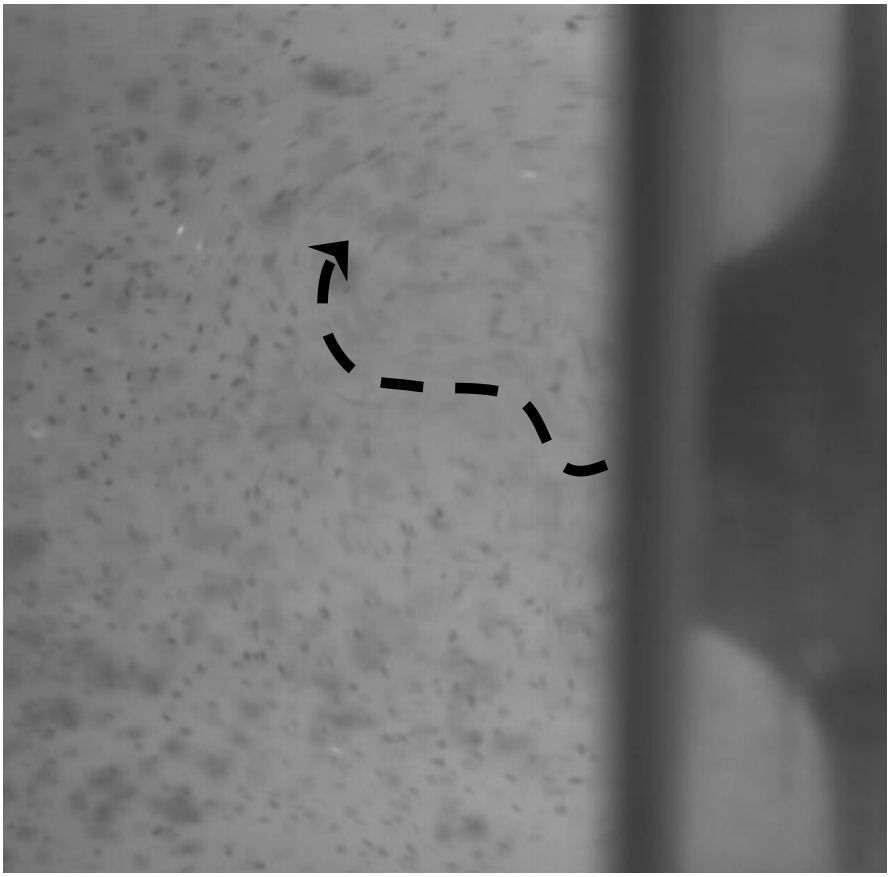

Figure 5.24: A snapshot of the Control case flow during valve closure. The strong b-datum jet is indicated by the dashed arrow.

VG case: Figure 5.25, also recorded at 500 frames per second and slowed 17 times, shows flow visualization of the closing of a BMHV operating under physiologic conditions with the R35T vortex generators fixed to the leaflets.

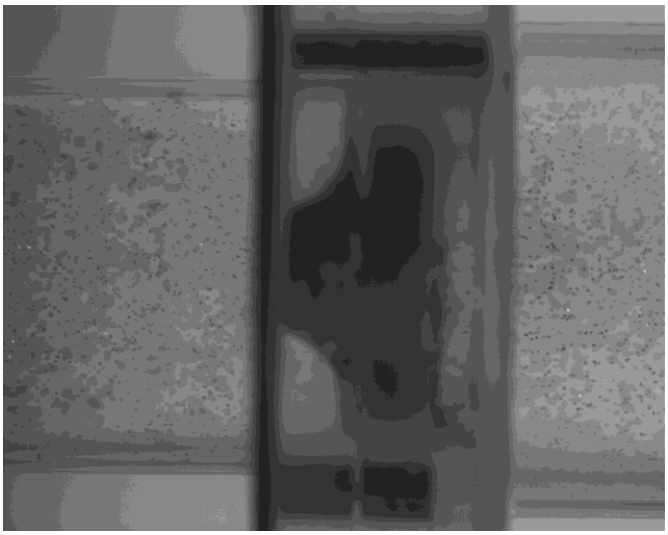

Figure 5.25: Flow visualization of BMHV under pulsatile conditions with R35T VG (murphy_david_w_200912_mast_Fig5-25_Puls-closure-R35TVG.avi, 28,568 K)

The movie begins near the end of systole, as the forward flow is slowing. Due to a slightly different camera view from that in Figure 5.23, the tips of the open leaflets are not visible on the downstream side of the valve housing. Closure of the valve is initiated in the same manner as was described for the Control case. At valve closure, a small jet is seen emanating from the valve b-datum line. As seen in Figure 5.26, this jet rapidly rolls up into two counter-rotating vortices that quickly dissipate. The jet with the vortex generators seems much weaker than the jet in the control case. In addition, in the case with the vortex generators, the upstream region affected by the jet and associated vortices seems to be about half of the size of the area affected for the Control case.

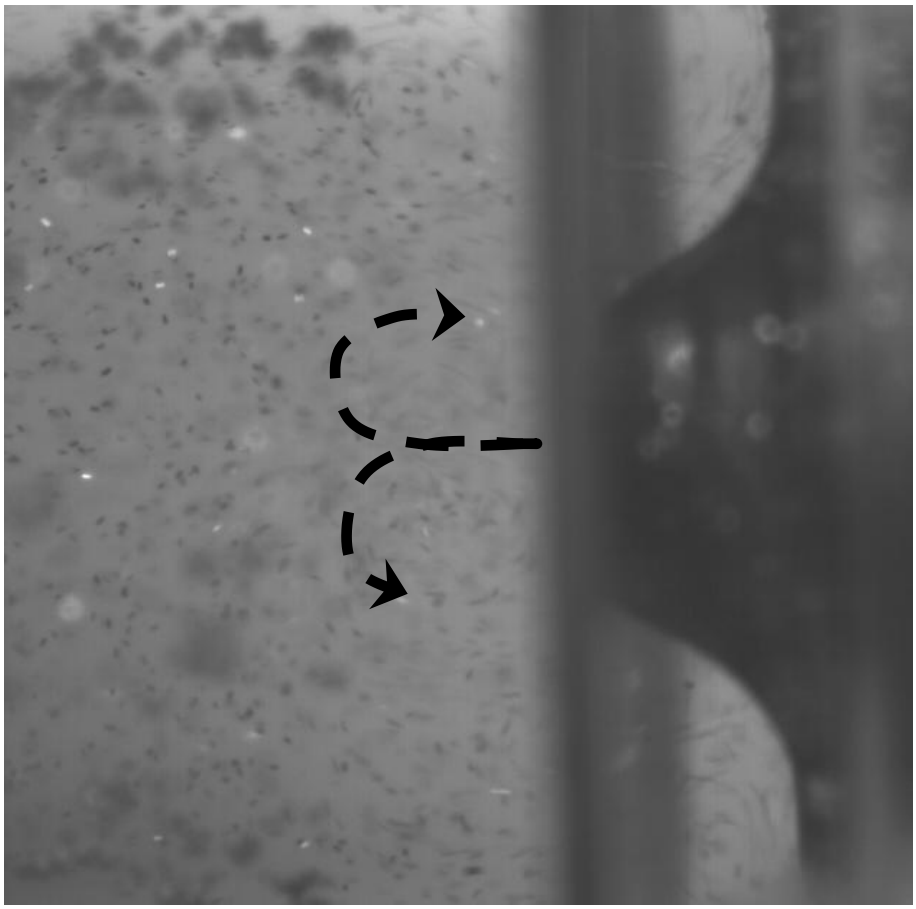

Figure 5.26: A snapshot of the R35T VG case flow during valve closure. The b-datum jet and subsequent vortex formation are indicated by the dashed arrows.

5.3.2. Flow Visualization of Valve Opening

Control case: Figure 5.27, recorded at 500 frames per second and slowed 17 times, shows flow visualization of a BMHV operating under physiologic conditions with no vortex generators (Control case).

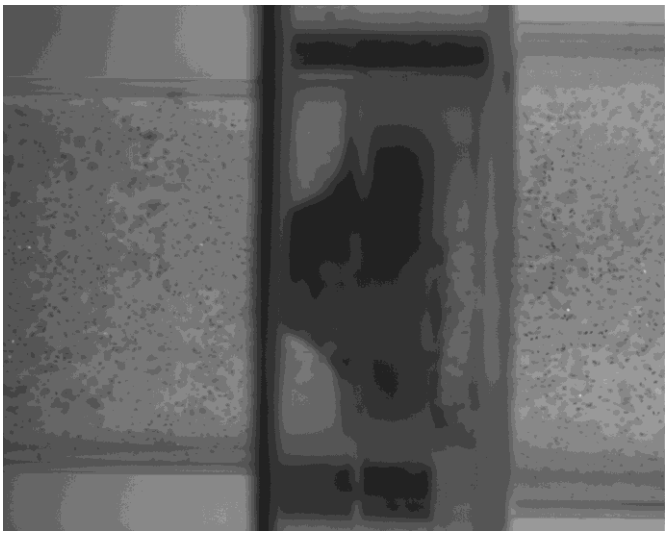

Figure 5.27: Flow visualization of BMHV under pulsatile conditions with no VG (murphy_david_w_200912_mast_Fig5-27_Puls-opening-Control.avi, 36,144 K)

The movie starts at the beginning of systole just before the valve leaflets begin to open. As the leaflets open, high-velocity flow can be seen going through the two peripheral gaps, above and below the b-datum gap. In the central region downstream of the b-datum gap, however, the fluid remains relatively still, thus creating a velocity defect. Once the valve is fully open, the flow through the central orifice accelerates to match the surrounding flow, and the velocity defect disappears. Figure 5.28 shows the flow well into systole and shows flow through both the central and peripheral valve orifices.

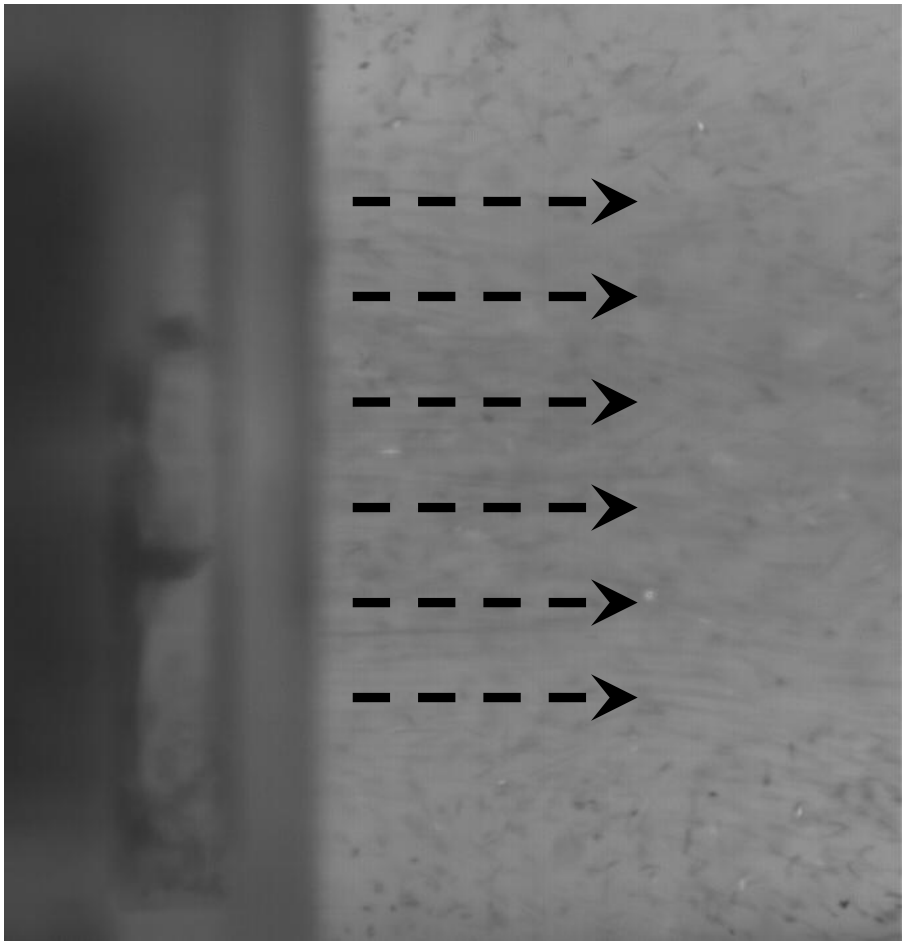

Figure 5.28: A snapshot of the Control case flow during valve opening. The dashed arrows indicate flow through both the central and peripheral orifices.

VG Case: Figure 5.29, recorded at 333 frames per second and slowed 11 times, shows flow visualization of the opening of a BMHV under physiologic conditions with the R35T vortex generators affixed to the leaflets.

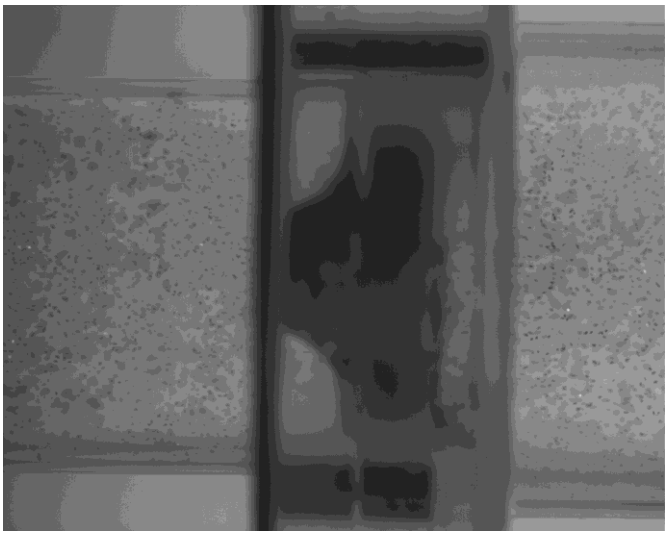

Figure 5.29: Flow visualization of BMHV under pulsatile conditions with R35T VG (murphy_david_w_200912_mast_Fig5-29_Puls-opening-R35TVG.avi, 20,721 K)

This movie also begins as systole is starting. As was seen in the Control case, the leaflets open, and high velocity flow can be seen going through the two peripheral gaps, above and below the b-datum gap. In this case, however, a velocity defect downstream of the central orifice is maintained throughout systole. While fluid smoothly travels through the peripheral gaps at a high velocity, the flow downstream of the central orifice is complex and three-dimensional, as low-velocity particles appear and disappear from the plane of focus. Figure 5.30 also shows the effect of the vortex generators on the flow through the central orifice. This vortex generator-induced velocity defect phenomenon can also be seen at the beginning of Figure 5.25, which includes a portion of systole before the closure of the valve.

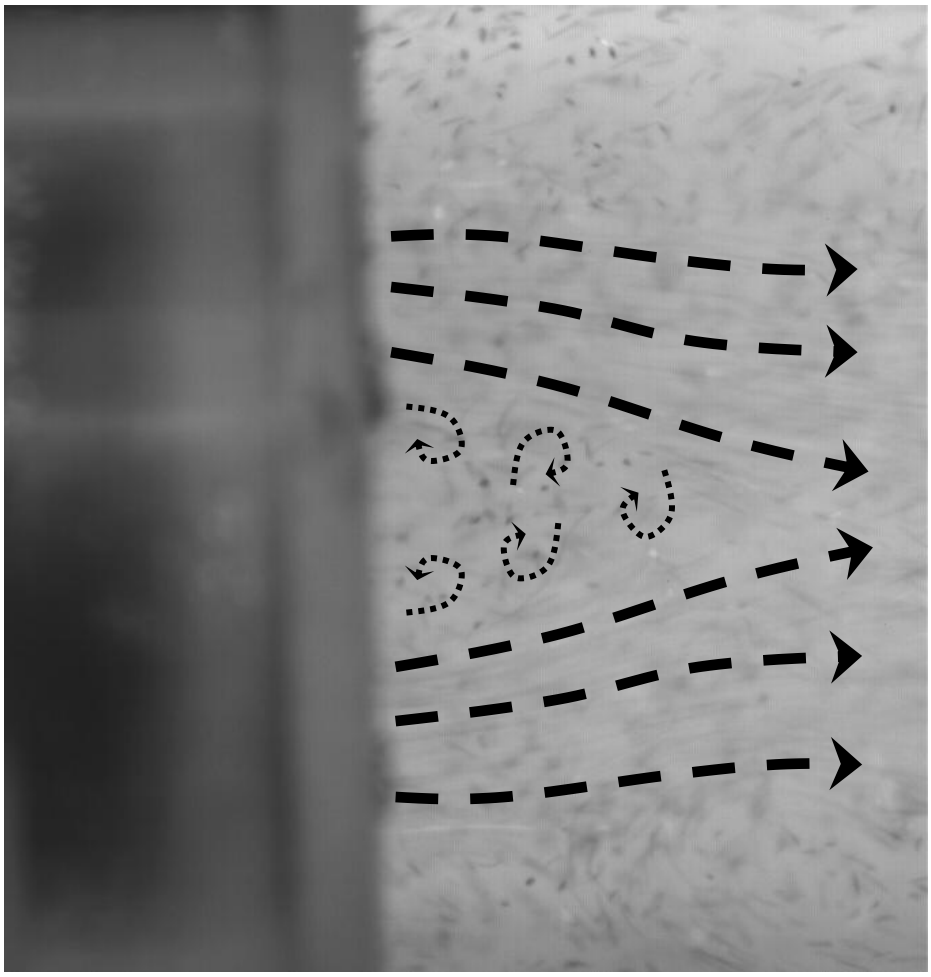

Figure 5.30: A snapshot of the VG (R35T) case flow during valve opening. The bold, dashed arrows indicate flow through the peripheral orifices. The smaller dashed arrows indicate the well-mixed flow through the central orifice.

CHAPTER 6

DISCUSSION

Organization of Discussion

In this chapter, the discussion will be organized along the lines of the Specific Aims put forth in Chapter 3. First, the effect of the vortex generators on the steady jet emanating from the valve b-datum line will be discussed from a fluid mechanics perspective. The performance of various vortex generator designs will be compared one to another and to previously published data on cardiovascular hardware-induced blood damage Second, the effect of the vortex generators on the blood's procoagulant potential will be discussed, with an eye towards correlating vortex generator-induced fluid features with the blood damage results. Third, the effect of the vortex generators on the pulsatile b-datum jet under physiologic conditions will be discussed and related to possible mechanisms of blood damage trauma. Finally, the implications of this research for prosthetic valve design will be presented.

6.1. Effect of Vortex Generators on Steady Flow

6.1.1. General Features of Steady B-datum Jet

A simplified proxy of the jet that momentarily emanates from the b-datum line orifice of a closing bileaflet mechanical heart valve was created. This model attempted to remove the transient nature of the jet emanating from the closing leaflets by imposing steady flow through an 'almost-closed' valve with the peripheral orifices and the hinge regions blocked. The characteristics of the resulting jet will be discussed here.

Of first importance in characterizing the b-datum jet is the fact that it was seen to exhibit self-sustaining oscillations. This jet oscillation along the b-datum line length is a large-scale that occupies the entire chamber width and is a low frequency phenomenon that was observed in the flow visualization to occur at approximately 2 Hz. Unforced jet oscillation has previously been observed and studied in other confined jet configurations, particularly in models of thin slab casting molds (Lawson and Davidson, 1999; 2001; 2002). The oscillation is generally understood to be caused by the jet's confinement and the subsequent formation of two alternating recirculation cells. The two recirculation cells are linked by azimuthal crossflow between the chamber wall and the nozzle, which provides the feedback necessary for the alternation to occur (Lawson and Davidson, 1999).

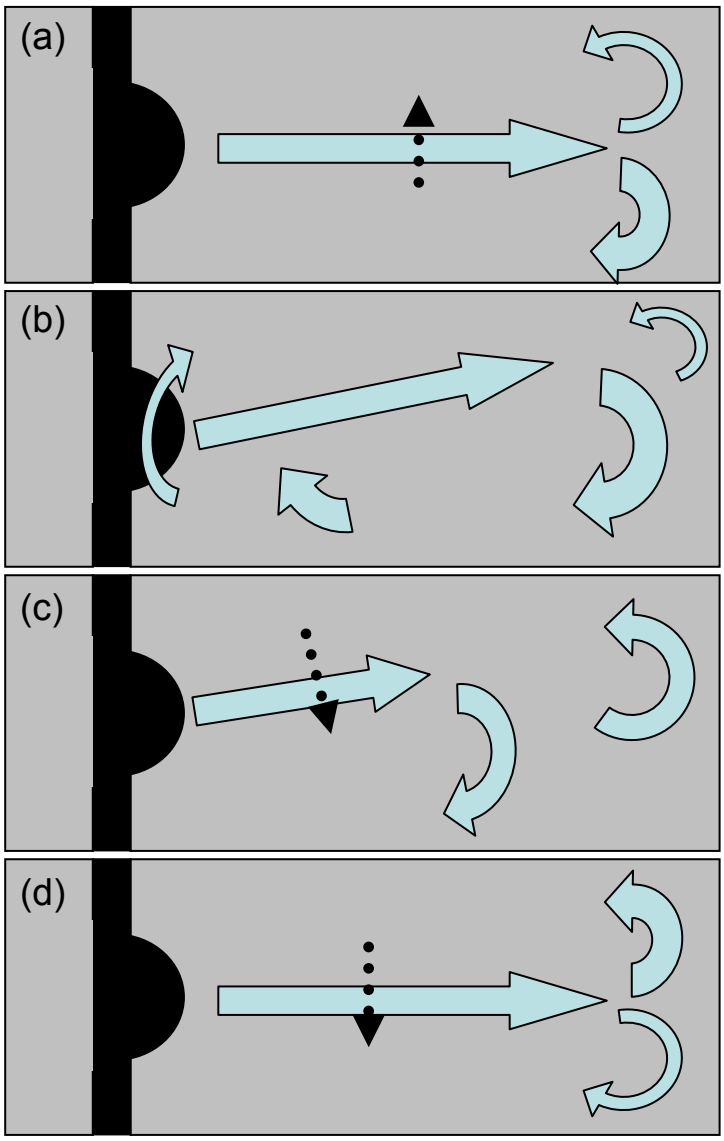

Figure 6.1: Panels a-d illustrate the cycle of jet oscillation seen in the current experiments and described by Lawson and Davidson (1999).

A schematic of the oscillation process described by Lawson and Davidson (1999) adapted to the jet under study is shown in Figure 6.1. In panel (a), the jet is in the process of moving upwards due to momentum from the previous cycle. The bottom recirculation cell thus grows stronger than the upper recirculation cell. In panel (b), the jet is at its maximum deflection and the bottom recirculation cell has grown to encompass almost the entire chamber. The momentum of the recirculating fluid which impinges on and is

entrained by the emanating planar jet near the nozzle likely acts to maintain the jet's upward-pointing direction. Deflection of the jet so close to the nozzle was not seen in the studies of Lawson and Davidson, a fact that can likely be attributed to the relatively wider chamber used in those experiments (1999). A strong azimuthal crossflow also occurs around the valve thumbnail and base of the jet during this portion of the cycle, thus linking the two sides of the jet. In panel (c), the angular momentum of the bottom recirculation cell increases under the influence of the jet's shear layer. As shown by Lawson and Davidson (1999), the result is a decrease in pressure in the cell. This decrease in pressure, combined with the enlargement of the upper recirculation cell, causes the jet to swing downwards towards its central position in panel (d). In a situation analogous to that seen in panel (b), a recirculation cell then forms in the opposite direction (counter-clockwise) and fills almost the entire chamber. The process described in the panels above thus occurs in the opposite direction, and the cycle continues indefinitely. The result is a jet that oscillates back and forth across the chamber.

Previous investigators have found that the low frequency oscillations characteristic of large-scale jet flapping are distinct from the jet oscillations driven by the inherent hydrodynamic instability of the shear layer (Rockwell, 1983; Nathan et al, 1998). In classifying shear layer oscillations bounded by a recirculation zone, Rockwell pointed out that the Strouhal number (St), a dimensionless frequency, can be used to differentiate between the two types. For confined jet oscillation, Nathan et al (1998) defined *St* as

$$St = \frac{f_f d}{\overline{u}}$$

where f_f is the frequency of jet flapping, d is the jet nozzle width, and u is the bulk mean velocity at the jet nozzle (Nathan et al, 1998). While *St* is on the order of one for a classical hydrodynamic instability, Strouhal numbers of much less than one are indicative of large-scale, low frequency oscillations (Rockwell, 1983). For instance, Lawson and Davidson reported St ~ 0.002 – 0.01 for an oscillating jet emanating into a thin slab casting mold model. Likewise, Mi et al reported a Strouhal number of 6.7×10^{-4} (2001) and Nathan et al reported a Strouhal number of 2×10^{-3} (1998) for various configurations of a jet nozzle similar to that used in the current experiments. In the jet under study, the Strouhal number was estimated to be 7.48×10^{-4}, based on a jet flapping frequency of 2 Hz, a jet nozzle width of 0.86 mm, and a bulk velocity of 2.3 m/s. This value places the behavior of the current jet within the Strouhal number range associated with large-scale, low frequency jet oscillations.

The behavior of flapping jets and, in particular, the jet flapping frequency, has been found to strongly depend on several geometric parameters. For instance, Maurel et al found that the ratio of the chamber length to the nozzle width was a key factor affecting the flapping frequency (1996). In their model of a thin slab casting mold, Lawson and Davidson found that the frequency depended on nozzle diameter, with an increase in frequency for larger nozzles. Their work also found that the flapping frequency decreased as the ratio of the cavity length to width increased (Lawson and Davidson, 2001). Mi et al also found that the distance the nozzle protrudes into the confined flow chamber is important in determining the frequency (Mi et al, 2001). This is expected since this parameter determines the resistance to crossflow around the jet nozzle (Lawson and

Davidson, 1999). In the current study, the ratio of chamber length to nozzle width is approximately 100, and the chamber length to width ratio is 2.8. The protrusion of the valve nozzle into the chamber is approximately 6 mm. The geometry of the chamber was not a variable in the current study.

Two other factors, namely the upstream conditions and the Reynolds number of the flow, also affect the jet properties. Well-defined upstream conditions are useful in identifying and eliminating confounding upstream influences on the jet behavior (Nathan et al, 1998). In the current study, however, the upstream conditions are not well defined. The upstream conditions consist of a cylindrical jet emanating into a cylindrical cavity, as shown in figures of the flow chamber in Chapter 4. Flow visualization showed that the jet is unstable and that the mixing in the upstream chamber is vigorous. The Reynolds number Re, which corresponds to the ratio of inertial to viscous forces is defined as

$$\mathrm{Re} = \frac{\rho V d}{\mu}$$

where ρ is the fluid density (1640 kg/m^3), V is the bulk mean velocity (2.3 m/s), d is the gap width of the valve's b-datum line (0.86 mm), and μ is the dynamic viscosity of the fluid (5.74 x 10^{-3} kg/(m*s)). The Reynolds number is approximately 570 for the jet under consideration. Considering the magnitude of the Reynolds number and the unsteady upstream flow conditions, the b-datum jet can be placed in the transitional range between laminar and turbulent flow. The Reynolds number has been found by several investigators to affect the flapping frequency of the jet. For instance, Lawson and Davidson found a linear dependence of the crossflow frequency on the jet velocity, a result that is consistent with a constant Strouhal number (1999). Villermaux and

Hopfinger (1994) and Maurel et al (1996) also found that the jet flapping frequency was linearly dependent on the Reynolds number. The Reynolds number was kept constant in the current study and so the dependence of the jet behavior on this parameter was not investigated.

6.1.2. Effect of Vortex Generators on Jet Fluid Mechanics

The effect of the vortex generators on the fluid mechanics of the steady b-datum line jet seems to be played out at multiple scales. It was expected that vortex generators would alter the jet behavior on a small scale. It seems, however, that the applied passive flow control also affects large scale jet phenomenon and that some interplay between the small and large scales occurs. The effect of the vortex generators, in particular on the flow field immediately downstream of the nozzle, will now be discussed. It is important to remember throughout this discussion that the presented PIV data represent only one plane in the global flow field. Measurements in other planes might produce significantly different results.

The spreading rates of the jet with and without the application of flow control, as seen in Figure 5.9, provide evidence of vortex generator-induced changes to the b-datum jet structure. The jet half-width, $Y_{0.5}$, defined as the distance from the jet centerline to the "cross-stream" position at which the mean streamwise velocity component is half of the mean centerline velocity, is a useful measure in this regard (Mi et al, 2001). Figure 6.2 shows the jet half-width, normalized by the b-datum gap width W, as a function of normalized distance downstream of the nozzle. It is interesting to notice the substantial

difference between the two cases. The Control case jet spreads more quickly after approximately four jet widths downstream of the nozzle. Whether or not this difference is an artifact of the jet oscillation will shortly be examined.

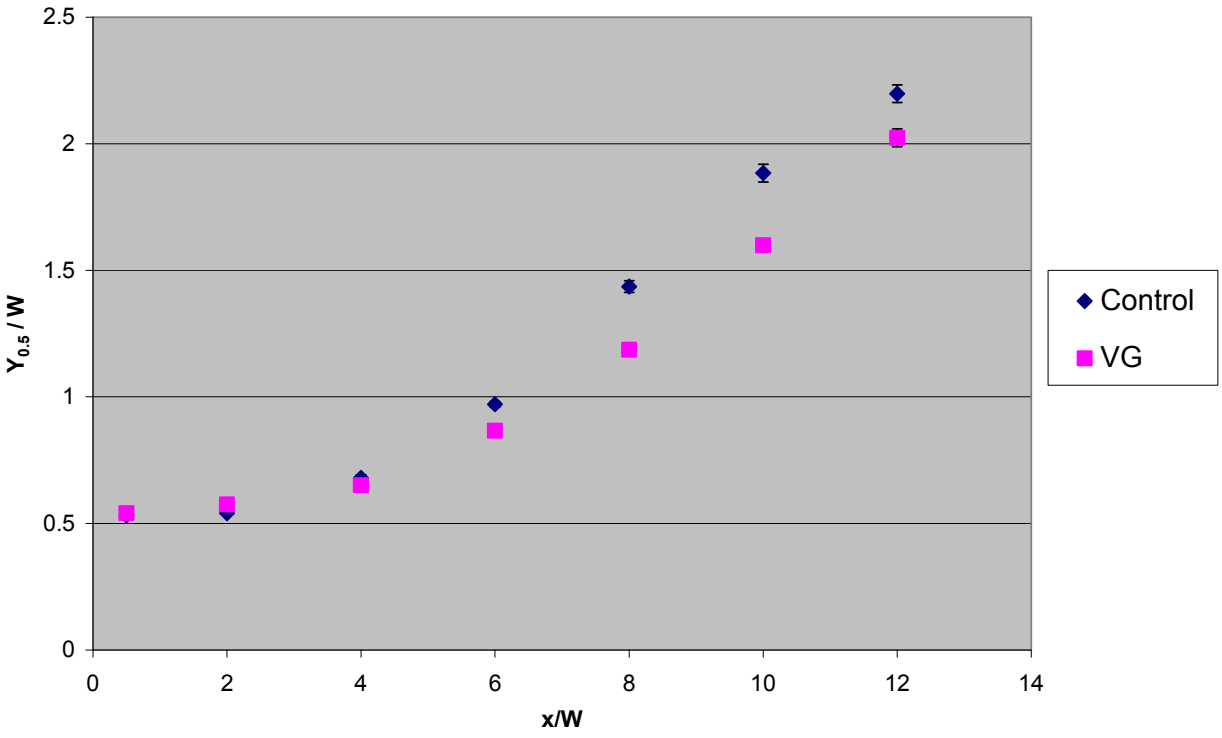

Figure 6.2: Normalized jet widths for the Control and R20T VG cases

The RMS velocities in both the streamwise and cross-stream directions provide another instance in which a substantial difference is seen between the Control and R20T VG cases (Figure 5.10). Figure 6.3 shows a comparison of the streamwise and cross-stream RMS velocity profiles normalized by the mean centerline jet velocity (at y = 0 mm) for the control and VG cases. These profiles are taken at eight gap widths (8W) downstream of the nozzle. For both of the velocity components' RMS values, the Control case values

are greater than those with the vortex generators. One possible explanation of this difference is that variations in the large-scale jet behavior (i.e. jet oscillation frequency or magnitude) could contribute to the difference in velocity RMS values between the two cases. Whether this theory truly explains the data will be examined shortly.

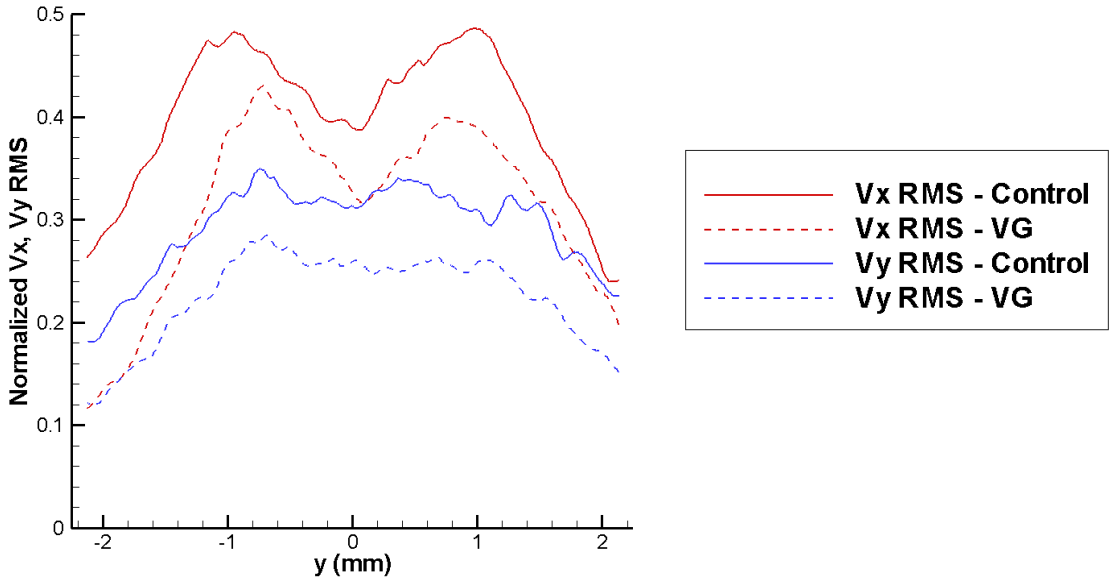

Figure 6.3: Streamwise and cross-stream velocity RMS profiles taken at 8W with (VG) and without (Control) the use of vortex generators.

A final difference between the Control and R20T VG cases is that the Control case exhibited higher levels of Reynolds shear stress (RSS), as seen in Figure 5.12. In addition, Figure 6.4 shows a comparison of the RSS profiles, normalized by the square of the mean centerline jet velocity (at y = 0 mm) taken at 8W downstream of the nozzle for the Control and R20T cases. Both figures show that the RSS levels were greater for the

Control case than for the VG case. However, the possible role of differences in the jet oscillation between the two cases is not factored into this comparison.

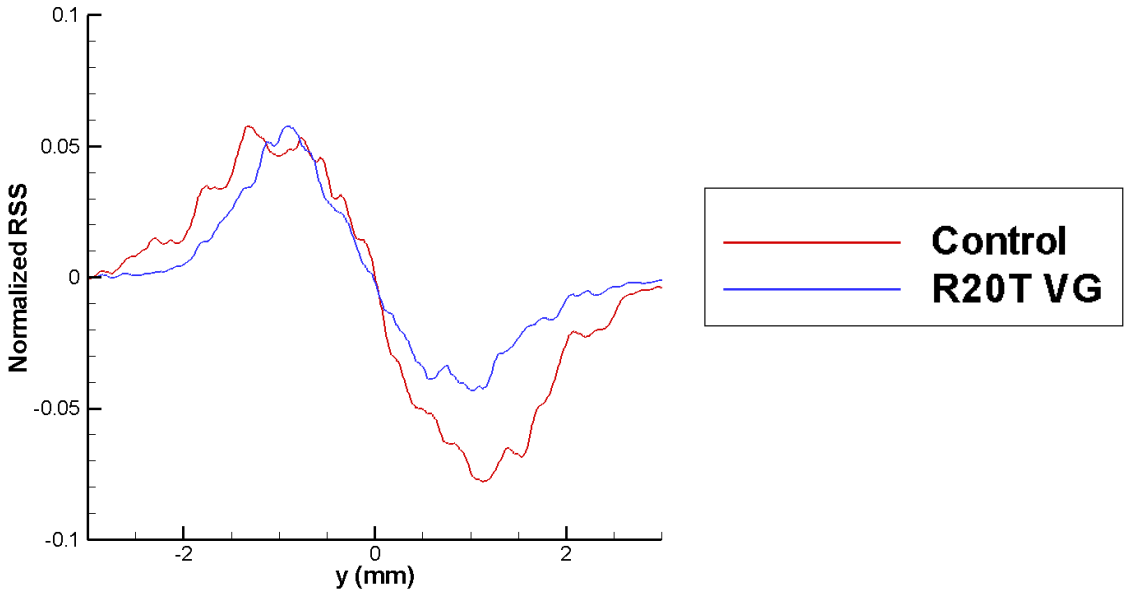

Figure 6.4: RSS profiles at 8W normalized by the square of the mean centerline velocity for both Control and R20T VG cases.

It is possible that the differences described above (i.e. jet spreading rates, RMS of velocity, and RSS) are primarily due to vortex generator-induced differences in the large-scale flow characteristics, such as the jet oscillation magnitude or frequency. If this is the case, any small-scale changes in the fluid flow induced by the presence of the vortex generators would be hidden. Persistent differences between the distributions of the instantaneous jet position for the Control and R20T VG cases, as shown in Figure 4.15, lend weight to the theory that vortex generators induce large-scale differences in the flow. These differences, namely the discrepancy in standard deviation and overall dissimilarity in shape, provide circumstantial evidence that the jet oscillation is somehow varied by the

presence of the vortex generators. Further evidence for this VG-induced difference is supplied by the histograms of instantaneous jet position for all eight cases of the large-scale PIV data. Figure 5.18, for instance, shows some variation in the standard deviation and overall shape of the distributions among the various VG designs.

In order to address the concern that variations in jet oscillation might confound the detection of small-scale vortex generator-induced differences, the binning procedure and conditional analysis described in Chapter 4 were carried out. This analysis was similar to the triple decomposition and phase-averaging scheme used by Mi et al to estimate the contribution of a jet's coherent flapping motion to the Reynolds stresses (Mi et al, 2001).

A comparison of jet characteristics (i.e. jet spreading rates, cross-stream velocity RMS, and RSS) between the unfiltered data previously discussed and the binned, phase-averaged data should elucidate what previously observed differences are due to changes in the coherent flapping motion of the jet and those that are due to small-scale VG-induced changes.

The jet spreading rates, as described by the jet half width $Y_{0.5}$, were found for the conditional (phase-averaged) data from Bin 5 and compared to the unfiltered data. Bin 5 was selected because it is the central bin which adheres most closely to the original, unfiltered jet position. Figure 6.5 shows that the spreading rates for the Control and R20T VG cases are basically identical, thus indicating that the perceived discrepancy in jet spreading rates was a consequence of differences in the large scale jet oscillation. Figure

6.5 also shows the spreading rates for the unbinned results, which, due to the jet oscillation, are much higher than those of the binned results. It is surprising to note that the spreading rates for the two cases are identical after the oscillation effect is removed. Previous investigators have found that the addition of vortex generators or mixing tabs to round and slit jets increased the jet spreading rate. Hui et al, for instance, found that the addition of tabs to their round jet increased the angle of jet spreading by 15 degrees. This effect was attributed to tab-induced streamwise vortices which entrain ambient fluid into the jet and eject core jet flow into the surrounding fluid (1999). Zaman et al (1994) also found an increase in the rate of axisymmetric jet spreading with the addition of vortex generators while Yu et al (1998) found an increase in spreading and entrainment for a square jet with mixing tabs. The lack of a difference between the two cases investigated here may be due to the location of the measurement plane. For instance, Hui et al investigated a round jet with two opposing tabs at the nozzle and found that the jet expanded at different rates in perpendicular planes. The authors attributed this difference to the presence of the protruding tabs (i.e. the initially round jet became an oval) (1999). It is therefore hypothesized that a similar effect may be responsible for the similarity observed between the two cases investigated here. Specifically, the jet spreading may vary along the length of the b-datum jet. Differences in jet spreading could be caused by proximity or relative location to a vortex generator fin. At the plane bisecting the b-datum jet (where data was taken), for instance, the jet may not spread as quickly as it does at a location several millimeters away.

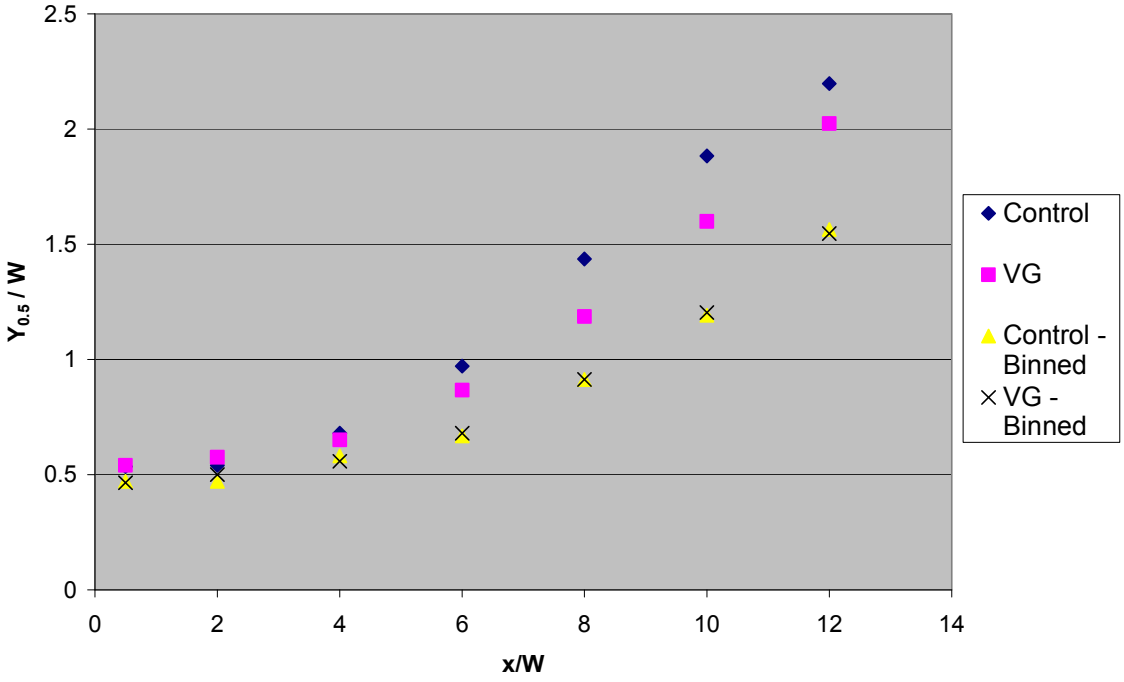

Figure 6.5: Normalized jet widths for the Control and R20T VG cases, for both the binned and unbinned analyses.

In order to further explore the effects of the jet oscillation, normalized velocity RMS profiles were found for the conditional (Binned) data from Bin 5 and compared to the unfiltered data. Figure 6.6 shows these profiles, both for the streamwise and cross-stream velocity components, for the unfiltered (unbinned) and conditional (Binned) data. As would be expected, phase averaging (binning) decreased the magnitude of the RMS values substantially for both the Control and VG cases. In comparing the Control and VG cases, it can be seen that much of the difference between the two cases is now absent, especially in the core of the jet. This indicates that most of the differences seen in the time-averaged case were due only to differences in jet oscillation. However, the profiles suggest that, even with phase-averaging, the jets with vortex generators experience

slightly lower RMS values (both streamwise and cross-stream) at the jet periphery (at approximately y = ± 0.75 mm). Since it has already been shown that the jet spreading is identical between the two cases for the phase-averaged (binned) data, the lower RMS values for the VG case cannot be attributed to differences in jet oscillation. Possible reasons for this difference will be explored shortly. This effect can also be seen by comparing the unfiltered velocity RMS contour plots (Figure 5.10) with the phase-averaged contour plots (Appendix C.2).

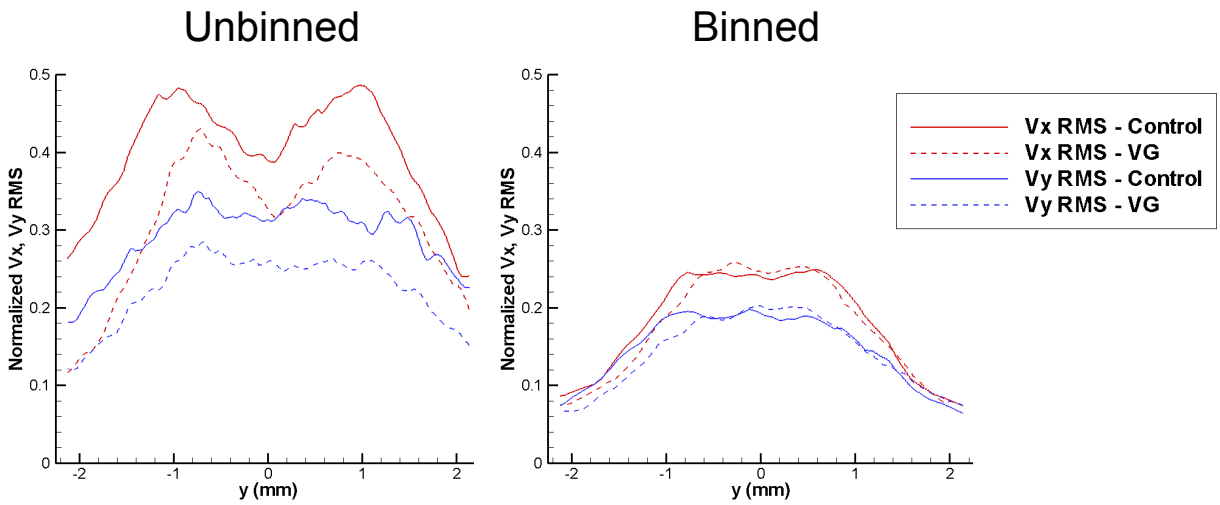

Figure 6.6: Streamwise and cross-stream velocity RMS profiles taken at 8W with (VG) and without (Control) the use of vortex generators with the effect of oscillation removed.

In investigating the effects of jet oscillation, a similar conclusion can be drawn from the RSS contour plots. When the contribution of the large-scale oscillations to the RSS was removed (as shown in Figures 5.12 and 5.14), the RSS values remain lower for the VG case than for the Control case. Normalized profiles at eight gaps widths downstream of the nozzle (8W) for the conditional (phase-averaged) data from Bin 5 compared to the

unfiltered data are shown in Figure 6.7. This figure shows higher RSS values for the Control case.

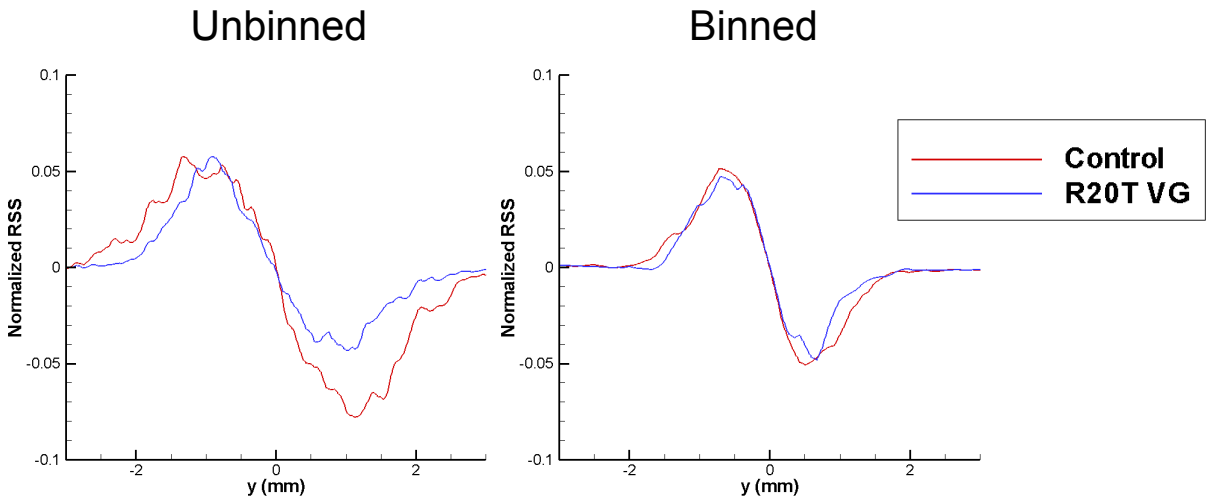

Figure 6.7: RSS profiles (at 8W) normalized by the square of the mean centerline jet velocity for the time-averaged (unbinned) and phase-averaged (binned) results.

By removing the effect of the large-scale jet oscillation via phase-averaging, it becomes clear that vortex generators significantly affect both the large scale nature of the flow and the small scale fluctuations. The proposed mechanism by which these differences occur will now be discussed.

Previous investigators have elucidated the effect of vortex generators and mixing tabs and have postulated two mechanisms by which the generation of streamwise vorticity occurs (Zaman et al, 1994; Yu et al, 1998; Foss and Zaman, 1999; Hui et al 1999). The first source originates from a 'pressure hill' formed upstream of the tab or vortex generator. With the presence of the wall, a pair of counter-rotating streamwise vortices is produced as the flow wraps around the tab. The second source is the vorticity shed from the sides

of the tab or vortex generators. At its formation, this vorticity is parallel to the edge of the tab. As it is convected downstream, however, it is reoriented by the velocity gradients in the shear layer into a streamwise orientation (Zaman et al, 1994; Foss and Zaman, 1999). This streamwise vorticity has been shown by many investigators to increase jet mixing by entraining ambient fluid into the jet and ejecting core jet flow into the surrounding fluid (Bradbury and Khadem, 1975; Zaman et al, 1994; Yu et al, 1998; Foss and Zaman, 1999; Hui et al 1999; Wang et al, 2003).

In the present case, however, it seems as if an increase in mixing was not present with the addition of vortex generators. For instance, phase-averaged jet spreading was identical with and without vortex generators, thus indicating that, at least within in the field of view investigated, jet entrainment did not vary with the application of vortex generators. In addition, a small decrease in mixing (as evidenced by the slight reduction in velocity RMS values) was seen with the addition of vortex generators. This seeming contradiction can likely be explained by considering the effect of the vortex generators on the onset of the Kelvin-Helmholtz instability in the jet. It is proposed that the production of vorticity parallel to the vortex generator fin edges (i.e. as in the second source of streamwise vorticity) delays the onset of the Kelvin-Helmholtz instability. The proposed mechanism is illustrated in Figure 6.8.

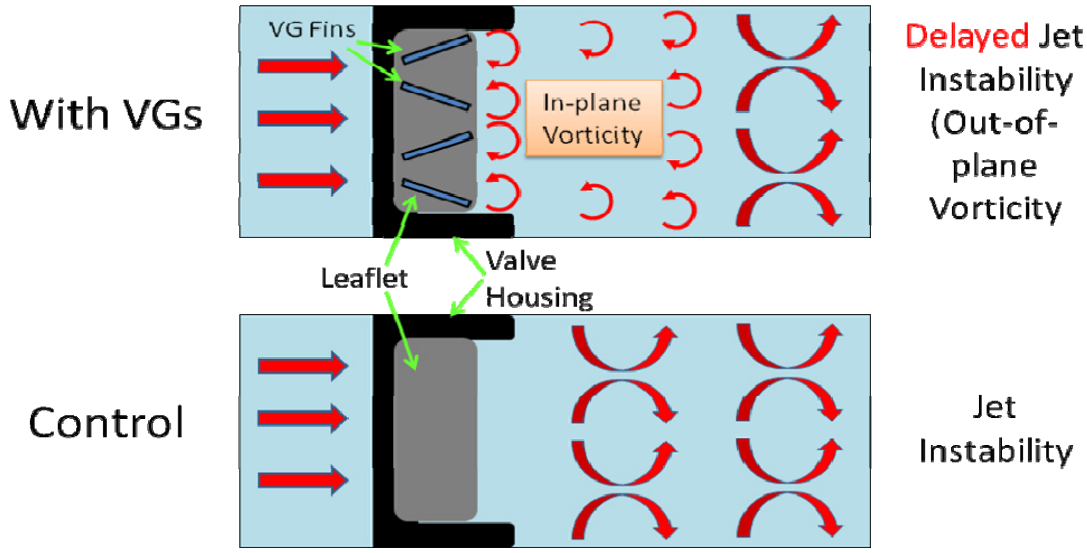

Figure 6.8: An illustration of how vortex generator fins might delay the onset of the Kelvin-Helmholtz instability (shear layer roll-up) via inducing vorticity in the plane of the jet.

The delay in the roll-up of the shear layer caused by the production of vorticity shed from the sides of the vortex generator fins is then sufficient to explain the decrease in RMS velocities witnessed at the jet periphery with the addition of vortex generators. Without vortex generators, the jet shear layers become unstable more quickly and generate vortices along the jet periphery. These vortices are likely responsible for the relatively high velocity RMS values seen at approximately y = ± 0.75 mm for the Control case in Figure 6.6. With vortex generators, on the other hand, the onset of vortex roll-up is delayed. The more coherent jet then yields lower velocity RMS values. This proposed mechanism is also supported qualitatively by examining a series of instantaneous velocity vector fields for both the Control and R20T VG cases. As seen in Figure 6.9 (Control) and Figure 6.10 (VG), large vortices resulting from the roll-up of the shear layer are often present for the Control case and are almost entirely absent for the case with vortex generators. (Figure 6.9 and Figure 6.10 were acquired in a flow setup identical to that

used for the other experiments with the exception that a chamber with slightly different dimensions was used. The same effect is present in the original chamber but is more difficult to see.)

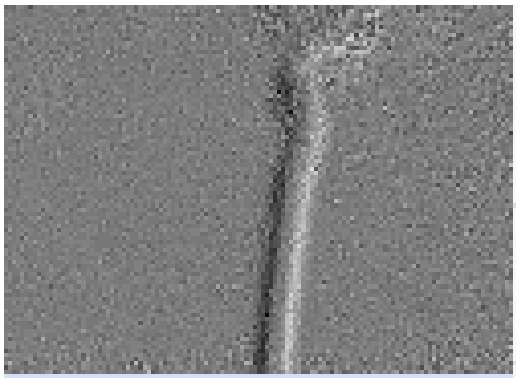

Figure 6.9: Instantaneous vorticity fields for the Control case (murphy_david_w_200912_mast_Fig6-9_Vorticity-Control.avi, 11,492 K)

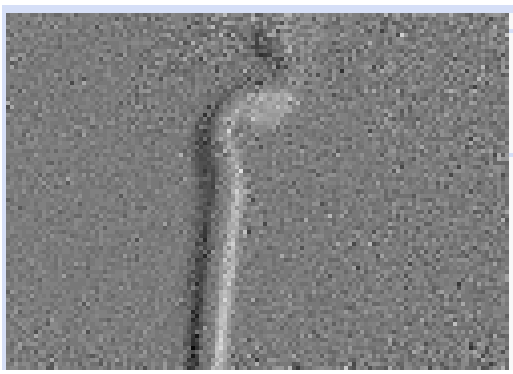

Figure 6.10: Instantaneous vorticity fields for the VG case (murphy_david_w_200912_mast_Fig6-10_Vorticity-VG.avi, 12,688 K)

A similar qualitative effect was observed by Fallon in examining the instantaneous vorticity fields produced by circular jets with nozzles designed to simulate BMHV hinge geometries with varying levels of "smoothness." Those geometries with abrupt changes in diameter led to jets that exhibited higher levels of vorticity and mixing at points closer to the jet nozzle (Fallon, 2006).

6.1.3. Comparison of Various VG Designs

The various vortex generator designs were seen to cause large-scale differences in the jet behavior. For instance, based on the standard deviation of the instantaneous jet position, as seen in Figure 5.18 and 5.19, the vortex generator designs with the smallest fin angle (5°) showed behavior substantially different from the other vortex generator designs. The two small angle designs (R05S and R05T) exhibited a smaller magnitude of oscillation than any of the other cases. These designs also had a larger number of fins (8) than either the designs with the 20° angle (6) or the 35° angle (4). It is therefore speculated that, according to the theory proposed earlier, the vortices shed from the additional fins acted to stabilize the jet, both on the small scale and on the large scale.

Based on the data acquired with the large-scale camera view, a clear difference is observed between the Control case and all other cases in both RSS values (Figure 5.20) and in cross-stream velocity RMS values (Appendix C.3). For both of these parameters, the Control case exhibited higher values. However, based on the smaller number of samples, a statistical analysis and comparison of the various vortex generator designs was not possible. This issue is exacerbated when the effect of the jet oscillation is removed via binning and phase averaging. The resulting contour plots of RSS and velocity RMS are sufficient to show a difference between the Control and all other cases but not sufficient to show small-scale differences induced by changes in the vortex generator fin angle and fin height.

It is also interesting to note that the design consisting of a base plate with no vortex generator fins showed behavior, both on the large and small scales, that was more similar to the six vortex generator designs than to the Control case. This phenomenon is illustrated in the contour plots of RSS and velocity RMS in Figures 5.18 and Appendix C.3 and in the plots of Figures 5.19 and 5.20. These data suggest that the presence of the base plate is itself sufficient to prevent the early roll-up of vortices along the shear layer. This does not necessarily contradict the proposed action of the vortex generators described earlier since vorticity production similar to that around the fins would in fact occur around the edges of the base plate.

6.1.4. Summary of VG Effect

The effect of the applied flow control is played out at both the scale of the chamber (large-scale) and on the scale of the vortex generator fins (small-scale). On the large scale, the presence of vortex generators appeared to decrease the magnitude or frequency of jet oscillation, thereby stabilizing the jet. After removing the effect of the large-scale oscillations, the effect of the vortex generators on the small scale was examined. On the small scale, the jet without flow control was found to have higher levels of velocity RMS, particularly on the jet periphery, and higher levels of Reynolds shear stress. It is proposed that the vortex generators effect this change by generating vorticity in the plane of the jet, as shown in Figure 6.8. This vorticity is theorized to stabilize the jet, delaying roll-up of the jet shear layer which occurs via the Kelvin-Helmholtz instability.

6.2. Effect of Vortex Generators on the Blood Procoagulant Potential

The procoagulant potential of the valve b-datum jet with and without the application of passive flow control was investigated using an *in vitro* flow system with whole human blood. In comparing the Control Case and the case with the small rectangular 20 degree fins (Control and R20T VG), significant differences were found in the levels of TAT in the blood and in the TAT growth rates. An effort will now be made to relate the physics of the flow to the procoagulant potential in order to elucidate the beneficial effect of the vortex generators on the procoagulant potential. It is important to note that the flow physics are quantitatively known only in the plane bisecting the jet just downstream of the b-datum line. The presence of other flow phenomena that might affect the blood's procoagulant potential cannot be ruled out.

It is helpful to first examine the nature of the flow system in order to identify possible mechanisms by which the procoagulant potential was reduced with the application of passive flow control. In the development of the *in vitro* flow loop used in these experiments, Fallon found that the generation of the TAT in the system could be attributed directly to shear-induced platelet activation, which promotes coagulation reactions, and not to hemolysis, which occurred on a statistically insignificant scale. In addition, Fallon found that the TAT levels depended not just on the level of shear stress but also on the flow structures that promoted aggregation of activated platelets (Fallon, 2006), in particular regions of low flow and regions of high mixing. Stagnation regions and vortices downstream of the jet were hypothesized to favor platelet aggregation by entrapping activated platelets and promoting cell interactions. Increased fluid mixing, in

particular a rapidly decaying jet that entrains more fluid was also found to induce a more efficient propagation of platelet activation by inducing contact between activated platelets and resting (unactivated) platelets (Fallon, 2006). In fact, in investigating various geometries inside the jet nozzle, Fallon found that the geometries with sharp edges produced a jet associated with more fluid entrainment and thus more mixing and led to much higher levels of TAT concentration than in the jet produced by a nozzle with smooth features (Fallon, 2006). Jets with relatively smoother internal nozzle geometries led to less fluid entrainment and lower levels of procoagulant potential. In the current experiments, both contributors to TAT generation described above (i.e. activation by elevated shear levels and aggregation/propagation promoted by certain flow features) likely play a role. The role of activation by elevated shear stress levels will be examined first, followed by a discussion on the effect of flow structures on platelet aggregation and propagation.

Platelet activation by shear stress depends on the magnitude, exposure history and duration of the applied shear stress (Alemu and Bluestein, 2007). Both viscous and Reynolds shear stress levels may play a role in activating platelets in the current system. Figure 6.11 shows the mean viscous shear stress contour plots for both the control and VG cases. It can be seen from this Figure that the magnitude of the highest viscous shear stresses experienced in the system is on the order of 50 Pa, and no difference is seen between the viscous shear stresses in the Control case and in the R20T VG case. It can thus be concluded that the peak viscous shear stresses in the measurement region are experienced in the jet shear layer near the nozzle during the first few millimeters of the

jet. Assuming that a blood particle travels along the edge of the jet, an estimate of the exposure time can be obtained by dividing the length along the shear layer over which the platelet might experience the peak shear levels (~3 mm) by the typical velocity value within the shear layer (~2 m/s). This calculation results in an estimate of a 1.5 ms exposure time for peak shear stresses. However, Colantuoni *et al* found that platelet activation occurred in 5 ms at a laminar shear stress level of 650 Pa (Colantuoni *et al.*, 1977). It is therefore believed that such an exposure of 50 Pa for an exposure time of 1.5 ms is likely not sufficient to activate a platelet. However, the shear stress history (in particular previous damage inflicted on individual cells) has been recognized as an important parameter governing platelet activation (Alemu and Bluestein, 2007). In the *in vitro* flow loop, the platelets are approximated to make 900 passes through the valve b-datum line in 60 minutes as the blood recirculates through the loop. It is thus possible that the cumulative effect of multiple passes through the high shear stress jet will initiate platelet activation. However, since both the Control and R20T VG cases experience the same levels of viscous shear stress, this factor cannot explain the difference seen in the procoagulant potential between the two cases.

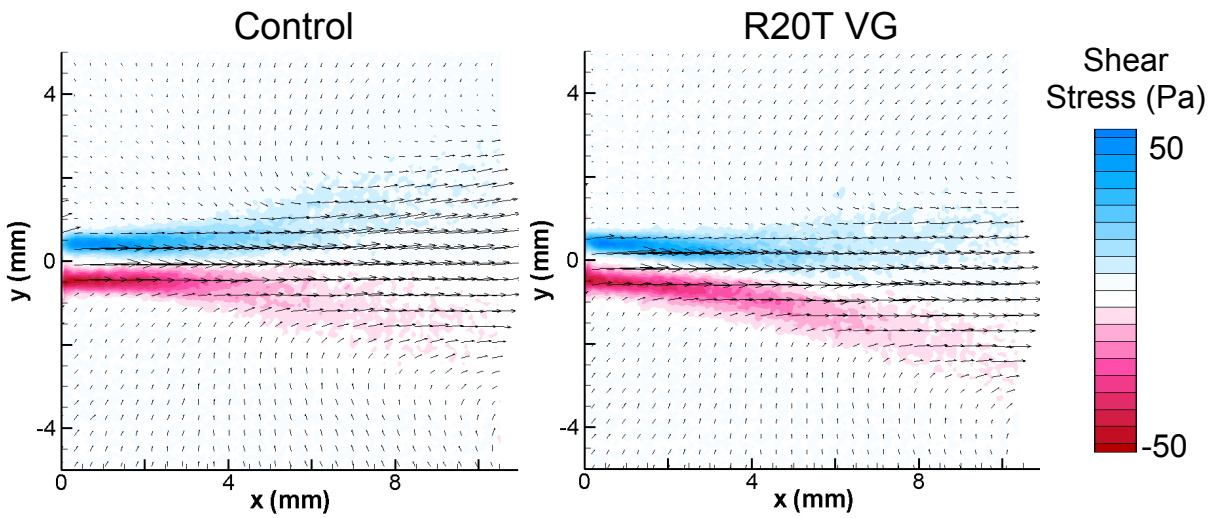

Figure 6.11: Mean viscous shear stress contour plots for the unfiltered Control and R20T cases

Reynolds shear stresses were also investigated as a potential contributor to platelet activation and TAT generation. The peak RSS values found for either the Control or R20T VG case were approximately 250 Pa. An estimate of the exposure time can be obtained by dividing the length along the jet over which the platelet might experience the peak shear levels (~4 mm) by the typical velocity value within the shear layer (~2 m/s). This calculation results in an estimate of a 2 ms exposure time for peak Reynolds shear stresses. These values (250 Pa at an exposure time of 2ms) were well below the 800 Pa threshold necessary for hemolysis found by Lu et al (2001) for an exposure time of 1 ms. Whether or not this RSS level and exposure time is sufficient to affect platelets, however, is an open question since neither the exact mechanism of turbulent stress damage to platelets nor a RSS threshold for platelet activation at these time scales is currently known (Yoganathan, 2000). It is, however, conceivable that the RSS levels seen in the current experiments were sufficient to contribute to platelet activation, particularly after repeated exposure during multiple passages through the valve. After the phase-averaging

analysis was carried out to remove the effect of jet oscillation, it was found that the Control case jet experienced peak Reynolds shear stresses that were 10-20% greater in magnitude than those experienced by the jet influenced by the vortex generators. Even if only a small percentage of platelets are affected or activated during each passage through the valve, the cumulative effect of such a difference in stresses can lead to significant differences in thrombogenic performance (Dumont et al., 2007). It therefore seems possible that the difference in RSS magnitude between the two test cases contributed to the significant difference observed in the TAT levels.

It is suspected that the main contributor to the decreased procoagulant potential found for the blood experiments with vortex generators was the decreased level of opportunity for aggregation afforded to activated platelets. As described previously, the vortex generators are thought to have prevented or delayed the onset of jet instability and the accompanying roll-up of the jet shear layer into the discrete vortices that were seen in the jet without vortex generators. It is thought that these vortices provided the proximity and the long residence times necessary for recently activated platelets emanating from the high-shear stress jet nozzle region to mingle, aggregate, and activate resting platelets. Even though platelets emanating from jet nozzles with and without vortex generators may experience the same levels of stress and activation, the platelets emanating from the jet with VGs are more likely to remain in the core of the stable jet for a longer time (as opposed to becoming entrained in vortices formed at the onset of jet instability). This environment (the jet core) is certainly not as conducive to the aggregation of platelets as a high residence time vortex. When the jet with vortex generators eventually does become

unstable, the passage of time may have allowed any platelets that were activated to return to a non-activated state. The vortices formed at jet instability thus serve as discrete micro-reactors for the activation of resting platelets and the aggregation of activated platelets. In a similar vein, Bluestein et al proposed that vortices shed from the leaflets of bileaflet mechanical heart valves during systole, particularly those implanted improperly (at an angle to the bulk flow), could promote free emboli formation by allowing activated platelets to aggregate (Bluestein et al, 2000; Bluestein et al, 2002).

In considering the factors that may influence blood damage, it is important to note that high Reynolds and viscous shear stress levels are experienced in regions that are not in the measurement region. For instance, the blood is exposed to high levels of wall shear stress within the jet nozzle. In particular, recent work by Travis et al has emphasized the importance of elevated wall and viscous shear stresses relative to the significance of turbulent shear stresses when considering shear-induced blood damage (Travis et al., 2008). The round jet that emanates into the chamber upstream of the valve is another example of an unquantified shear factor that could influence blood damage. Exposure to these elevated shear levels are not included in the estimates of shear stress and exposure times previously calculated but nonetheless contribute to the platelets' shear stress history. In considering the aforementioned thresholds for blood damage, it is also important to note that the blood used in this experiment was treated with and anti-coagulation agent and was infused with a reversing agent throughout the experiments. It is unknown if these conditions may affect blood element thresholds for hemolysis or activation.

An alternative interpretation of the TAT data is that the jet in the Control case yielded higher levels of TAT because of increased mixing in the chamber due to a higher level of jet oscillation. In this scenario, the Control case jet oscillated with a greater magnitude than the VG case, leading to higher levels of mixing throughout the chamber. The jet influenced by the vortex generators, on the other hand, was relatively more stable and yielded fewer opportunities for recently activated platelets to meet and propagate the coagulation cascade.

In summary, it is thought that two factors contributed to the lower levels of procoagulant potential for the case with vortex generators in the blood experiments. First, the Reynolds shear stress levels were 10-20% lesser in the VG case compared to the Control case. Such a reduction in shear stress is likely to contribute to the smaller rate of platelet activation observed in the VG case compared to the Control case. Second, it is thought that the presence of the vortex generators led to decreased opportunities for aggregation among activated platelets by preventing or delaying the onset of jet instability, thereby delaying the entrainment of platelets into "micro-reactor" vortices. Lower platelet aggregation would thus lead to lower levels of TAT. In addition, it is possible that viscous stresses played a role in activating platelets. Viscous stresses were not affected by the presence or absence of vortex generators, however, and so these stresses are thought not to have played a role in the different levels of TAT seen in the blood experiments.

6.3. Effect of Vortex Generators on Pulsatile Jet

Visualization of BMHV flow was conducted under physiologic conditions with and without the influence of vortex generators (R35T VG case). In this section, the effect of the passive flow control on the jet fluid mechanics will be discussed, considering both the opening and closing of the valve leaflets. Based on knowledge gained from the steady flow experiments, the possible effects of the vortex generators on the procoagulant potential of blood will be discussed.

Flow visualization of the jet produced by the closing valve leaflets with and without the impact of vortex generators reveals striking differences in the jet fluid mechanics. While the Control case produced several large, coherent vortices that persisted for several milliseconds, the R20T VG case dissipated much more quickly and on a much smaller scale. It appears that the vortex generators cause increased mixing along the plane of the jet by re-directing the flow with their fins. In the flow visualization, this mixing is an out-of-plane effect and appears as "blooms" of particles (i.e. a group of particles moving away from each other). Such differences in the fluid mechanics of the pulsatile jet may explain the changes on the level of platelet activation and resulting thrombus-forming potential. The *in vitro* blood experiments seemed to show, in agreement with the conclusions of Fallon (2006), that limiting opportunities for propagation of platelet activation was the key to decreasing the blood's procoagulant potential. In the blood experiments, it was hypothesized that these opportunities likely came in the form of vortices rolled up from the planar jet shear layer via the Kelvin-Helmholtz instability. Similar large-scale, discrete vortices appear to form as a result of the pulsatile jet

becoming unstable. It is likely that platelets recently activated by passage in the high-shear stress planar jet shear layer will become entrained in these vortices. These vortices are likely to also contain resting platelets entrained from the surround relatively stagnant flow, thereby providing an opportunity for propagation of platelet activation. It is thought that, by increasing mixing along the plane of the jet, the action of the vortex generators will quickly dissipate the regurgitant jet and prevent the formation of large-scale vortices. This action may decrease the volume of resting platelets exposed to the platelets activated by high shear stress in the regurgitant jet, thus preventing the propagation of platelet activation. Vortex generators thus have the potential to reduce platelet aggregation by preventing the formation of large, persistent regurgitant vortices.

It is also important to consider the effect of the vortex generators on the forward flow through the BMHV during systole. While the Control case shows relatively smooth flow through the central and peripheral orifices (Figure 5.27 and Figure 5.28), the forward flow through the central orifice is significantly influenced by the vortex generators. The central flow is chaotic and shows evidence of out-of-plane mixing. Such a situation is however undesirable for several reasons. First, the vortex generators, by reducing the orifice offered to the flow might increase the pressure drop across the valve, leading to a decrease in the Effective Orifice Area. A valve with reduced EOA forces the heart to work harder to pump the same volume of blood. Second, the forward flow created by the vortex generators is likely characterized by elevated turbulent shear stresses and would probably lead to increased thrombus-forming potential in the blood.

A further consideration in how VGs affect valve function is the effect of the vortex generators on the kinematics of the leaflets. The presence of the vortex generators undoubtedly changes the moment of inertia of the leaflets and could thus affect leaflet opening and closing. The speed with which the valve closes, for instance, could significantly affect the jet emanating upstream through the b-datum line.

6.4. Implications for Valve Design

The results drawn from the current experiments provide guidance in the application of passive flow control to bileaflet mechanical heart valves. The proposed mechanism by which the passive flow control used in the current study reduced procoagulant potential is that the vortex generators created vorticity in the jet plane that delayed the onset of the Kelvin-Helmholtz instability, thereby depriving activated platelets of the persistent vortices needed for platelet aggregation and the propagation of the coagulation cascade. Use of this insight can help evaluate the vortex generator designs tested in the current study and lead to better designs. For instance, the vortex generator designs with the fins set at a 5° angle (R05T and R05S) seem the most promising because they exhibited the lowest level of jet oscillation. It is possible that this is because these designs also had the most fins, which would generate more vorticity in the jet plane.

Perhaps the most glaring problem with the current vortex generators designs is the disturbance of the forward flow through the central orifice. In order to solve this problem, flexible or actuated vortex generators could be designed to passively lie down during systole and rise back up during valve closure. An alternative and perhaps more attractive

option that would remove that need for moving vortex generator fins would be to incorporate corrugation or micro-texturing into the leaflet surface itself. In particular, corrugation of the leaflet edges along the b-datum line would effectively change the b-datum jet from a planar jet into a "wavy" jet. The characteristics of flow from irregularly shaped nozzles (i.e. lobed nozzles) have been investigated, and it has been found that these nozzles are often effective in increasing jet spreading due to the action of streamwise vortices (Gutmark and Grinstein, 1999; Zaman, 2001). Corrugations on the leaflet, similar to those found on a clam shell, could therefore by used in the nozzle to produce an effect on the b-datum jet similar to that of the vortex generators investigated here. An additional benefit of the corrugation technique would be that the forward flow would naturally be unobstructed, even with the application of passive flow control.

Additional opportunities to apply passive flow control exist in bileaflet mechanical heart valves. Regurgitant jets emanating from the peripheral gaps, for instance, have been implicated as high shear stress, thrombus-forming phenomenon (Krishnan et al, 2006). Corrugation of the leaflets could also serve to dissipate the jets emanating from these two orifices. Surface texturing or the application of fins to interior of the valve body could also be used to address this problem. Finally, micro-surface texturing could be used to address leakage flows through the BMHV hinge regions.

CHAPTER 7

STUDY LIMITATIONS

One of the main limitations in these experiments is that the steady flow loop system neglects the transient nature of the true, physiologic jet emanating from the b-datum line during valve closure. In such a steady test case, it cannot be assured that the effects of the applied passive flow control observed in the steady flow system (both on the jet flow and on the blood properties) will be the same as that seen in a pulsatile system. Nonetheless, applying passive flow control to a steady flow system allows for well-controlled experiments, thereby providing the opportunity to draw meaningful conclusions on a simple test case before applying it to more complicated flow systems.

Another limitation that was not initially anticipated was the oscillatory nature of the jet in the steady flow loop. This behavior obscured the effect of the flow control and necessitated the phase averaging analysis to separate the effects of the vortex generators on the jet oscillation versus that on the jet structure and mixing. It would be much simpler to detect the effects of passive flow control in studying a free jet with no oscillation and no wall effects. A system with a much larger volume would be required for this setup, though. The current system was limited in this regard by the need to replicate the *in vitro* blood loop, which is itself limited in volume by the amount of blood that can be safely drawn from a single donor. A further limitation with regard to the jet oscillation was the lack of a thorough characterization of the flapping frequency and magnitude. The steady flow visualization videos could possibly have been used to determine the actual jet

flapping frequencies. However, data was not recorded over enough cycles to gain an accurate estimate of the frequency. An experimental technique with a higher acquisition rate than PIV, such as Laser Doppler Velocimetry (LDV), would also have been ideal for determining the frequency of jet oscillation.

Another limitation was that flow measurements were only acquired in the 8mm x 10mm plane bisecting the b-datum line just downstream of the jet nozzle. These measurements thus represent only a sample of the flow physics that might influence the thrombus-forming potential of the blood. Other flow phenomena either upstream or downstream of the mounted valve may have played a role in the difference in procoagulant potential witnessed in the blood experiments.

Another limitation was the lack of knowledge regarding the flow conditions upstream of the valve mounting position. It is known that the upstream flow consisted of a circular jet emanating into a circular chamber and that much recirculation was observed. However, this flow was not quantified, and the effect of this flow on the blood properties is unknown. Finally, the chamber in conjunction with the valve mounting system used in the DPIV experiments prevented optical access to flow in several locations, particularly just upstream of the valve.

The limitations experienced in the blood studies are similar to those experienced by Fallon and have to do with the nature of the *in vitro* system (2006). For instance, although shear-induced platelet activation has been shown to increase at temperatures less than 37°

C, the temperature of the blood was not maintained at body temperature throughout the experiments. However, since these experiments sought to compare two outcomes based only on varying valve geometries, the temperature was not considered to be a factor that would affect these results. In addition, the leveling off of the TAT concentrations after approximately 30 minutes, an effect also seen in Fallon (2006), shows that the haemostasis factors may be starting to break down. Since whole blood was used (without manipulation to keep erythrocyte and platelet counts constant between donors), another limitation is the natural variation in human blood known to exist between donors. Fallon, however, measured that variation and found it to be less than 15% between donors. Finally, it is not known to what extent the flow loop without the valve, particularly the centrifugal blood pump and the chamber upstream of the valve, may initiate and promote the coagulation cascade.

CHAPTER 8

CONCLUSIONS

This study has investigated the possibility of applying passive flow control in the form of various vortex generator designs to bileaflet mechanical heart valve leaflets for the purpose of reducing the thrombogenic state of the blood induced by elevated fluid shear stress levels. By studying a steady model of the regurgitant b-datum line jet, it was found, using an *in vitro* system with whole human blood, that the presence of vortex generators significantly decreased the blood's propensity for thrombus formation. The potential of applying passive flow control to cardiovascular hardware in order to mitigate the injurious effects of shear-induced platelet activation is thus demonstrated.

The method by which the vortex generators acted on the fluid mechanics of the steady jet system to decrease the blood's procoagulant potential was investigated via flow visualization and DPIV. The results from these studies implicate two possible mechanisms by which the vortex generators may act. First, the peak turbulent shear stresses in the jet were reduced by 10-20% with the application of vortex generators. Even if only a few platelets were activated in each passage through the valve, the cumulative effect of this difference in peak stresses after many passes would be greatly magnified. Thus, this reduction in turbulent shear stresses may be sufficient to explain the change seen in the blood's procoagulant potential with the application of passive flow control. It is suspected, though, that the second mechanism is dominant. The flow fields revealed that the presence of the vortex generators delayed or prevented the roll-up of the

Kelvin-Helmholtz instability in the b-datum jet's shear layers into discrete vortices. By doing so, it is thought that opportunities for the interaction of activated and unactivated platelets entrained in these vortices were prevented, thereby inhibiting further propagation of the coagulation cascade. Even if the rate at which platelets were activated was similar for cases with and without flow control, it seems that the flow fields experienced by the platelets subsequent to activation can determine the level of procoagulant potential. Under the steady conditions observed in this experiment, the jet influenced by vortex generators was thus shown to induce significantly lower levels of procoagulant potential.

The effect of the vortex generators on the b-datum jet that occurs under physiologic conditions was investigated via high-speed flow visualization in a pulsatile flow loop. It was found that the presence of the vortex generators decreased the scale of the regurgitant jet by increasing mixing along the plane of the jet. By dissipating the jet over a smaller volume, it is speculated that the vortex generators may serve to decrease opportunities for the mixing of activated and resting platelets, thereby lowering the blood's procoagulant potential. By showing the obstructive effect of the vortex generators on the forward flow through the valve during systole, the flow visualization also highlighted the importance of designing passive flow control with a holistic consideration of valve function.

CHAPTER 9

FUTURE WORK

Although the current work has proven the concept of using passive flow control to mitigate the negative effects of shear-induced platelet activation, the physical mechanism by which it does so was not completely established. For instance, the current work has raised the hypothesis that the vortex generators delay the onset of jet instability by inducing vorticity perpendicular to the plane of the jet. Further work with fluid measurements taken in the plane of the jet, however, would be required to confirm or refute this hypothesis. Indeed, a separate study with a redesigned steady flow system that eliminates jet oscillation is required to truly determine the action by which the vortex generators affect the b-datum line jet. Future investigations with a redesigned steady flow system could also be used to optimize vortex generator designs or to explore completely different options for passive flow control such as corrugated leaflet surfaces.

Further work with the blood loop could investigate the hypothesis supported here that increased mixing is a key to increased procoagulant potential. Incorporating Lagrangian particle tracking into the experimental side of the work would prove extremely valuable. For instance, since platelet activation involves a calcium influx, using fluorescently labeled Ca2+ as the infusion medium would allow the observation of activation and aggregation in real time using confocal microscopy. Finally, designing and testing a pulsatile blood flow loop is essential to determining the effectiveness of passive flow control in mitigating the effects of shear-induced platelet activation. This is a challenging

prospect due to the small volume of blood available for such a flow loop. Achieving physiologic flow and pressure waveforms throughout the cardiac cycle would no doubt be difficult. Furthermore, considering that the mixing of activated platelets is likely of prime importance, designing an experiment that investigates this facet of blood damage and accounting for the mixing inherent in a flow loop would be a challenge. Finally, determining the effect of the passive flow control device on the leaflet kinematics would also be an essential step towards establishing the efficacy of that device.

APPENDIX A

METHODS-RELATED MATERIALS

Appendix A contains materials related to Chapter 4, Experimental Methods and Protocols. CAD-generated images of the various vortex generator designs are shown first in section A.1 In section A.2, code relating to the binning and cross-correlation analysis of the instantaneous velocity vector field images is shown. In section A.3, the IRB-approved consent form for the process of drawing blood is reproduced.

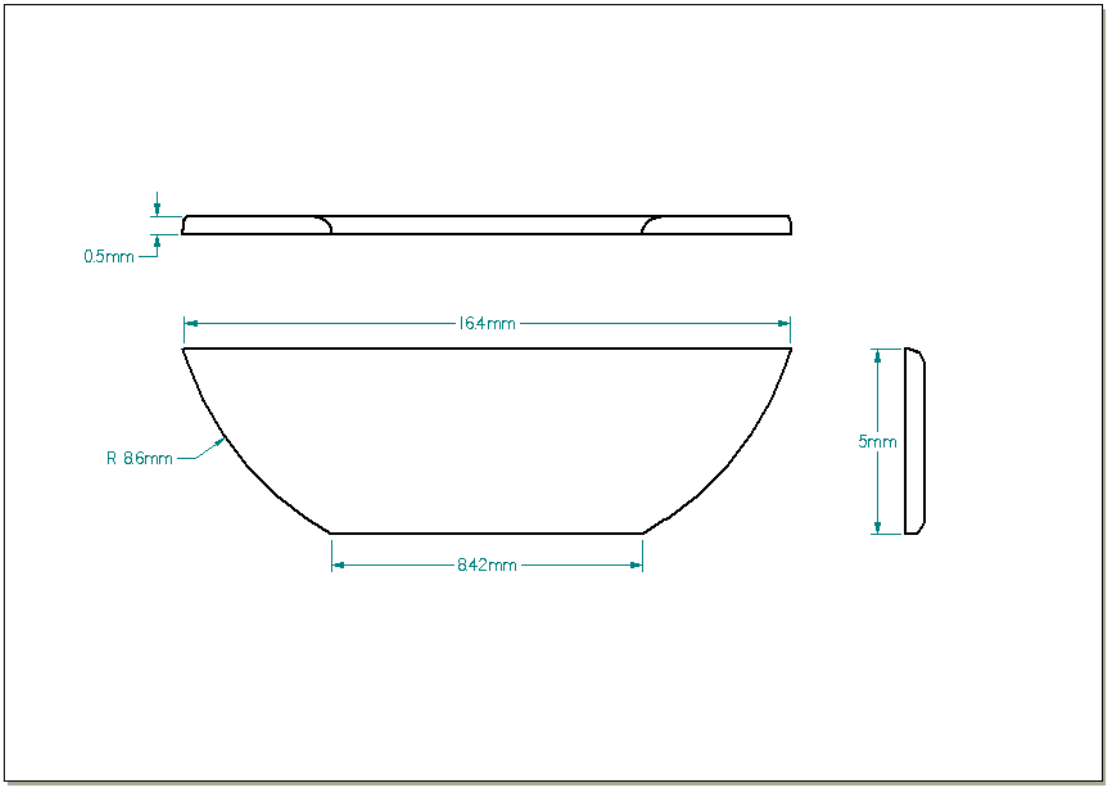

Figure A.1.1: CAD drawing of the No Fins vortex generator design

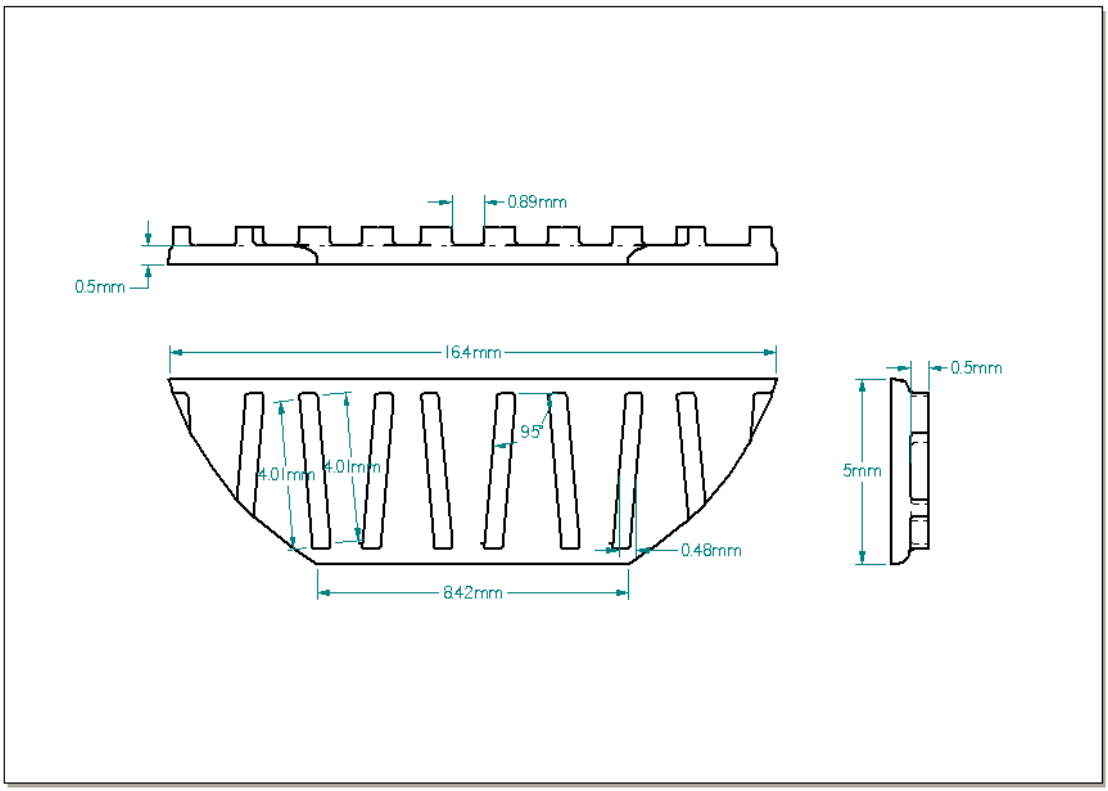

Figure A.1.2: CAD drawing of the R05S vortex generator design

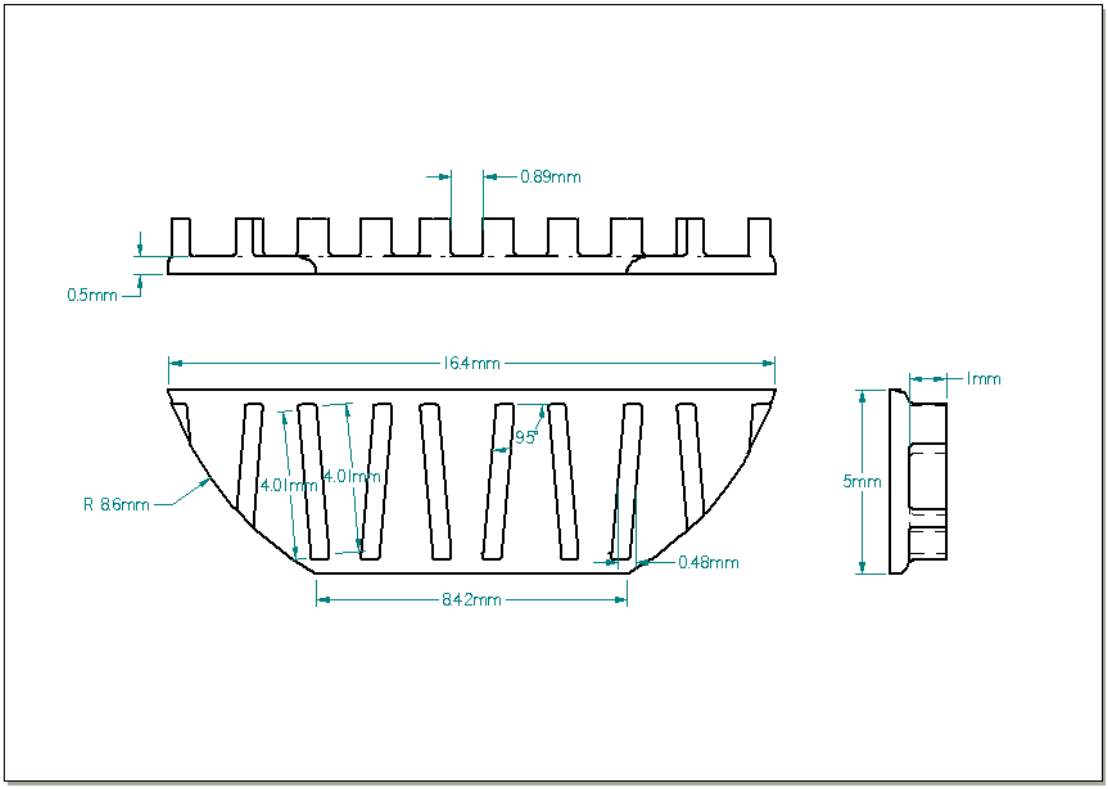

Figure A.1.3: CAD drawing of the R05T vortex generator design

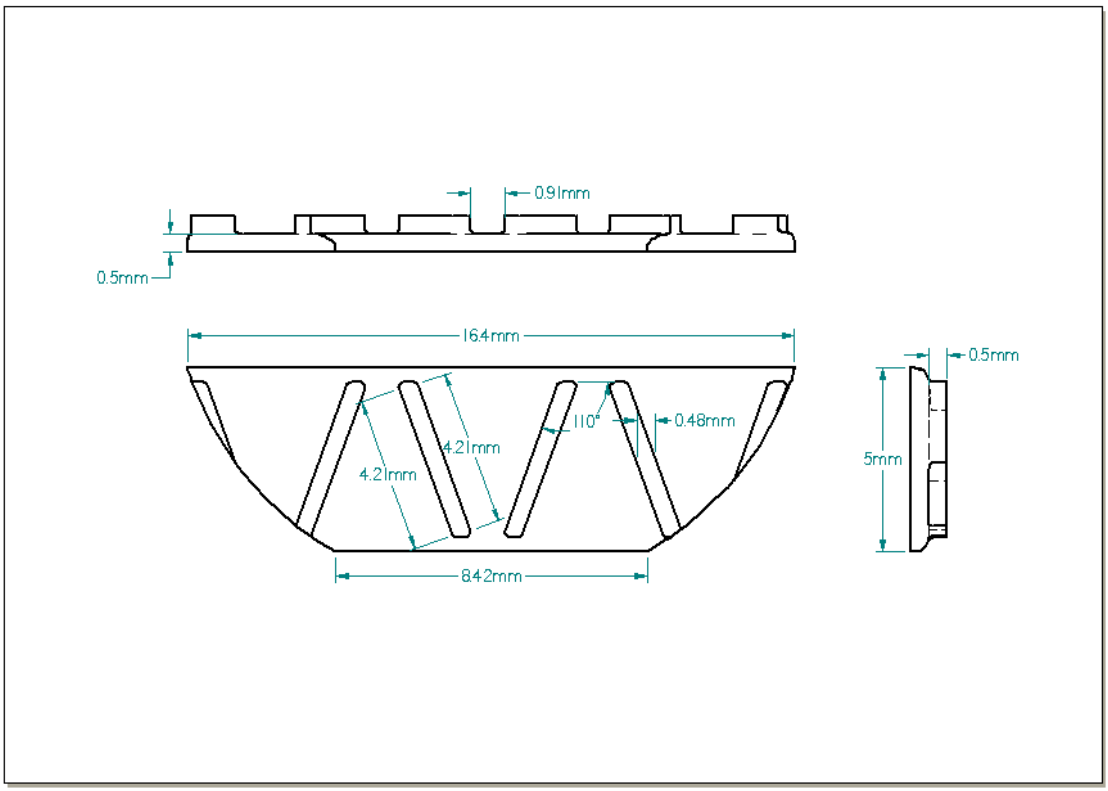

Figure A.1.4: CAD drawing of the R20S vortex generator design

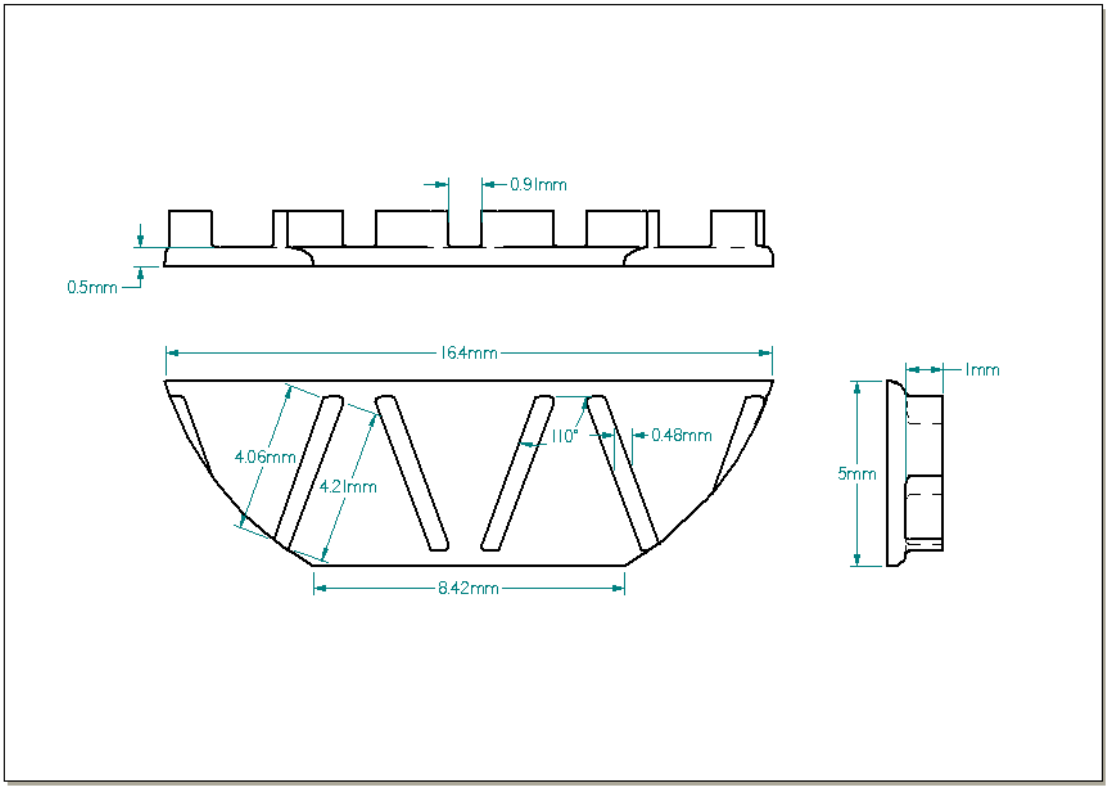

Figure A.1.5: CAD drawing of the R20T vortex generator design

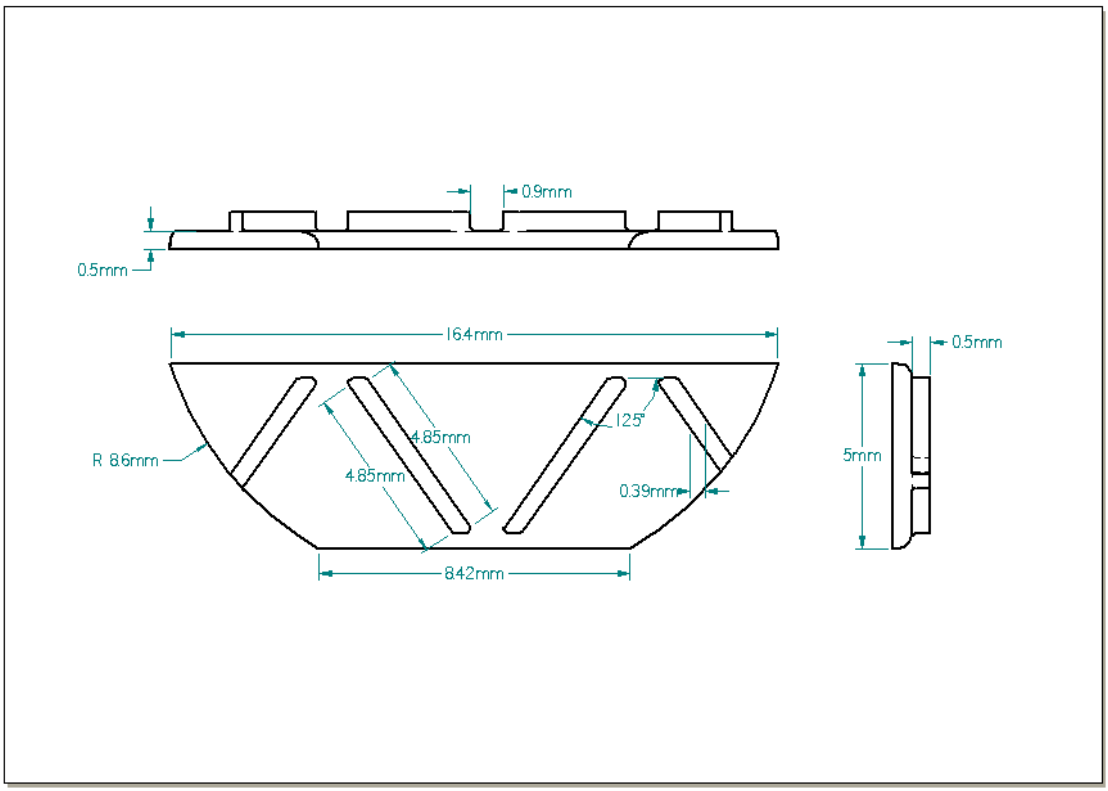

Figure A.1.6: CAD drawing of the R35S vortex generator design

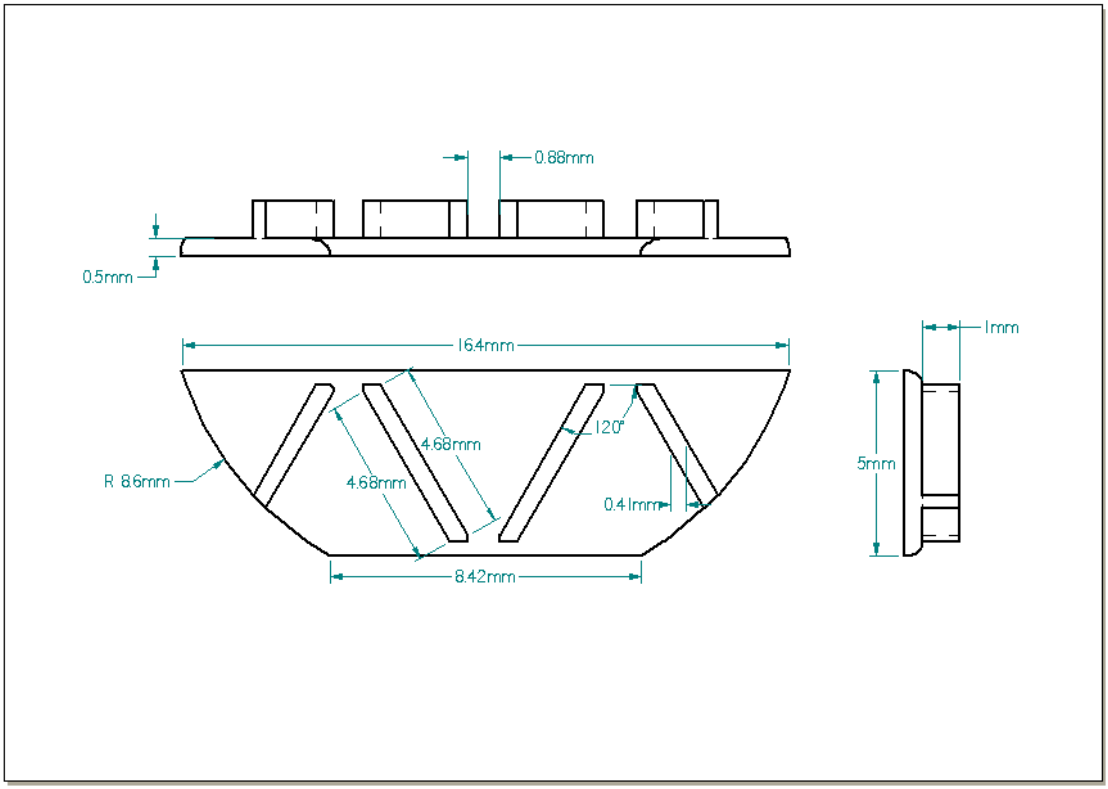

Figure A.1.7: CAD drawing of the R35T vortex generator design

Appendix A.2: Matlab code associated with Binning and cross-correlation analysis

```
%Binning of instantaneous velocity fields
%%%%%%%%%%%%%%%%%%%%%%%%%%%%%%%%%%%%%%%%%%%%%%%%%%%%%%%%%%%%%%%%%%%%%%%%%%%%
 function binninganalysis
 control=load('W:\David\Binning Analysis\Newer Data\control mid
vortstrength - newer.dat')

for i=1:9
    i
    name1=['\B0000' num2str(i)];
    path1=['W:\David\Binning Analysis\Newer Data\VG -
VorticityStrength'];
    path=[path1 name1 '.dat'];
    [h data]=hdrload(path);
    [a b]=size(data);
    strength=[];
    datatoadd=data(1:a,3);
    strength = cat(1,strength,datatoadd);
    strength = nonzeros(strength);
end

for i=10:99
    i
    name1=['\B000' num2str(i)];
    path=[path1 name1 '.dat'];
    [h data]=hdrload(path);
    [a b]=size(data);
    datatoadd=data(1:a,3);
    strength = cat(1,strength,datatoadd);
    strength = nonzeros(strength);
end

for i=101:400
    i
    name1=['\B00' num2str(i)];
    path=[path1 name1 '.dat'];
    [h data]=hdrload(path);
    [a b]=size(data);
    datatoadd=data(1:a,3);
    strength = cat(1,strength,datatoadd);
    strength = nonzeros(strength);
end

%newstrength = nonzeros(strength);
 %strengthoutput = hist(strength, 100)
[n, xout] = hist(strength,control(1:100,1))
%xout = xout'
n=n'
output = [xout n]
 save ('W:\David\Binning Analysis\Newer Data\vg mid vortstrength -
newer.dat', 'output','-ASCII')
Y = cat(2,control(1:100,2),n)
bar(xout,Y,'grouped')
%%%%%%%%%%%%%%%%%%%%%%%%%%%%%%%%%%%%%%%%%%%%%%%%%%%%%%%%%%%%%%%%%%%%%%%%%%%%
```

```
%Cross-correlation code
%%%%%%%%%%%%%%%%%%%%%%%%%%%%%%%%%%%%%%%%%%%%%%%%%%%%%%%%%%%%%%%%%%%%%%%%%%%%
for j=1:9
j  %For each bin
%Determine number of files in each bin
binpath = ['Z:\Correlation\DAT\VG'];
binfolder = ['\Bin' num2str(j) '\*.dat'];
binsizepath = [binpath binfolder];
all_files = dir(binsizepath);
numfiles=size(all_files);
numfiles(1);

%load mean velocity field
    path2=['Z:\Statistics\VG'];
    folder = ['\Bin' num2str(j) '_TimeMeanQF_Vector\B00001.dat'];
    path=[path2 folder];
    [h meann]=hdrload(path);
    [a1 b1]=size(meann);
    for k = 1:a1
        if (abs(meann(k,3)) < .5) && (abs(meann(k,4) < .5))
            meann(k,3) = 0;
            meann(k,4) = 0;
        end
    end
xcor=[];
ycor=[];

%load individual files
for i=1:numfiles(1)
j
i
    path1=['Z:\Correlation\DAT\VG'];
    folder = ['\Bin' num2str(j)];

    if i <= 9
        file=['\B0000' num2str(i)];
    elseif i <= 99
        file=['\B000' num2str(i)];
    elseif i<= 999
        file=['\B00' num2str(i)];
    else
        file=['\B0' num2str(i)];
    end

    path=[path1 folder file '.dat'];
    [h inst]=hdrload(path);
    [a2 b2]=size(inst);

    for m = 1:a2
        if (abs(inst(m,3)) < .5) && (abs(inst(m,4) < .5))
            inst(m,3) = 0;
            inst(m,4) = 0;
        end
    end

%Do cross-correlation
```

```
  xr = corrcoef(meann(:,3),inst(:,3))
  yr = corrcoef(meann(:,4),inst(:,4))
  xcor(i) = (xr(1,2));
  ycor(i) = (yr(1,2));
  end

n=[1:numfiles(1)]';
xycor = [n xcor' ycor'];
savepath = ['Z:\Correlation\Output1\VG'];
savefile = ['\Bin' num2str(j) '.dat'];
savepath1 = [savepath savefile];
save (savepath1, 'xycor', '-ASCII')
  end
%%%%%%%%%%%%%%%%%%%%%%%%%%%%%%%%%%%%%%%%%%%%%%%%%%%%%%%%%%%%%%%%%%%%%%%%%%%%%%%
```

Characterization of clot deposition on mechanical heart valves

Principal Investigator David Murphy_

Purpose of the Research

You are being asked to volunteer for a research project in which your blood will be used to identify and characterize the areas in which clots are initiated in mechanical heart valves (MHVs). To accomplish this goal blood will be run through either a steady flow loop or a pulsatile flow loop in which a MHV has been inserted. The steady flow loop will test clot deposition on MHVs during the leakage phase of the cardiac cycle, in which blood is forced back through the MHV. The pulsatile flow loop will approximate the physiologic conditions that blood is exposed to during the cardiac cycle. For both of these flow conditions, different MHVs will be used to demonstrate differences in clot magnitude depending upon different leakage tolerances through the valves or different hinge geometries.

Approximately 30 subjects will be used on a rotating basis to ensure a good donor base from which to draw. Approved subjects will be healthy, over the age of 17 and weigh at least 110 pounds.

Procedures

The amount of blood needed for each flow loop is 155 ml for the steady loop and 550 ml for the pulsatile loop. Blood will be drawn by a trained individual, and certification for any person drawing 550 ml will be assured. Subjects donating 155 ml will be allowed to give once a month, and subjects donating 550 ml will be allowed to give once every two months.

Foreseeable Risks or Discomforts

Foreseeable risks or discomforts may be bruising caused by the insertion of the needle or drawing of the blood and illness such as lightheadedness or fainting. At the onset of such illness, blood drawing will be stopped immediately and care given.

Benefits

There is no proven benefit to the subject by having blood drawn. Potential benefit to society is a better understanding of how MHV hinge design affects clot deposition so that they can be designed to minimize this complication.

Compensation

Payment for the blood will be $15.00 for 155 ml and $50.00 for 550 ml.

Figure A.3a: Consent form for *in vitro* blood experiments (front side)

Confidentiality

All information concerning you will be kept private. Privacy will be ensured with a code used to identify subjects to which the key will be kept in a secure, password-protected computer.

Injury/Adverse Reactions

Reports of injury or reaction should be made to David Murphy at 205-746-9135. Neither Georgia Institute of Technology nor the principal investigator has made provisions for payment of cost associated with any injury resulting from participation in this study.

Contact Persons

If you have questions about the research, call or write David Murphy at 205-746-9135 or 315 Ferst Drive, Room 2119, Atlanta, GA 30332.

Voluntary Participation/Withdrawal

You have rights as a research volunteer. Taking part in this study is completely voluntary. If you do not take part, you will have no penalty. You may stop taking part in this study at any time with no penalty. If you have questions about your rights as a research volunteer, call or write:

Office of Research Compliance
Georgia Institute of Technology
Atlanta, GA 30332-0420
Voice (404) 894-6944 Fax (404) 385-0864

Signatures

A copy of this form will be given to you.

Your signature below indicates that the researchers have answered all of your questions to your satisfaction and that you consent to volunteer for this study.

Subject's Signature: _____ Date: _____

Person Obtaining Consent – Signature: _____ Date:_____

Figure A.3b: Consent form for *in vitro* blood experiments (back side)

APPENDIX B

BLOOD RESULTS

Table B.1.1: Original TAT concentrations (in ug/L) from the in vitro blood experiments

Original Data

	Control	Time Point				
Control	**Date**	**0**	**15**	**30**	**45**	**60**
	7/2/07a		6.40	7.60	7.24	5.16
	7/2/07b	3.41	6.49	6.54	6.62	6.11
	7/3/07	3.51	4.57	4.30	3.87	5.18
	7/5/07	6.33	6.76	7.46	10.22	7.88
	7/11/07	2.49	2.16	2.83	2.91	4.20
	7/10/07	8.44	7.67	9.23	7.66	6.68
	7/16/07	3.02	2.89	3.49	2.74	3.29
	7/30/07	3.65	3.40	6.69	6.20	6.13
	Average	4.00	5.04	6.02	5.93	5.58
	Std Dev	1.81	2.06	2.24	2.60	1.44

	Rect VG	Time Point				
R20T VG	**Date**	**0**	**15**	**30**	**45**	**60**
	7-3-07a	2.30	3.08	4.70	5.91	6.46
	7/5/07	4.08	4.68	4.23	5.02	4.07
	7/6/07	2.58	3.48	3.10	3.76	3.41
	7-9-07a	5.28	4.05	5.39	5.53	5.27
	7-9-07b	2.18	2.76	3.56	2.61	2.89
	7/10/07	4.77	4.30	3.28	3.36	4.45
	Average	4.00	3.73	4.04	4.37	4.43
	Std Dev	1.81	0.75	0.89	1.31	1.29

Table B.1.2: TAT concentrations (in ug/L) from the in vitro blood experiments adjusted for the initial dilution by saline

Removal of "Outliers" - adjusted for initial dilution

	Control	Time Point				
Control	**Date**	**0**	**15**	**30**	**45**	**60**
	7/2/07a	-	6.98	8.29	7.90	5.62
	7/2/07b	3.71	7.08	7.14	7.22	6.66
	7/3/07	3.83	4.98	4.69	4.23	5.65
	7/5/07	6.55	6.99	7.72	10.57	8.15
	7/11/07	2.64	2.28	2.99	3.08	4.44
	7/10/07	8.94	8.12	9.78	8.12	7.08
	7/16/07	3.12	2.99	3.61	2.83	3.40
	7/30/07	3.81	3.55	6.98	6.47	6.39
	Average	4.66	5.37	6.40	6.30	5.93
	Std Dev	2.26	2.22	2.39	2.72	1.50

	Rect VG	Time Point				
R20T VG	**Date**	**0**	**15**	**30**	**45**	**60**
	7-3-07a	2.51	3.36	5.13	6.45	7.05
	7/5/07	4.45	5.11	4.61	5.47	4.44
	7/6/07	2.78	3.75	3.35	4.05	3.68
	7-9-07a	5.32	4.09	5.43	5.58	5.32
	7-9-07b	2.21	2.79	3.60	2.64	2.92
	7/10/07	5.20	4.69	3.58	3.67	4.85
	Average	3.75	3.97	4.28	4.64	4.71
	Std Dev	1.41	0.86	0.89	1.42	1.43

Table B.1.3: TAT concentrations (in ug/L) from the in vitro blood experiments adjusted for the initial dilution by saline and dilution throughout the experiment.

Removal of "Outliers" - adjusted for initial and sample dilution

	Control	**Time Point**				
Control	**Date**	**0**	**15**	**30**	**45**	**60**
	7/2/07a		7.01	8.37	8.01	5.73
	7/2/07b	3.71	7.11	7.20	7.32	6.78
	7/3/07	3.83	5.01	4.73	4.28	5.76
	7/5/07	6.55	7.02	7.79	10.71	8.30
	7/11/07	2.64	2.29	3.02	3.12	4.52
	7/10/07	8.94	8.16	9.86	8.23	7.20
	7/16/07	3.12	3.00	3.64	2.87	3.46
	7/30/07	3.81	3.56	7.04	6.55	6.51
	Average	4.66	5.39	6.46	6.39	6.03
	Std Dev	2.26	2.23	2.41	2.75	1.53

	Rect VG	**Time Point**				
R20T VG	**Date**	**0**	**15**	**30**	**45**	**60**
	7-3-07a	2.51	3.38	5.18	6.54	7.18
	7/5/07	4.45	5.13	4.65	5.55	4.52
	7/6/07	2.78	3.77	3.38	4.11	3.74
	7-9-07a	5.32	4.11	5.48	5.66	5.41
	7-9-07b	2.21	2.80	3.63	2.67	2.98
	7/10/07	5.20	4.71	3.61	3.72	4.94
	Average	3.75	3.98	4.32	4.71	4.79
	Std Dev	1.41	0.86	0.90	1.44	1.45

APPENDIX C

FURTHER STEADY RESULTS

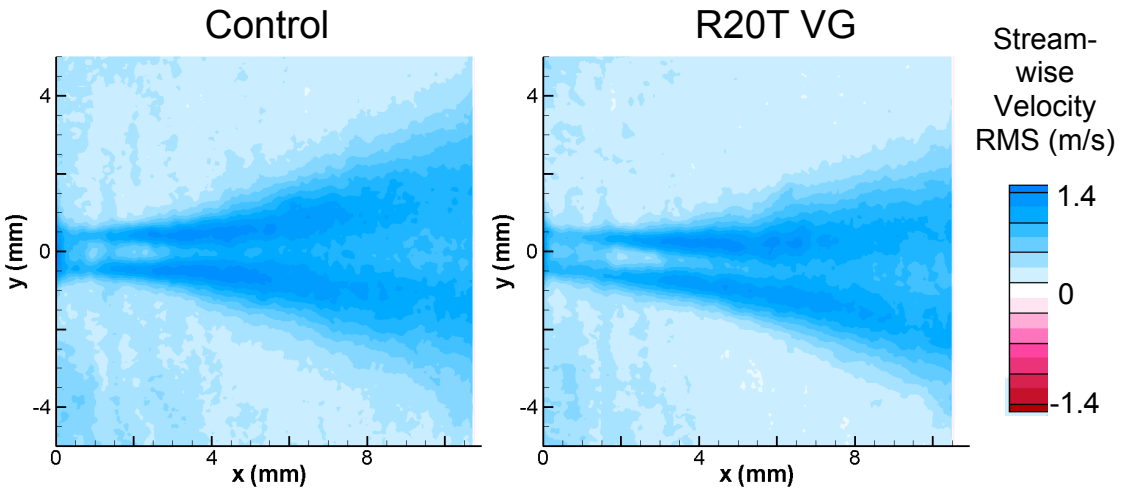

Figure C.1.1: Streamwise velocity RMS of small-scale jet

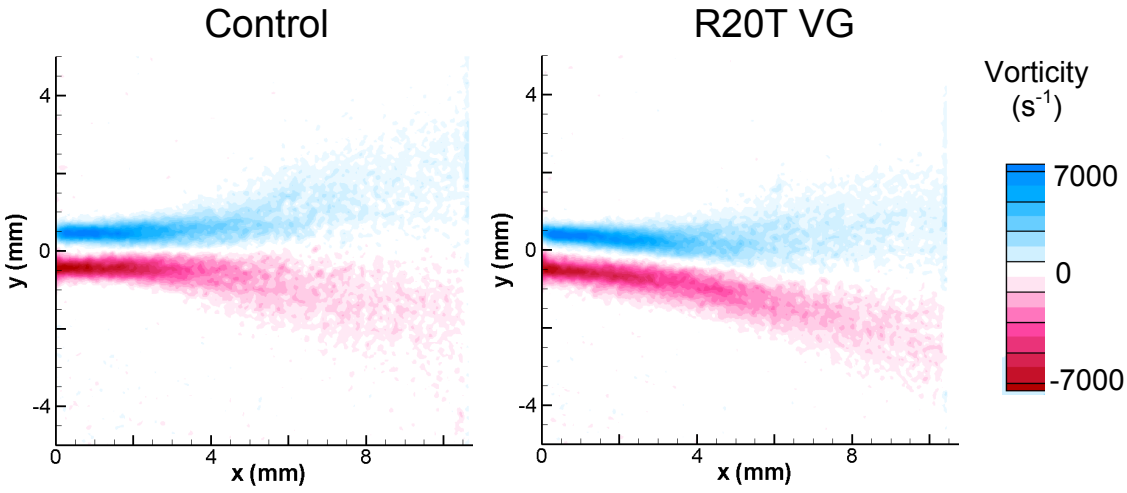

Figure C.1.2: Mean vorticity of small-scale jet

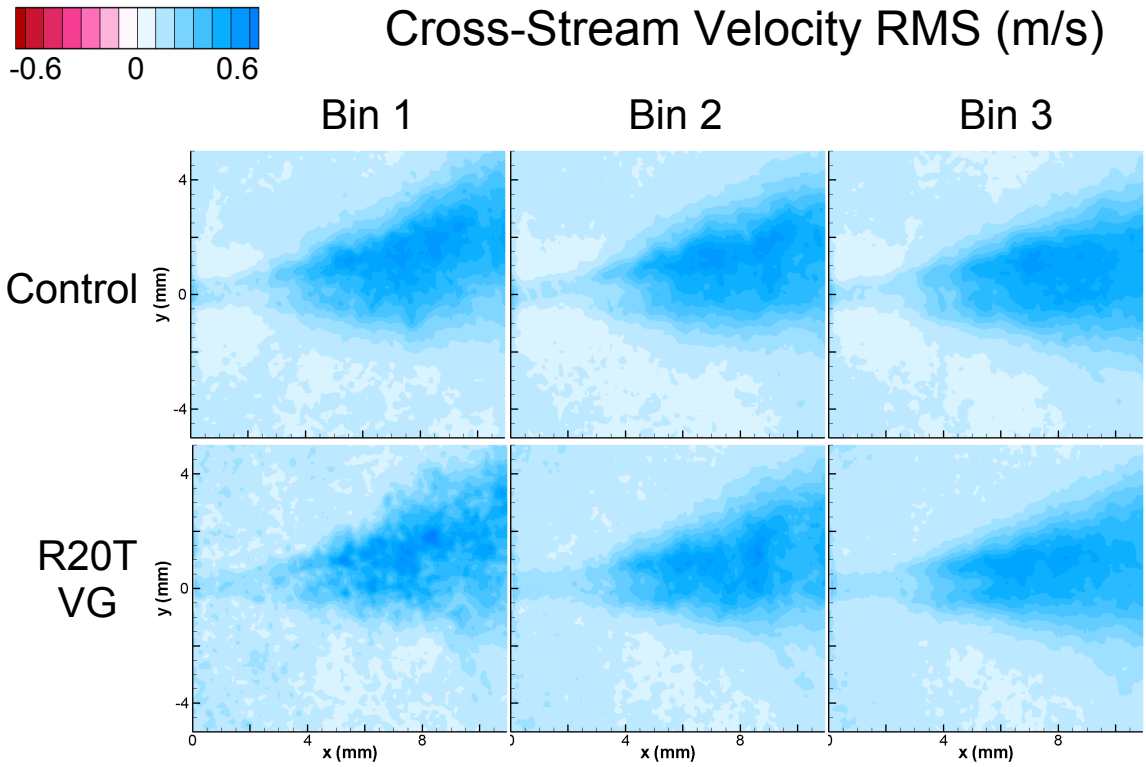

Figure C.2.1a: Cross-stream velocity RMS of small-scale jet

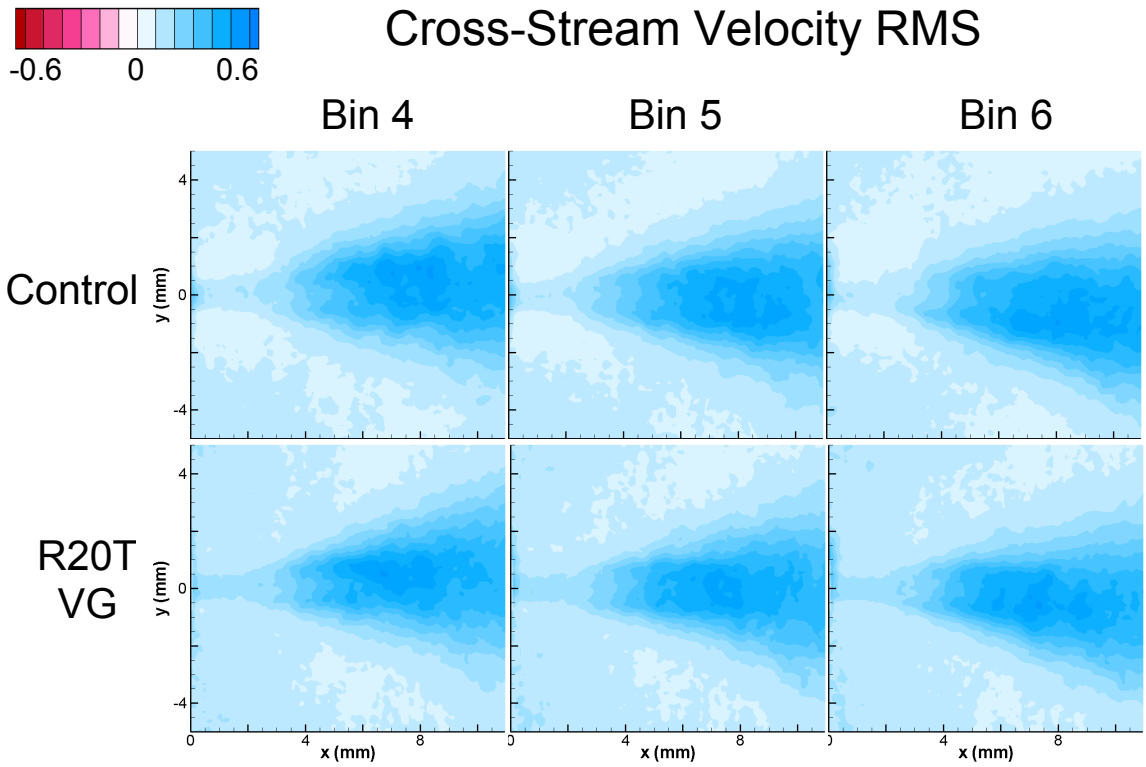

Figure C.2.1b: Cross-stream velocity RMS of small-scale jet

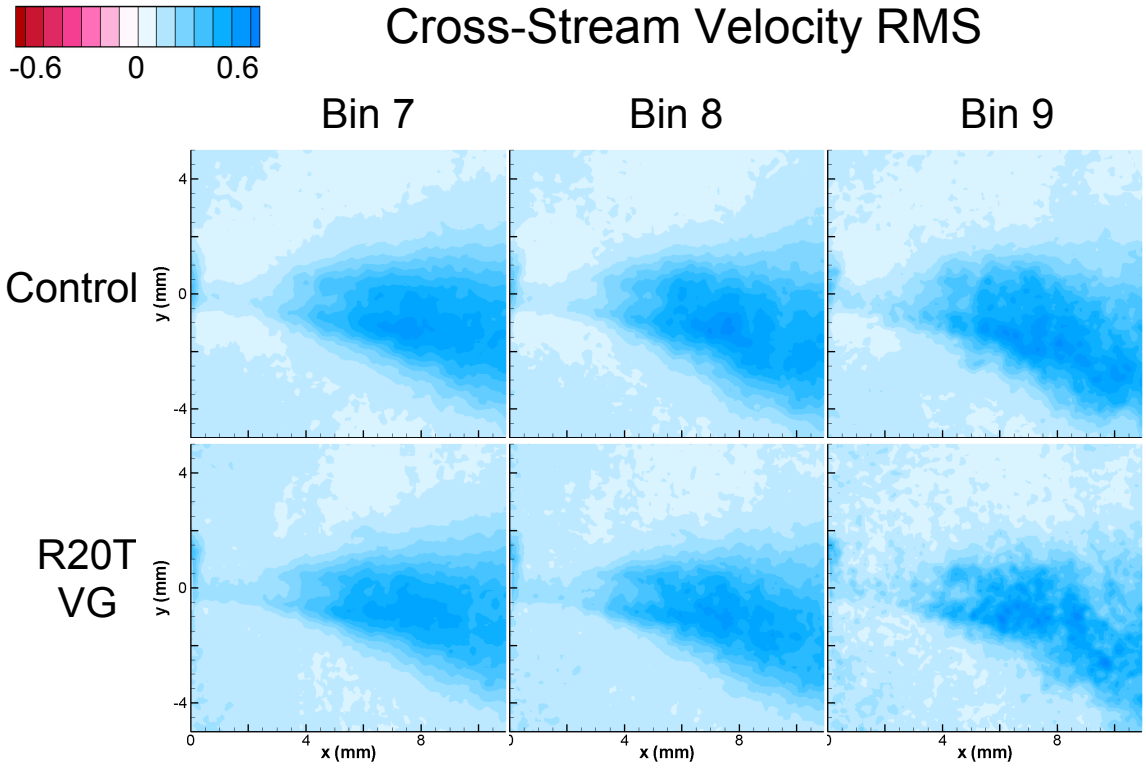

Figure C.2.1c: Cross-stream velocity RMS of small-scale jet

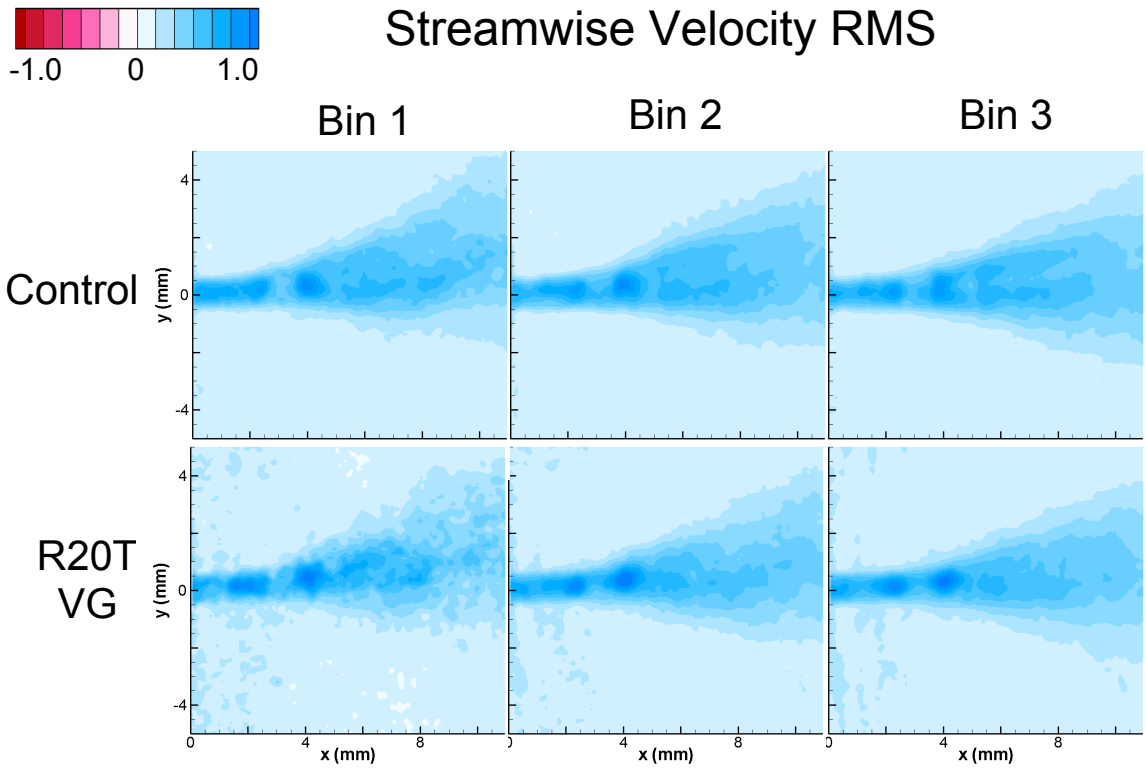

Figure C.2.2a: Streamwise velocity RMS of small-scale jet

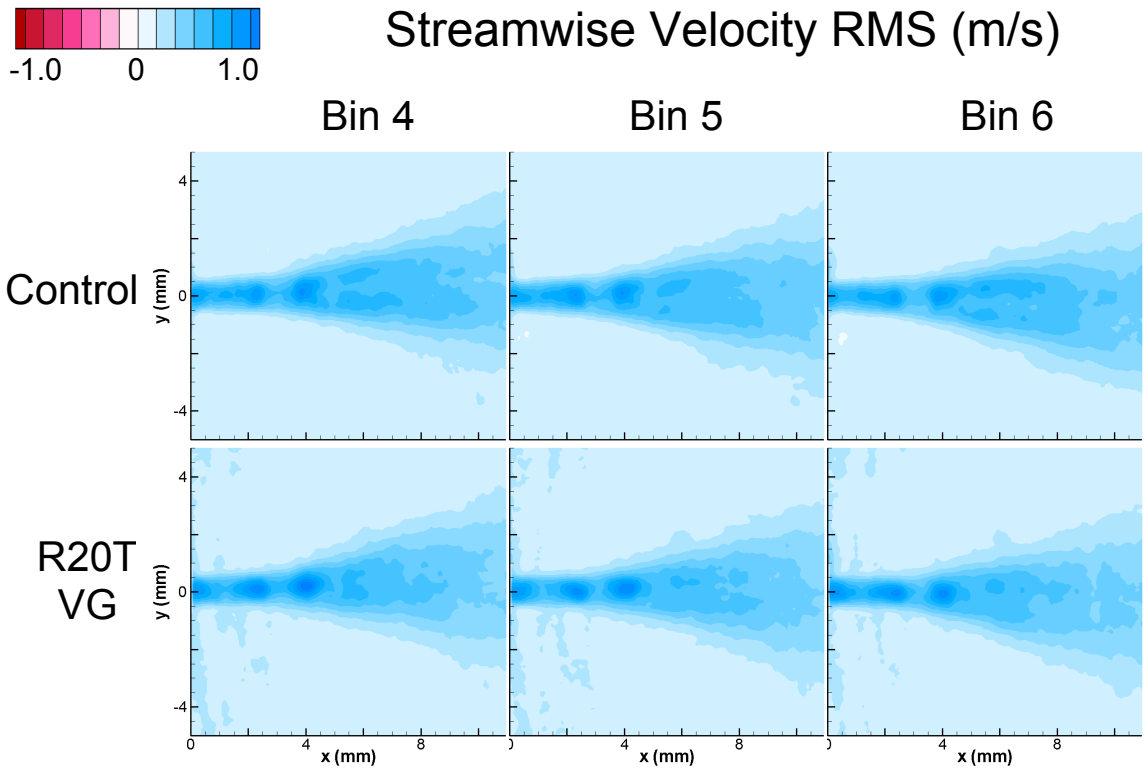

Figure C.2.2b: Streamwise velocity RMS of small-scale jet

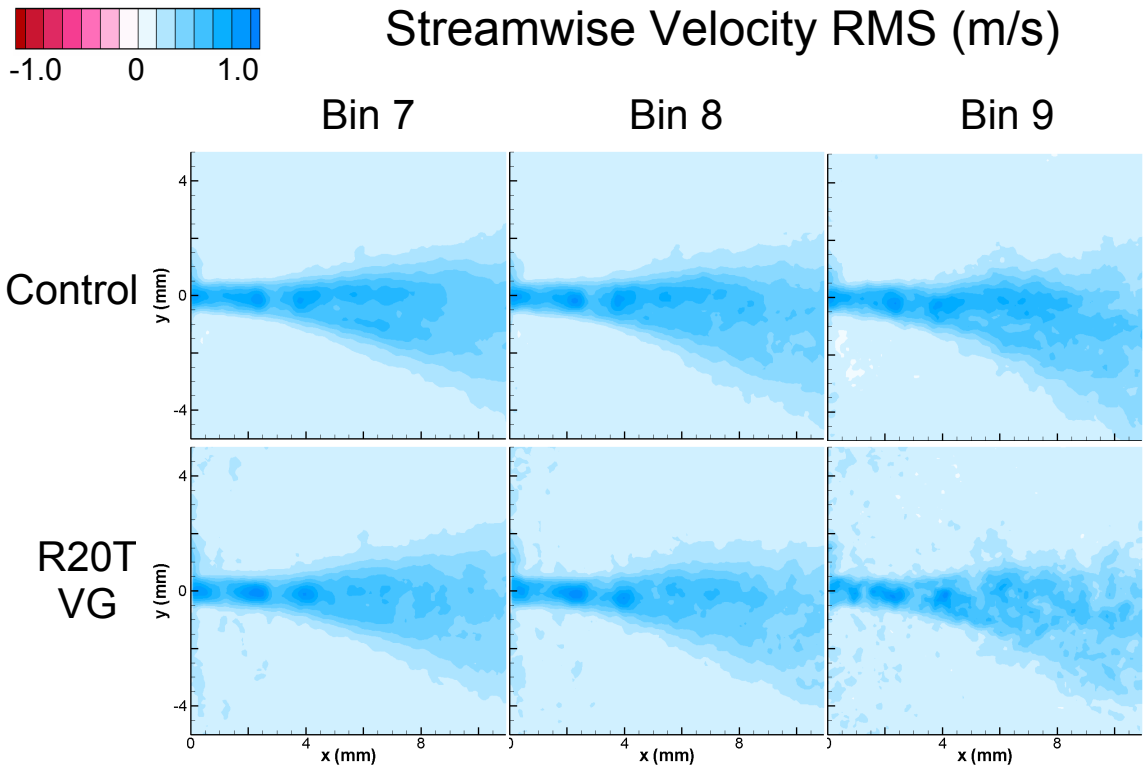

Figure C.2.2c: Streamwise velocity RMS of small-scale jet

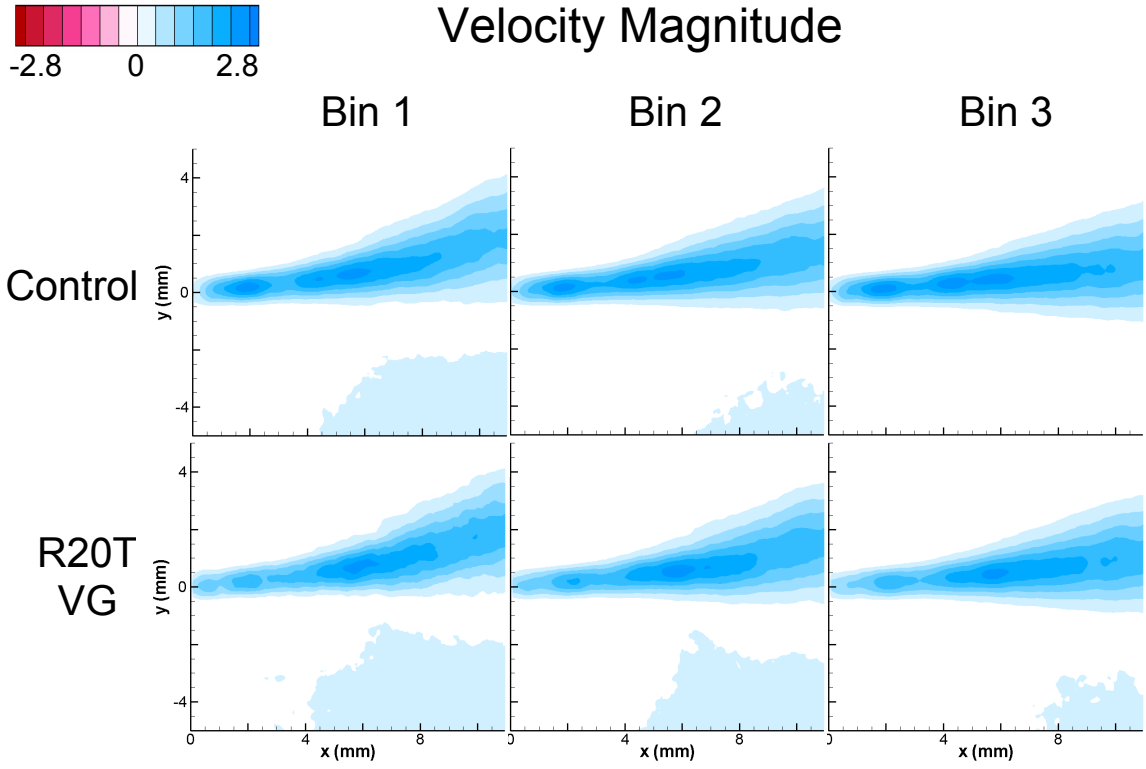

Figure C.2.3a: Velocity magnitude of small-scale jet

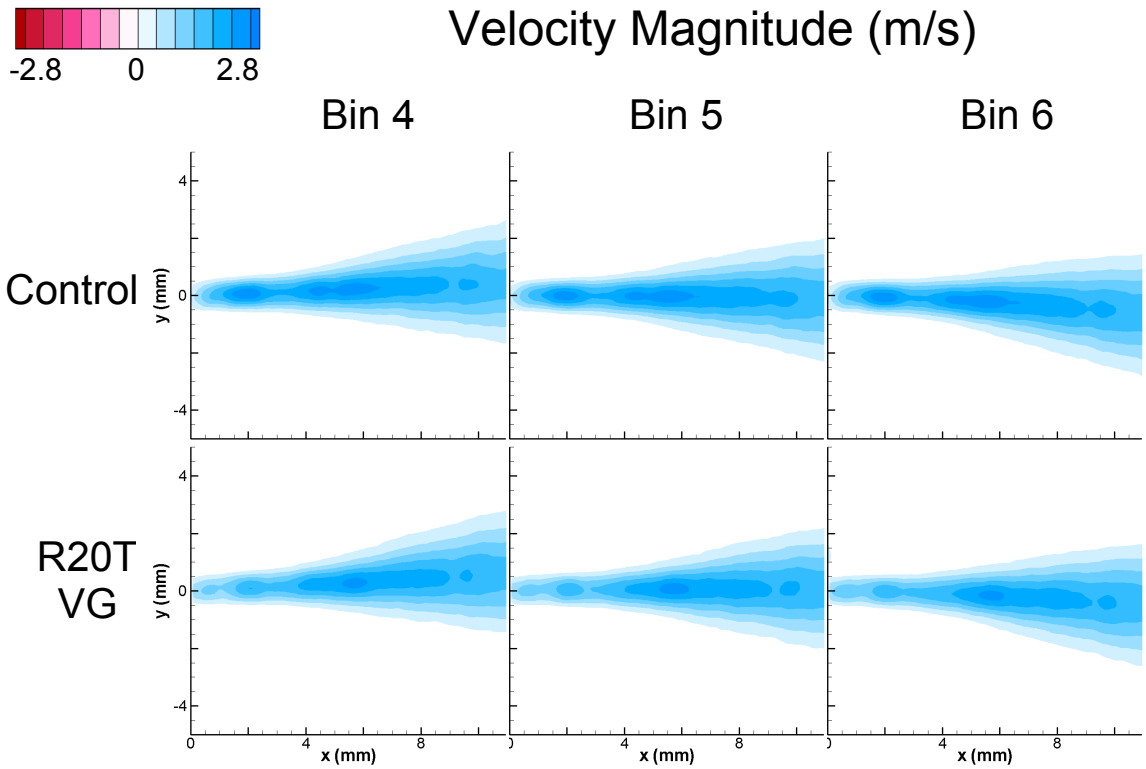

Figure C.2.3b: Velocity magnitude of small-scale jet

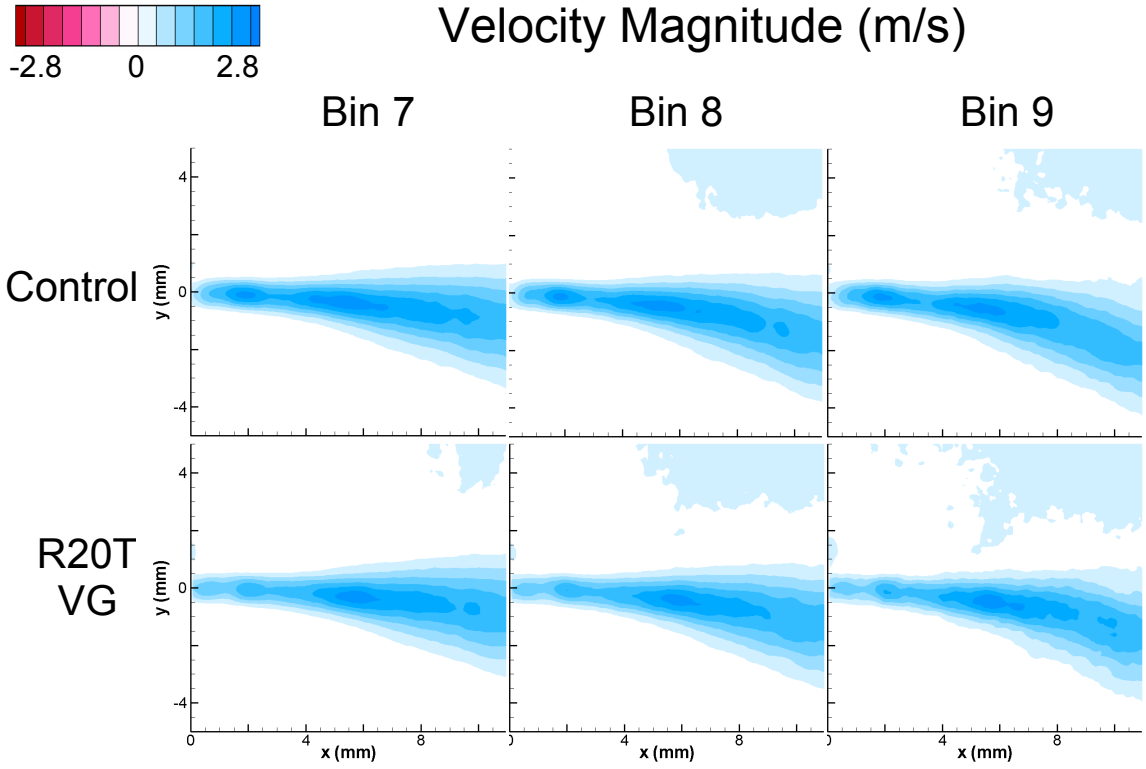

Figure C.2.3c: Velocity magnitude of small-scale jet

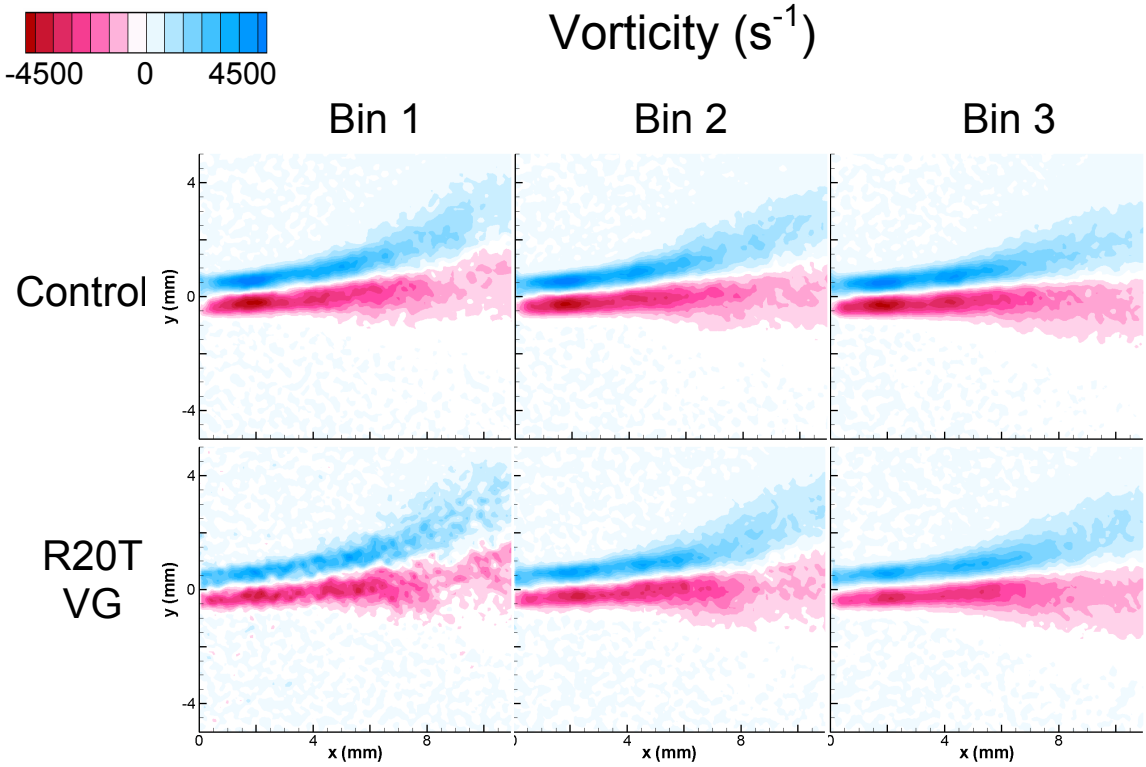

Figure C.2.4a: Mean vorticity of small-scale jet

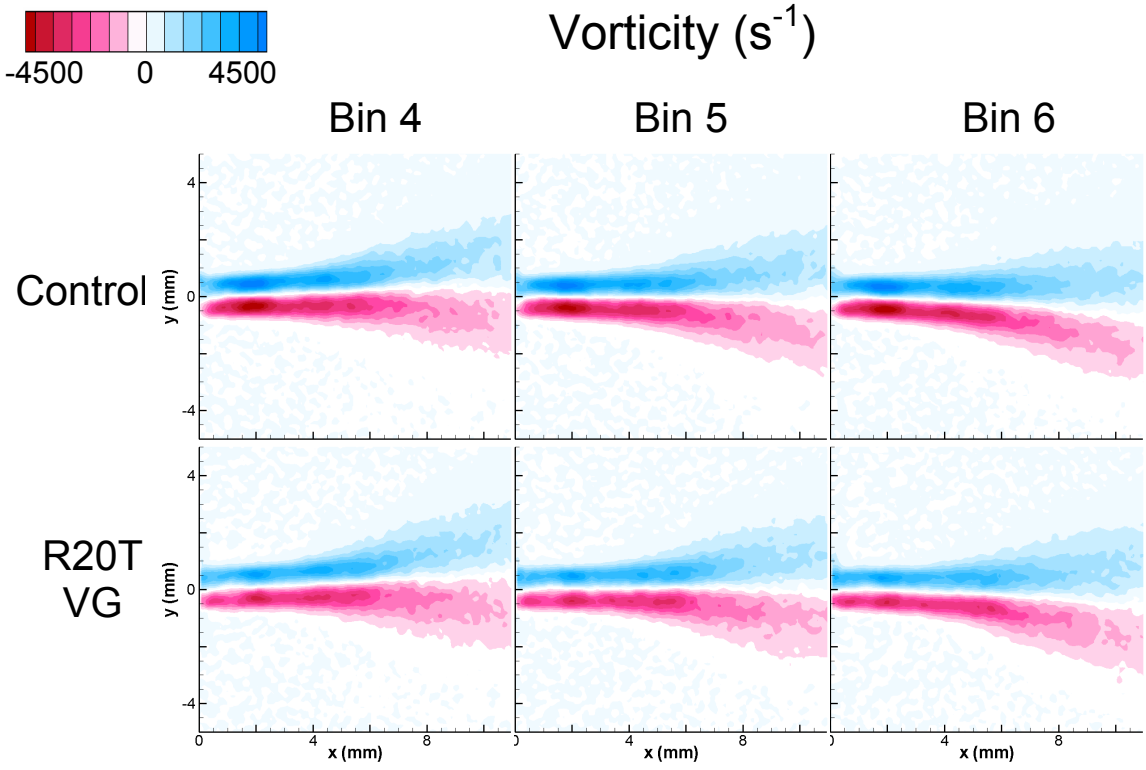

Figure C.2.4b: Mean vorticity of small-scale jet

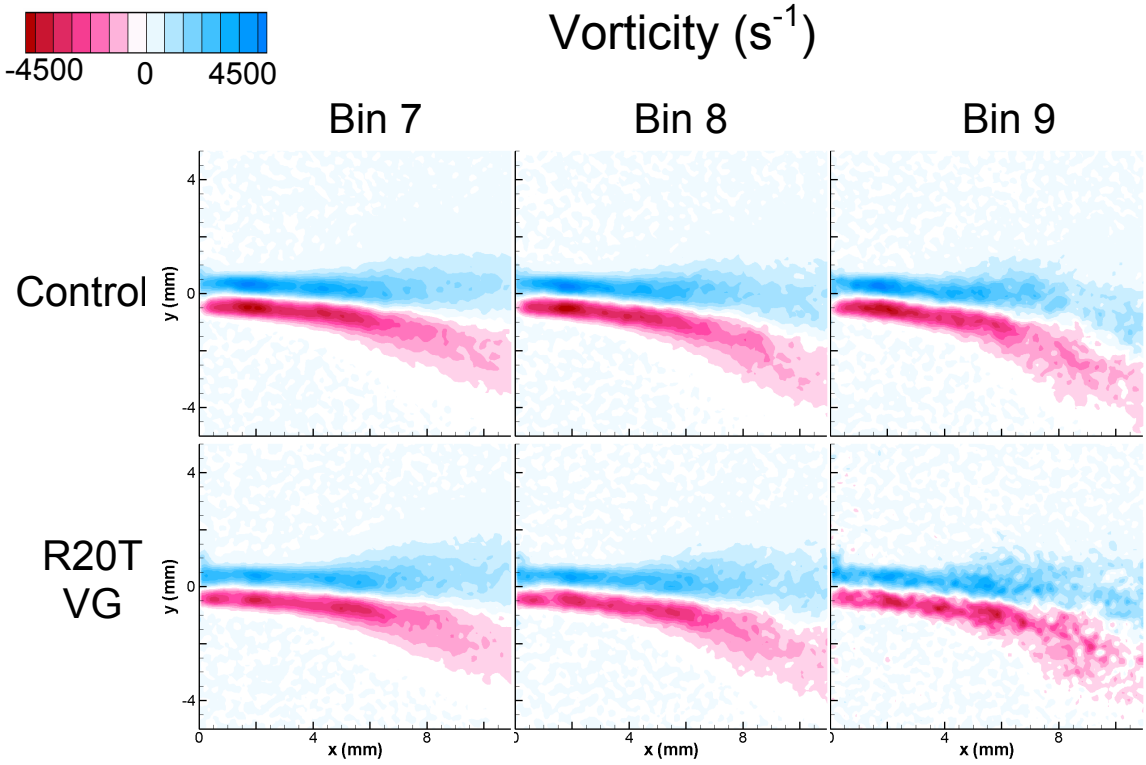

Figure C.2.4c: Mean vorticity of small-scale jet

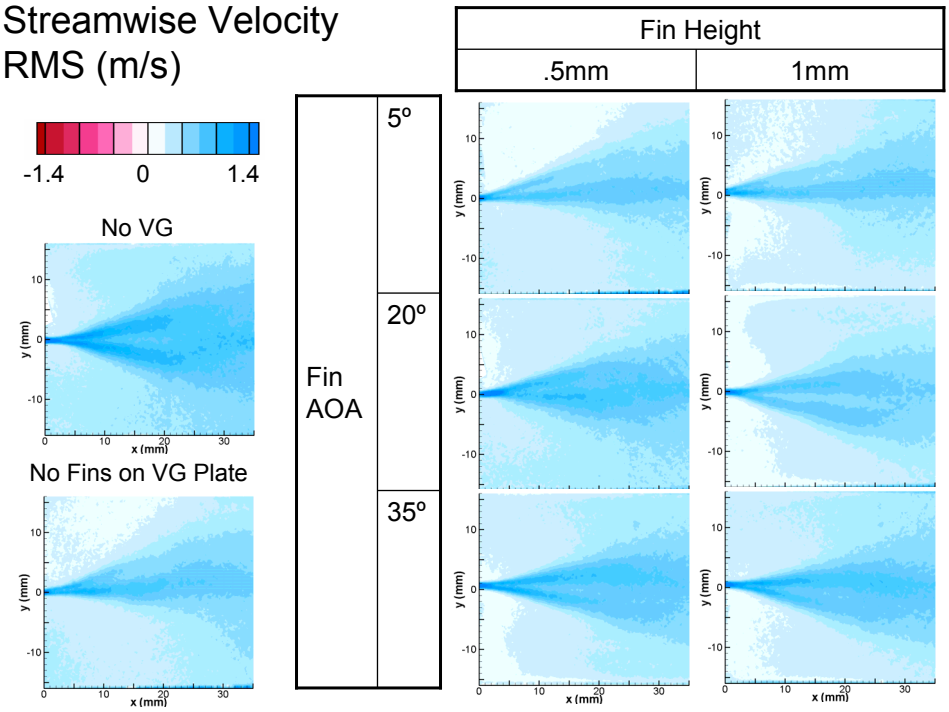

Figure C.3.1: Streamwise velocity RMS of large-scale jet in all bins

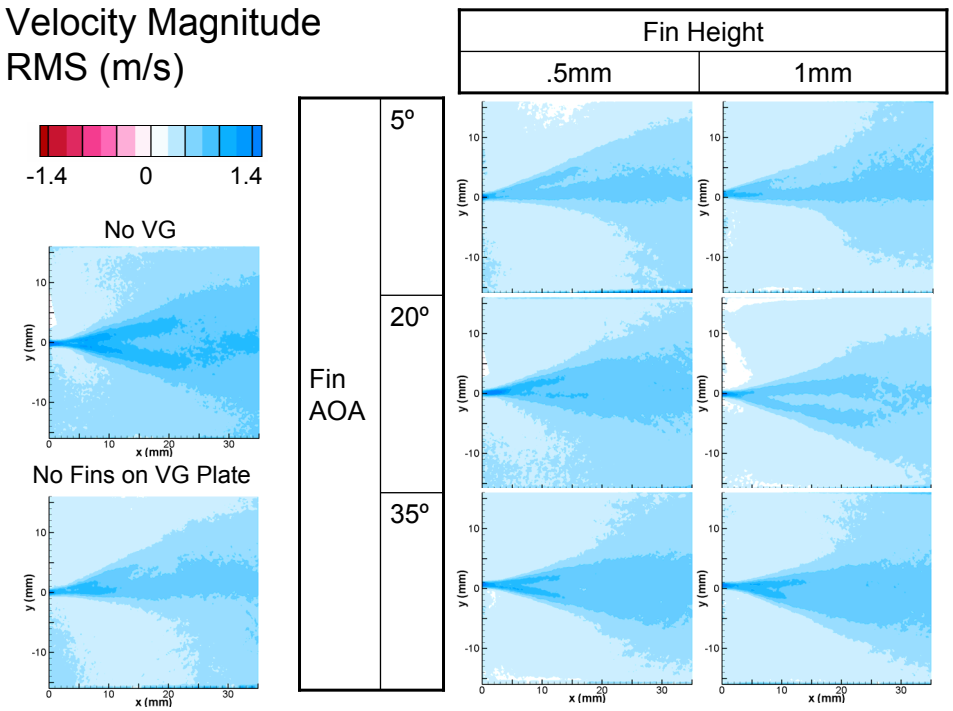

Figure C.3.2: Mean velocity magnitude of large-scale jet in all bins

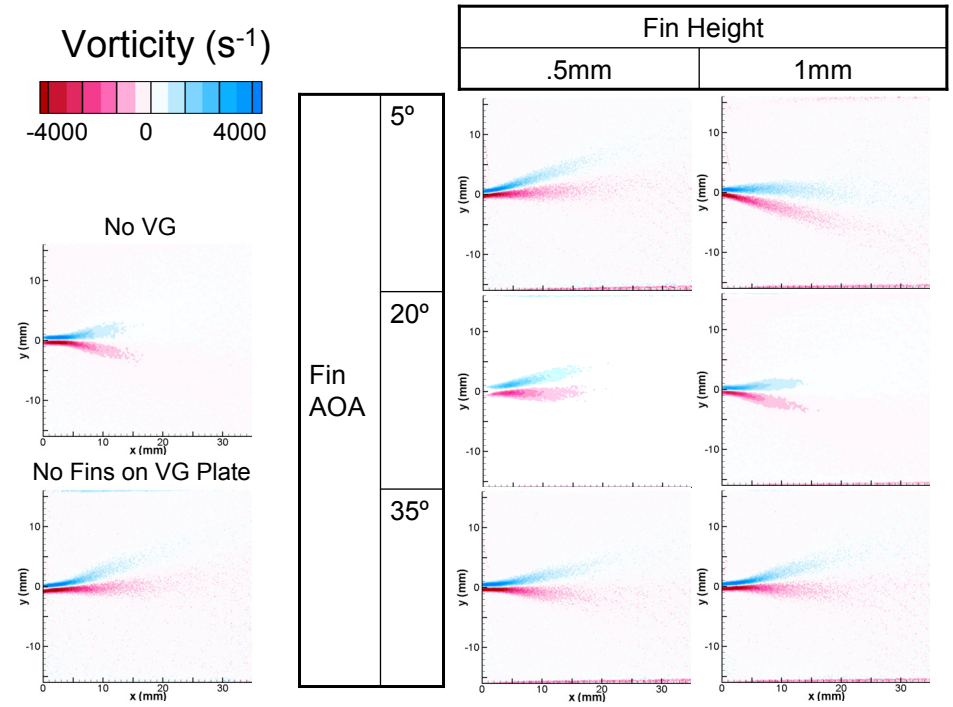

Figure C.3.3: Mean vorticity of large-scale jet in all bins

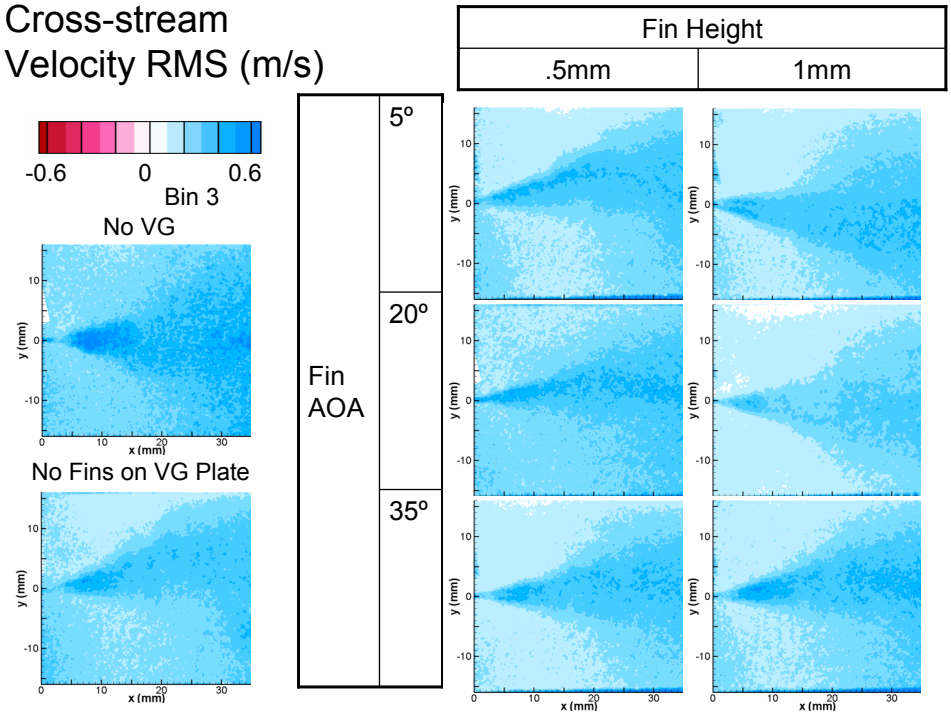

Figure C.3.4: Cross-stream velocity RMS of large-scale jet in Bin 3

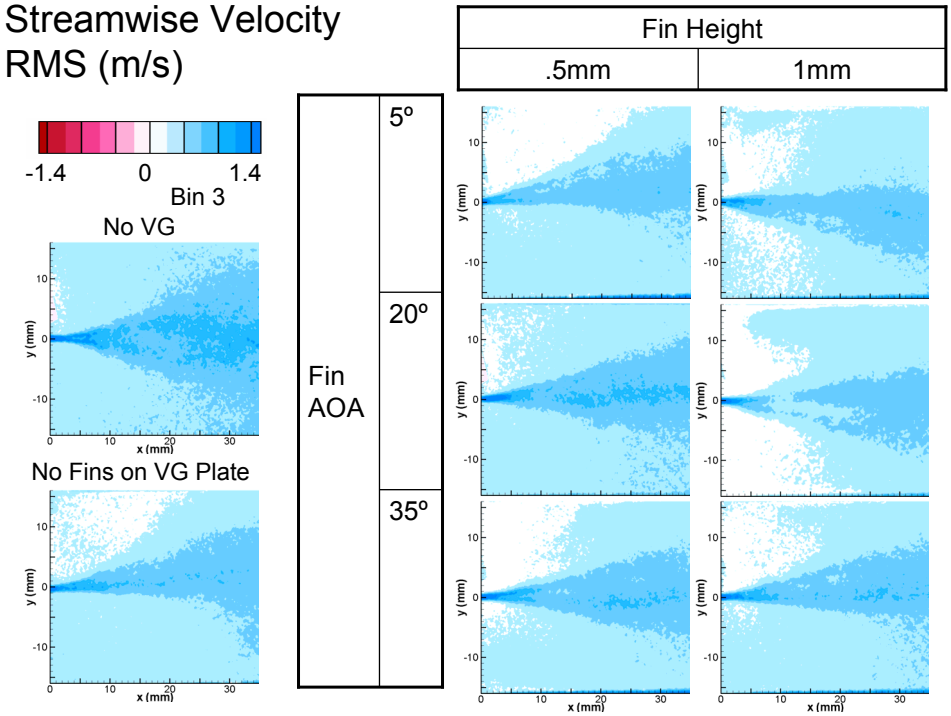

Figure C.3.5: Streamwise velocity RMS of large-scale jet in Bin 3

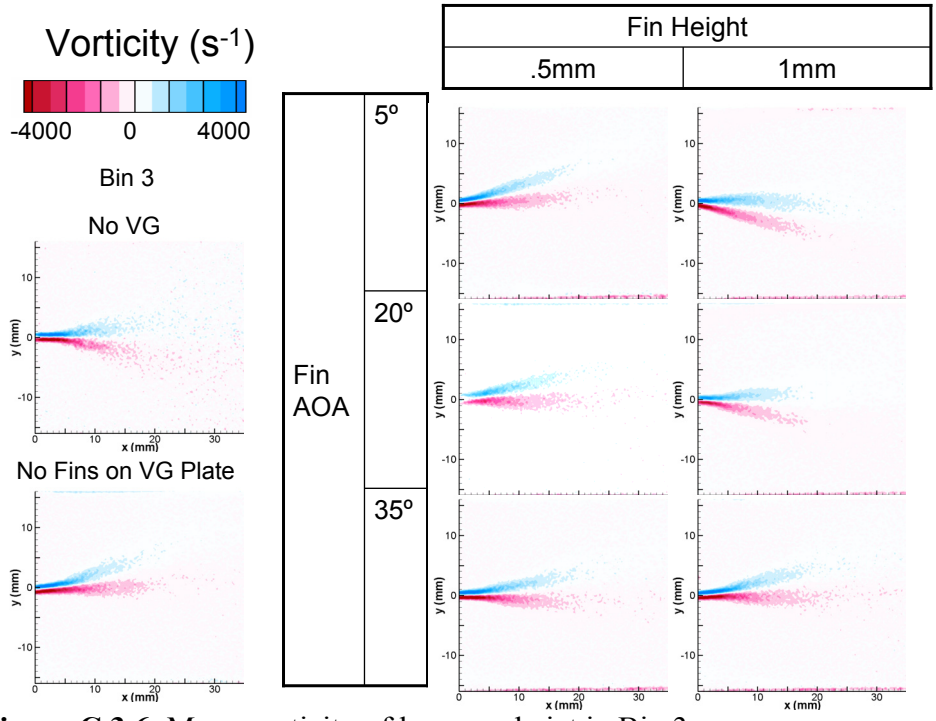

Figure C.3.6: Mean vorticity of large-scale jet in Bin 3

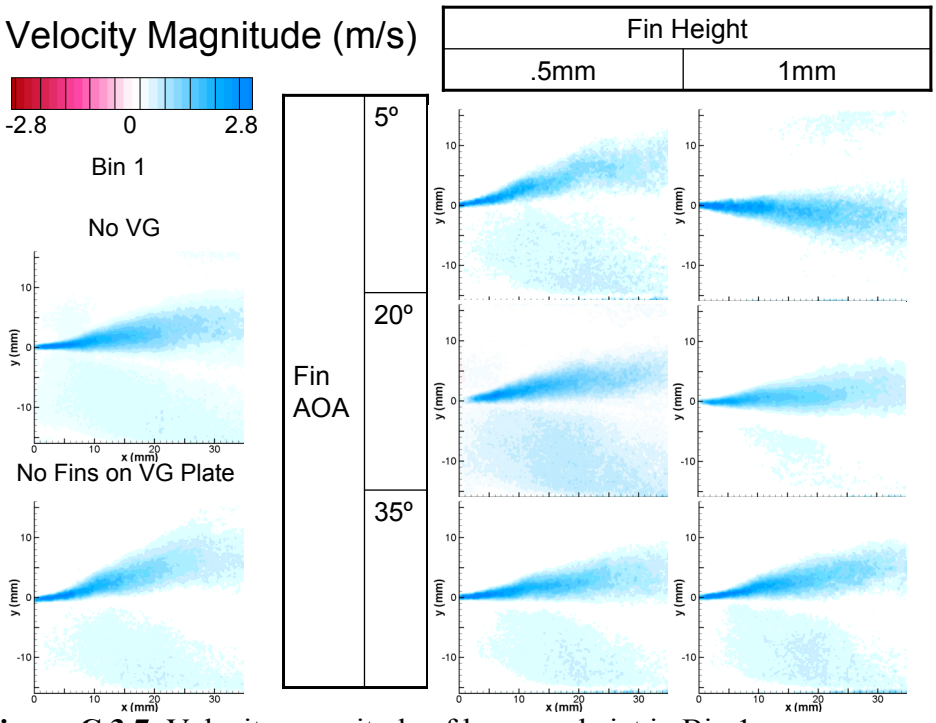

Figure C.3.7: Velocity magnitude of large-scale jet in Bin 1

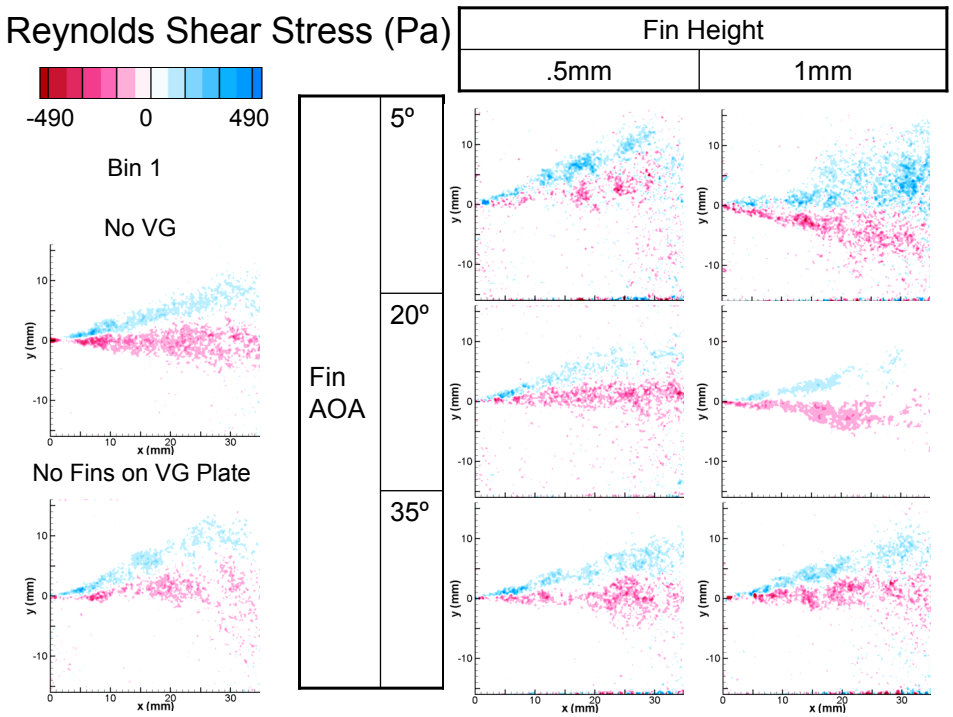

Figure C.3.9: Reynolds shear stress of large-scale jet in Bin 1

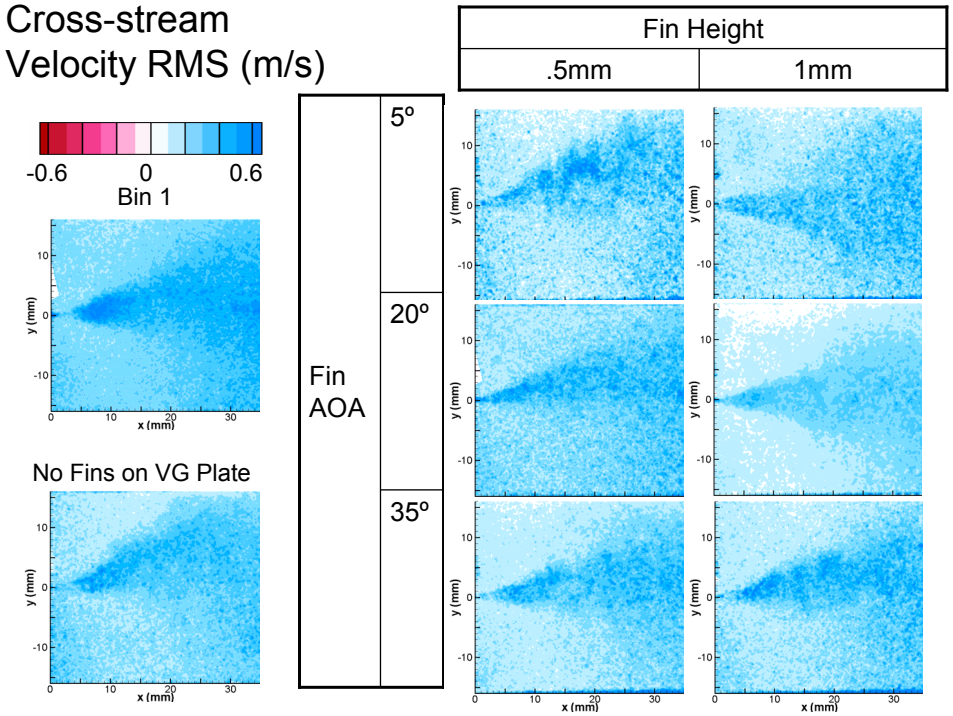

Figure C.3.10: Cross-stream velocity RMS of large-scale jet in Bin 1

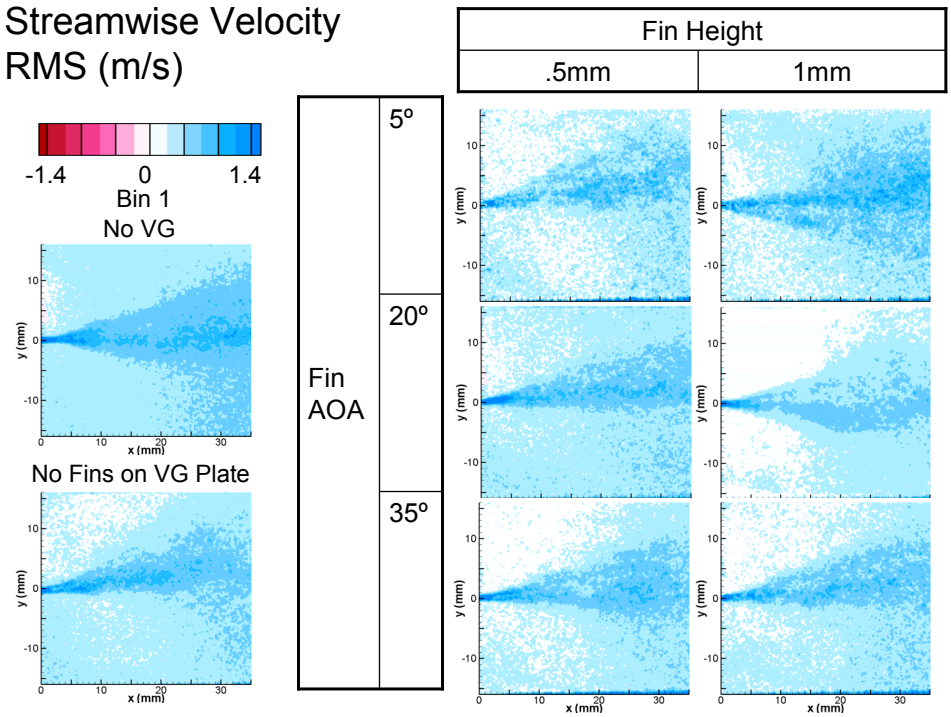

Figure C.3.11: Streamwise velocity RMS of large-scale jet in Bin 1

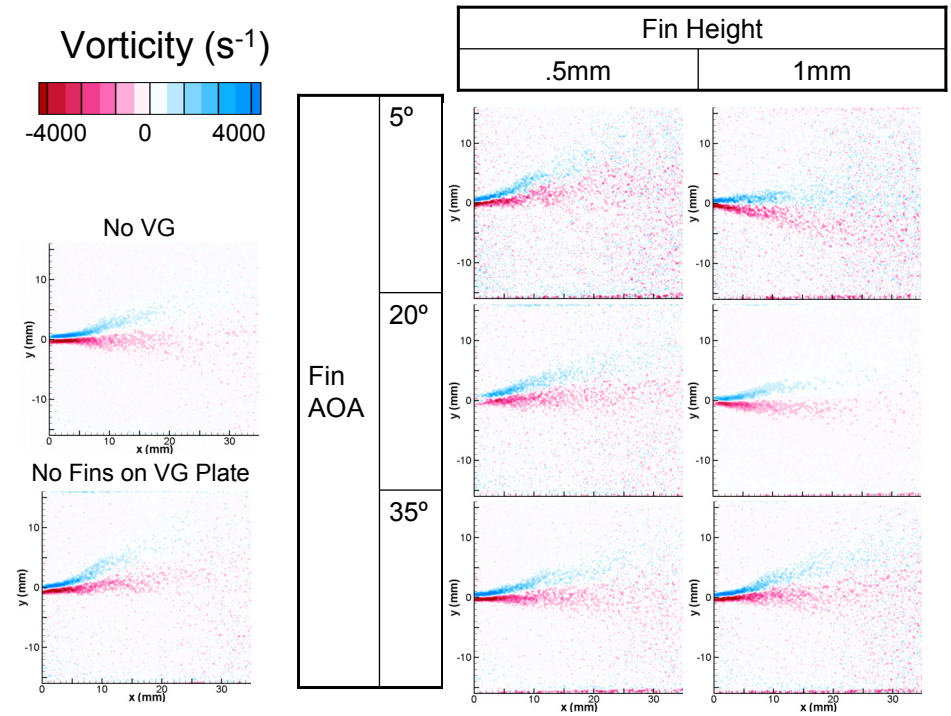

Figure C.3.12: Mean vorticity of large-scale jet in Bin 1

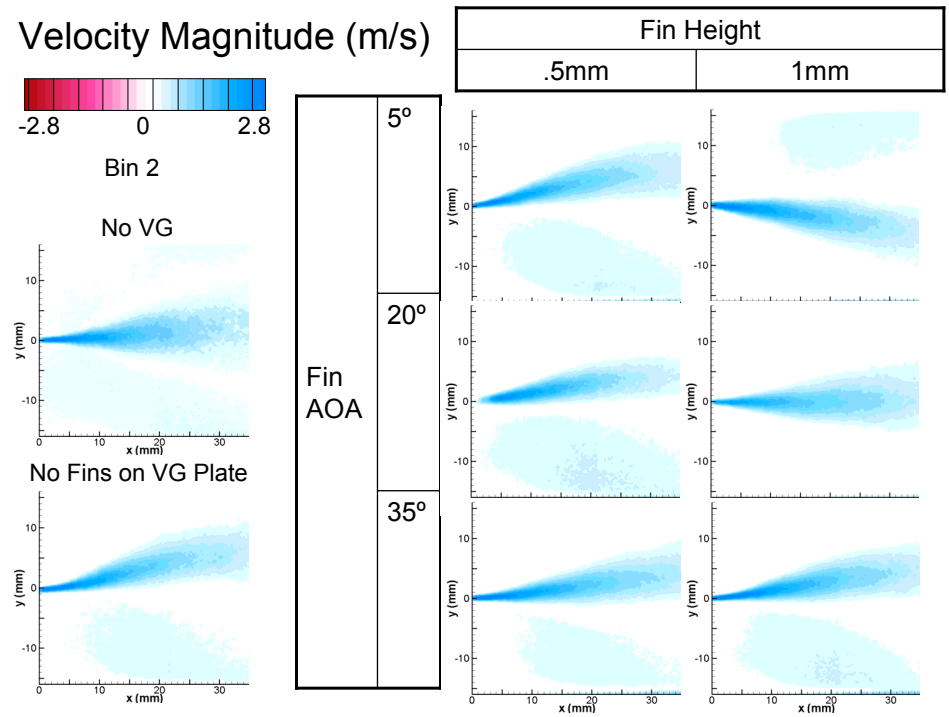

Figure C.3.13: Velocity magnitude of large-scale jet in Bin 2

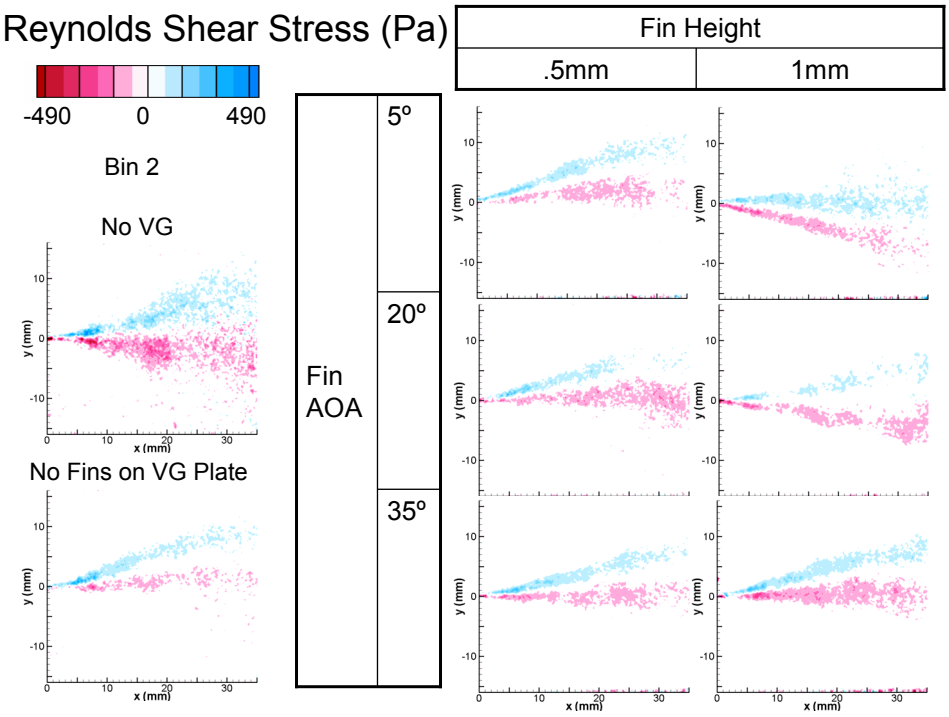

Figure C.3.14: Reynolds shear stress of large-scale jet in Bin 2

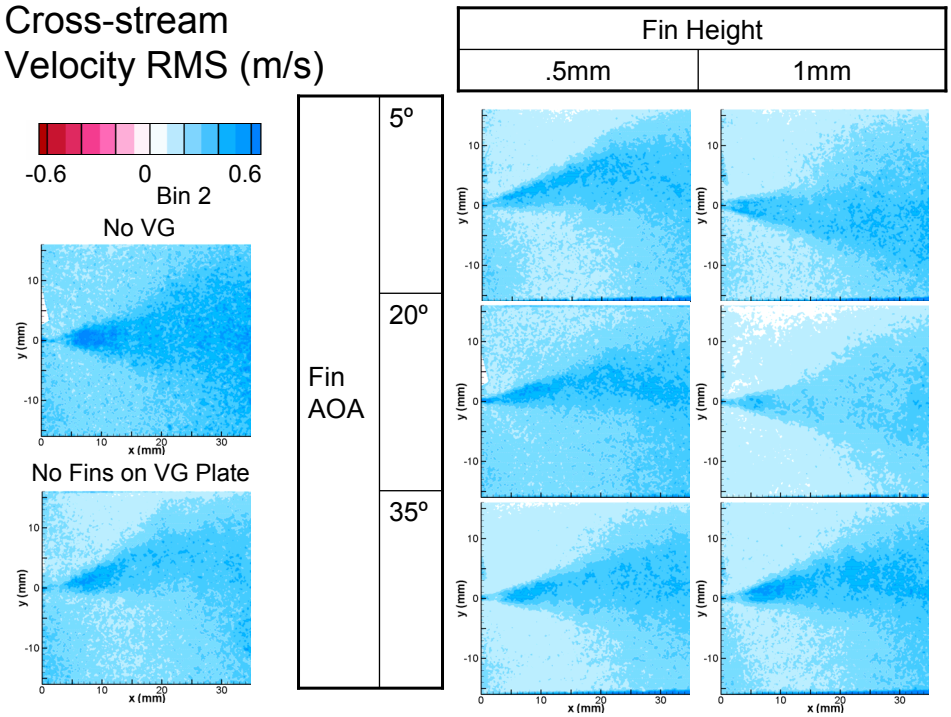

Figure C.3.15: Cross-stream velocity RMS of large-scale jet in Bin 2

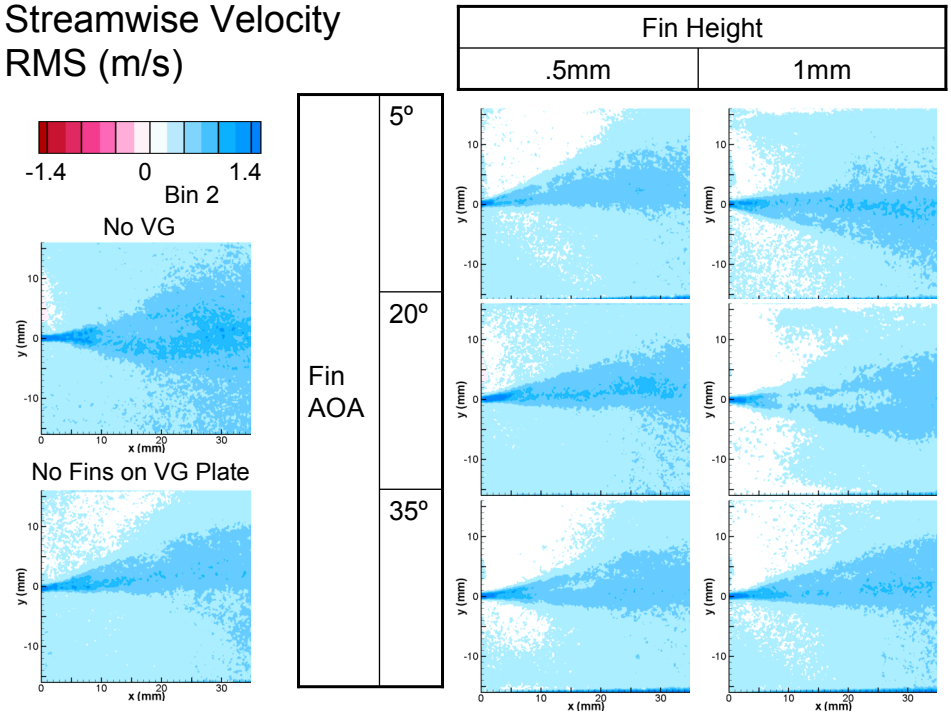

Figure C.3.16: Streamwise velocity RMS of large-scale jet in Bin 2

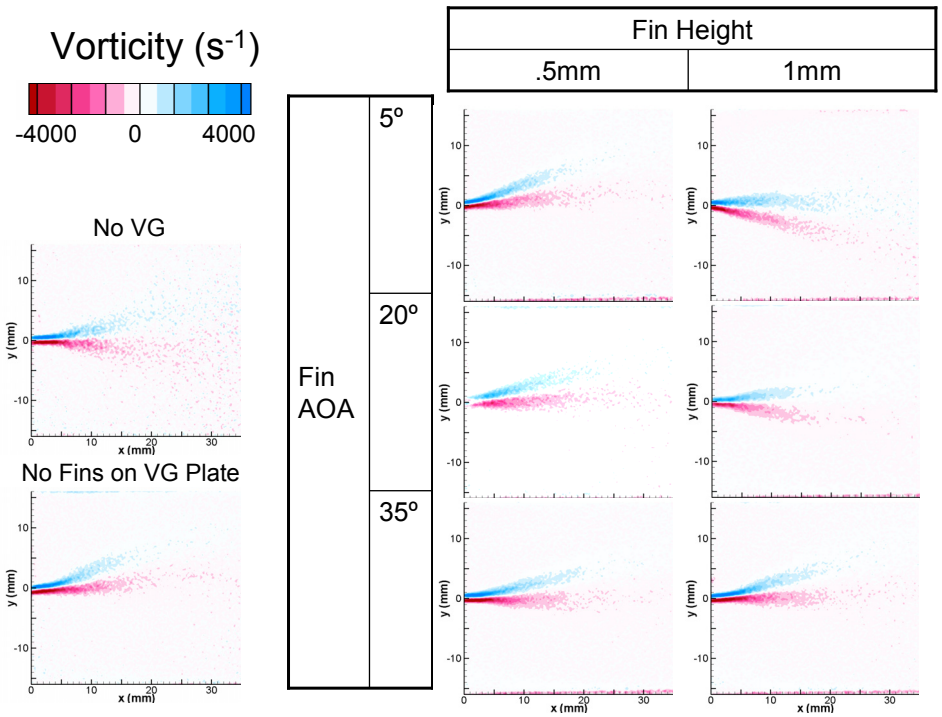

Figure C.3.17: Mean vorticity of large-scale jet in Bin 2

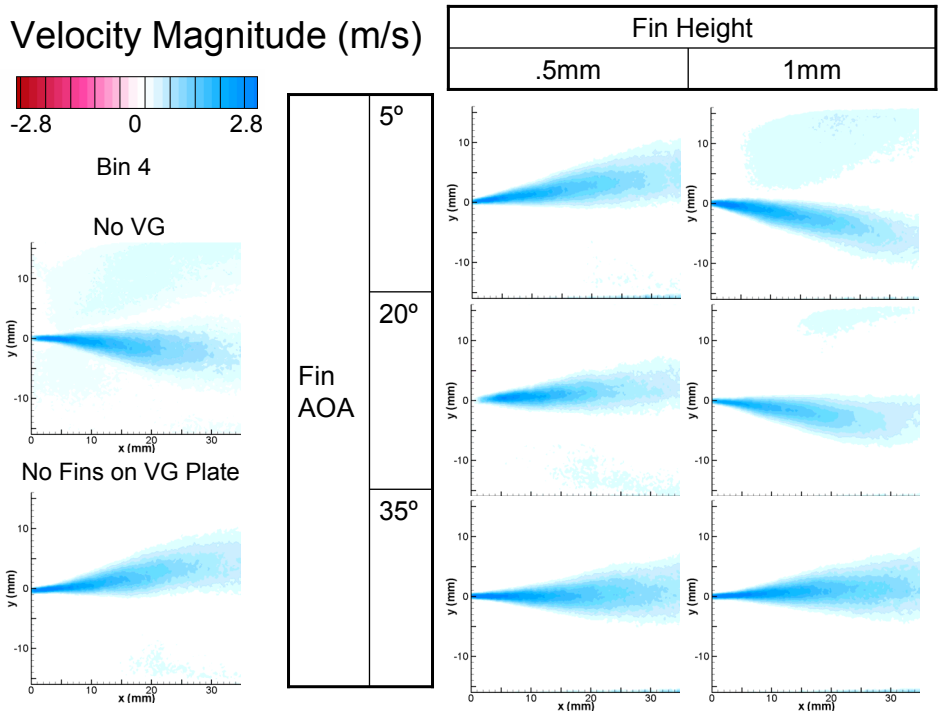

Figure C.3.18: Velocity magnitude of large-scale jet in Bin 4

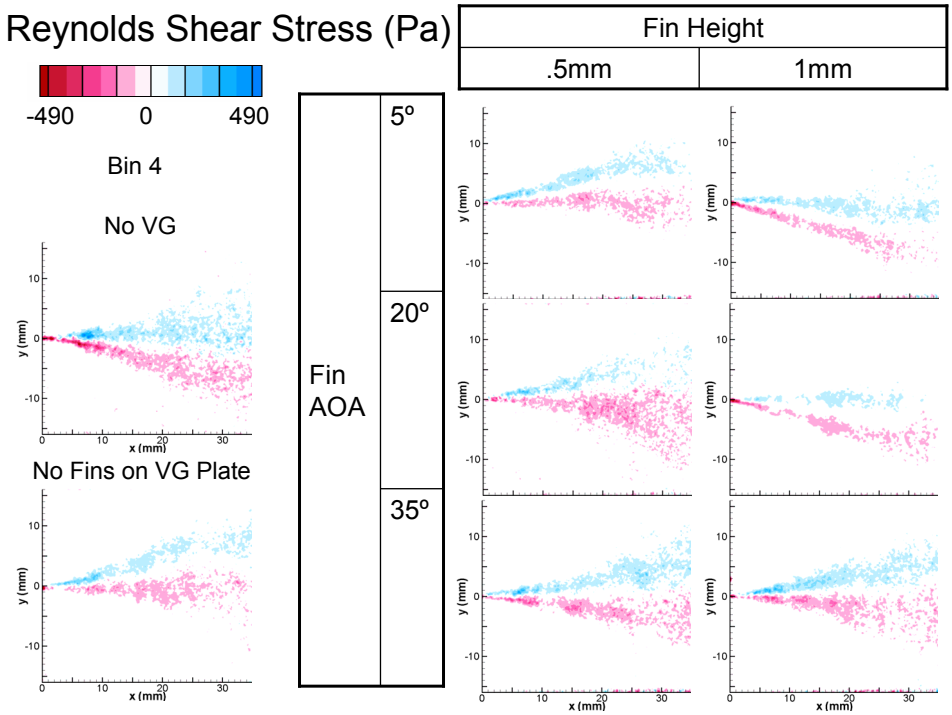

Figure C.3.19: Reynolds shear stress of large-scale jet in Bin 4

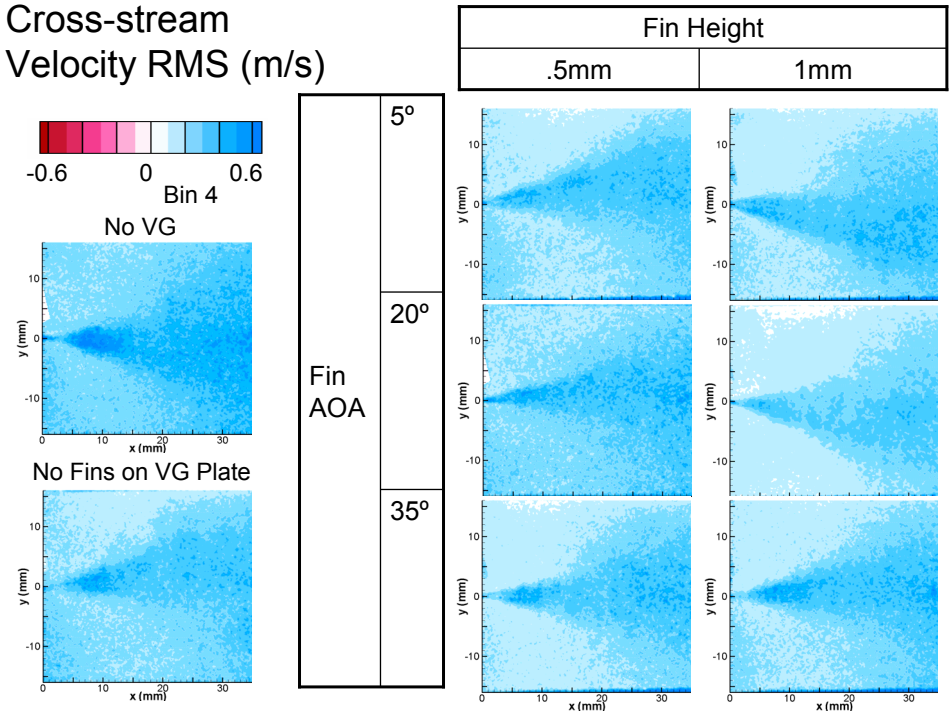

Figure C.3.20: Cross-stream velocity RMS of large-scale jet in Bin 4

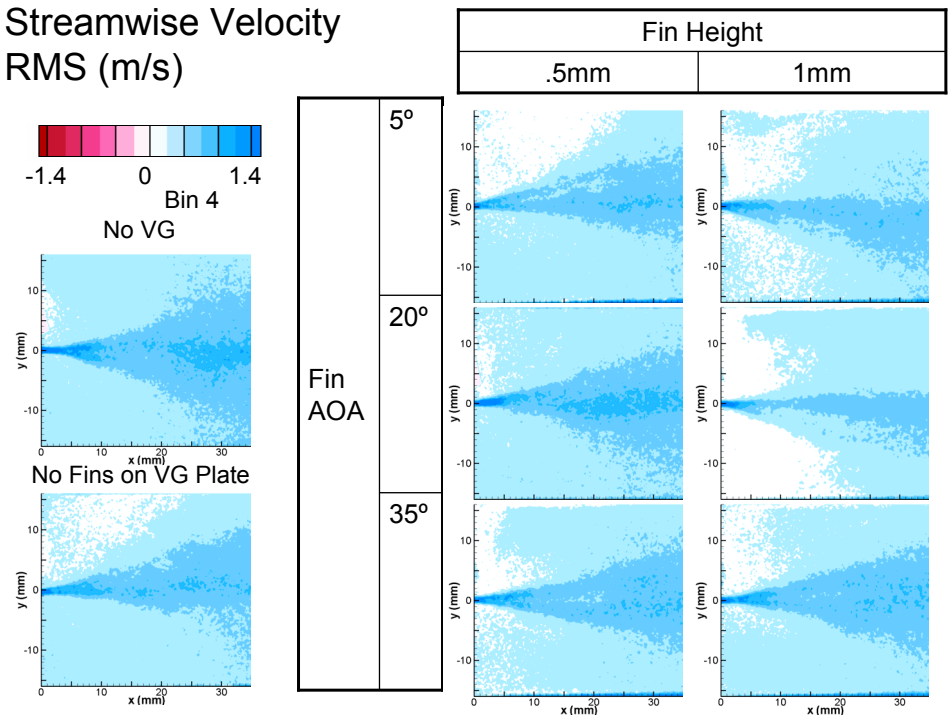

Figure C.3.21: Streamwise velocity RMS of large-scale jet in Bin 4

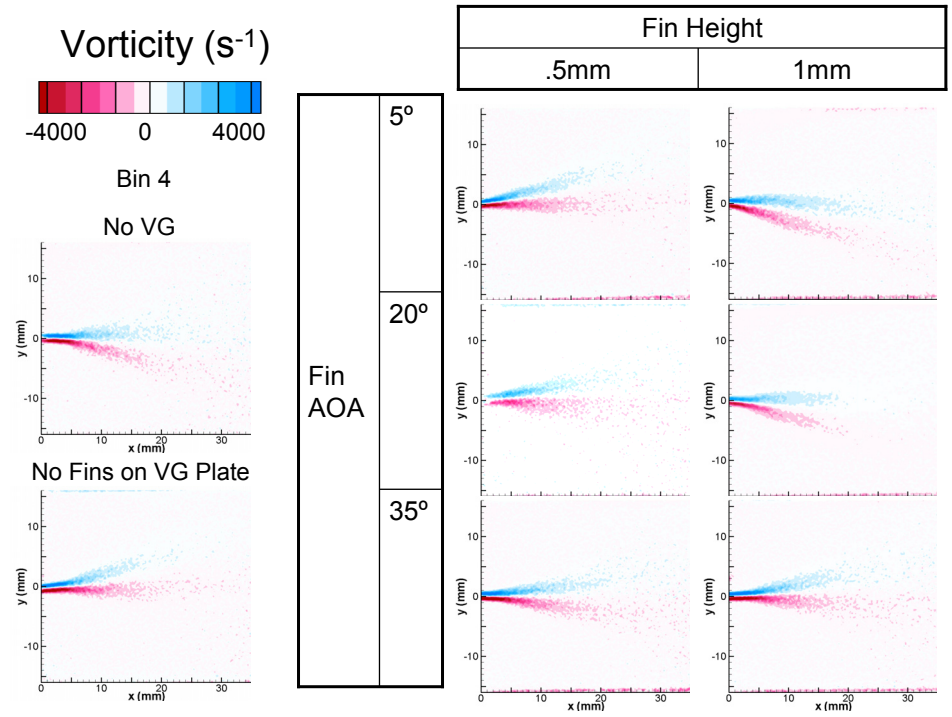

Figure C.3.22: Mean vorticity of large-scale jet in Bin 4

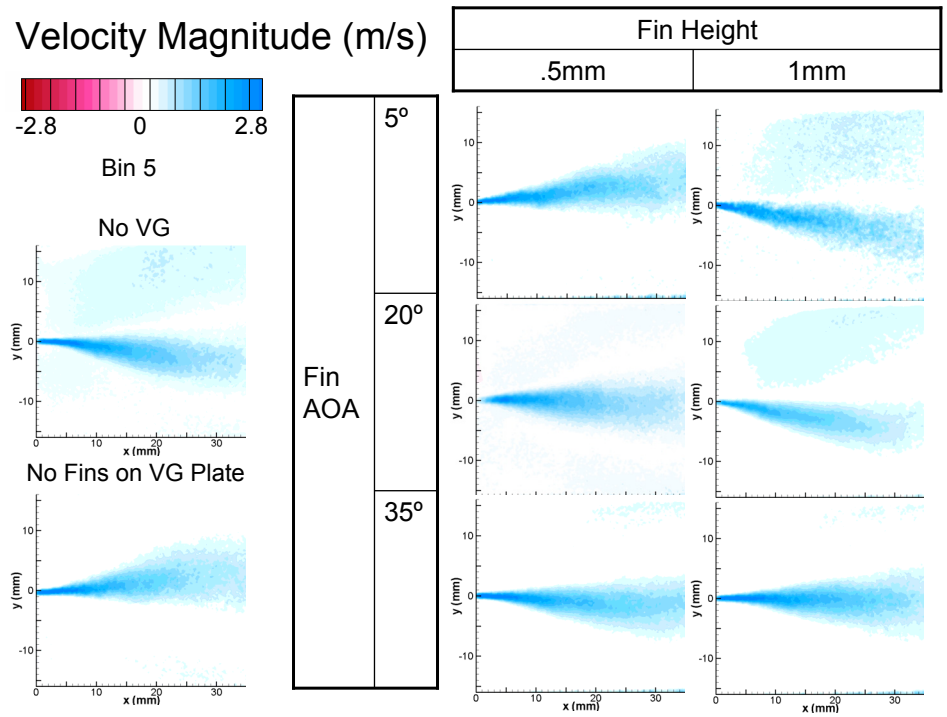

Figure C.3.23: Velocity magnitude of large-scale jet in Bin 5

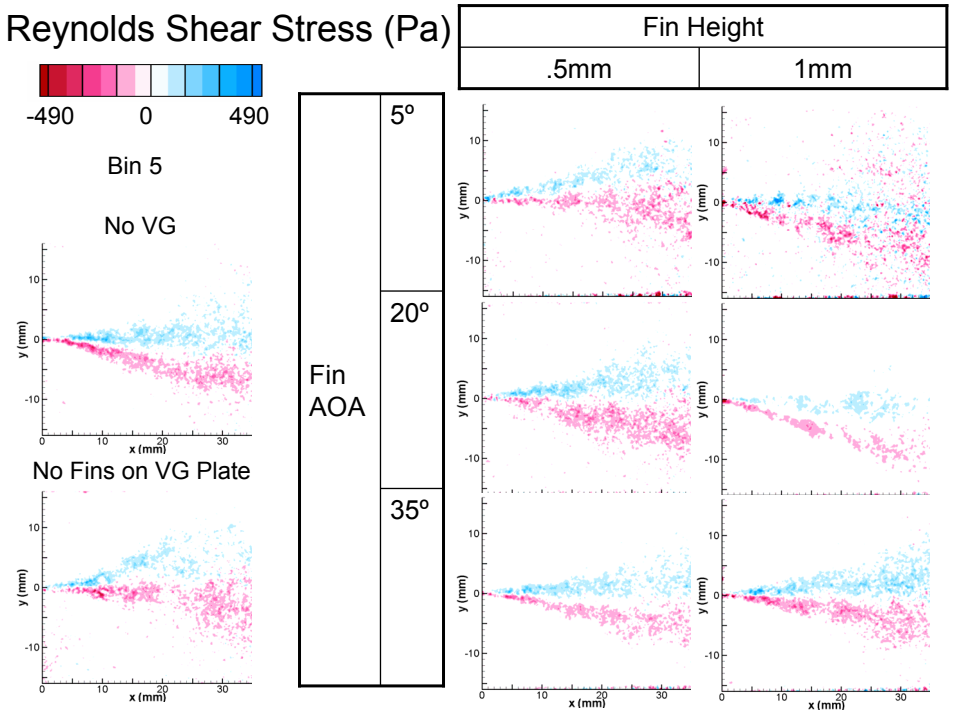

Figure C.3.24: Reynolds shear stress of large-scale jet in Bin 5

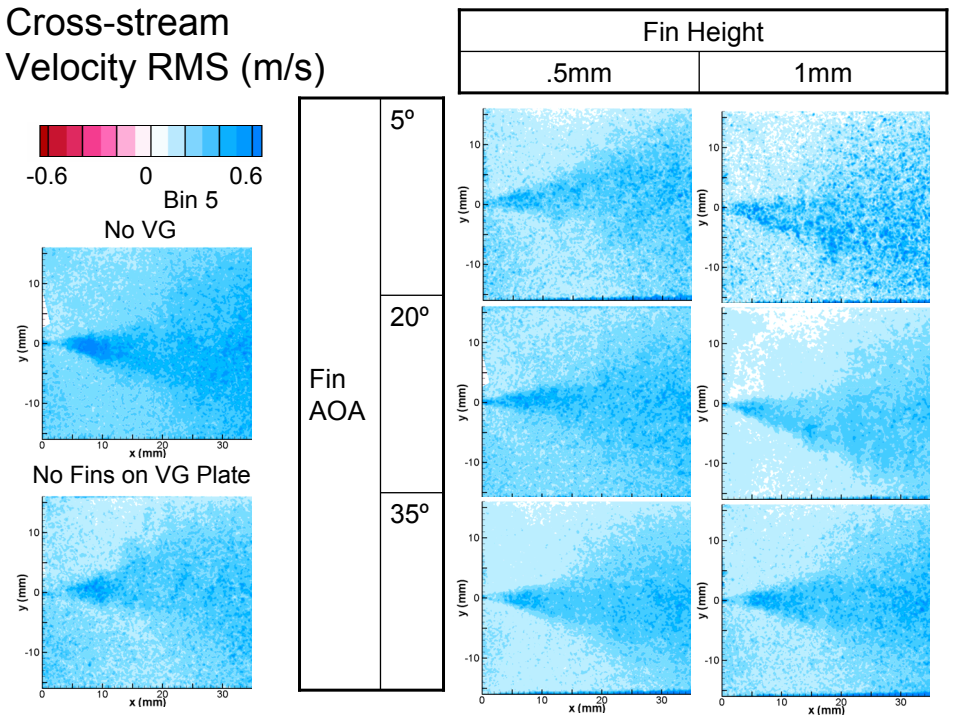

Figure C.3.25: Cross-stream velocity RMS of large-scale jet in Bin 5

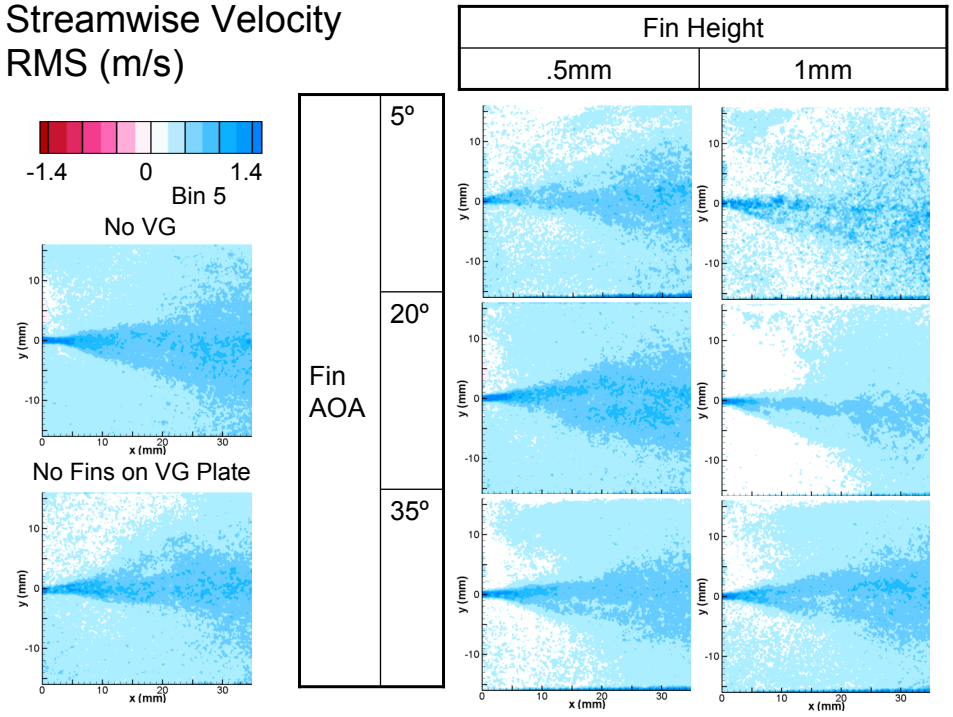

Figure C.3.26: Streamwise velocity RMS of large-scale jet in Bin 5

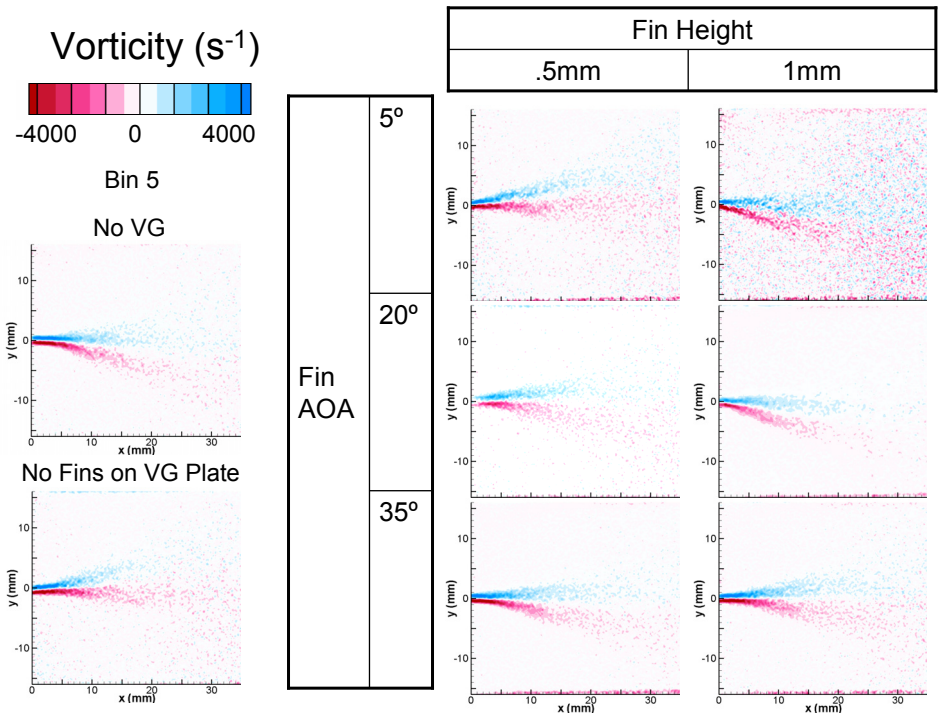

Figure C.3.27: Mean vorticity of large-scale jet in Bin 5

APPENDIX D

PULSATILE PIV RESULTS

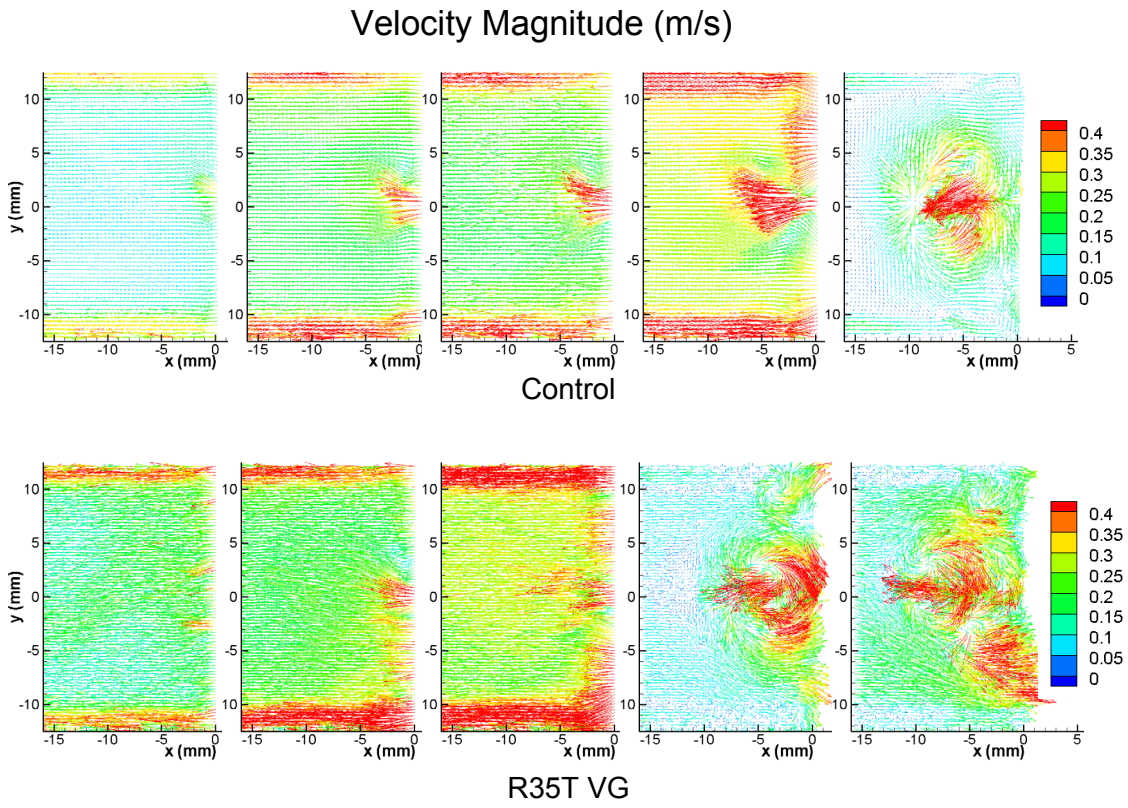

Figure D.1: A series of instantaneous velocity vector images detailing the flow field of the regurgitant jet upstream of the BMHV during valve closure. The data was acquired in the central plane of the valve with the jet emanating to the left. This series of images covers approximately 30ms during the cardiac cycle, and so the images are spaced about 6 ms apart. The instantaneous images in each series are representative of the velocity vector field at that point in time and do not come from a single cardiac cycle. The Control case is shown in the top row while the case with the R35T vortex generator design is shown on the bottom row.

Figures D.2 and D.3 (below): Two series of instantaneous velocity vector field for the Control (Figure D.2) and R35T VG (Figure D.3) cases. Eleven instantaneous images spaced 3ms apart are shown for each case, beginning at 454ms into the cardiac cycle and concluding at 484ms (as shown in the pressure and velocity waveforms in Figure 4.11). The images show the regurgitation jet (emanating to the right) for each case and are similar to the results obtained with the flow visualization.

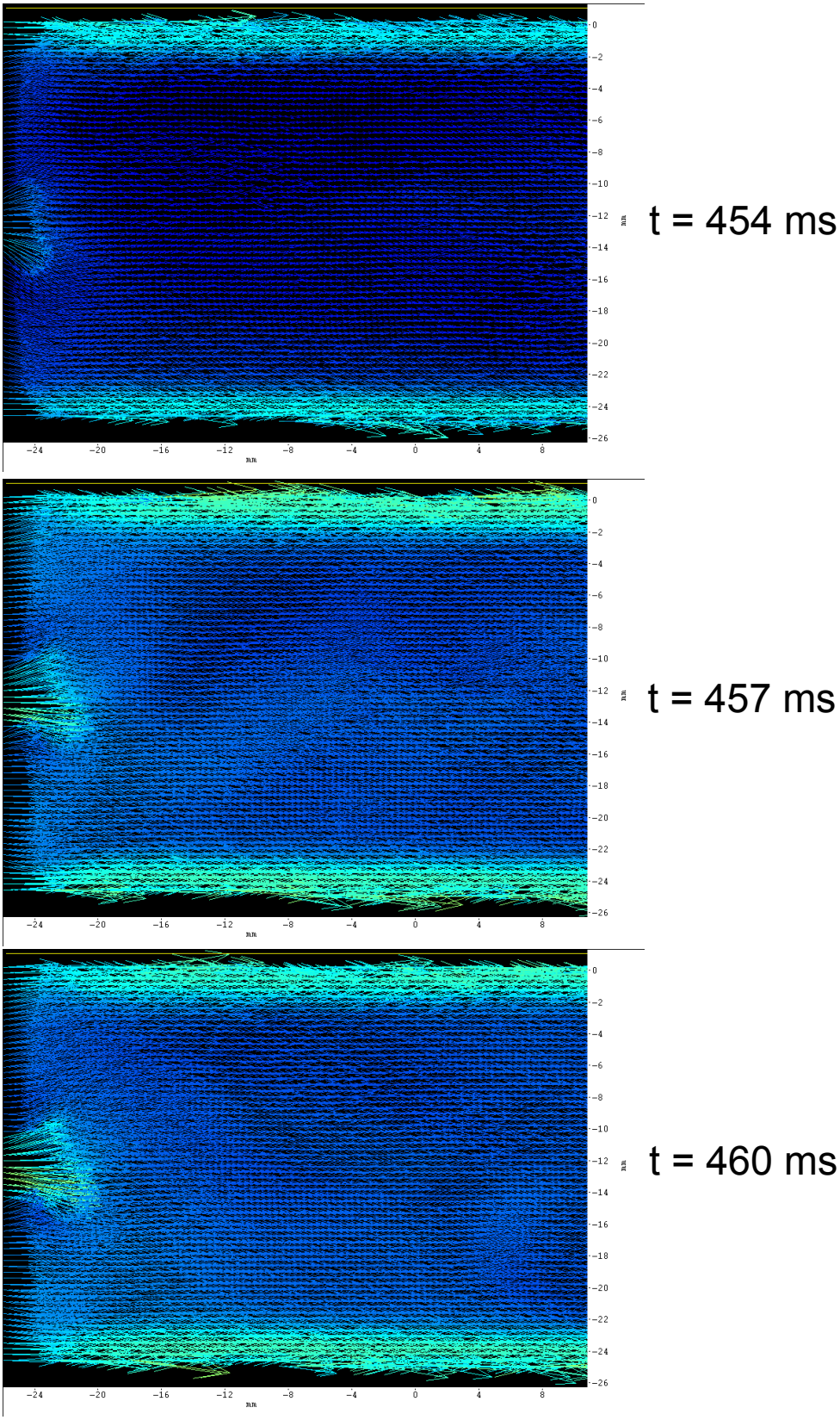

Figure D.2a: Representative instantaneous velocity fields upstream of the Control case

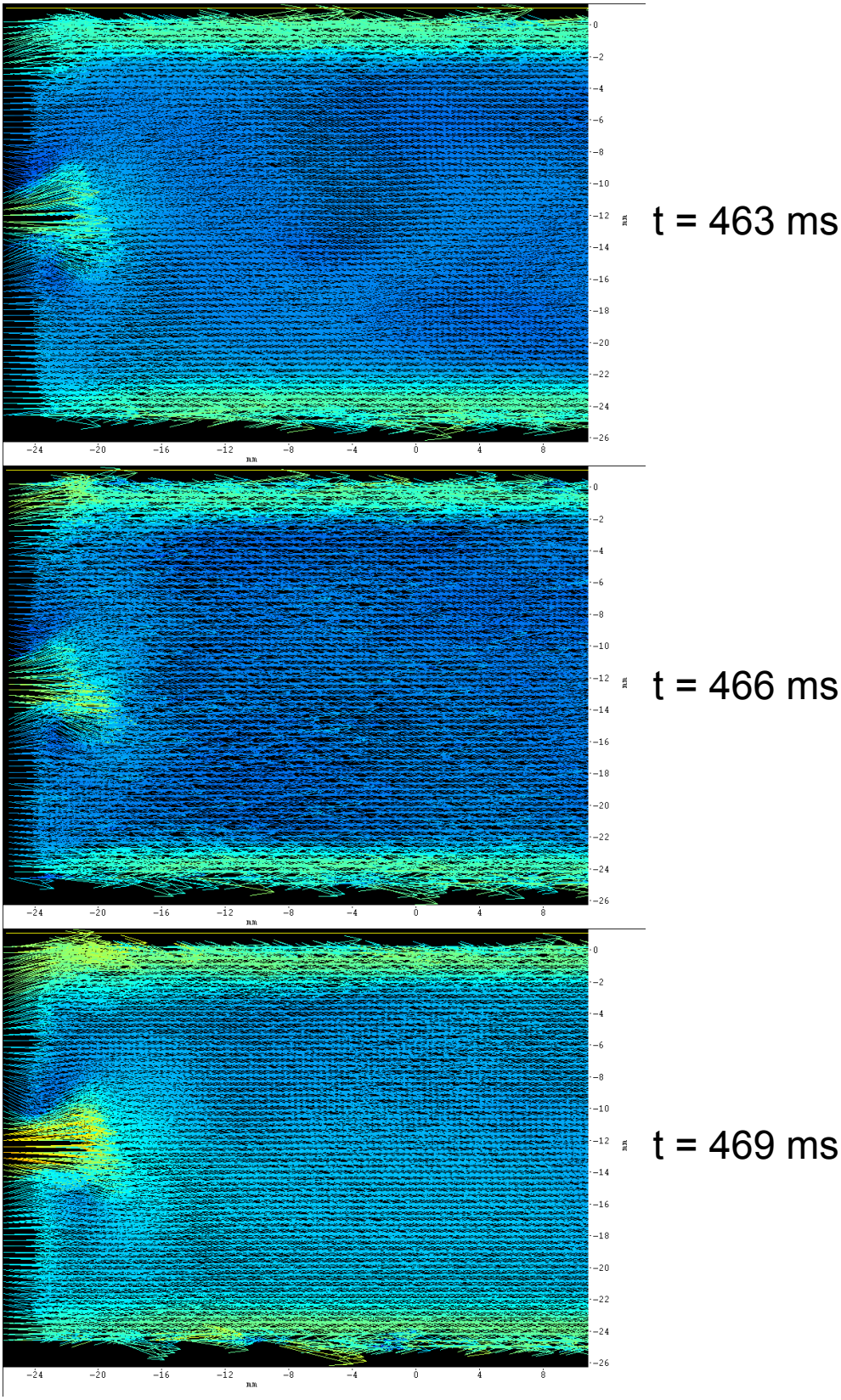

Figure D.2b: Representative instantaneous velocity fields upstream of the Control case

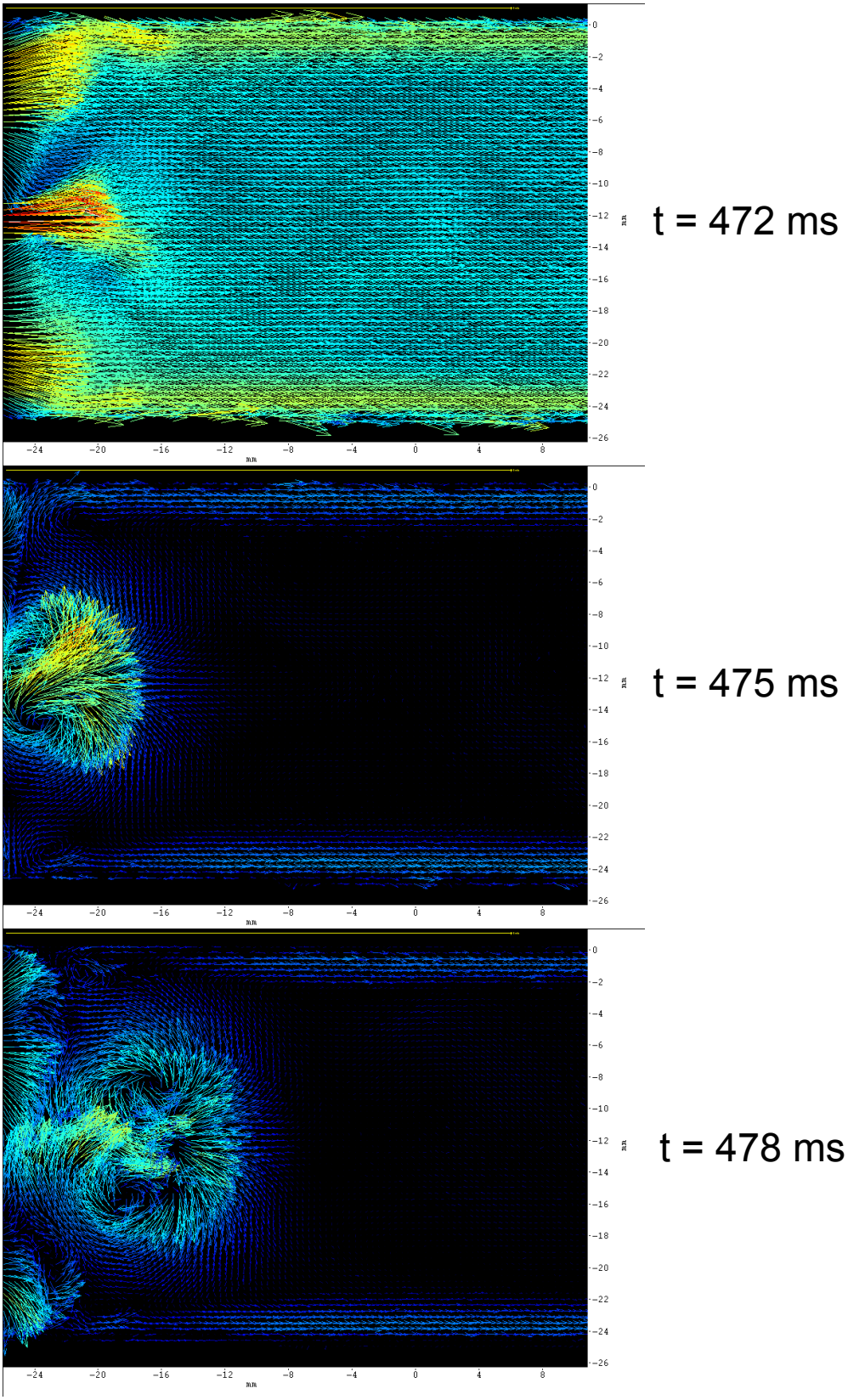

Figure D.2c: Representative instantaneous velocity fields upstream of the Control case

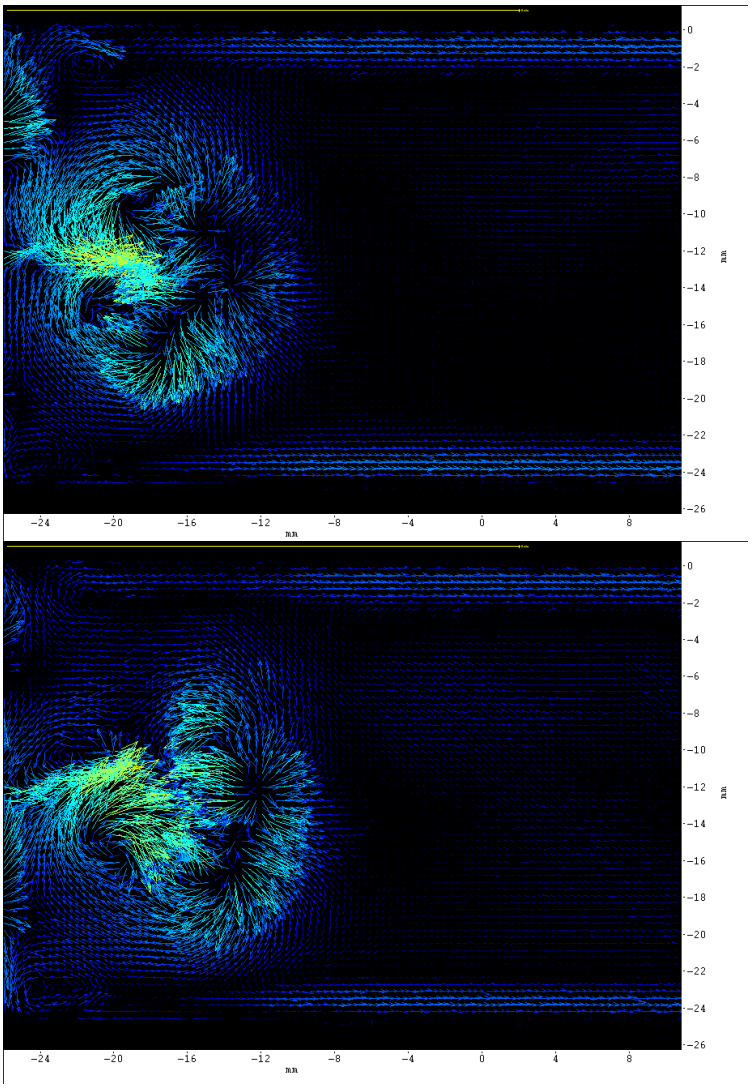

Figure D.2d: Representative instantaneous velocity fields upstream of the Control case

Figure D2a-d (Description of Image Sequence - Control): At the time of 454ms, systole has just concluded. The forward flow through the valve has stopped, and reverse flow has just begun, particularly along the edges of the chamber. A small increase in velocity is seen at the center of the chamber where the two leaflets form the b-datum line. The velocity magnitude of this jet increases up through approximately 469ms or 472ms, with the b-datum line jet being progressively pinched off by the closing leaflets. At about 475ms, the jet becomes unstable and forms counter-rotating vortices; the velocity in the remainder of the upstream chamber also decreases and becomes chaotiD. Up until 484ms, the vortices formed at closure move further upstream and begin to disintegrate.

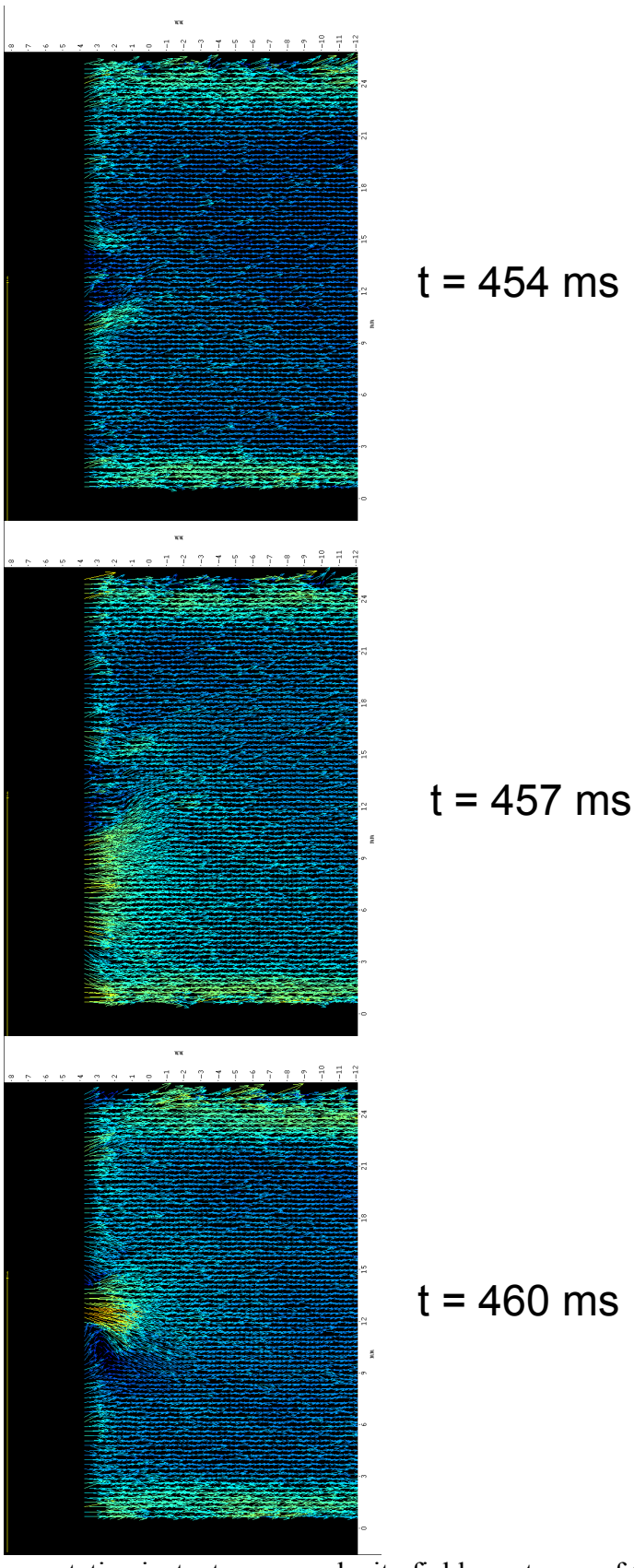

Figure D.3a: Representative instantaneous velocity fields upstream of the R35T VG case

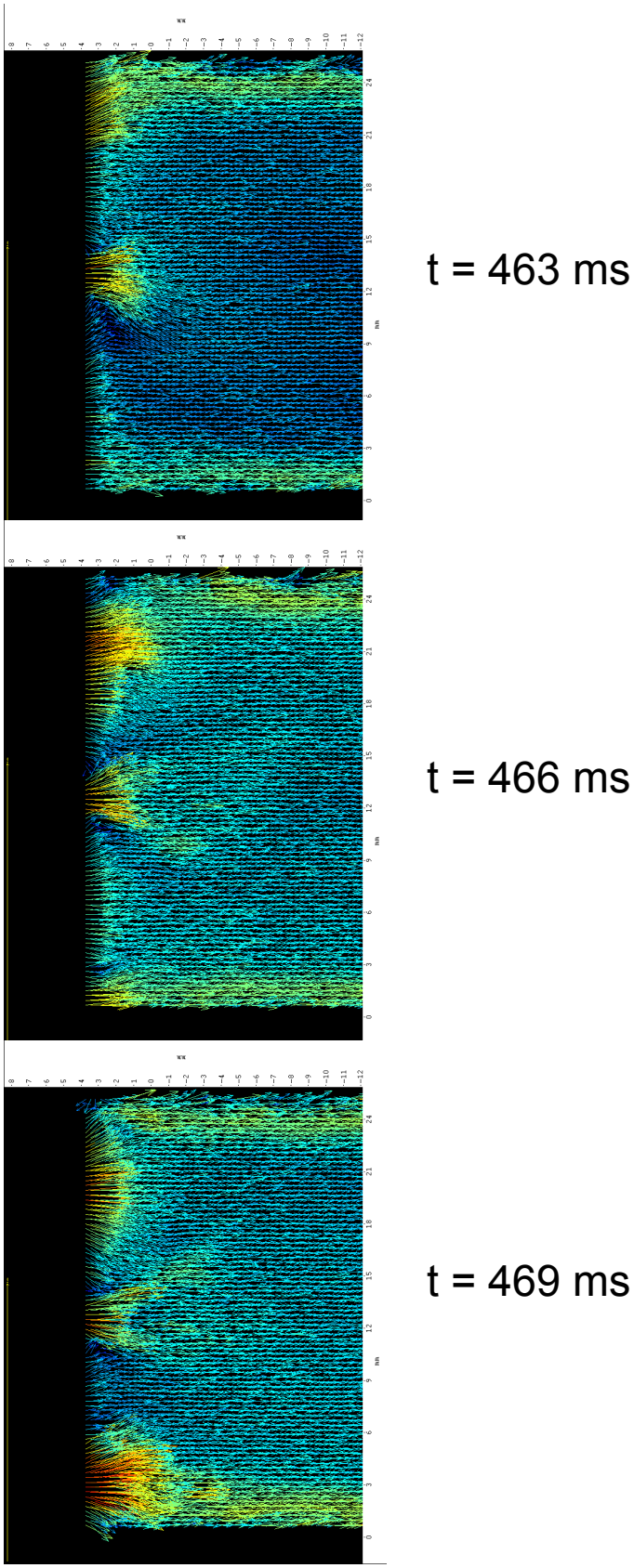

Figure D.3b: Representative instantaneous velocity fields upstream of the R35T VG case

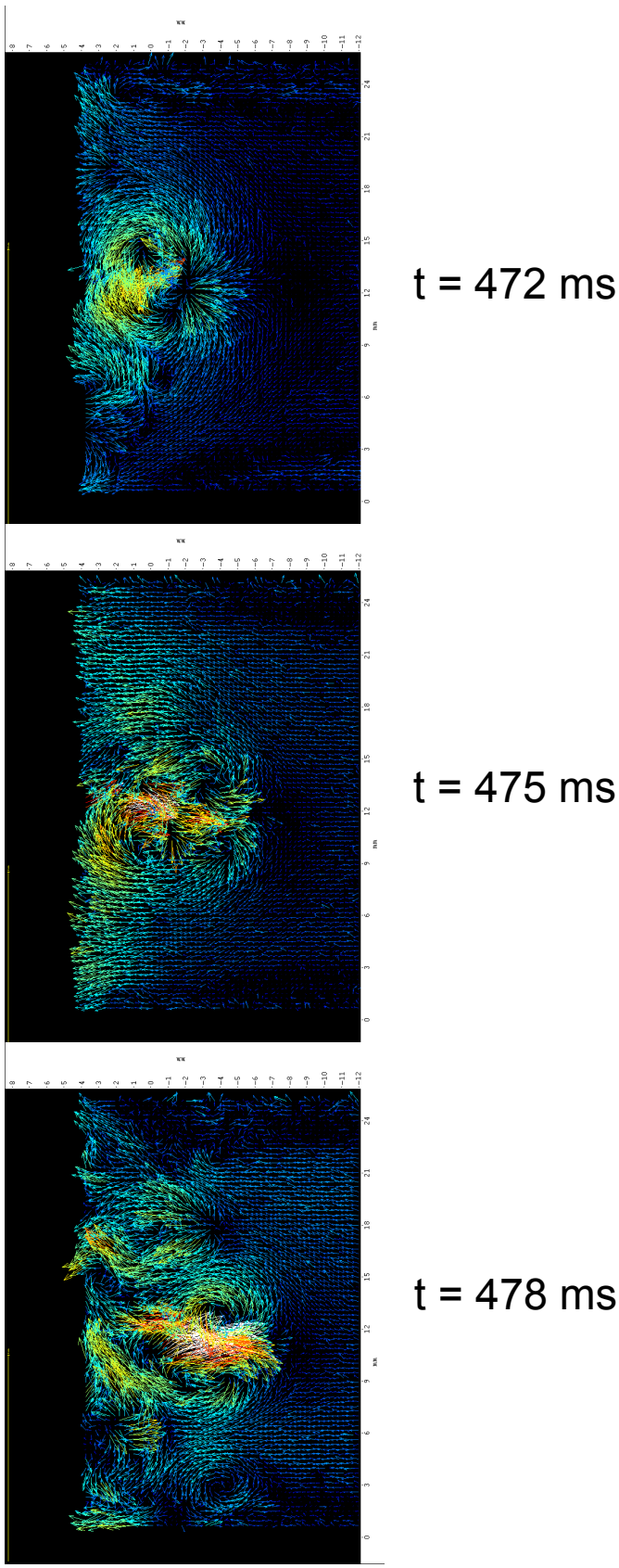

Figure D.3c: Representative instantaneous velocity fields upstream of the R35T VG case

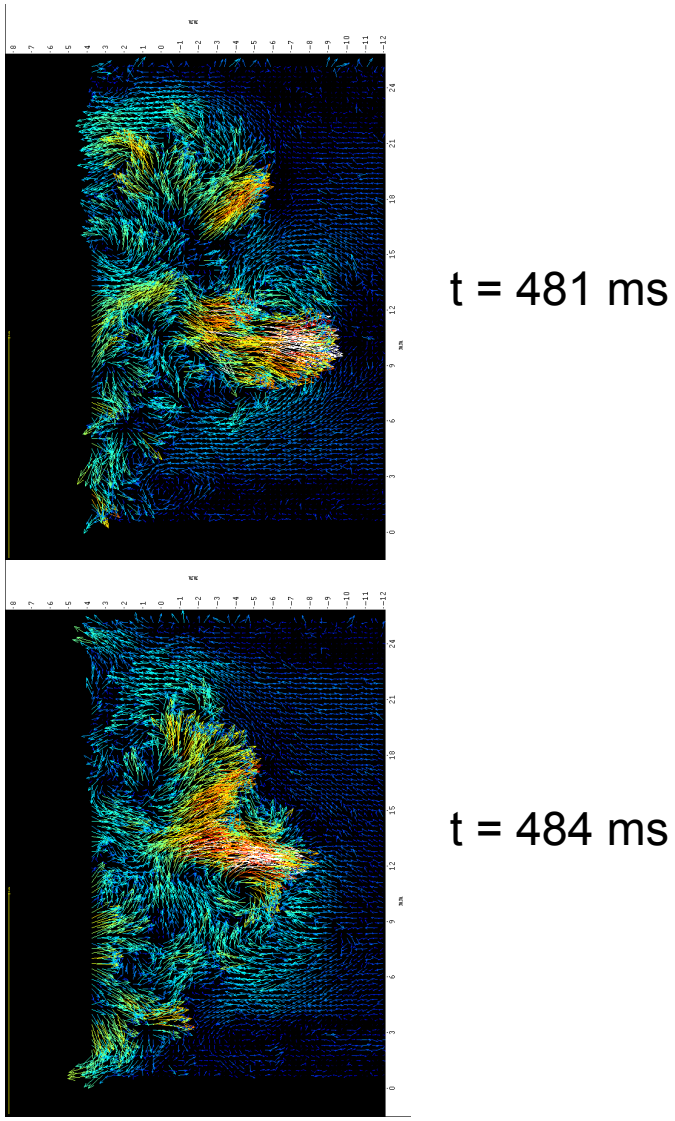

Figure D.3d: Representative instantaneous velocity fields upstream of the R35T VG case

Figure D2a-d (Description of Image Sequence - R35T VG): Up to a certain point, the flow follows a similar pattern as that seen in the Control case. The regurgitant jet again forms around 460ms and grows in magnitude with time. In the images here, the peripheral jets are also much more evident. This may be due to changes in the pressure or velocity waveforms and are one reason why a proper comparison cannot be made. At 472ms, the regurgitant jet is again cut off, and counter-rotating vortices appear to form. However, these vortices are not as coherent and are not maintained as long as those seen in the Control case. This is presumably due to fluid motion out of the plane caused by the vortex generator fins. The vortices decay up through 484ms in this image series and continue to do so until the next cycle of systole starts.

(Bacher and Williams, 1970; Bradbury and Khadem, 1975; Brown *et al.*, 1975a; Brown *et al.*, 1975b; Colantuoni *et al.*, 1977; Baudet *et al.*, 1985; Croughan *et al.*, 1987; Gieresiepen *et al.*, 1989; Alkhamis *et al.*, 1990; Giersiepen *et al.*, 1990; Gad-el-Hak and Bushnell, 1991; Baldwin *et al.*, 1994; Black and Drury, 1994; Bluestein *et al.*, 1994; Boreda *et al.*, 1995; Cannegieter *et al.*, 1995; Fish and Battle, 1995; Ellis *et al.*, 1996; Fontaine *et al.*, 1996; Anderson *et al.*, 1997; Barbaro *et al.*, 1997; Bluestein *et al.*, 1997; Chandran and Aluri, 1997; Garver *et al.*, 1998; Ellis, 1999; Foss and Zaman, 1999; Bechert *et al.*, 2000a; Bechert *et al.*, 2000b; Bluestein *et al.*, 2000; Ellis *et al.*, 2000; Enrique-Sarano *et al.*, 2000; Farb *et al.*, 2000; Gad-el-Hak, 2000; Ansell *et al.*, 2001; Chang *et al.*, 2001; Bluestein *et al.*, 2002; Baskurt and Meiselman, 2003; Behring, 2003; Arora *et al.*, 2004; Bluestein *et al.*, 2004; Cheng *et al.*, 2004; Desai *et al.*, 2004; Einav and Bluestein, 2004; Fallon, 2006; Fallon *et al.*, 2006; Fish and Lauder, 2006; Alemu and Bluestein, 2007; Bakir *et al.*, 2007; Dumont *et al.*, 2007; Fallon *et al.*, 2007)

(Harken *et al.*, 1960; Harken *et al.*, 1962; Leverett *et al.*, 1972; Hung *et al.*, 1976; Heuser and Opitz, 1980; Ho and Gutmark, 1987; Hoek *et al.*, 1988; Gieresiepen *et al.*, 1989; Klepetko *et al.*, 1989; Giersiepen *et al.*, 1990; Gad-el-Hak and Bushnell, 1991; Graf *et al.*, 1991; Hammermeister *et al.*, 1993; Lamson *et al.*, 1993; Hellums, 1994; Ibrahim *et al.*, 1994; Lee *et al.*, 1994; Lin *et al.*, 1994; Fish and Battle, 1995; Fontaine *et al.*, 1996; Gross *et al.*, 1996; Holme *et al.*, 1997; Garver *et al.*, 1998; Healy *et al.*, 1998; Island *et al.*, 1998; Foss and Zaman, 1999; Gutmark and Grinstein, 1999; Hui *et al.*, 1999; Jesty and Bluestein, 1999; Kim and Samimy, 1999; Lawson and Davidson, 1999; Farb *et al.*, 2000; Gad-el-Hak, 2000; Guyton and Hall, 2000; Lim *et al.*, 2000; Liu *et al.*, 2000; Lawson and Davidson, 2001; Lim *et al.*, 2001; Lu *et al.*, 2001; Lai *et al.*, 2002; Lawson and Davidson, 2002; Leo *et al.*, 2002; Jesty *et al.*, 2003; Lim *et al.*, 2003; Grigioni *et al.*, 2004; Leo, 2005; Fallon *et al.*, 2006; Fish and Lauder, 2006; Hathcock, 2006; Krishnan *et al.*, 2006)

(Schubauer and Spangenberg, 1960; Pearcey, 1961; Starr and Edwards, 1961; Rooney, 1970; Leverett *et al.*, 1972; Sutera and Mehrjardi, 1975; Sutera, 1977; Ramstack *et al.*, 1979; Rockwell, 1983; Selzer, 1983; Sallam and Hwang, 1984; Pelzer *et al.*, 1988; Rao and Kariya, 1988; Sutera *et al.*, 1988; Tiederman *et al.*, 1988; Nygaard *et al.*, 1990; Lamson *et al.*, 1993; Markus, 1993; Lee *et al.*, 1994; Lin *et al.*, 1994; Masters *et al.*, 1995; O'Brien *et al.*, 1995; Maurel *et al.*, 1996; Miyazaki *et al.*, 1996; Reeder and Zaman, 1996; Nathan *et al.*, 1998; Lawson and Davidson, 1999; Morsi *et al.*, 1999; Rambod *et al.*, 1999; Lim *et al.*, 2000; Liu *et al.*, 2000; Paraskos, 2000; Thai and Gore, 2000; Lawson and Davidson, 2001; Lim *et al.*, 2001; Lu *et al.*, 2001; Mi *et al.*, 2001; Stein *et al.*, 2001; Lai *et al.*, 2002; Lawson and Davidson, 2002; Leo *et al.*, 2002; Lim *et al.*, 2003; Manning *et al.*, 2003; Sherwood, 2003; Simon, 2004; Simon *et al.*, 2004; Leo, 2005; Thom *et al.*, 2006; Rambod *et al.*, 2007; Raz *et al.*, 2007)

(Schubauer and Spangenberg, 1960; Starr and Edwards, 1961; Rooney, 1970; Williams *et al.*, 1970; Sutera and Mehrjardi, 1975; Sutera, 1977; Rockwell, 1983; Selzer, 1983; Sallam and Hwang, 1984; Wurzinger *et al.*, 1985; Yoganathan *et al.*, 1986; Sutera *et al.*, 1988; Tiederman *et al.*, 1988; van der Meer *et al.*, 1993; Vijaykumar *et al.*, 1994; Villermaux and Hopfinger, 1994; Zaman *et al.*, 1994; Yoganathan, 1995; Reeder and

Zaman, 1996; Yu *et al.*, 1997; Yu *et al.*, 1998; Zaman, 1999; Thai and Gore, 2000; Whyte *et al.*, 2000; Stein *et al.*, 2001; Travis, 2001; Travis *et al.*, 2001a; Travis *et al.*, 2001b; Zaman, 2001; Travis *et al.*, 2002; Sherwood, 2003; Wang *et al.*, 2003; Simon, 2004; Simon *et al.*, 2004; Truskey *et al.*, 2004; Yin *et al.*, 2004; Yin *et al.*, 2005; Thom *et al.*, 2006; Tsai *et al.*, 2006; Yin *et al.*, 2006; Yoganathan, 2006; Zhang *et al.*, 2006)

Asd

BIBLIOGRAPHY

Alemu, Y. and D. Bluestein (2007). "Flow-induced Platelet Activation and Damage Accumulation in a Mechanical Heart Valve: Numerical Studies." Artificial Organs **31**(9): 677-688.

Alkhamis, T. M., R. L. Beissinger*, et al.* (1990). "Artificial surface effect on red blood cells and platelets in laminar shear flow." Blood **75**(7): 1568-1575.

Anderson, E. J., P. S. MacGillivray*, et al.* (1997). "Scallop Shells Exhibit Optimization of Riblet Dimensions for Drag Reduction." Biol Bull **192**(3): 341-344.

Ansell, J., J. Hirsh*, et al.* (2001). "Managing Oral Anticoagulant Therapy." Chest **119**(90010): 22S-38.

Arora, D., M. Behr*, et al.* (2004). "A Tensor-based Measure for Estimating Blood Damage." Artificial Organs **28**(11): 1002-1015.

Bacher, R. and M. Williams (1970). "Hemolysis in capillary flow." J Lab Clin Med. **79**(3): 485-96.

Bakir, I., M. F. Hoylaerts*, et al.* (2007). "Mechanical Stress Activates Platelets at a Subhemolysis Level: An In Vitro Study." Artificial Organs **31**(4): 316-323.

Baldwin, J., S. Deutsch*, et al.* (1994). "LDA measurements of mean velocity and Reynolds stress fields within an artificial heart ventricle." J Biomech Eng **116**(2): 190-200.

Barbaro, V., M. Grigioni*, et al.* (1997). "19 mm sized bileaflet valve prostheses' flow field investigated by bidimensional laser Doppler anemometry (part II: maximum turbulent shear stresses)." Int J Artif Organs **20**(11): 629-36.

Baskurt, O. M. D. and H. S. D. Meiselman (2003). "Blood Rheology and Hemodynamics." M.Sc.(5): 435-450.

Baudet, E. M., C. C. Oca*, et al.* (1985). "A 5 1/2 year experience with the St. Jude Medical cardiac valve prosthesis. Early and late results of 737 valve replacements in 671 patients." J Thorac Cardiovasc Surg **90**(1): 137-144.

Bechert, D. W., M. Bruse*, et al.* (2000a). "Experiments with three-dimensional riblets as an idealized model of shark skin." Experiments in Fluids **28**(5): 403-412.

Bechert, D. W., M. Bruse*, et al.* (2000b). "Fluid Mechanics of Biological Surfaces and their Technological Application." Naturwissenschaften **87**(4): 157-171.

Behring, D. (2003). Enzygnost TAT Micro: Enzyme immunoassay for the determination of human thrombin/antithrombin III complex.

Black, M. and P. Drury (1994). "Mechanical and other problems of artificial valves." Curr Top Pathol. **86**: 127-59.

Bluestein, D., S. Einav*, et al.* (1994). "A squeeze flow phenomenon at the closing of a bileaflet mechanical heart valve
prosthesis." J Biomech **27**(11): 1369-78.

Bluestein, D., Y. Li*, et al.* (2002). "Free emboli formation in the wake of bi-leaflet mechanical heart valves and the
effects of implantation techniques." J Biomech **35**(12): 1533-40.

Bluestein, D., L. Niu*, et al.* (1997). "Fluid mechanics of arterial stenosis: Relationship to the development of mural thrombus." Annals of Biomedical Engineering **25**(2): 344-356.

Bluestein, D., E. Rambod*, et al.* (2000). "Vortex Shedding as a Mechanism for Free Emboli Formation in Mechanical Heart Valves." Journal of Biomechanical Engineering **122**(2): 125-134.

Bluestein, D., W. Yin*, et al.* (2004). "Flow-induced platelet activation in mechanical heart valves." J Heart Valve Dis. **13**(3): 501-8.

Boreda, R., R. Fatemi*, et al.* (1995). "Potential for platelet stimulation in critically stenosed carotid and coronary arteries." J. Vasc. Invest. **1**: 26-37.

Bradbury, L. and A. Khadem (1975). "The distortion of a jet by tabs." Journal of Fluid Mechanics **770**: 801-813.

Brown, C., R. Lemuth*, et al.* (1975a). "Response of human platelets to shear stress." Trans Am Soc Artif Intern Organs **21**: 35-9.

Brown, C., L. Leverett*, et al.* (1975b). "Morphological, biochemical, and functional changes in human platelets subjected
to shear stress." J Lab Clin Med. **86**(3): 462-71.

Cannegieter, S. C., F. R. Rosendaal*, et al.* (1995). "Optimal Oral Anticoagulant Therapy in Patients with Mechanical Heart Valves." N Engl J Med **333**(1): 11-17.

Chandran, K. and S. Aluri (1997). "Mechanical valve closing dynamics: Relationship between velocity of closing, pressure transients, and cavitation initiation." Annals of Biomedical Engineering **25**(6): 926-938.

Chang, B., S. Lim*, et al.* (2001). "Long-term results with St. Jude Medical and CarboMedics prosthetic heart valves." J Heart Valve Dis. **10**(2): 185-194.

Cheng, R., Y. G. Lai*, et al.* (2004). "Three-Dimensional Fluid-Structure Interaction Simulation of Bileaflet Mechanical Heart Valve Flow Dynamics." Annals of Biomedical Engineering **32**(11): 1471-1483.

Colantuoni, G., J. D. Hellums*, et al.* (1977). "The response of human platelets to shear stress at short exposure times." Trans Am Soc Artif Intern Organs **23**(626-31).

Croughan, M., J. Hamel*, et al.* (1987). "Hydrodynamic effects on animal cells grown in microcarrier cultures." Biotechnology and Bioengineering **95**(2): 295-305.

Desai, N. D., O. Merin*, et al.* (2004). "Long-Term Results of Aortic Valve Replacement With the St. Jude Toronto Stentless Porcine Valve." The Annals of Thoracic Surgery **78**(6): 2076-2083.

Dumont, K., J. Vierendeels*, et al.* (2007). "Comparison of the Hemodynamic and Thrombogenic Performance of Two Bileaflet Mechanical Heart Valves Using a CFD/FSI Model." Journal of Biomechanical Engineering **129**(4): 558-565.

Einav, S. and D. Bluestein (2004). "Dynamics of Blood Flow and Platelet Transport in Pathological Vessels." Ann NY Acad Sci **1015**(1): 351-366.

Ellis, J. (1999). An in vitro investigation of the leakage and hinge flow fields through bileaflet mechanical heart valves and their relevance to thrombogenesis Mechanical Engineering. Atlanta, GA, Georgia Institute of Technology. **PhD**.

Ellis, J., T. Healy*, et al.* (1996). "Velocity measurements and flow patterns within the hinge region of a Medtronic
Parallel bileaflet mechanical valve with clear housing." J Heart Valve Dis. **5**(6): 591-9.

Ellis, J., B. Travis*, et al.* (2000). "An In Vitro Study of the Hinge and Near-Field Forward Flow Dynamics of the St. Jude Medical® Regent™ Bileaflet Mechanical Heart Valve " Annals of Biomedical Engineering **28**(5): 524-532.

Enrique-Sarano, M., H. Schaff*, et al.* (2000). Chronic Mitral Regurgitation. Valvular Heart Disease. J. Alpert, J. Dalen and S. Rahimtoola. Philadelphia, PA, Lippincott Williams & Wilkins.

Fallon, A. (2006). The Development of a Novel in vitro Flow System to Evaluate Platelet Activation and Procoagulant Potential Induced by Bileaflet Mechanical Heart Valve Leakage Jets. Chemical Engineering. Atlanta, GA, Georgia Institute of Technology. **PhD**.

Fallon, A., U. Marzec*, et al.* (2007). "Thrombin formation in vitro in response to shear-induced activation of platelets." Thromb Res. **Article in Press; Corrected Proof**.

Fallon, A. M., N. Shah*, et al.* (2006). "Flow and Thrombosis at Orifices Simulating Mechanical Heart Valve Leakage Regions." Journal of Biomechanical Engineering **128**(1): 30-39.

Farb, A., R. Virmani*, et al.* (2000). Pathogenesis and Pathology of Valvular Heart Disease. Valvular Heart Disease. J. Alpert, J. Dalen and S. Rahimtoola. Philadelphia, PA, Lippincott Williams & Wilkins.

Fish, F. and J. Battle (1995). "Hydrodynamic design of the humpback whale flipper." J Morphol. **221**(1): 51-60.

Fish, F. E. and G. V. Lauder (2006). "PASSIVE AND ACTIVE FLOW CONTROL BY SWIMMING FISHES AND MAMMALS." Annual Review of Fluid Mechanics **38**(1): 193-224.

Fontaine, A., J. Ellis*, et al.* (1996). "Identification of peak stresses in cardiac prostheses. A comparison of
two-dimensional versus three-dimensional principal stress analyses." ASAIO **42**(3): 154-63.

Foss, J. and K. B. M. Q. Zaman (1999). "Large-and small-scale vortical motions in a shear layer perturbed by tabs." Journal of Fluid Mechanics **382**: 307-329.

Gad-el-Hak, M. (2000). Flow Control: Passive, Active, and Reactive Flow Management. New York, NY, Cambridge University Press.

Gad-el-Hak, M. and D. M. Bushnell (1991). "Separation control: review." Journal of Fluids Engineering, Transactions of the ASME **113**(1): 5-30.

Garver, D., R. Kaczmarek*, et al.* (1998). "The Epidemiology of Prosthetic Heart Valves in the United States." Tex Heart Inst. J. **22**(1): 86-91.

Gieresiepen, M., U. Krause*, et al.* (1989). "Velocity and shear stress distribution downstream of mechanical heart valves in
pulsatile flow." Int J Artif Organs **12**(4): 261-9.

Giersiepen, M., L. Wurzinger*, et al.* (1990). "Estimation of shear stress-related blood damage in heart valve prostheses--in
vitro comparison of 25 aortic valves." Int J Artif Organs **13**(5): 300-6.

Graf, T., H. Fischer*, et al.* (1991). "Cavitation potential of mechanical heart valve prostheses." Int J Artif Organs **14**(3): 169-74.

Grigioni, M., C. Daniele*, et al.* (2004). "The Power-law Mathematical Model for Blood Damage Prediction: Analytical Developments and Physical Inconsistencies." Artificial Organs **28**(5): 467-475.

Gross, J., M. Shu*, et al.* (1996). "A microstructural flow analysis within a bileaflet mechanical heart valve hing." J Heart Valve Dis. **5**(6): 581-90.

Gutmark, E. J. and F. F. Grinstein (1999). Flow control with noncircular jets, Annual Reviews Inc, Palo Alto, CA, USA. **31:** 239-272.

Guyton, A. and J. Hall (2000). Textbook of Medical Physiology. Philadelphia, PA, W. B. Saunders Company.

Hammermeister, K. E., G. K. Sethi*, et al.* (1993). "A Comparison of Outcomes in Men 11 Years after Heart-Valve Replacement with a Mechanical Valve or Bioprosthesis." N Engl J Med **328**(18): 1289-1296.

Harken, D., H. Soroff*, et al.* (1960). "Partial and complete prostheses in aortic insufficiency." J Thorac Cardiovasc Surg **40**: 744-62.

Harken, D., W. Taylor*, et al.* (1962). "Aortic valve replacement with a caged ball valve." Am J Cardiol. **9**: 292-9.

Hathcock, J. J. (2006). "Flow Effects on Coagulation and Thrombosis." Arterioscler Thromb Vasc Biol **26**(8): 1729-1737.

Healy, T. M., A. A. Fontaine*, et al.* (1998). "Visualization of the hinge flow in a 5:1 scaled model of the medtronic parallel bileaflet heart valve prosthesis." Experiments in Fluids **25**(5): 512-518.

Hellums, J. (1994). "1993 Whitaker lecture: Biorheology in thrombosis research " Journal of Biomedical Engineering **22**(5): 445-455.

Heuser, G. and R. Opitz (1980). "A Couette viscometer for short time shearing of blood." Biorheology **17**(1-2): 17-24.

Ho, C.-M. and E. Gutmark (1987). "VORTEX INDUCTION AND MASS ENTRAINMENT IN A SMALL-ASPECT-RATIO ELLIPTIC JET." Journal of Fluid Mechanics **179**: 383-405.

Hoek, J. A., A. Sturk*, et al.* (1988). "Laboratory and clinical evaluation of an assay of thrombin-antithrombin III complexes in plasma." Clin Chem **34**(10): 2058-2062.

Holme, P. A., U. Orvim, *et al.* (1997). "Shear-Induced Platelet Activation and Platelet Microparticle Formation at Blood Flow Conditions as in Arteries With a Severe Stenosis." Arterioscler Thromb Vasc Biol **17**(4): 646-653.

Hui, H., T. Kobayashi, *et al.* (1999). "Changes to the Vortical and Turbulent Structure of Jet Flows Due to Mechanical Tabs." Proceedings of the Institution of Mechanical Engineers -- Part C -- Journal of Mechanical Engineering Science **213**(4): 321-329.

Hung, T., R. Hocmuth, *et al.* (1976). "Shear-induced aggregation and lysis of platelets." Trans Am Soc Artif Intern Organs **22**: 285-91.

Ibrahim, M., H. O'Kane, *et al.* (1994). "The St. Jude Medical prosthesisA thirteen-year experience." J Thorac Cardiovasc Surg **108**(2): 221-230.

Island, T. C., W. D. Urban, *et al.* (1998). "Mixing enhancement in compressible shear layers via sub-boundary layer disturbances." Physics of Fluids **10**(4): 1008.

Jesty, J. and D. Bluestein (1999). "Acetylated prothrombin as a substrate in the measurement of the procoagulant
activity of platelets: elimination of the feedback activation of platelets by thrombin." Anal Biochem. **272**(1): 64-70.

Jesty, J., W. Yin, *et al.* (2003). "Platelet activation in a circulating flow loop: combined effects of shear stress and exposure time " Platelets **14**(3): 143-149.

Kim, J. H. and M. Samimy (1999). "Mixing enhancement via nozzle trailing edge modifications in a high speed rectangular jet." Physics of Fluids **11**(9): 2731-2742.

Klepetko, W., A. Moritz, *et al.* (1989). "Leaflet fracture in Edwards-Duromedics bileaflet valves." J Thorac Cardiovasc Surg **97**(1): 90-94.

Krishnan, S., H. S. Udaykumar, *et al.* (2006). "Two-Dimensional Dynamic Simulation of Platelet Activation During Mechanical Heart Valve Closure." Annals of Biomedical Engineering **34**(10): 1519-1534.

Lai, Y., K. Chandran, *et al.* (2002). "A numerical simulation of mechanical heart valve closure fluid dynamics " Journal of biomechanics **35**(7): 881-892.

Lamson, T., G. Rosenberg*, et al.* (1993). "Relative blood damage in the three phases of a prosthetic heart valve flow cycle." ASAIO **39**(3): 626-33.

Lawson, N. J. and M. R. Davidson (1999). "Crossflow Characteristics of an Oscillating Jet in a Thin Slab Casting Mould." Journal of Fluids Engineering **121**(3): 588-595.

Lawson, N. J. and M. R. Davidson (2001). "SELF-SUSTAINED OSCILLATION OF A SUBMERGED JET IN A THIN RECTANGULAR CAVITY." Journal of Fluids and Structures **15**(1): 59-81.

Lawson, N. J. and M. R. Davidson (2002). "Oscillatory Flow in a Physical Model of a Thin Slab Casting Mould With a Bifurcated Submerged Entry Nozzle." Journal of Fluids Engineering **124**(2): 535-543.

Lee, C., K. Chandran*, et al.* (1994). "Cavitation dynamics of mechanical heart valve prostheses." Artificial Organs **18**(10): 758-67.

Leo, H.-L., Z. He*, et al.* (2002). "Microflow fields in the hinge region of the CarboMedics bileaflet mechanical heart valve design." J Thorac Cardiovasc Surg **124**(3): 561-574.

Leo, H. (2005). An In Vitro Investigation of the Flow Fields Through Bileaflet and Polymeric Prosthetic Heart Valves. Biomedical Engineering. Atlanta, GA, Georgia Institute of Technology. **PhD**.

Leverett, L. B., J. D. Hellums*, et al.* (1972). "Red Blood Cell Damage by Shear Stress." Biophys. J. **12**(3): 257-273.

Lim, W., Y. Chew*, et al.* (2000). "In Vitro Squeeze Flow Phenomena at Instant of Mechanical Valve Closure." Japanese Journal of Artificial Organs **3**(2): 162-65.

Lim, W., Y. T. Chew*, et al.* (2001). "Pulsatile flow studies of a porcine bioprosthetic aortic valve in vitro: PIV measurements and shear-induced blood damage." Journal of Biomechanics **34**(11): 1417-1427.

Lim, W. L., Y. T. Chew*, et al.* (2003). "Cavitation phenomena in mechanical heart valves: the role of squeeze flow velocity and contact area on cavitation initiation between two impinging rods." Journal of biomechanics **36**(9): 1269-1280.

Lin, J. C., S. K. Robinson, *et al.* (1994). "Separation control on high-lift airfoils via micro-vortex generators." Journal of Aircraft **31**(6): 1317-1323.

Liu, J., P. Lu, *et al.* (2000). "Turbulence characteristics downstream of bileaflet aortic valve prostheses." J Biomech Eng **122**(2): 118-24.

Lu, P., H. Lai, *et al.* (2001). "A reevaluation and discussion on the threshold limit for hemolysis in a turbulent shear flow." Journal of Biomechanics **34**(10): 1361-1364.

Manning, K. B., V. Kini, *et al.* (2003). "Regurgitant Flow Field Characteristics of the St. Jude Bileaflet Mechanical Heart Valve under Physiologic Pulsatile Flow Using Particle Image Velocimetry." Artificial Organs **27**(9): 840-846.

Markus, H. (1993). "Transcranial Doppler detection of circulating cerebral emboli. A review." Stroke **24**(8): 1246-1250.

Masters, R. G., A. L. Pipe, *et al.* (1995). "Comparative results with the St. Jude Medical and Medtronic Hall mechanical valves." J Thorac Cardiovasc Surg **110**(3): 663-671.

Maurel, A., P. Ern, *et al.* (1996). "Experimental study of self-sustained oscillations in a confined jet." Physical Review E **54**(4): 3643.

Mi, J., G. J. Nathan, *et al.* (2001). "Mixing Characteristics of a Flapping Jet from a Self-Exciting Nozzle." Flow, turbulence and combustion **67**(1): 1-23.

Miyazaki, Y., S. Nomura, *et al.* (1996). "High shear stress can initiate both platelet aggregation and shedding of procoagulant containing microparticles." Blood **88**(9): 3456-3464.

Morsi, Y., M. Kogure, *et al.* (1999). "Relative blood damage index of the jellyfish valve and the Bjork-Shiley tilting-disk valve." Journal of Artificial Organs **2**(2): 163-169.

Nathan, G. J., S. J. Hill, *et al.* (1998). "An axisymmetric 'fluidic' nozzle to generate jet precession." Journal of Fluid Mechanics **370**: 347-380.

Nygaard, H., M. Gieresiepen, *et al.* (1990). "Estimation of turbulent shear stresses in pulsatile flow immediately downstream
of two artificial aortic valves in vitro." J Biomech **23**(12): 1231-8.

O'Brien, M. F., E. Gregory Stafford*, et al.* (1995). "Allograft aortic valve replacement: Long-term follow-up." The Annals of Thoracic Surgery **60**(Supplement 2): S65-S70.

Paraskos, J. A. (2000). Combined Valvular Disease. Valvular Heart Disease. J. Alpert, J. Dalen and S. Rahimtoola. Philadelphia, PA, Lippincott Williams & Wilkins.

Pearcey, H. (1961). Shock-Induced Separation and its Prevention by Design and Boundary Layer Cotnrol. Boundary Layer and Flow Control. G. Lachmann. New York, NY, Pergamon Press. **2**.

Pelzer, H., A. Scwarz*, et al.* (1988). "Determination of human thrombin-antithrombin III complex in plasma with an enzyme-linked immunosorbent assay." Thromb Haemost. **59**(1): 101-6.

Rambod, E., M. Beizai*, et al.* (2007). "Role of Vortices in Growth of Microbubbles at Mitral Mechanical Heart Valve Closure." Annals of Biomedical Engineering **35**(7): 1131-1145.

Rambod, E., M. Beizaie*, et al.* (1999). "A Physical Model Describing the Mechanism for Formation of Gas Microbubbles in Patients with Mitral Mechanical Heart Valves." Annals of Biomedical Engineering **27**(6): 774-792.

Ramstack, J., L. Zuckerman*, et al.* (1979). "Shear-induced activation of platelets." J Biomech. **12**(2): 113-25.

Rao, D. and T. Kariya (1988). Boundary-layer submerged vortex generators for separation control - An exploratory study. National Fluid Dynamics Congress. Cincinnati, OH, American Institute of Aeronautics and Astronautics; p. 839-846.

Raz, S., S. Einav*, et al.* (2007). "DPIV Prediction of Flow Induced Platelet Activation—Comparison to Numerical Predictions." Annals of Biomedical Engineering **35**(4): 493-504.

Reeder, M. F. and K. B. M. Q. Zaman (1996). "Impact of tab location relative to the nozzle exit on jet distortion." AIAA Journal **34**(1): 197-199.

Rockwell, D. (1983). "Oscillations of Impinging Shear Layers." AIAA Journal **21**(5): 645-664.

Rooney, J. A. (1970). "Hemolysis Near an Ultrasonically Pulsating Gas Bubble." Science **169**(3948): 869-871.

Sallam, A. and N. Hwang (1984). "Human red blood cell hemolysis in a turbulent shear flow: contribution of Reynolds shear stresses." Biorheology **21**(6): 783-97.

Schubauer, G. B. and W. G. Spangenberg (1960). "Forced mixing in boundary layers." Journal of Fluid Mechanics **8**(Part 1): 10-32.

Selzer, A. (1983). "Present status of prosthetic cardiac valves." Arch Intern Med **143**(10): 1965-1967.

Sherwood, L. (2003). Human Physiology: From Cells to Systems, Brooks/Cole Publishing Company.

Simon, H. (2004). Influence of the Implant Location on the Hinge and Leakage Flow Fields Through Bileaflet Mechanical Heart Valves. Chemical Engineering. Atlanta, GA, Georgia Institute of Technology. **MS**.

Simon, H. A., H.-L. Leo*, et al.* (2004). "Comparison of the Hinge Flow Fields of Two Bileaflet Mechanical Heart Valves under Aortic and Mitral Conditions." Annals of Biomedical Engineering **32**(12): 1607-1617.

Starr, A. and M. Edwards (1961). "Mitral Replacement: Clinical Experience with a Ball-Valve Prosthesis." Annals of Surgery **154**(4): 726-740.

Stein, P. D., J. S. Alpert*, et al.* (2001). "Antithrombotic Therapy in Patients With Mechanical and Biological Prosthetic Heart Valves." Chest **119**(90010): 220S-227.

Sutera, S., M. Nowak*, et al.* (1988). "A programmable, computer-controlled cone-plate viscometer for the application of
pulsatile shear stress to platelet suspensions." Biorheology **25**(3): 449-59.

Sutera, S. P. (1977). "Flow-induced trauma to blood cells." Circ Res **41**(1): 2-8.

Sutera, S. P. and M. H. Mehrjardi (1975). "Deformation and fragmentation of human red blood cells in turbulent shear flow." Biophys. J. **15**(1): 1-10.

Thai, H. and J. Gore (2000). Prosthetic Heart Valves. Valvular Heart Disease. J. Alpert, J. Dalen and S. Rahimtoola. Philadelphia, PA, Lippincott Williams & Wilkins.

Thom, T., N. Haase*, et al.* (2006). "Heart Disease and Stroke Statistics--2006 Update: A Report From the American Heart Association Statistics Committee and Stroke Statistics Subcommittee." Circulation **113**(6): e85-151.

Tiederman, W. G., R. M. Privette*, et al.* (1988). "Cycle-to-cycle variation effects on turbulent shear stress measurements in pulsatile flows." Experiments in Fluids **6**(4): 265-272.

Travis, B. (2001). The effects of bileaflet prosthesis pivot geometry on turbulence and blood damage potential. Chemical Engineering. Atlanta, GA, Georgia Institute of Technology. **PhD**.

Travis, B., U. Marzec*, et al.* (2001a). "The sensitivity of indicators of thrombosis initiation to a bileaflet prosthesis
leakage stimulus." J Heart Valve Dis. **10**(2): 228-38.

Travis, B., U. Marzec*, et al.* (2001b). "Bileaflet Aortic Valve Prosthesis Pivot Geometry Influences Platelet Secretion and Anionic Phospholipid Exposure." Annals of Biomedical Engineering **29**(8): 657-664.

Travis, B. R., H. L. Leo*, et al.* (2002). "An Analysis of Turbulent Shear Stresses in Leakage Flow Through a Bileaflet Mechanical Prostheses." Journal of Biomechanical Engineering **124**(2): 155-165.

Travis, B.R., Anderson, M., *et al*. (2008) "The Effect of Gap Width on Viscous Stresses within the Leakage across a Bileaflet Valve Pivot." Journal of Heart Valve Disease, **17**:309-316.

Truskey, G., F. Yuan*, et al.* (2004). Transport Phenomena in Biological Systems. Upper Saddle River, NJ, Pearson, Prentice Hall.

Tsai, F. K., J. L. Lauer*, et al.* (2006). "Aggregation of blood components on a surface in a microfluidic environment." Journal of Applied Physics **99**(2): 024701.

van der Meer, F. J., F. R. Rosendaal*, et al.* (1993). "Bleeding complications in oral anticoagulant therapy. An analysis of risk factors." Arch Intern Med **153**(13): 1557-1562.

Vijaykumar, M., J. Narula*, et al.* (1994). "Incidence of rheumatic fever and prevalence of rheumatic heart disease in India." International Journal of Cardiology **43**(3): 221-8.

Villermaux, E. and E. J. Hopfinger (1994). "Self-sustained oscillations of a confined jet: a case study for the non-linear delayed saturation model." Physica D: Nonlinear Phenomena **72**(3): 230-243.

Wang, X. K., L. P. Chua*, et al.* (2003). "On the near-field of a square jet with vortex-generating tabs." Fluid Dynamics Research **32**(3): 99-117.

Whyte, I., N. Buckley*, et al.* (2000). "Acetaminophen Causes an Increased International Normalized Ratio by Reducing Functional Factor VII." Therapeutic Drug Monitoring **22**(6): 742-748.

Williams, A. R., D. E. Hughes*, et al.* (1970). "Hemolysis Near a Transversely Oscillating Wire." Science **169**(3948): 871-873.

Wurzinger, L., R. Opitz*, et al.* (1985). "Platelet and coagulation parameters following millisecond exposure to laminar
shear stress." Thromb Haemost. **54**(2): 381-6.

Yin, W., Y. Alemu*, et al.* (2004). "Flow-Induced Platelet Activation in Bileaflet and Monoleaflet Mechanical Heart Valves." Annals of Biomedical Engineering **32**(8): 1058-1066.

Yin, W., S. Gallocher*, et al.* (2005). "Flow-induced Platelet Activation in a St. Jude Mechanical Heart Valve, a Trileaflet Polymeric Heart Valve, and a St. Jude Tissue Valve." Artificial Organs **29**(10): 826-831.

Yin, W., I. Krukenkamp*, et al.* (2006). "Thrombogenic performance of a st. Jude bileaflet mechanical heart valve in a
sheep model." ASAIO **52**(1): 28-33.

Yoganathan, A. (1995). Cardiac Valve Prostheses. The Biomedical Engineering Handbook. J. Bronzino. Boca Raton, FL, CRC Press**:** 1847-1870.

Yoganathan, A. (2006). Cardiac Valve Prostheses. Biomedical Engineering Fundamentals. J. Bronzino, CRC Taylor and Francis.

Yoganathan, A., Y. Woo*, et al.* (1986). "Turbulent shear stress measurements in the vicinity of aortic heart valve
prostheses." J Biomech. **19**(6): 433-42.

Yu, S., Y. Hou*, et al.* (1998). "The flow characteristics of a confined square jet with mixing tabs." Proceedings of the Institution of Mechanical Engineers, Part G: Journal of Aerospace Engineering **212**(2): 63-76.

Yu, S., T. Yip*, et al.* (1997). "Mixing Characteristics of Forced Mixers with Scalloped Lobes " Journal of Propulsion and Power **13**(2): 305-311.

Zaman, K. B. M. Q. (1999). "Spreading characteristics of compressible jets from nozzles of various geometries." Journal of Fluid Mechanics **383**: 197-228.

Zaman, K. B. M. Q. (2001). Effect of Delta Tabs on Free Jets from Complex Nozzles. NASA.

Zaman, K. B. M. Q., M. F. Reeder*, et al.* (1994). "Control of an axisymmetric jet using vortex generators." Physics of Fluids **6**(2): 778-793.

Zhang, P., J. Yeo*, et al.* (2006). "Development of Squeeze Flow in Mechanical Heart Valve: A Particle Image Velocimetry Investigation." ASAIO **52**(4): 391-397.